Development and Optimization of Novel Cryogenic Calorimeters for COSINUS

Mukund Raghunath Bharadwaj

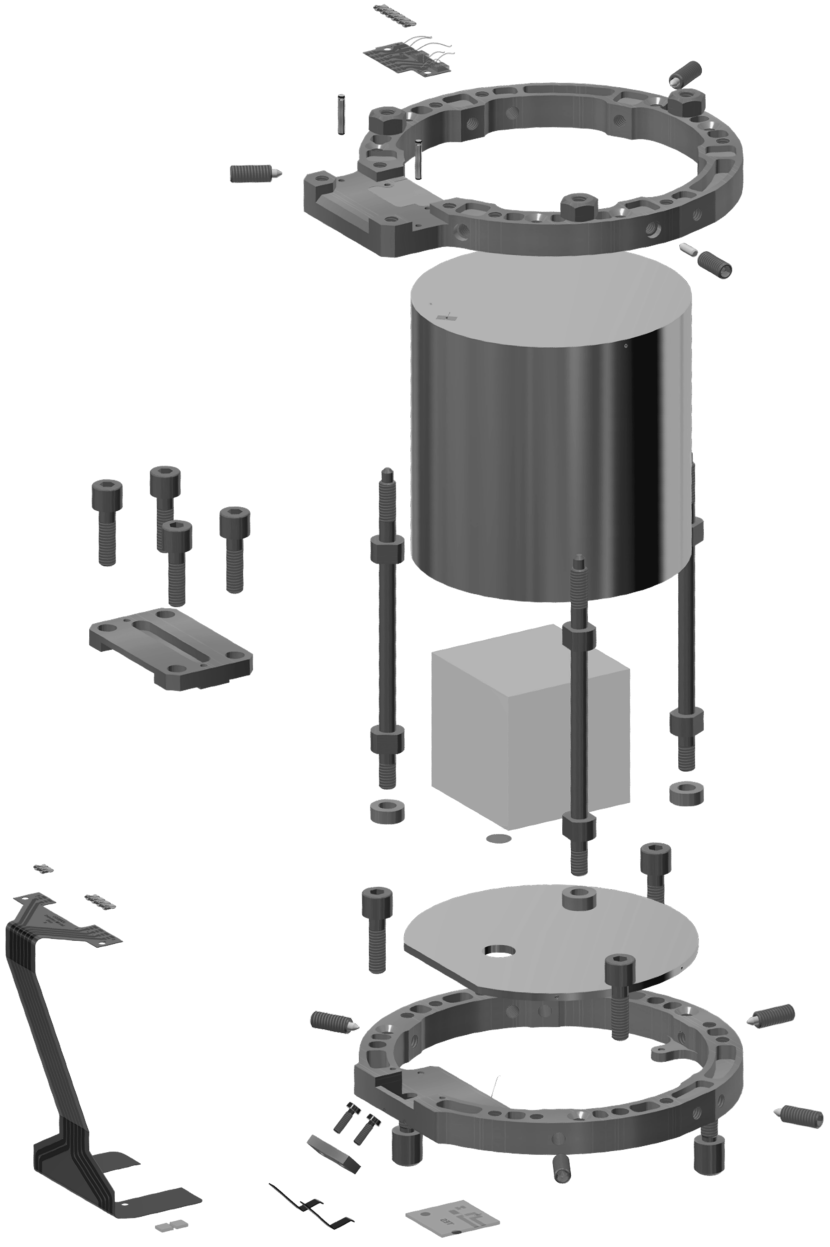

MAX-PLANCK-INSTITUT
FÜR PHYSIK

Development and Optimization of Novel Cryogenic Calorimeters for COSINUS

Mukund Raghunath Bharadwaj

Dissertation
an der Fakultät für Physik
der Ludwig–Maximilians–Universität
München

vorgelegt von
Mukund Raghunath Bharadwaj
aus New Delhi, India

München, den 12.05.2025

Erstgutachter: Prof. Dr. Otmar Biebel
Zweitgutachter: Dr. Stefan Kluth
Tag der mündlichen Prüfung: 01.07.2025

Zusammenfassung

Das Verständnis der Teilchennatur der Dunklen Materie zählt zu den zentralen Herausforderungen der modernen Physik. Trotz umfangreicher astrophysikalischer Evidenz für ihre Existenz, besteht bisher kein direkter experimenteller Nachweis solcher Teilchen. Diese Arbeit beschreibt die systematische Entwicklung, Optimierung und Charakterisierung kryogener Natriumiodid (NaI) Kalorimeter für das COSINUS-Experiment, ein Experiment zur direkten Suche von Dunkler Materie, das die Beobachtungen des DAMA/LIBRA-Experiment und insbesondere eines möglicherweise durch Dunkle Materie verursachten Modulationssignals unabhängig überprüfen soll.
Kernstück der vorliegenden Arbeit bildet das sogenannte remoTES-Konzept, ein neuartiger Ansatz für kryogene Detektoren, bei dem ein Absorberkristall über eine dedizierte thermische Goldverbindung bei kryogenen Temperaturen mit einem räumlich davon getrennten Transition-Edge-Sensor (TES) gekoppelt wird. Diese Entkopplung vereinfacht die massenhafte TES-Herstellung in großer Stückzahl und vermeidet zudem zusätzliche Oberflächenbehandlungen, welche die Radioreinheit beeinträchtigen können.

Der erste Teil der Arbeit widmet sich den zentralen Herausforderungen rein szintillationsbasierter NaI-Experimente, die zur Zeit betrieben werden oder sich in Planung befinden, und präsentiert eine detaillierte Untersuchung der energieabhängigen Quenching-Faktoren der Szintillation von NaI-Kristallen. Die Quenching-Faktoren sind essenziell zur für die exakten Interpretation experimenteller Ergebnisse unerlässlich, da Elektronen- und Kernrückstöße unterschiedliche Lichtausbeuten zeigen. COSINUS verwendet hierfür ein zweikanaliges, auf TES basierendes Auslesesystem, das nicht nur die in-situ-Bestimmung der Quenching Faktoren, sondern insbesondere auch eine Unterscheidung der wechselwirkenden Teilchen. Dabei werden hochreine szintillierende NaI-Kristalle verwendet, deren Phononsignal mittels des remoTES ausgelesen wird. Zur simultanen Erfassung des korrespondierenden Szintillationssignals dienen umgebende Siliziumdetektoren. In den nachfolgenden Kapiteln werden die Errichtung und Inbetriebnahme einer Untergrundanlage an den Laboratori Nazionali del Gran Sasso (LNGS), Italien, dokumentiert. Diese Anlage umfasst einen eigens für COSINUS konzipierten, trockenen Entmischungskryostat, einen speziellen Reinraum und ein Myon-Vetosystem. Sämtliche Arbeiten erfolgten im Rahmen dieser Dissertation.

Mit ersten erfolgreichen Tests an Standardabsorbern (Silizium, Tellurdioxid) konnte die technische Machbarkeit des remoTES-Konzeptes demonstriert werden. Nachfolgende Optimierungen hatten zum Ziel, leistungsmindernde Effekte zu reduzieren, die durch die Goldverbindung verursacht wurden.

Auf diese Optimierungen folgten experimentelle Untersuchungen mit NaI, welche in zunächst oberirdischen Messungen eine erfolgreiche Unterscheidung der wechselwirkenden Teilchen für jedes einzelne Ereignis. Diese Ergebnisse wurden anschließend durch unterirdische Messungen am LNGS validiert, wobei bereits mit geringer Datenmenge (11.6 g d) Ausschlussgrenzen in der Nähe des DAMA/LIBRA-Signals erzielt werden konnten.

Weitere Verfeinerungen umfassten gezielte Studien an siliziumbasierten Lichtdetektoren, Machbarkeitsuntersuchungen zu aufgedampften Goldschichten auf NaI-Kristallen sowie eine systematische Standardisierung der Fertigungsschritte. Daraus resultierte das optimierte 4π-Moduldesign, welches für die Run 1 von COSINUS verwendet wird.

Abstract

Understanding the particle nature of dark matter remains one of the central challenges in modern physics. Despite extensive astrophysical evidence supporting its existence, direct experimental detection of such particles remains elusive. This thesis presents the systematic development, optimization, and characterization of cryogenic sodium iodide (NaI) calorimeters tailored for the COSINUS experiment, a direct dark matter detection experiment designed to independently verify the DAMA/LIBRA findings of a potential dark matter-induced modulation signal.

Central to this research is the *remo*TES design - a novel approach for cryogenic detectors, in which an absorber crystal is connected to a Transition Edge Sensor (TES) via a dedicated thermal gold link. This decoupling allows mass fabrication of TES devices on separate wafers, preserving the radiopurity of the absorber by eliminating additional surface treatments.

The first part of the thesis addresses some of the crucial challenges faced by scintillation-only NaI-based readout experiments currently operational or under planning, and presents a detailed study of the energy-dependent quenching factors of NaI crystals - essential for accurately interpreting experimental results as electron recoils and nuclear recoils have dissimilar scintillation light yields. COSINUS utilizes a two-channel readout system based on TESs that allows for particle discrimination and in-situ determination of these quenching factors. It consists of ultrapure scintillating NaI crystals, read out using the *remo*TES design to measure the phonon signal of a particle interaction. A silicon detector surrounding the crystal is used to measure the light signal from the same particle interaction.

Subsequent chapters document the construction and commissioning of the low-background experimental facility at Laboratori Nazionali del Gran Sasso (LNGS), Italy, featuring a muon veto system, dedicated clean room, and a specialized dry dilution refrigerator tailored for COSINUS commissioned in the context of this work.

Initial demonstrations with standard absorbers, namely silicon and tellurium dioxide, validated the feasibility of *remo*TES technology. Performance bottlenecks introduced due to the introduction of the gold link were addressed in subsequent optimization studies.
In parallel to these optimizations, experimental tests on NaI were performed, beginning with above-ground measurements on NaI crystals, demonstrating successful event-by-event particle discrimination. These results were followed up with an underground measurement at LNGS, achieving dark matter exclusion limits close to the benchmark set by the DAMA/LIBRA experiment with only a limited exposure (11.6 g d).

Additional refinements included dedicated studies on the silicon-based light detector, feasibility investigations into evaporated gold films on NaI crystals, and systematic standardization of fabrication techniques, culminating in the optimized 4π module design prepared for COSINUS Run 1.

Declaration

The work presented in this thesis was carried out in the COSINUS group at the Max-Planck-Institut für Physik (Werner-Heisenberg-Institut).

Creative Commons License

This work is licensed under the Creative Commons Attribution 4.0 International License. You are free to share and adapt this work, provided you give appropriate credit to the author.

To view a copy of the license, visit:
https://creativecommons.org/licenses/by/4.0/

COLOPHON

This document was typeset using KOMA-Script and LaTeX with the kaobook class.

Development and Optimization of Novel Cryogenic Calorimeters for COSINUS

Mukund Bharadwaj

Acknowledgements

As you progress through life, one often pieces together an image of their idealized self. I have been exceptionally fortunate to find this embodiment in my supervisor, Dr. Karoline Schäffner at the Max-Planck-Institut für Physik. Karo, your seemingly inexhaustible passion for anything that sparks interest and excitement is infectious; I often reflect that if I possess even a fraction of your vibrant energy and enthusiasm as my career unfolds, I will count myself incredibly fortunate :D. I am infinitely grateful for the opportunity to be part of COSINUS and for the invaluable mentoring you've provided. The vision you shared will guide my endeavors for years to come.
To Prof. Dr. Otmar Biebel, thank you for agreeing to be my Ph.D. supervisor at LMU and all the patient and helpful guidance provided throughout, especially towards the ending stretch.

Thank you to my colleagues at the Max-Planck-Institut für Physik for all the time together spanning the lab, office, and coffee/tea/cake sessions. In no particular order:

I'm thankful to Martin Stahlberg and Vanessa Zema for all the time they took to patiently explain any and all of my questions during the initial months (repeatedly!).

To Max Hughes, I'll always remember our time in the lab, from detector mounting and vDAQ debugging sessions to the unforgettable Weird Al singalongs at cryo2 :)

Kumrie Shera and Kilian Heim, thank you for making lab work sessions, everything from assembly to mounting and cool-downs, genuinely enjoyable occasions (even on days that Murphy's law was in full swing). Our fun discussions, both on and off-topic, were the perfect fuel that made all the difference.

To Moritz Kellermann, I appreciate your patience and willingness to engage on every topic imaginable during our impromptu office chats over the past four years :) Our divergent skill sets, while sometimes a unique dynamic, provided a valuable complement to my own, which ultimately proved very helpful to my progress.

Pablo Falla, I cherish the memories of table tennis matches, countless wide-ranging discussions, and the lively parties.
To Clemens Dittmar, Maximilian Gapp, Elisa Gaido, Sarah Braun, and Lutz Ziegele, I am confident that the next generation of COSINAUTs are an amazing group, and I eagerly anticipate the excellent results we will achieve together in the near future.
I couldn't have asked for a more wholesome group to help me stay on track.

Additionally, a special thanks extends to all members of the CRESST group. I must particularly mention Abhijit Garai, whose immense help during my initial months was invaluable. He patiently imparted his extensive cryogenics knowledge whenever I had any nagging questions regarding the setup, and was also incredibly supportive with bureaucratic matters.

Diana Werner, for all the help in navigating through the never-ending paperwork, and without whom I truly could not have managed to find a suitable apartment when I first moved to Munich.

To all my non-physicist friends (particularly Chinmaya, Vishruth and Arvind) who were always willing to listen to my monologue sessions about work, thank you for reminding me that the world does not actually revolve around physics.

To my parents and sister, your unwavering, unconditional love and support (even across several oceans and timezones) have been the bedrock of my life and are the primary reason I am where I am today. I know I wasn't always the easiest child (or younger brother) to handle while growing up and often found myself in some sort of mischief, but your constant belief in me means everything. I am eternally grateful to have had you by my side. This thesis is just as much my achievement as it is yours :)

Finally, to Reema, I am glad that I have the rest of my life to repay my debt to you, because it will indeed take at least that long.

Mukund Bharadwaj

asato mā sadgamaya,

tamaso mā jyotirgamaya,

mṛtyormā' mṛtaṃ gamaya.

oṃ śāntiḥ śāntiḥ śāntiḥ

"From ignorance, lead me to truth;

From darkness, lead me to light;

From death, lead me to immortality."

— *Brihadāraṇyaka Upaniṣad*, 1.3.28

Contents

List of Figures

List of Tables

Prologue

A Primer to Dark Matter 1

"The universe is full of magical things patiently waiting for our wits to grow sharper."
— Eden Phillpotts, *Author*

In 1906, Santiago Ramón y Cajal published his *History of the Nervous system*, which contained the first sketches of neuronal morphology using a piece of brain tissue stained with silver chromate, observed under a microscope. While rudimentary by modern standards, his work laid the foundation for modern day neuroscience. Since then, the field has evolved from tracing anatomical sketches to one probing consciousness itself, with the potential to treat conditions like Parkinson's and epilepsy emerging from its progress (not to mention the ever-growing field of machine learning emerging from parallel studies). None of this would have been possible without the iterative, and sometimes novel, development of instruments like functional Magnetic Resonance Imaging (fMRI) and optogenetics to push our understanding of the unknown further.

The search for Dark Matter (DM) is closing in on its own centennial milestone, with a quest to uncover what it is: it's fundamental properties and interactions are still open questions. Unlike neurons, DM has remained elusive (so far) despite constituting roughly 85% of the matter in the universe. While this statement might not appear particularly promising at first glance (given the similar timescales), it is, in fact, the exact opposite. Just as neuroscience required the expertise of a multidisciplinary approach which led to the invention of electrodes, MRI machines and genetic engineering, the hunt for DM has also been filled with a number of notable, but often overlooked innovations that developed along the journey taken to even begin to answer some of the above questions. The following chapter traces this evolution through the lens of the instrumentation. Sec. 1.1 and Sec. 1.2 chronicles the observational clues that transformed our understanding of DM from a theoretical 'curiosity' to a cosmological necessity. Sec. 1.3 briefly addresses some of the DM candidates one can choose from the sea of beyond WIMP paradigm candidates based on some key properties we can deduce from observational studies. Sec. 1.4 delves into the broad classification schemes of different DM detection methods.

1.1 The Beginnings

In 1933, a Swiss-born astronomer based in Caltech by the name of Fritz Zwicky made a rather counter-intuitive observation that would forever change our understanding of the universe. While studying the Coma Cluster, Zwicky noticed something peculiar: the luminous mass of the galaxies was far too small to account for the gravitational forces holding the cluster together [1].

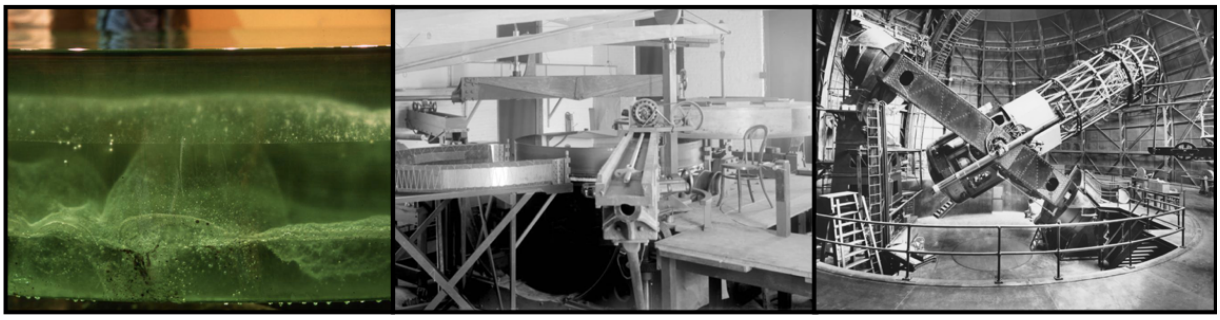

Figure 1.1: Left: A side view close-up of the 2.45 m mirror. It was cast in three layers: The lower layers contained numerous bubbles, swirls, and inclusions visible under torchlight, while the top layer was mostly bubble-free. Despite initial rejections due to these imperfections, the opticians decided to use the original blank in desperation after other recasting attempts failed; **Centre:** Grinding and polishing of the mirror blank; **Right:** The fully assembled Hooker telescope; *Image credits:* [8, 9]

Zwicky utilized the 2.45 m Hooker telescope, located at the Mount Wilson Observatory in Los Angeles County, California, United States [2]. The 2.45 m-wide telescope is most notable for its use in the discovery of Hubble's law [3] and was also the largest telescope for over 30 years before being succeeded by its younger sibling, the 4.9 m Palomar Observatory [4].

The mirror for the Hooker telescope was cast as a single piece at the Saint-Gobain factory in France [5] and left to cure for over 4 months. The casting process itself was fraught with challenges, requiring multiple attempts to achieve the desired glass properties. The final 29.4 cm thick, roughly 4.5 ton mirror blank, made of solid plate glass with a distinctive bottle-green hue, was shipped to Pasadena in December 1908*. It remains the largest monolithic glass mirror ever made, as modern telescopes that have followed since utilize a honeycomb mirror design. Water cooling via the support cells of the mirror helped ensure it did not undergo any internal stresses due to thermal gradients. A new mercury flotation bearing system, inspired by the system first used in the lighthouse tower at La Teignouse Lighthouse in France in 1892 [7] ensured that the bulky telescope could be precisely and smoothly moved.

The observatory allowed Zwicky to capture extensive photographic plates of the Coma Cluster as seen in Fig. 1.2, which was the primary medium to capture astronomical images at that time and allowed for a detailed, permanent record of positions and movements of numerous galaxies. Now, the *virial theorem* is a powerful tool in astrophysics, allowing one to roughly estimate the total mass of a gravitationally bound system, such as a globular cluster. Despite the inherent complexity of the N-body problem, the virial theorem provides a useful approximation for systems in equilibrium, where the distribution of velocities is roughly isotropic, and the overall system is not undergoing significant expansion or contraction.

* The mirror's green tint, visible under torchlight, has led to the legend that it might be made of Champagne bottle glass, given the proximity of Saint-Gobain to the Champagne region. The grinding process, completed over five years (!), was primarily performed using the world's largest grinding machine of the period [6], specifically designed to shape the glass into the desired parabolic form.

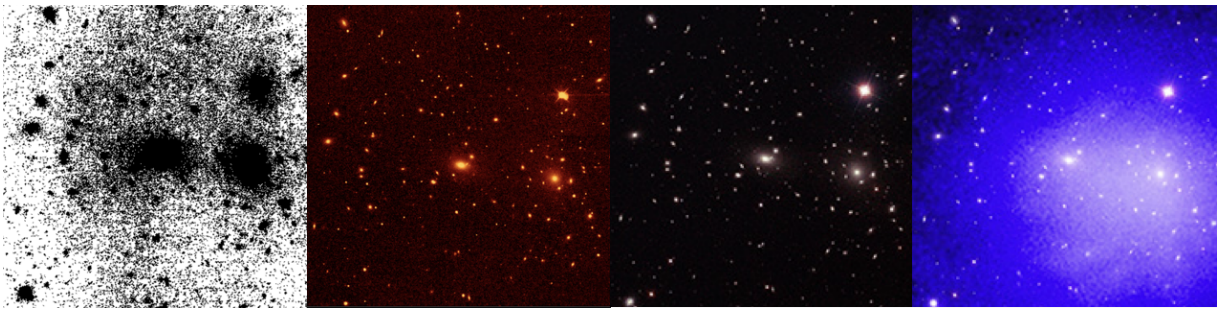

Figure 1.2: The Coma Cluster (zoom-in), observed across different wavelengths; From left: Photographic plate image of the cluster captured by Zwicky [10]; The cluster imaged by the ISO [11] in the infrared (~100 K); Hubble snapshot in the optical wavelength [12](~300-10,000 K); XMM-Newton image in the X-ray regime [13].

In such a system, it states that:

$$2 < T > + U = 0$$

where $< T >$ is the mean kinetic energy and U is the total gravitational potential energy. This relationship can be used to infer the total mass of the system if we can measure the velocities of its constituent bodies.

Zwicky applied the virial theorem to the Coma Cluster in his seminal 1937 paper [10]. He assumed that the cluster was in equilibrium and contained approximately 1000 galaxies within a radius of 2×10^6 light years. Using the observed velocity dispersion of 700 km/s, one could determine the total mass of the cluster and, subsequently, the average mass of a galaxy within it.

Given the assumptions and the virial theorem, the mass M of the cluster can be estimated using:

$$M = \frac{\alpha \langle v^2 \rangle R}{G}$$

where $\langle v^2 \rangle$ is the mean square velocity of the galaxies, R is the effective radius of the cluster, and G is the gravitational constant. The constant α typically accounts for the specific distribution of mass within the cluster.

His calculations yielded a total mass for the Coma Cluster of approximately $4.5 \times 10^{13}\, M_\odot$, where $M_\odot \approx 2 \times 10^{30}$ kg denotes the solar mass. Given the number of galaxies in the cluster, Zwicky estimated the average mass per galaxy to be $4.5 \times 10^{10}\, M_\odot$.

Zwicky then considered the luminosity of the galaxies, assuming an average absolute luminosity of $8.5 \times 10^7\, M_\odot$. From these figures, he computed a mass-to-light ratio:

$$\frac{4.5 \times 10^{10}\, M_\odot}{8.5 \times 10^7\, M_\odot} \approx 500$$

This extraordinarily high mass-to-light ratio was a significant anomaly. Zwicky's results for the Coma Cluster suggested that either the cluster was not in equilibrium, the laws of physics differed in this region, or, most intriguingly - there was a substantial amount of unseen "dark matter" contributing to the gravitational mass without emitting light.

Zwicky's analysis in 1937 did not definitively favor any single explanation but laid the groundwork for the DM hypothesis. Subsequent observations of other galaxies and clusters through the 1940s and 50s consistently supported the existence of "dark matter", which appeared to outmass ordinary, luminous matter [14].

The 1960s marked the next big milestone in optical astronomy, with the development of the image tube spectrograph. These instruments combined the spectral dispersion of traditional spectrographs with the light amplification of image tubes, which converted incoming light into an electron stream, amplified it, and then reconverted it into visible light. This amplified signal was recorded using photographic emulsion plates, which allowed astronomers to detect and analyze much fainter objects than what was previously possible.

Early emulsion photographic plates were made by coating a glass substrate with a light-sensitive emulsion containing silver halide crystals suspended in gelatin. Upon exposure to star-light, these crystals would form a latent image, which could then be developed into a visible photograph[†]. However, these plates had relatively large grain sizes, which limited their resolution and sensitivity. Advancements in the manufacturing processes (coincidentally) around the 1960s led to the development of emulsion plates with much finer grain structures. Baking the plates at a defined temperature, resulted in the shrinkage of the silver halide crystals and thus, became more uniformly distributed [15], making it an ideal pairing with image tube spectrographs.

A key focus of these spectrographs was the H_α line, a specific red spectral line at 656.3 nm which is a crucial tracer of ionized hydrogen in star-forming regions and the interstellar medium, making it ideal for studying galactic dynamics. By analyzing the Doppler shift of this line, astronomers could measure the rotational velocities of stars and gas, particularly in faint regions within galaxies. In contrast, traditional spectrographs required long exposure times to detect such faint signals, which posed several challenges, including motion blur from the dynamic movement of stars and increased noise from other sources.

Vera C. Rubin and W. Kent Ford Jr. employed such an image tube spectrograph (Fig. 1.3) to observe the Andromeda galaxy (M31) over the course of two years beginning in 1968. By measuring the Doppler shifts of the H_α line, they were able to determine the velocities of stars far from the galactic center. Fig. 1.3 shows the Doppler shifts in different regions of M31, with most of them revealing a shift very similar to each other, irrespective of distance or orientation. Their observations revealed that the velocities of stars did not decrease with increasing distance from the galactic center, as expected based on the distribution of visible matter [17]. Instead, the rotation curve remained relatively flat, implying the presence of unseen mass influencing the motion, later identified as DM. Rubin and Ford continued to document the behavior of many galaxies which were not rotating in a plane perpendicular to line-of-sight on Earth, observing a similar behavior among them all [18].

Radio astronomy significantly expanded the understanding of galactic rotation curves by allowing one to also observe neutral hydrogen (HI) gas in the outer regions of galaxies.

[†] The vintage film camera rolls popularized in the 1980s and 90s used a very similar principle to capture and develop photographs, albeit they used a glossy plastic film to sandwich the silver halide emulsion.

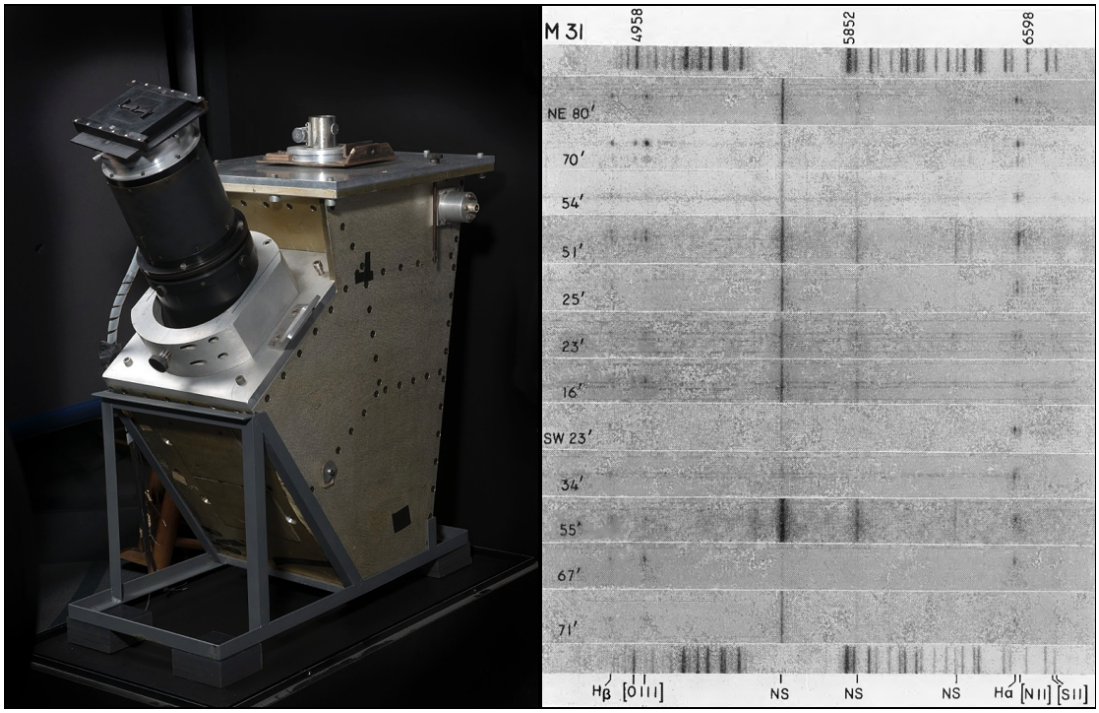

Figure 1.3: Left: Image of the original image tube spectrograph developed by W. Kent Ford Jr., *Image credits:* [16]; **Right:** Representative spectra of emission regions in the Andromeda Galaxy (M31), displayed as a function of distance from the galaxy's center. Each horizontal band corresponds to a different region in M31, with distances labeled in arcminutes. The vertical lines represent specific emission lines, namely H_β, doubly ionized oxygen [O III], H_α, singly ionized nitrogen [N II], and singly ionized sulfur [S II], which provide information about the chemical composition and motion of gas within the galaxy. The top strip shows a reference spectrum of neon (Ne) and iron (Fe) for wavelength calibration, with a scale in angstroms (Å). It can be observed that the Doppler shift of the H_α line is almost the same with increasing distance from the galactic center, irrespective of orientation. *Image credits:* [17].

Unlike stars, which are confined to the visible disk, HI gas extends far beyond the optical limits of galaxies, providing a means to probe the gravitational potential of these regions. The construction of large radio telescopes, such as the 76.2 m Lovell Telescope at Jodrell Bank in 1957 which was the largest steerable radio telescope of it's time, provided a new way to observe the universe beyond the visible spectrum. It had a sensitivity in the 21 cm (corresponding to the hyperfine transition of HI) to ~10 m wavelength, which enabled it to study the distribution of cold, non-luminous gases, previously unseen in optical measurements. By measuring the Doppler shifts of the 21 cm line, astronomers could determine the rotational velocities of HI gas far from the galactic center. ‡

The results from these radio observations were consistent with Rubin's optical findings: the rotation curves of spiral galaxies remained flat at large radii, well beyond the region populated by stars. This provided further evidence that the outer regions of galaxies are dominated by DM, forming an extended halo that influences the dynamics of the galaxy

‡ The frequency range this (and almost every ground-based) radio telescope is sensitive to, is unfortunately right in the zone where FM/TV broadcasts, satellite communications and other terresetrial signals lie in. Thus, in addition to the usual shielding and data processing pipelines, the surrounding areas (on-ground and in the sky) are designated as "radio quiet" zones where use of all electronic devices is restricted. With thousands of low-Earth orbit satellites expected to become operational over the next years by private companies, a valid concern of radio-pollution exists with no regulatory framework in place.

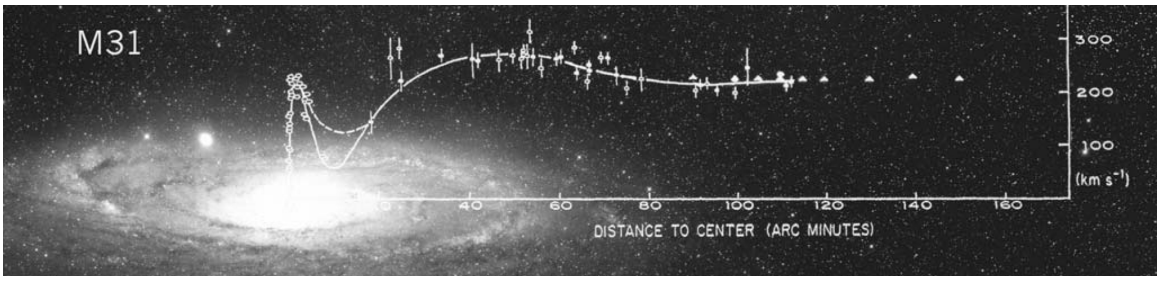

Figure 1.4: Rotation curves superimposed on M31 image from the 200-inch Hale telescope at Palomar Observatory. Reprinted with permission from [19]. The rotation curves obtained by Rubin *et al.* in [17] are indicated by the circles, extending up to 120 arcmin. The triangles represent measurements taken by a subsequent radio observation [20], extending up to 150 arcmin.

as a whole. Fig. 1.4 shows the rotational curves obtained by a combination of optical and radio measurements of M31.

1.2 Further Evidence for Dark Matter

The large fraction of DM deduced from the observations of rotation curves in spiral galaxies and galactic clusters places implications on other observable phenomena. The following subsections delve into more detail as to how the presence of DM influences large scale astronomical observations and plays a role in the structure formation of the universe.

1.2.1 Gravitational Lensing in Galactic Clusters

Gravitational lensing occurs when the gravitational field of a massive object - such as a galaxy cluster, bends the light from a more distant object. The degree of lensing depends on the total mass of the lensing object, including both visible matter and DM.

The first detailed observations of strong lensing in galactic clusters was carried out by the Hubble Space Telescope (HST). For example, in the galaxy cluster Abell 2218, HST images revealed multiple arcs and distorted images of background galaxies. Lens modeling showed that 85% of the cluster's mass must be non-luminous DM [21].

In addition to optical measurements, X-ray and radio telescopes are also employed, usually in tandem. X-ray telescopes like the Chandra X-ray Observatory have provided detailed maps of the hot gas in clusters, which can be compared with the mass distribution inferred from lensing to help confirm the presence of DM.

While strong gravitational lensing events tend to form distinct arcs and multiple images of background galaxies as seen in Fig. 1.5, weak gravitational lensing provides a kind of statistical evidence for DM on larger scales. [§] It's usually observed as subtle distortions

[§] The Bullet Cluster utlilized a combination of optical mass estimates using weak gravitational lensing and X-ray data from the Chandra observatory to deduce the proportion of DM in the cluster [23] and is among the most compelling evidence of the existence of DM as seen in galactic collisions, mergers, and acquisitions.

Figure 1.5: Gravitational lensing observed in the galaxy cluster Abell 2218 by the HST [22]. The arcs are images of distant galaxies distorted by the cluster's gravitational field.

of background galaxies' shapes, which can be detected over large areas of the sky using wide-field surveys such as the Sloan Digital Sky Survey (SDSS) [24].

1.2.2 Cosmic Microwave Background Radiation and Large Scale Structure Formation

In the early universe, a thermal equilibrium existed among a series of reactions involving photons, electrons, positrons, and protons. As the universe expanded and cooled below the binding energy of hydrogen (13.6 eV), approximately 380,000 years after the Big Bang, electrons and protons combined to form HI. This epoch, known as recombination, marked the decoupling of matter and radiation, allowing photons to travel freely. These photons, originating from a thermal background of ~3000 K, have since redshifted due to the universe's expansion, resulting in the Cosmic Microwave Background (CMB) radiation we observe today. This radiation exhibits a nearly isotropic blackbody spectrum with a temperature of 2.725 K, superimposed with minute anisotropies on the order of $\Delta T/T \sim 10^{-5}$, where T is the average CMB temperature. The corresponding frequency spectra lies in the microwave regime, peaking at around 160.4 GHz. These fluctuations represent the primordial density perturbations that, under the influence of gravity, helped 'seed' the formation of the large-scale structures we observe today. The Lambda Cold Dark Matter (ΛCDM) model, the prevailing cosmological framework, explains this evolution through a universe dominated by dark energy and cold dark matter (CDM).

The first detailed observation of these photons were conducted by the Cosmic Background Explorer (COBE) satellite, launched in 1989 [25]. The onboard Differential Microwave Radiometer (DMR) measured temperature anisotropies at three main frequencies: 31.5, 53 and 90 GHz, which confirmed the existence of tiny fluctuations in the CMB's temperature.

The Wilkinson Microwave Anisotropy Probe (WMAP) [29], launched in 2001, provided a ~20x better angular resolution than COBE, primarily due to its use of High Mobility

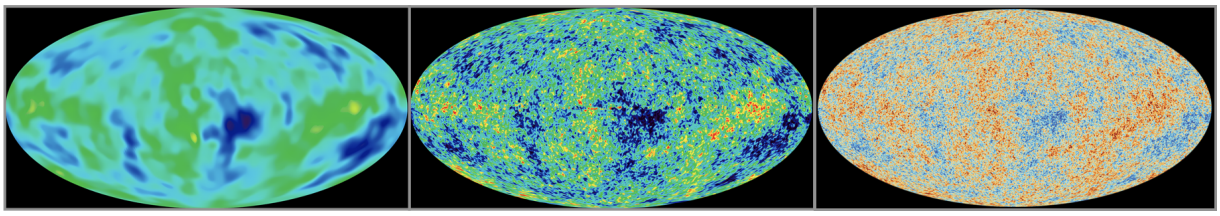

Figure 1.6: A comparison that shows the increasing resolution of the CMB missions over the years. The years correspond to the first data release; From left: The COBE satellite (1992) had an angular resolution of 7°, WMAP (2003) improved this down to 0.3°, while the Planck satellite further improved it down to just 0.08°. *Image credits:* [26–28]

Electron Transistor (HEMT) sensors paired with a DMR that could scan the skies at five frequencies ranging from 23 to 94 GHz. This allowed for a more detailed map of these fluctuations, refining estimates of the universe's composition. WMAP's 9-year data constrained DM density to $\Omega_{\text{DM}} = 0.268 \pm 0.013$ and revealed acoustic peak positions consistent with ΛCDM [29].

The most precise measurements of the CMB were made by the Planck Satellite, launched in 2009. It employed two instruments: A DMR focussed on frequencies the sub-100 GHz regime, paired with a High Frequency Instrument which consisted of a cryogenic bolometer array read out via Neutron Transmutation Doped (NTD) germanium thermistors (See Chapter 3) thermally linked to the array.

This combination of excellent angular resolution along with a broad frequency coverage allowed the expansion of CMB anisotropies into angular multipole moments, revealing a distinctive plateau for angular moments $l \lesssim 30$, followed by a series of acoustic peaks that diminish for $l \gtrsim 1000$ as seen in Fig. 1.7. The position and height of these peaks are highly sensitive to the universe's mass-energy content, with the ΛCDM model providing the most precise fit to the data. From the Planck dataset-3 release, the current estimates of the density parameters for DM (Ω_{CDM}) and baryonic matter (Ω_{b}) are: $\Omega_{\text{CDM}} = 0.2589 \pm 0.0057$ and $\Omega_{\text{b}} = 0.0486 \pm 0.0003$, respectively [31].

Numerical cosmological simulations, such as the Millenium simulation [32] discretize the DM density into particles that interact gravitationally, allowing researchers to model the evolution of structure from the early universe to the present day. The results from these simulations point towards a process of structure formation in the universe that is hierarchical, with smaller DM halos forming first and later merging to create larger structures. This hierarchical assembly leads to the formation of large, spherically symmetric DM halos that surround galaxies. These simulations demonstrate that DM forms the backbone of the large-scale structure, with baryons falling into the gravitational potential wells created by the DM halos. The resulting structures are also consistent with observations from galaxy surveys (such as SDSS), which reveals a similar neuronal-mesh like structure. Hydrodynamic simulations like the Illustris simulation [33] go a step further by incorporating both DM and baryonic physics. One key distinction between the baryonic physics modeled in such simulations and DM is that DM interacts solely via gravity and lacks dissipative mechanisms. Baryons, however, can cool and collapse due to radiative processes, forming compact structures like stars and galactic disks. This difference in behavior results in DM

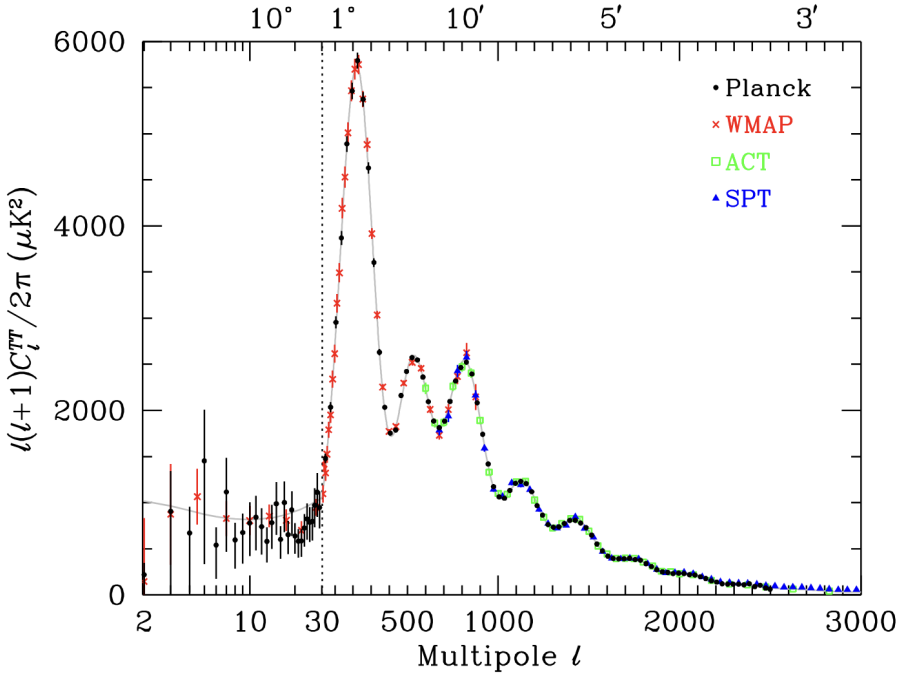

Figure 1.7: CMB power spectrum obtained by WMAP and Planck, overlaid with measurements from ground-based telescopes: The Atacama Cosmology Telescope (ACT) and the South Pole Telescope (SPT). *Image credits:* [30]. The horizontal axis is logarithmic for the lowest multipoles to show the plateau, and linear for other multipoles.

forming extended, quasi-spherical halos around galaxies, while baryons settle into more compact, disk-like formations. These DM halos extend far beyond the visible components of galaxies, which fits in well with observations discussed thus far. Baryonic processes, on the other hand, can lead to a variety of outcomes, from the formation of dense galactic centers to the ejection of matter that flattens the inner profiles of DM halos. For example, baryonic feedback processes such as supernova driven outflows, can dynamically heat DM, flattening the steep central density cusps predicted by ΛCDM simulations into observed constant-density cores[¶]. However, the previously discussed outcome still holds true: without DM halos serving as a "cosmic scaffolding", the large-scale structure formation observed today would not be possible.

1.3 Dark Matter Candidates

Based on the observations and phenomena described previously, a few key properties of DM have been derived and are as follows:

- It's elusive nature implies that an interaction with baryonic matter would be on the scale of the weak nuclear interaction.

[¶] This discrepancy, termed the core-cusp problem, is compounded by the central density conflict, where simulations overpredict dark matter in galactic centers compared to observations.

- DM is expected to be electrically neutral, as no absorption or emission of electromagnetic radiation is observed.
- As a result of the above points, DM is of non-baryonic character.
- The gravitational influence of DM on baryonic matter across cosmic scales indicates that it is massive.
- It must be stable on cosmological time scales, given its observed influence since the early universe.
- Simulations modelling structure formation in the universe [32], along with observations of large-scale structures, suggest that DM is non-relativistic, or cold.

These well-established properties necessitate that any new models or theories proposing DM candidates must align with the accepted models of large-scale structure formation and the Big Bang Nucleosynthesis (BBN) framework. Further, experimental verification of a DM candidate is contingent upon the existence of an interaction channel with baryonic matter.

1.3.1 WIMPs and WIMP Extensions

Weakly Interacting Massive Particles (WIMPs) have long been considered one of the most promising candidates for DM. Their appeal lies in their mass and weak interactions, which naturally arise in several extensions of the Standard Model, such as supersymmetry. WIMPs are expected to interact with normal matter through weak nuclear forces, making them detectable via direct and indirect methods. Direct detection experiments aim to observe WIMPs scattering off atomic nuclei, while indirect detection searches for the products of WIMP annihilation or decay. Collider experiments search for potential signatures of DM in high-energy baryonic collisions. Despite extensive efforts, no definitive detection of WIMPs has been made thus far.

Extensions of the WIMP paradigm include scenarios where the interaction strength or mass range of the WIMPs differs from the traditional expectations. For instance, models with heavier or lighter WIMPs, or those with interactions mediated by particles not yet discovered, continue to be an active area of research. The ongoing experiments, discussed in more detail in Chapter 2, seek to probe these extended models with increasing sensitivity.

1.3.2 Axions and ALPs

Beyond WIMPs, axions have emerged as a significant candidate for DM. Initially proposed as a solution to the strong CP problem in quantum chromodynamics, axions are light particles that interact weakly with matter, making them difficult to detect. The Axion Dark Matter eXperiment (ADMX) is at the forefront of axion searches, utilizing microwave cavity techniques to detect axions by their conversion into photons in the presence of a magnetic field.

In addition to axions, a broader class of particles known as axion-like particles (ALPs) is also considered as potential DM candidates. ALPs share many properties with axions but arise in a wider variety of theoretical frameworks, including string theory. These particles are characterized by their weak interactions and low mass, similar to axions, and could also be detected through their interactions with electromagnetic fields via the Primakoff effect. A comprehensive review is covered in [34].

1.3.3 Other Candidates

Apart from WIMPs and axions, other DM candidates have been proposed, each with distinct properties and theoretical motivations. These include sterile neutrinos, which are hypothesized to interact only via gravity and potentially weakly through a new force [35], and dark photons, which could mediate a new dark force [36]. Another intriguing possibility is the existence of primordial black holes, which could account for DM if they formed in sufficient abundance in the early Universe [37].

1.4 Searches for Dark Matter

DM searches can be broadly categorized into three types as outlined in Sec. 1.3.1. Each approach employs different methodologies and technologies, which are briefly explained below.

1.4.1 Types of Searches

Indirect Detection

Indirect searches for DM involve observing secondary particles that are potentially produced via DM annihilations or decays, which is governed by the DM annihilation cross-sections or the DM decay rate. These products include γ-rays, positrons, neutrinos, and other particles that can be detected by looking for an excess in the cosmic ray fluxes measured by detectors on (or nearby) Earth. Fig. 1.8 shows an example of how such a signal would look like.

The low energy photon spectrum is captured via data from land-based radio observatories and X-ray detectors in space like the Chandra X-ray observatory [39], XRISM [40] and/or eROSITA [41]. Cherenkov imaging telescopes like MAGIC [42] and CTA [43] operate by detecting the Cherenkov light generated by air showers that are produced when energetic γ-rays collide with atoms in the upper atmosphere. They are particularly sensitive and help provide a picture of the very high energy cosmic ray spectrum from the TeV to PeV range. Sky-survey instruments such as the Fermi-LAT [44] and AMS-02 [45] have provided valuable data by scanning the sky for positrons, anti-proton and heavy anti-nuclei fluxes. While no conclusive results have been obtained by most experiments, they help to set upper bounds on the expected DM annihilation cross-sections and decay rates, thus providing

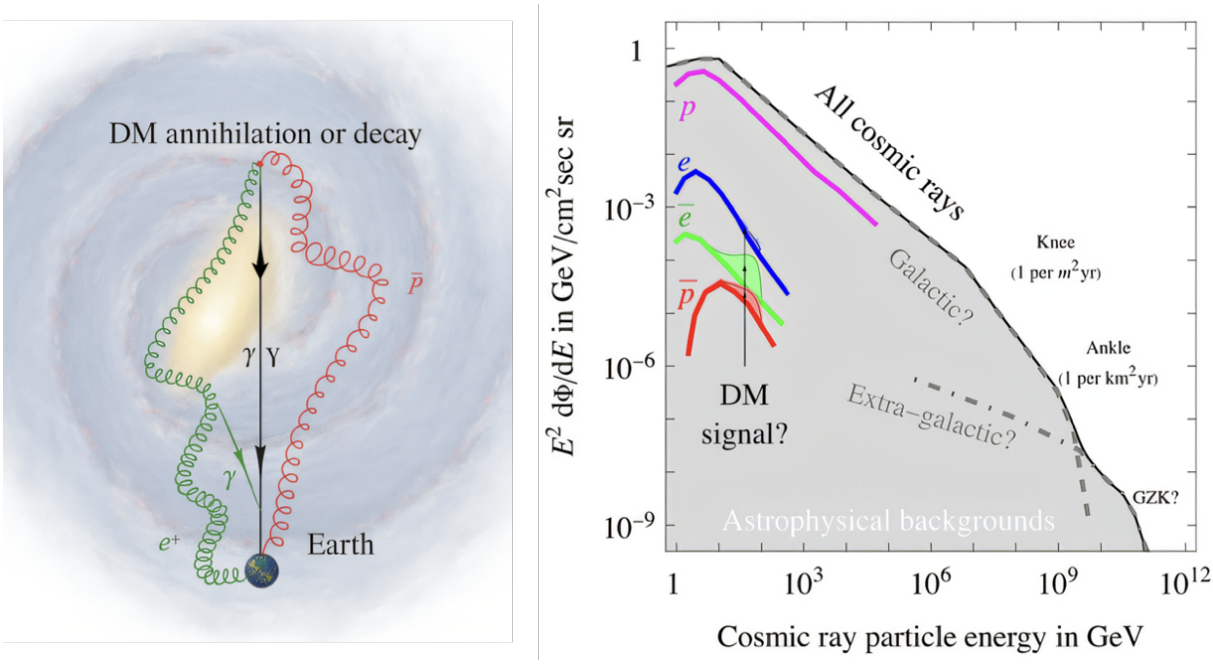

Figure 1.8: A sketch of indirect detection: A possible excess in the energy spectrum of cosmic rays could be produced due to DM annihilations or decays in the Milky Way. Adapted from [38].

a clearer picture on some properties of DM. A comprehensive summary of the current state-of-the art limits as on Autumn 2024 is given in [38].

Collider Searches

Collider searches aim to produce DM particles in high-energy collisions, such as those achieved in the Large Hadron Collider (LHC) [46]. These experiments are not sensitive enough to directly look for recoils of the produced DM particles, but rather, to look for missing energy signatures, which could indicate the production of DM.

Initial efforts at the Large Electron-Positron Collider (LEP) [47] (1989 - 2000) and Tevatron (1987-2011) [48] set the first limits on possible WIMP masses below 100 GeV using mainly electromagnetic calorimeters and Si detectors for energy reconstruction. The ATLAS [49] and CMS [50] experiments at LHC, operational since 2008, use a stack of Si pixel/strip detectors and calorimeters to reconstruct particle tracks and their corresponding energies. Although these searches have set stringent limits on DM interactions with Standard Model particles, no direct observation has been made so far [51]. The High-luminosity LHC (HL-LHC) [52] and future particle colliders like the Future Circular Collider (FCC) [53] will continue to play a key role in exploring this space with the help of improved precision timing detectors and high-granularity calorimeters.

Direct Detection

Direct detection experiments aim to observe DM particles interacting with normal matter primarily through atomic excitations, be it nuclear, or more recently electronic recoils.

The early experiments, which one could loosely call them as the first-generation detectors, utilized scintillation (eg. DAMA [54]) or ionization signals in low-background underground laboratories to search for WIMPs with masses in the $\mathcal{O}(100)$ GeV regime.

Second-generation experiments brought about a two-channel readout approach, which improved/introduced particle identification and discrimination. Experiments like XENON100 [55] and LUX [56] combined the scintillation and ionization signals to reach lower thresholds and cover a wider range of WIMP masses and cross-sections. CDMS [57] and CRESST-II [58] used low-temperature calorimetry (covered in Chapter 3) to read out phonon signals in coincidence with ionization/scintillation, respectively, to probe unexplored parameter space.

Current third-generation detectors like PandaX 4T [59], Lux-Zeplin (LZ) [60] and XENONnT [61] utilize multi-tonne detector volumes with a greater focus on background reduction/minimization which have enabled some of them to reach thresholds wherein solar neutrinos can be detected due to CEνNS [62, 63]. With SuperCDMS [64] and CRESST-III [65] leading the frontier on low-mass DM searches, a number of new experiments like COSINUS [66], HeRALD [67] and DARWIN [68] (to name a few) are also moving forward, utilizing and iterating on existing technologies to design novel readout schemes.

1.4.2 Focus of The Thesis

This thesis focuses on developing and optimization of a novel sensor technology for signal readout in cryogenic calorimeters, as utilized in the Cryogenic Observatory for SIgnatures seen in next-generation Underground Searches (COSINUS) experiment for readout of NaI crystals.

Chapter 2 examines the theoretical framework for direct DM detection, detailing interaction mechanisms and anticipated signal characteristics. Chapter 3 and Chapter 4 detail the COSINUS experiment, including its detector design, data acquisition techniques, and experimental setup.
Furthermore, Chapter 5, Chapter 6, and Chapter 7 provide an in-depth discussion on technological advancements aimed at standardizing detector development processes and describe the specific optimizations implemented for NaI-based cryogenic calorimeters.

Hunting for Dark Matter 2

"Truth is rarely hunted down easily; it must be tracked through tangled paths."
— Frank Herbert

2.1 Direct Detection Searches

The differential interaction rate of a target Standard Model (SM) particle with DM as a function of recoil energy, E_R, can be described by the equation:

$$\frac{dR}{dE_R} = \frac{\rho_\chi}{m_\chi m_T} \int v f(v) \frac{d\sigma_T(E_R, v)}{dE_R} d^3v \tag{2.1}$$

where ρ_χ is the galactic DM density, m_χ and m_T are the masses of the DM and the target, respectively, $f(v)$ represents the DM velocity distribution, and $\sigma_T(E_R, v)$ is the model-dependent cross-section of the interaction. The velocity distribution $f(v)$ typically assumed (but not necessarily precise as seen in Sec. 2.3) for galactic DM in Eq. 2.1 is the given by the Standard Halo Model (SHM), where the DM follows a truncated Maxwell-Boltzmann distribution:

$$f_{\text{SHM}}(v) = \frac{1}{(\pi v_0^2)^{3/2}} \exp\left[-\frac{1}{v_0^2}(\mathbf{v})^2\right]. \tag{2.2}$$

However, direct detection experiments are (mostly) conducted in terrestrial laboratories. Consequently, the DM velocity distribution in the galactic frame $f(v)$ (informed by astrophysical observations and simulations) must be transformed to yield the velocity distribution in the lab frame:

$$f_{\text{lab}}(\mathbf{v}) = f(|\mathbf{v} + \mathbf{v}_E|), \tag{2.3}$$

where $\mathbf{v}_E = (\mathbf{v}_\odot + v_\oplus \cos(\theta) \cos[\omega(t - t_0)])$ is the Earth's velocity, accounting for the solar velocity $\mathbf{v}_\odot$ and the Earth's rotation around the Sun $v_\oplus$. θ is the inclination of Earth's orbit with respect to the galactic plane and $\simeq 60°$. This rotation introduces a time dependence in the relative velocity, producing an annual cosine modulation that peaks roughly in June, when the Earth is traveling in the same direction as the Sun, as illustrated in Fig. 2.1.

Thus, for a detector on Earth, the differential scattering rate outlined in Eq. 2.1 can be re-written as:

$$\frac{dR}{dE_R} = \frac{\rho_\chi}{m_\chi m_T} \int_{v_{\text{min}}}^{v_{\text{esc}}} v f_{lab}(v) \frac{d\sigma_T(E_R, v)}{dE_R} d^3v \tag{2.4}$$

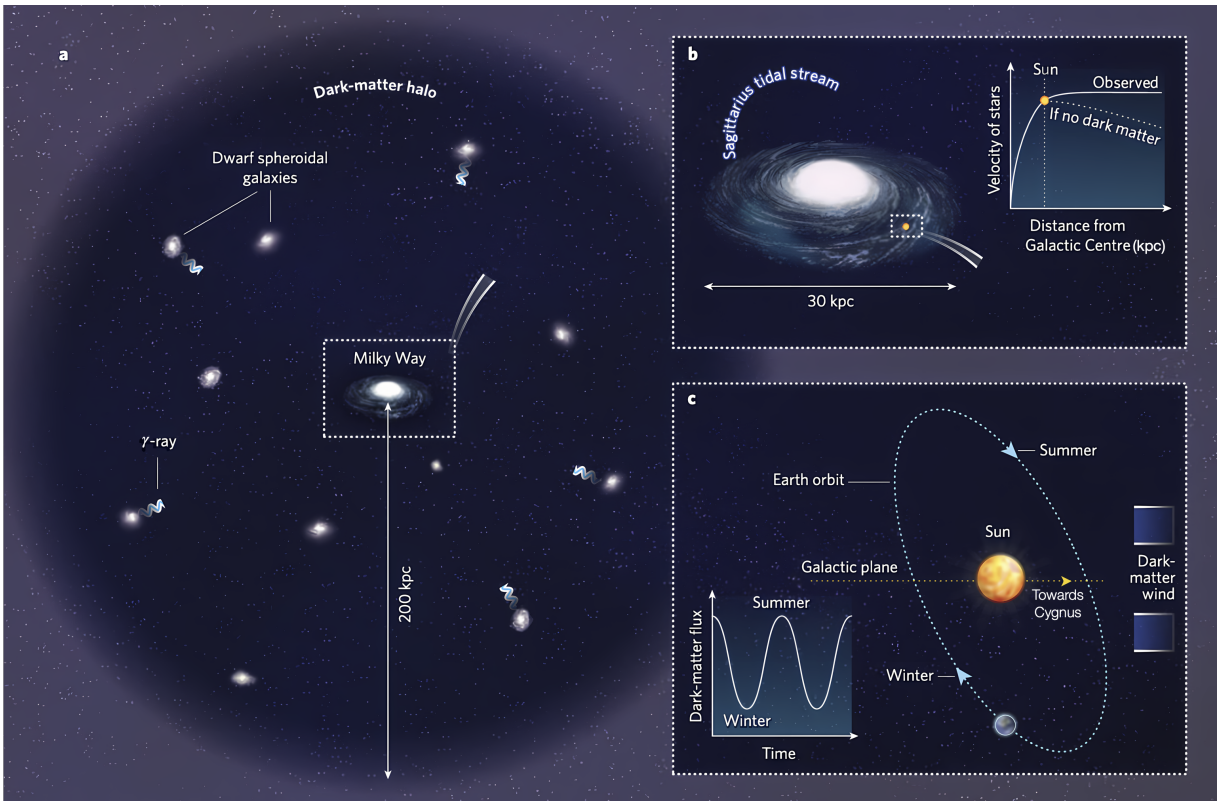

Figure 2.1: a) The Milky Way galaxy (approx. 30 kpc in diameter, inset) is depicted embedded within a vast, quasi-spherical DM halo (extending to 200 kpc); **b)** Evidence for the DM halo is provided by galactic rotation curves. The observed velocity of stars remains unexpectedly high at large distances from the galactic centre (Sun's position shown for reference), deviating from the Keplerian fall-off predicted if only visible matter existed. The Sagittarius tidal stream, a result of galactic interactions, is also shown; **c)** The annual modulation effect, a key signature for direct DM detection experiments. The Sun, and by extension the Earth, moves through the DM halo (towards the constellation Cygnus). Earth's revolution around the Sun causes its velocity relative to the DM "wind" to vary annually. This results in a periodic modulation of the expected DM interaction rate in terrestrial detectors, with a peak typically occurring in summer (when Earth's orbital velocity adds maximally to the Sun's galactic velocity) and a minimum in winter. (Note: Diagrams are not to scale). Image adapted from [69].

where $v f_{lab}(v)$ is the DM velocity distribution in the lab frame, with the integral ranging from the minimum velocity in the lab frame that can produce a recoil of a given energy, $v_{\min}$, up to the galactic escape velocity v_{esc}.

For elastic scattering, $v_{\min} = \sqrt{\frac{m_T E_R}{2\mu_{\chi,T}^2}}$, where $\mu_{\chi,T}$ is the reduced mass of the system and is given by:

$$\mu_{\chi,T} = \frac{m_\chi m_T}{m_\chi + m_T}.$$

In the case of inelastic scattering, a portion of the deposited energy will be spent on exciting the nucleus, denoted as E^*, thus $v_{\min}$ in this case would be: $\sqrt{\frac{m_T E_R}{2\mu_{\chi,T}^2}} + \sqrt{\frac{E^*}{m_T E_R}}$.

The differential scattering cross-section can further be expanded as:

$$\frac{d\sigma(E_R, v)}{dE_R} = \frac{m_T}{2\mu^2_{\chi,T} v^2} \left(\sigma_0^{SI} F^2_{SI}(E_R) + \sigma_0^{SD} F^2_{SD}(E_R) \right) \tag{2.5}$$

assuming only first-order spin-independent (SI) and spin-dependent (SD) interactions, which couple to the charge/mass and the spin of the nucleus, respectively. Here, $F^2(E_R)$ are the nuclear form factors and σ_0 is the effective cross-section for DM scattering on the nucleus in the limit of zero momentum transfer to the nucleus. In nuclei assuming DM coupling strength to protons and neutrons are the same:

$$\sigma_0^{SI} = \frac{\mu^2_{\chi,T}}{\mu^2_{\chi,T_n}} A^2 \sigma^{SI}_{0,nucleon}$$

where $\sigma^{SI}_{0,nucleon}$ is the cross-section for DM scattering on a nucleon and μ^2_{χ,T_n} is the reduced mass of the DM-nucleon system.

In other words, for a given standard process of a DM particle undergoing a SI elastic scattering off a target containing only one species of nuclei, Eq. 2.4 can be re-written as:

$$\frac{dR}{dE_R} = \frac{\rho_\chi A^2 \sigma^{SI}_{0,nucleon} F^2_{SI}(E_R)}{m_\chi 2\mu^2_{\chi,T_n}} g(v, t) \tag{2.6}$$

where, $g(v, t)$ is the velocity distribution $\int_{v_{\min}}^{v_{\text{esc}}} \frac{f_{lab}(v)}{v} d^3v$. This has a time-dependent component that arises naturally in accordance with Eq. 2.3. When the Earth's velocity is at its maximum in June, $g(v, t)$ peaks at a higher speed compared to January (with the June peak at $\sim$ 250 km/s and January at $\sim$ 225 km/s). As these distributions are normalized and integrated from a non-zero minimum velocity, this shift in peak position produces an annual modulation in the total interaction rate.

The observation of this modulating signal is considered a clear indicator of DM within the galaxy and can be detected without assuming any specific DM interaction model, as this time dependence arises solely from the velocity integral. The expected modulation value is typically on the order of a few percent of the average rate. However, in reality, this value depends on the particular interaction model and the velocity distribution under consideration, as well as the lower integral limit, $v_{\min}$, which is strongly dependent on the relative masses of the DM and the target used. Therefore, while the presence of a non-zero modulation is indeed indicative of galactic DM, its manifestation can vary significantly from one target to another as well as background modelling considerations in each experiment.

Referring back again to Eq. 2.6, the sensitivity of these searches is highly influenced by the target mass relative to m_χ, with the greatest sensitivity typically achieved when $m_\chi \approx m_T$. Therefore, to comprehensively explore the available parameter space, it is essential to employ a range of targets with varying masses (for both SI and SD interactions). Such plots, which constrain the parameter space of an (many) experiment(s) across a range of different DM masses and DM-nucleon cross-sections, are referred to as limit plots or

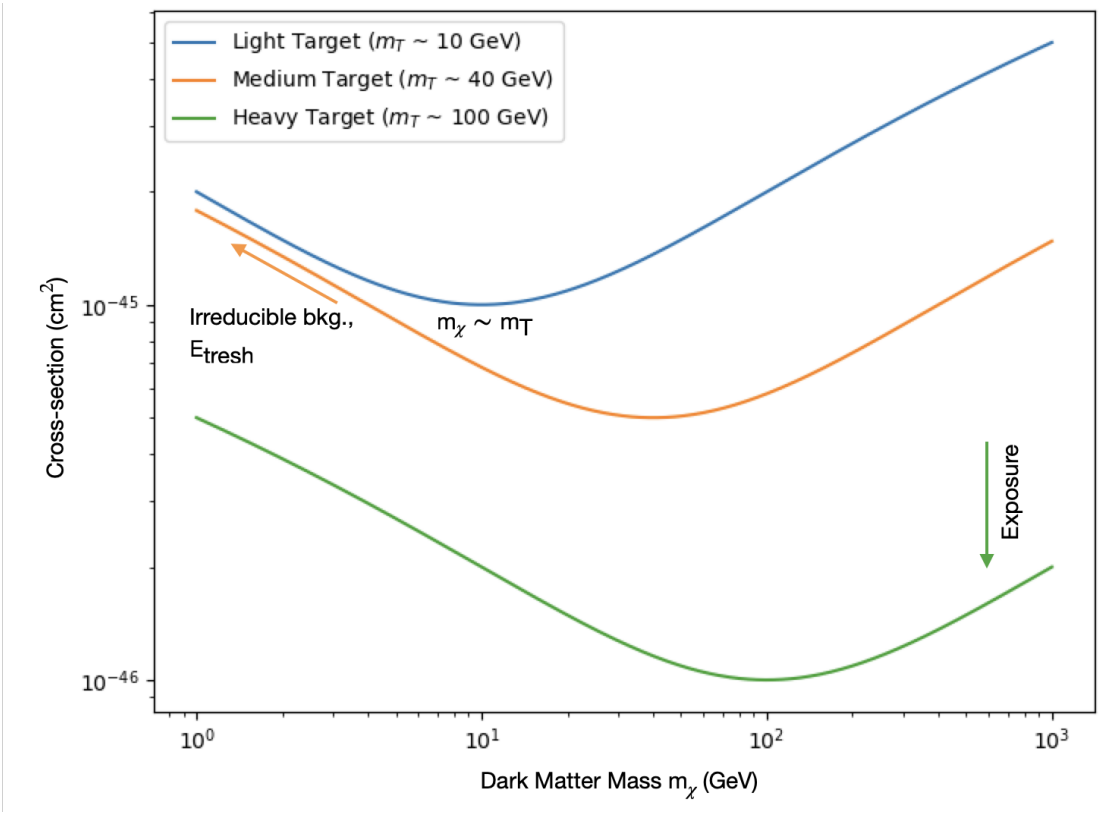

Figure 2.2: An example exclusion curve for three different experiments with different target masses (m_T) and exposures. An experiment is most sensitive in the region where $m_\chi \sim m_T$. For lower DM masses, it becomes less sensitive because for very light dark matter particles, the recoil energy imparted to the detector is often too small to be effectively detected (mainly due to the finite energy threshold of the detector itself but also due to irreducible backgrounds). For very heavy DM, the number density of DM particles in our galaxy for a given total DM mass density decreases. This leads to a lower interaction rate, and thus, the experiment becomes less sensitive, requiring a larger cross-section to be detectable. This scales roughly inversely with the DM mass.

exclusion curves (assuming no signature of DM was found). A typical exclusion plot has a boomerang shaped curve as depicted in Fig. 2.2. Points *above* the curve represent parameter space regions consistent with the null results of the experiment, meaning DM with these properties would not have been detected. Conversely, the area *below* the curve corresponds to parameter space that is not yet excluded by the experiment.

Over the years, there has been enormous progress in scaling up experiments to probe a wide range of cross-sections and masses. The scale of this progress is nicely represented in a plot shown by Rick Gaitskell in IDM 2022, and reproduced in Fig. 2.3.

Most of these direct detection experiments typically measure the energy of events via photon, charge, or phonon collection, or a combination of these channels. The primary target types and their detection methods are detailed in the following subsections.

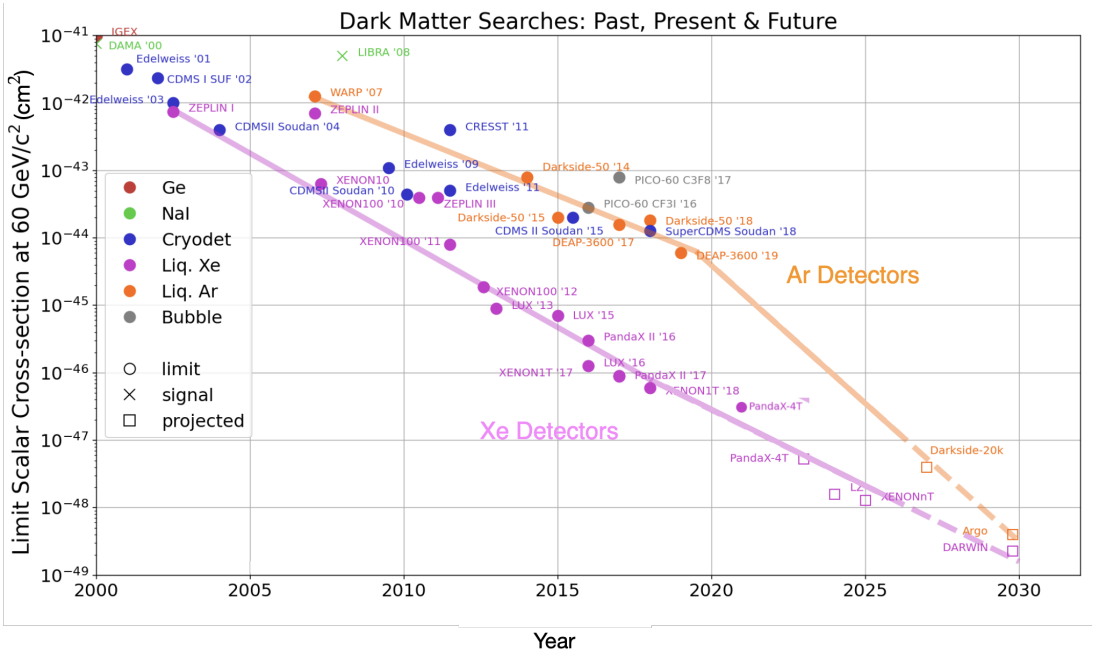

Figure 2.3: Rick's law: DM search experiments (in particular, experiments using noble liquids like Liq. Xe/Ar) in the ~60 GeV mass range gain a factor 10 improvement in sensitivity every 3.3 years [70].

2.1.1 Room Temperature Scintillators

These scintillators produce light upon DM interaction and include materials such as NaI(Tl) or CsI. Initially significant in the mid to late 1990s, their primary current use is to test the DAMA claim (see Sec. 2.2), as other methods can detect smaller cross-sections under standard WIMP assumptions. These setups, based on photon detection, probe recoil energy ranges on the keV scale, setting m_χ limits in the tens of GeV range.

2.1.2 Noble Liquids

Noble liquid detectors, which often operate in a dual-phase time projection chamber (TPC) configuration, exploit the simultaneous detection of prompt scintillation (S1) and delayed ionization (S2) signals. This dual-channel readout enables excellent discrimination between electron recoils (ER) and nuclear recoils (NR) while providing precise three-dimensional position reconstruction. Experiments such as XENONnT [61], LUX-ZEPLIN [60], and the proposed DARWIN [71] project leverage the scalability and high mass of noble liquids to set some of the most stringent limits on DM cross-sections, particularly for DM masses above 10 GeV.

2.1.3 Cryogenic Searches

Cryogenic solid-state detectors measure heat as the primary signal, often supplemented with light or charge to improve event reconstruction and differentiate between ER and

NR events. Operating at ultra-low temperatures down to the milli Kelvin (mK) scale, these detectors can achieve energy thresholds of $\mathcal{O}$(eV), making them ideal for probing low-mass DM (<10 GeV with cross-sections above 10^{-44} cm^2). Notable experiments include SuperCDMS [72], CRESST [65], COSINUS [66], EDELWEISS [73] and HeRALD [67].

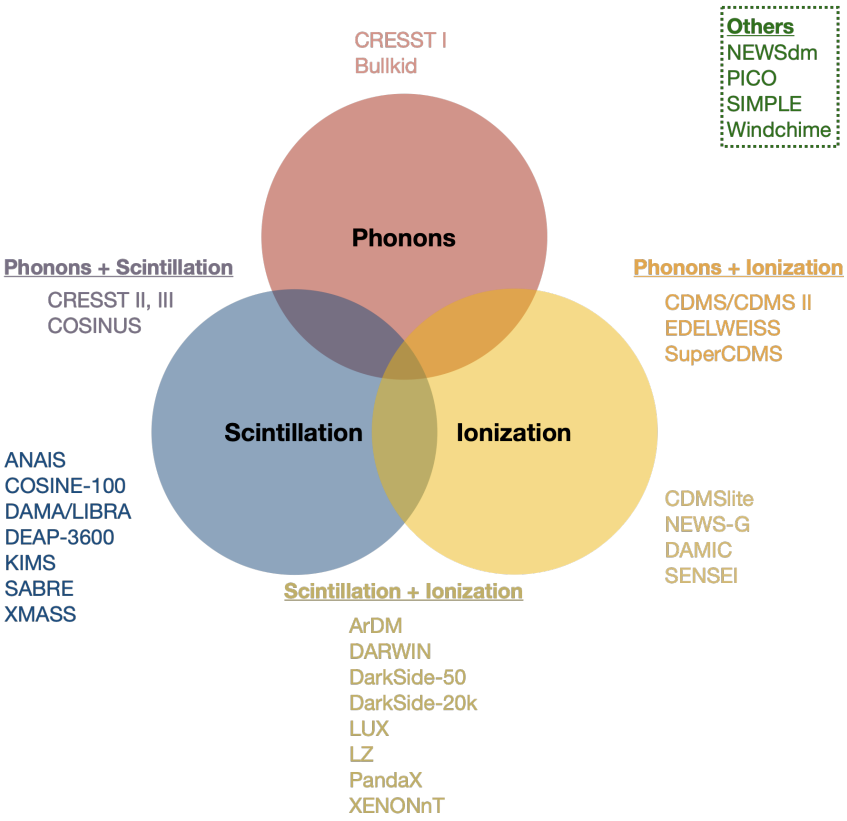

Figure 2.4: A snapshot of the common detection channels used in direct DM searches. Refer to text for more details.

2.1.4 Other Techniques

Recent efforts focus on adapting existing technology or developing new methods to explore yet undiscovered WIMP parameter space, particularly the sub-GeV range and methods to probe the neutrino fog. One promising strategy involves exploiting the Migdal effect. In this process, the sudden acceleration of a recoiling nucleus can ionize its bound electrons, producing a secondary electron signal that is detectable even when the primary nuclear recoil energy is below the threshold of conventional detectors. This mechanism effectively lowers the detection threshold for low-mass DM particles [74].
Consideration of superfluids, using superconducting materials, and direction-sensitive detectors to provide both energy and angular information of recoil events are just a few approaches. In parallel, experiments such as NEWSdm, PICO, and paleo detectors have adopted distinct technological approaches to probe light DM. NEWSdm employs high-resolution nuclear emulsions that capture microscopic recoil tracks, providing detailed event topology information [75]. PICO utilizes superheated bubble chambers that detect nuclear recoils through bubble nucleation and acoustic discrimination, offering robust

sensitivity, particularly for spin-dependent interactions [76]. Meanwhile, paleo detectors propose to use ancient minerals to record nuclear recoil damage tracks accumulated over geological timescales, effectively integrating the dark matter signal over millions of years and probing extremely low interaction cross-sections [77]. Together, these complementary techniques expand the DM search strategy by addressing different challenges inherent to low-mass detection.

2.2 Present Status

Among all experimental searches listed in Fig. 2.4, there has been almost no experiment that has reported a signal attributed to DM so far [78]. Fig. 2.5 shows the combined exclusion plot of a number of different experiments discussed in the earlier subsections. For $m_\chi \geq 10\,\text{GeV}$, liquid noble gas detectors have done an excellent job probing a vast area of the parameter space by effectively scaling up to multi-ton detector volumes, with recent results from the Xenon-nT [63] and PandaX-4T [62] collaborations even reporting the first signs of Solar neutrino detection respectively. For masses $\leq 10\,\text{GeV}$, cryogenic detectors due to their higher sensitivities, can probe this space more effectively. Due to inherent complexities in scaling up such experiments, as will be covered in Chapter 3, the parameter space in the sub- GeV mass range is yet to be fully explored.

A closer look at Fig. 2.5 reveals two shaded islands, highlighting the only reported experiment to have claimed a statistically significant signal consistent with DM interactions. The DAMA collaboration has been in operation since the early 1990s [80], having observed an annual modulation in their data above background for over 20 years of data taking. For this, they utilize thallium-doped sodium iodide (NaI(Tl)) crystals as their main target material. Now, using NaI(Tl) crystals as particle detectors was not new as it had been a cornerstone in nuclear, medical and particle physics since their discovery in 1949. These detectors are notable for their high intrinsic scintillation light yield and the ease of growing large-size crystals. This made them an ideal target material of choice for the early generation of direct DM searches [81]. Having a 2 nuclei system with different masses, Na ($M_A = 23$) and I ($M_A = 127$), it can effectively probe both the lower and higher GeV mass range (the Tl was only added as dopant to improve the light yield and is not present in significant enough numbers to provide an additional DM target). An additional benefit is that both Na and I have unpaired protons, making NaI(Tl) a target well suited for probing spin-dependent DM models too. However, this does also provide a drawback, as in the event of a positive signal there is no way to distinguish between the Na and I recoils, making it difficult to conclusively fit the result to a single DM model.

As of this writing, DAMA has accumulated a total exposure period of a little over 2.86 tonne years. The NaI(Tl) targets are an array of 25 crystals (≈ 10 kg each) directly coupled to two photomultiplier tubes (PMTs), shielded by Cu tubes and sealed within a low radioactive Cu box continuously flushed by high purity N_2. This is then surrounded by a passive shielding system made up of more Cu, Pb, and polyethylene (PE), as shown in Fig. 2.6.

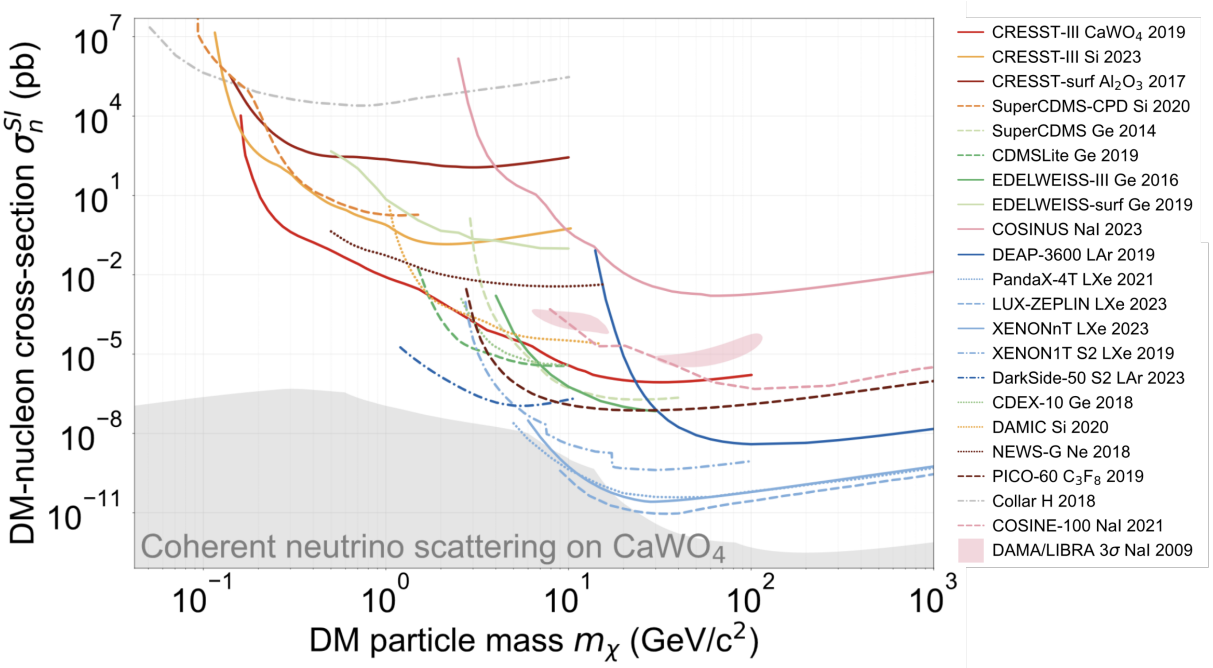

Figure 2.5: Results from direct DM search experiments probing the SI elastic DM-nucleus scattering scenario. Figure adapted from [79].

In the (2-6) keV$_{ee}$* region, they observe a modulation amplitude of (0.01014±0.00074) cpd/kg/keV with a phase and period of (142.4±4.2) days and (0.99834±0.00067) years respectively [83]. This modulation is also observed in the 1-6 keV$_{ee}$ range (with the low energy threshold of DAMA/LIBRA-phase2) with an amplitude of (0.01058±0.00090), period of (0.99882±0.00065) years, and phase of (144.5±5.1) days, [83] but recent results have indicated that this modulation continues below the 1 keV$_{ee}$ threshold, albeit at a lower amplitude [83]. While a number of explanations have been put forth by different groups over the years to explain the observed modulation, none have managed to fully demonstrate a non-DM origin.

Referring back to Eq. 2.6, one can conservatively state that in order to have a truly model-independent test of the observed modulation, a cross-check with the same target material is required. The following sub-section provides a brief overview of the NaI-based experimental landscape that has since originated as a result. It is important to note here that due to the difficulties in both the purification of NaI(Tl) to achieve ultra-low backgrounds and lack of discrimination between nuclear and electron recoils at low energies† for the experiments listed below, these experiments are less competitive compared to the much larger liquid TPC detectors or cryogenic detectors.

* Interpreting the keV$_{ee}$ energy scale is discussed in detail in Sec. 2.3 and 2.4.
† While PID on a statistical basis is possible, it is more relavant for higher energy scales.

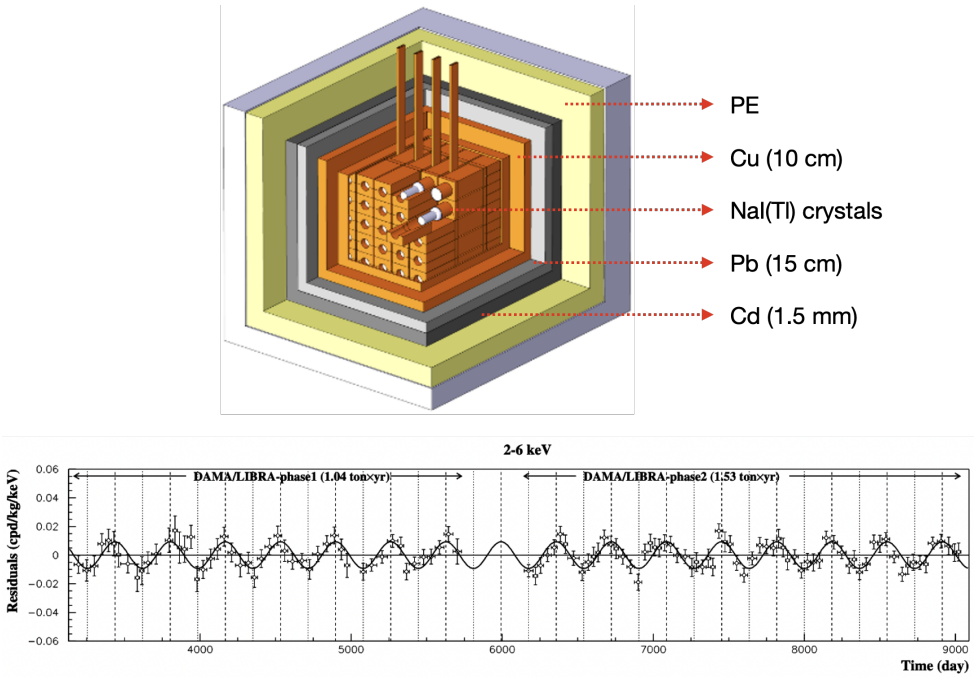

Figure 2.6: Top: Schematic of the DAMA/LIBRA detector [82]; **Bottom:** Reported residual rate of single-hit scintillation events over time in the (2-6) keV$_{ee}$ energy interval [83].

2.2.1 NaI-based Experimental Landscape

ANAIS-112

ANAIS-112 is a NaI(Tl)-based experiment located at the Canfranc Underground Laboratory (LSC) in Spain, operating with 112.5 kg of crystals arranged in a 3×3 array of 12.5 kg modules. The detector is shielded by 2500 m water equivalent depth, Pb/Cu layers, and a radon-purged enclosure, with active muon veto systems and polyethylene/water shielding. As of 2024, ANAIS-112 has accumulated 6 years of data, reporting a modulation amplitude of (-0.0034 ± 0.0042) counts per day (cpd)/kg/keV in the [1–6] keV energy range. These results are inconsistent with the DAMA/LIBRA signal at the 3.9σ confidence level, with sensitivity projected to reach 5σ by late 2025 [84].

COSINE-100 and COSINE-100U

COSINE-100, operating at the Yangyang Underground Laboratory (2100 m water equivalent), uses 106 kg of NaI(Tl) crystals (61.4 kg fiducial mass) submerged in 2.2 tonnes of liquid scintillator for active vetoing. The setup includes copper (Cu) encapsulation, Pb/Cu shielding, and a 360° muon detection system [85]. After 6.4 years of data, COSINE-100 found no annual modulation, reporting a $> 3\sigma$ tension with DAMA's signal and excluding spin-independent WIMP cross-sections above 10^{-41} cm^2 for $m_\chi \sim 10$ GeV/c^2. An upgraded phase, COSINE-100U, began in 2024 at Yemilab with enhanced light collection and sub-GeV

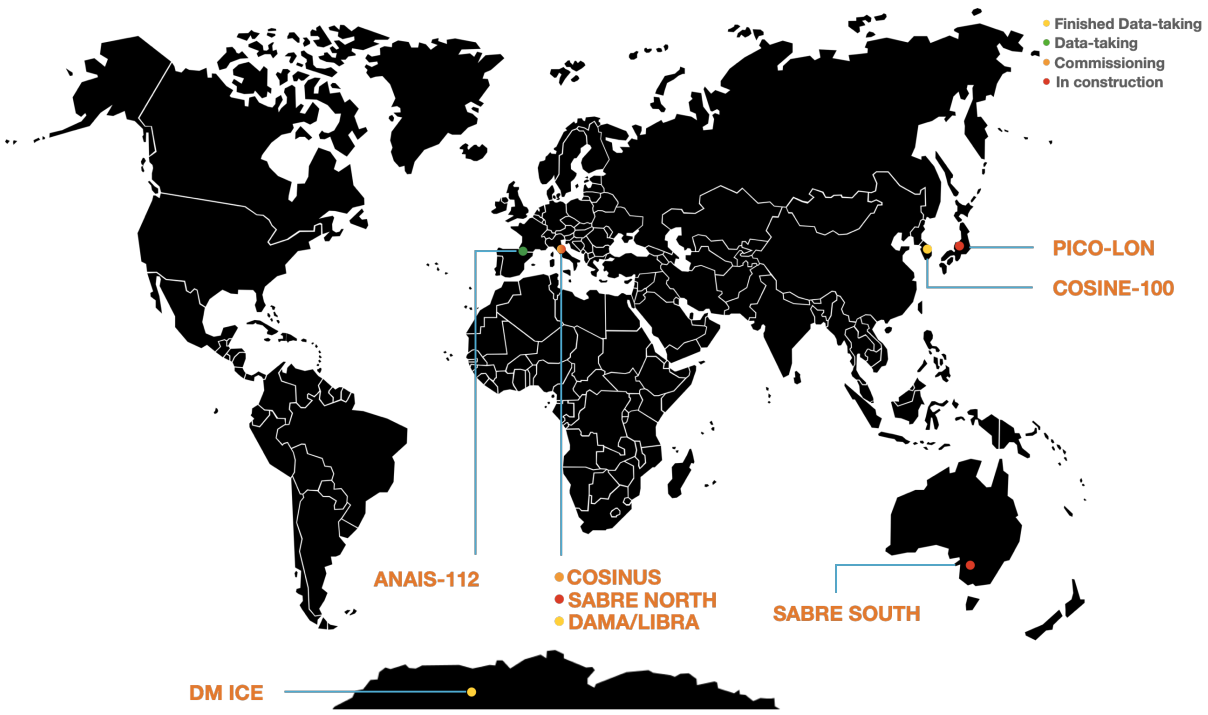

Figure 2.7: A map of various NaI-based direct DM search experiments.

sensitivity via a lowered energy threshold of 0.7 keV [86]. Preliminary results disfavor DAMA's 3σ allowed regions by an order of magnitude in cross-section limits [87].

PICOLON

PICOLON (Pure Inorganic Crystal Observatory for LOw-energy Neutr(al)ino) is an R&D project aiming to deploy ultra-pure NaI(Tl) detectors with sub-keV thresholds. Current designs focus on reducing internal backgrounds from ^{40}K and ^{210}Pb to levels below 1 mBq/kg, critical for probing low-mass WIMPs [88].

SABRE

The SABRE (Sodium-iodide with Active Background Rejection) experiment employs twin detectors in the Northern (Laboratori Nazionali del Gran Sasso) and Southern (Stawell Underground Laboratory) hemispheres to identify seasonal systematic effects. Its 50 kg NaI(Tl) crystals are paired with liquid scintillator veto systems, achieving a background rate of <1 cpd/kg/keV above 1 keV [89, 90] .

ASTAROTH

ASTAROTH (Advanced Scintillator Target for Rare Event Observables with THermo-electrics) explores novel NaI(Tl) crystal growth techniques to minimize ^{210}Pb contamination.

The project aims for a 500 kg array with <0.1 cpd/kg/keV backgrounds, targeting the neutrino fog region [91].

2.3 Diving Deeper into the DAMA Modulation

2.3.1 Model Dependent Parameters

The interpretation of direct detection experiments for DM relies heavily on theoretical models that describe both the particle physics interactions and the astrophysical properties of the DM halo. The standard halo model (SHM) is the de-facto standard when it comes to building the DM halo model one wants to use in analysis. It assumes a spherically symmetric isothermal halo as depicted in Fig. 2.1, with a Maxwellian velocity distribution:

$$f_{\text{lab}}(\mathbf{v}) = \frac{1}{(2\pi\sigma_v^2)^{3/2}} e^{-\frac{|\mathbf{v}+\mathbf{v}_{\text{obs}}|^2}{2\sigma_v^2}} \tag{2.7}$$

where σ_v is the velocity dispersion, and $\mathbf{v}_{\text{obs}}$ is the velocity of the observer (Earth) relative to the DM halo.

However, this model is a simplification. Recent observations and simulations from the GAIA-3 data release suggest that the actual DM halo may have substructures, anisotropies, and deviations from spherical symmetry. Furthermore, the velocity distribution may not be perfectly Maxwellian due to tidal streams [92]. These uncertainties can significantly impact the predicted event rates, especially near the experimental energy thresholds where small changes in $f_{\text{lab}}(\mathbf{v})$ can lead to large differences in v_{min} and thus the integral over velocities as indicated by Eq. 2.6. Consequently, there has to be a gradual push towards incorporating values from the GAIA-3 dataset, dubbed the SHM++ model [93]. Table 2.1 compares the changes between the halo properties outlined in the two models.

Table 2.1: Comparison of selected halo properties in the SHM and SHM++ models.

Property	**SHM**	**SHM++**
Local DM density ρ_0	0.3 GeV/cm^3	(0.55 ± 0.17) GeV/cm^3
Velocity distribution	Maxwell - Boltzmann	Non-isotropic
Velocity dispersion v_0	220 km/s	(233 ± 3) km/s
Escape velocity v_{esc}	544 km/s	(528 ± 25) km/s

In order to compare results of future experiments with current and past experiments in a model independent way, having a DM analysis separately with halo properties outlined by both SHM and SHM++ seems to be the next natural way ahead.

The differential scattering cross-section $\frac{d\sigma(E_R,v)}{dE_R}$ given in Eq. 2.5 is typically expressed in terms of the DM-nucleon scattering cross-section $\sigma^{SI}_{0,nucleon}$, as this allows for the comparison of different target nuclei employed in different experimental setups. It also

depends on the nuclear form factor $F_{SI}(E_R)$, which accounts for the spatial distribution and structure of the nucleons within the nucleus. The standard way to express $F_{SI}(E_R)$ is the analytical approximation of the Helm form factor [94] suggested by Lewin and Smith [95]:

$$F(E_R) = 3\frac{j_1(qr_n)}{qr_n}e^{-q^2s^2/2} \tag{2.8}$$

where j_1 is the spherical Bessel function of the first kind, $q = \sqrt{2m_T E_R}$ is the momentum transfer, r_n is the effective nuclear radius and s is the skin thickness parameter. s represents the diffuseness of the nuclear surface ,where $s \approx 0.9$–1.0 fm. The effective radius r_n is derived from the nuclear radius $c \approx 1.23A^{1/3}$ fm (for mass number A) through the relation:

$$r_n^2 = c^2 + \frac{7}{3}\pi^2 a^2 - 5s^2 \tag{2.9}$$

where $a \approx 0.5$–0.6 fm describes the surface thickness of the nuclear density profile.

This formalism introduces systematic uncertainties that are often unaccounted for. Uncertainties in r_n and s can arise due to limitations in nuclear models and experimental measurement [‡], which alter the predicted recoil spectrum, especially at lower energies where the form factor suppression is no longer significant. Despite these limitations, experimental analyses often adopt fixed global values for s, a, and c, neglecting their correlations and variances. This simplification introduces irreducible systematic errors into DM exclusion limits and signal interpretations.

By using the same materials (NaI in this case) and accounting for uncertainties, we can perform a more reliable, model-independent comparison of the DAMA signal claim.

2.3.2 Detector Dependent Parameters

Going back to Eq. 2.6, one can estimate the total differential scattering rate for a terrestrial detector. The actual number of events an experiment would observe can be obtained by integrating Eq. 2.6 over the detector's dynamic range:

$$N = T\int_{E_{\text{low}}}^{E_{\text{high}}} dE_{\text{nr}}\,\epsilon(E_{\text{nr}})\frac{dR}{dE_{\text{nr}}} \tag{2.10}$$

where T denotes the total exposure time, $\epsilon(E_{nr})$ denotes the detector efficiency (which in turn also has an energy dependence) and E_{low} denotes the energy threshold of the detector. Thus, these detector-specific parameters also play an important role in the sensitivity and interpretation of direct detection experiments. These include the energy resolution,

[‡] For example, the model assumes a smooth, spherical nuclear density profile, neglecting complexities such as neutron skin effects [96], nuclear deformation, or shell structure variations, which can induce discrepancies in $F(E_R)$ for specific isotopes or kinematic regimes.

detection efficiency, background noise levels, and quenching factors. The energy resolution determines the detector's ability to precisely measure the recoil energy E_R. As one would expect, a high-resolution detector can better resolve features in the recoil spectrum, such as spectral peaks or edges that may be indicative of specific DM interactions. The detector efficiency, ϵ, represents the probability that a recoil event of a given energy will be detected and correctly recorded. Efficiency in detectors typically decreases at lower energies due to threshold effects and increases with energy up to a saturation point. An accurate reconstruction of the efficiency curve is therefore vital for reconstructing the true recoil spectrum from the observed data.

Now, for a given detector threshold, the number of observed DM "signal" events, S(t), will also modulate throughout the year by virtue of Eq. 2.3. For this discussion, we can decompose this into three main sub-contributions:

$$S(t) = B + S_0 + S_m cos[\omega(t - t_0)] \tag{2.11}$$

Most of the DM signal is unmodulated, denoted here as S_0, while S_m can be considered quite small, of $O(v_\oplus/v_c) \sim 5\%$. The detector related background events, B(t), is typically the most dominant component. These background events can arise from various sources, including environmental radioactivity, cosmic rays, and intrinsic radioactive contaminants from isotopes such as ^{40}K, ^{210}Pb, ^{238}U and ^{232}Th decay chains in the detector target and holding structure. It is also well known that certain background sources also exhibit a seasonal modulation. Thus, for experiments looking for an annual modulation signature of DM, an effective background modeling and subtraction is especially important for identifying excesses that could indicate DM interactions like the observations of the DAMA collaboration. In this context, it is worth highlighting that the background of DAMA in comparison to most of the early NaI-based cross-checks has always been a point of contention as the backgrounds reported by DAMA are a factor 2-3 better, especially at the low-recoil energies. A comparison of the background rates observed by some of the NaI-based experiments discussed are shown in Fig. 2.8 for reference.

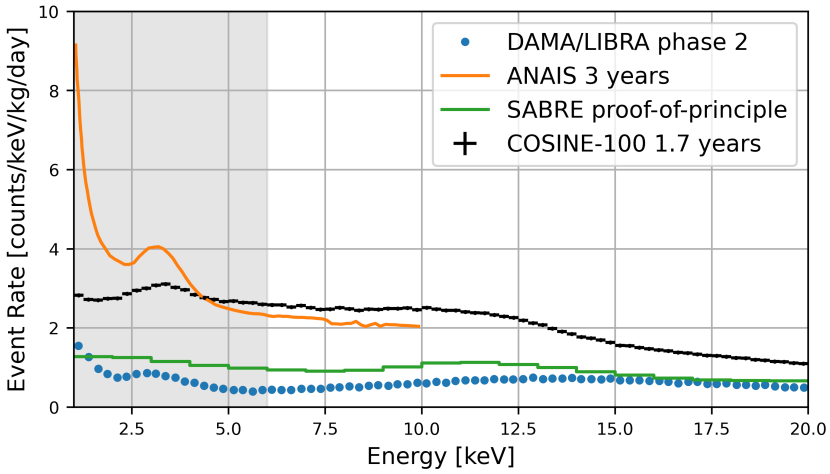

Figure 2.8: Background rates as a function of energy for different direct DM search experiments using a NaI target [97]. DAMA has the lowest resported background rate amongst all.

When there is an energy deposition in a detector due to particle interactions, the energy can be generally thought of to be distributed roughly as follows:

$$\left(\frac{\mathrm{d}E}{\mathrm{d}x}\right)_{tot} = \left(\frac{\mathrm{d}E}{\mathrm{d}x}\right)_{elec} + \left(\frac{\mathrm{d}E}{\mathrm{d}x}\right)_{nucl}. \tag{2.12}$$

The majority of this energy split goes into the nuclear energy losses, $\left(\frac{\mathrm{d}E}{\mathrm{d}x}\right)_{nucl}$, which in solid materials gives rise to phonons. A small portion (usually between 10 - 30 % depending on the detector material) are attributed to electronic energy losses, $\left(\frac{\mathrm{d}E}{\mathrm{d}x}\right)_{elec}$, which can excite or ionize the target atoms. Depending on the detector material, this can either manifest as ionization (doped Si, Ge) or as scintillation light (NaI(Tl), CsI). For single channel NaI(Tl)-based detectors discussed in Sec. 2.2, this smaller component of scintillation light is the observable which is read out via PMTs. In other words, an already small energy deposit (which is what is expected for DM candidates in the GeV mass range) leads to an even smaller signal in such experiments due to them being sensitive to only the scintillation light.

An arguably even bigger complication that plagues the setup of such experiments stems from the fact that this energy distribution outlined above is also dependent on the type of interacting particle.

The usual energy scale calibration typically performed by such experiments is using γ-rays from known sources, which interact primarily with electrons in the crystal, establishing the electron-equivalent energy scale (E_{ee}), noting that they only measure the corresponding scintillation light for this process. For heavier particles, such as neutrons which interact primarily via nuclear recoils, less energy is converted into scintillation light for the same initial recoil energy. The quenching factor (QF) quantifies this difference, and is needed to calculate the corresponding nuclear recoil energy E_{nr} from the measured light signal. Therefore, the interpretation of signals and the DM parameter space coverage in experiments relying on scintillation-only detection heavily depend on the estimation of the QF. The QF is defined as:

$$QF = \frac{E_{\mathrm{ee}}}{E_{\mathrm{nr}}}$$

where E_{ee} is the electron-equivalent energy observed, and E_{nr} is the actual recoil energy.

An accurate knowledge of the QF is essential for reconstructing the true recoil energy spectrum from the measured signals. If the QF is underestimated, nuclear recoil energies will be overestimated, shifting the interpreted spectrum to higher energies. This misinterpretation can affect the inferred DM parameter space being probed.

However, determining the QF for different detector materials and recoil energies remains challenging. Experimental measurements of QF often show discrepancies, and there are energy dependencies that deviate from empirical explanations.

2.4 A Study of QF Energy Dependence for NaI(Tl) Crystals

This section incorporates findings presented in the following pre-print and proceeding. The author contributed to these publications through data analysis, interpretation of results, and manuscript preparation, serving as one of the corresponding authors for both works.

Quenching factors for Na recoils as a function of Tl dopant concentrations in NaI(Tl) crystals, G. Angloher et al. (COSINUS Collaboration), Pre-print

Quenching factor estimation of Na recoils in NaI(Tl) crystals using a low-energy pulsed neutron beam measurement, M.R. Bharadwaj et al. (COSINUS Collaboration), SciPost Phys. Proc., **12**, 028, (2023)

As outlined in Sec. 2.3, for NaI(Tl) based DM experiments relying on scintillation-only detection, the interpretation of signals and the DM parameter space coverage heavily depend on the accurate estimation of the QF. Previous measurements have revealed discrepancies, particularly at lower energies [80, 98–107], which can significantly influence the interpretation of results from other DAMA-like direct DM experiments. These discrepancies may arise from factors such as crystal doping, manufacturing processes, and non-linearities in light output. Further, recent results [106, 107] have shown how the non-linear effects of scintillation light can lead to systematic shifts in the reported QF at lower energies. The following sections present a systematic examination of the sodium (Na) QF in 5 radio-pure NaI(Tl) crystals having differing Tl-dopant concentrations, with a focus on its energy dependent behavior in the low-energy recoil regime from (5-26) keV_{nr}.

2.4.1 Experimental Setup

Overview

The measurements were conducted at the Advanced Neutron Calibration Facility at the Triangle Universities Nuclear Laboratory (TUNL) in Durham, North Carolina. The quasi-monoenergetic neutrons that are required for QF measurements are produced using a tandem Van de Graff accelerator. Protons were created in a pulsed beam with a pulse period of 400 ns and a timing resolution of 2 ns using a Direct Extraction Negative Ion Source (DENIS) [108]. A 1434 nm lithium fluoride (LiF) foil evaporated onto a tantalum substrate placed at the target location was irradiated by the beam. Resultant monoenergetic neutrons with an energy of ~ 1284 keV (with a small spread due to proton energy loss in LiF as seen in Fig. 2.16) are produced via the $^{7}\mathrm{Li}(p,n)^{7}\mathrm{Be}$ reaction [109, 110]. The beam energy and LiF thickness were configured such that it would generate recoil energies of interest at relatively small scattering angles, while simultaneously ensuring a sufficient event rate for collecting adequate statistics for the measurement without pile-up concerns. Calculations were performed to determine the overall interaction rate in the NaI(Tl) crystal at low recoil energies, utilizing the $^{7}\mathrm{Li}(p,n)^{7}\mathrm{Be}$ cross-sections [109, 110] and the differential neutron elastic scattering cross-sections for $^{23}\mathrm{Na}$ and $^{127}\mathrm{I}$ at the relevant angles. A Beam Pulse Monitor (BPM) was used to record the timing information when the pulsed proton

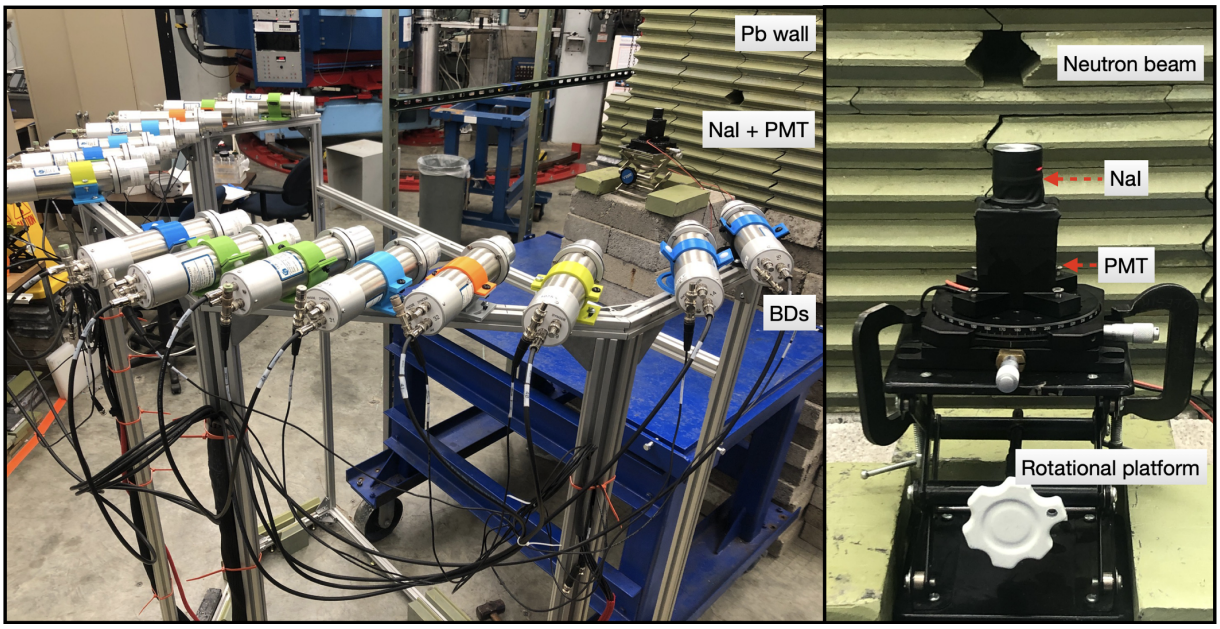

Figure 2.9: Left: The experimental setup at TUNL; **Right:** A close-up of the NaI(Tl) crystal coupled to the PMT.

beam interacted with the LiF target to produce the neutrons. Bi-layer shielding consisting of high density polyethylene (HDPE) and borated HDPE was placed around the enclosure of the LiF target to block any off-axis neutrons, and a collimated slit was used to direct the outgoing beam towards the NaI(Tl) crystal. The resultant beam had an angular spread of 2.356 °. An additional layer of lead (Pb, 10 cm thick) covered the front surface to reduce the fraction of secondary γ-rays produced by the neutron capture of hydrogen in the HDPE. The setup is pictured in Fig. 2.9.

Detector Configuration

The NaI(Tl) crystals were manufactured at the Shanghai Institute for Ceramics of the Chinese Academy of Sciences using a modified Bridgman technique described in Ref. [111]. "Astro-Grade" powder from Merck Co. (previously Sigma Aldrich) [112] was used as the starting material. Inductively coupled plasma mass spectrometry (ICP-MS) measurements performed at LNGS [113] showed contamination at a level of (6-22) ppb for ^{40}K, < 1 ppb for ^{232}Th and ^{238}U, respectively. Overall, five samples were prepared, with their Tl dopant levels varying from 0.1, 0.3, 0.5, 0.7 to 0.9 % respectively in the initial powder. The Tl dopant levels in the cut crystals were found to vary from 284 ppm to 1390 ppm as listed in Table 2.2 with an uncertainty of 20 % from the ICP-MS method.

The synthesized crystals are right-circular cylinders with a uniform height and diameter of 2.54 cm each, respectively. Given the hygroscopic nature of NaI(Tl), each crystal was encased in an aluminum enclosure with a wall thickness of 1.25 mm.

The housing material, in combination with the small size of the crystal, was chosen to minimize the possibility of multiple scatters. Assembly was carried out inside a nitrogen-flushed glovebox to ensure the crystals did not degrade. A photo-multiplier tube (PMT)

Table 2.2: Tl-dopant concentration, for both powder and cut crystal, and run time for each NaI(Tl) crystal

Crystal	Tl conc. Powder (%)	Tl conc. Cut crystal (%)	Run time (h)
1	0.7	1270 ± 254	32.27
2	0.3	425 ± 85	28.57
3	0.9	1390 ± 278	35.95
4	0.1	284 ± 56	33.72
5	0.5	800 ± 160	35.45

manufactured by Hamamatsu Photonics (weighing 74 g; Model number: H11934-200) was optically coupled to the bottom face of the crystal (using EJ-550 silicone grease) to measure the light output. This setup was covered with a layer of black adhesive tape before being mounted on a custom 3D printed motorized unit that could be tuned to rotate slowly about its axis to minimize the impact of any channeling effects during data-taking, as seen in Fig. 2.9. Each crystal to be tested was placed at a distance of 1.016 m from the LiF target in line with the beam axis.

Liquid scintillation detectors, which we denote as backing detectors (BD), were installed to tag the neutrons scattered off the Na or I nuclei (see Fig. 2.9). The BD contain a cylindrical EJ-309 liquid scintillation cell of diameter and length 2 inches manufactured by Eljen Technology [114], coupled to a Hamamatsu R7724 PMT. Previous measurements [105, 106] demonstrated the excellent pulse-shape discrimination capability of these detectors, allowing for accurate tagging of neutron events. In total, 15 BDs were deployed for the current run, with their corresponding scattering angles and distance from the NaI(Tl) crystal provided in Table 2.3.

Table 2.3: Scattering angles and distances for each backing detector. The measuring uncertainty on the angles is negligible considering the surface area of the BD.

Detector no.	Scattering angle (°)	Distance (cm)
BD0	40	101.5
BD1	35	115.7
BD2	27.5	131.6
BD3	22.5	136.1
BD4	18	142.0
BD5	14.5	145.9
BD6	11	152.5
BD7	7	154.3
BD8	9	155.3
BD9	12	151.1
BD10	15.5	145.9
BD11	22	139.0
BD12	27	131.3
BD13	32.5	123.5
BD14	37.5	107.8
TOF	0	195.7

The aforementioned BD angles were chosen to constrain our region of interest below 30 $\mathrm{keV_{nr}}$ for Na recoils in the current study. Each of the BDs was encapsulated inside a 1.5 mm thick Al housing and equipped with a Pb shielding cap in front and around their enclosure during operation to reduce the background gamma trigger rate. An additional BD was employed as a time-of-flight (TOF) detector to measure and monitor the spread of the neutron beam energy.

For the alignment of the entire setup, a laser range finder was used. A set of reference points were used for lining up the NaI(Tl) crystal to the center of the beam, which was checked after each rotation and crystal swap. The range finder was used to align all the BDs on the same plane as that of the NaI(Tl) crystal and the beam line.

Electronics and DAQ

For data acquisition, a pair of SIS3316 14-bit digitizers with a sampling rate of 250 MHz manufactured by Struck Innovative Systeme was used to capture the data from all 15 BDs, the TOF detector, the beam pulse monitor (BPM), and the NaI(Tl) PMT whenever one of the BD triggered. The clocks of the two SIS3316 digitizers are synchronized, and the trigger is handled by an external NIM module. Communication with the digitizers is carried out via the VME backplane using a *Struck* 3150 VME interface. The acquisition control is managed by the NGMDAQ software package, developed by J. Newby at Oak Ridge National Laboratory [115].

Measurement Summary

The measurement was carried out by the TUNL group over two weeks in September 2021, with cumulative run times for each crystal presented in Table 2.2. The NaI(Tl) crystals were calibrated with ^{133}Ba and ^{241}Am γ-sources at the beginning and end of each individual run, respectively. For the calibration datasets, the trigger scheme was changed to record events in the NaI(Tl) PMT.

2.4.2 Data Analysis

Data Processing

A coincidence mechanism was employed between the NaI(Tl) detector and each of the BDs to select events of interest in the NaI(Tl) detector. For each coincidence event, the contributing BD was determined by comparing the pulse onset timing information with the coincidence trigger time, which was ~350 ns, depending on the position of the BD. An additional timing cut of ~240 ns between the NaI(Tl) pulse onset and the prior BPM pulse was applied to serve as a first rough filter for beam-induced recoil event selection, as outlined in Fig. 2.10.

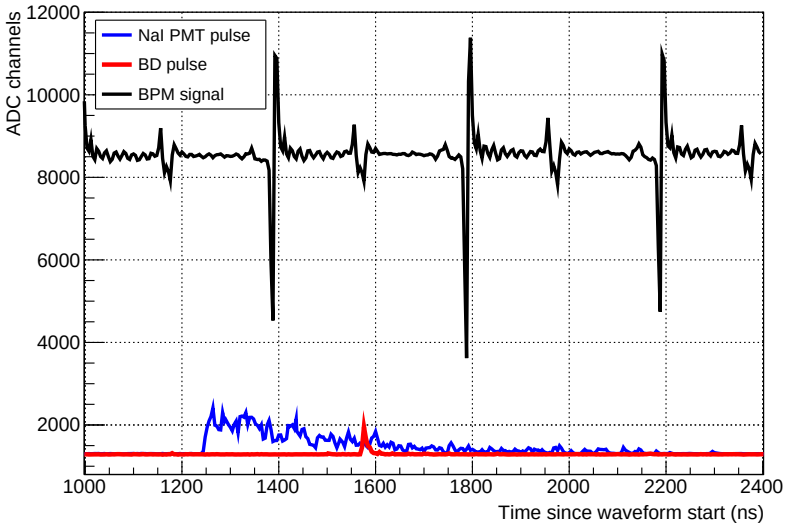

Figure 2.10: Time correlation of pulses detected in the PMT attached to the NaI(Tl) crystal and the BD for a neutron-induced nuclear recoil event. The BPM provides a shaped signal as timing reference for identifying beam-induced neutron events.

Using an estimate of the time window in which pulses occur within the record, a fixed window integration pulse reconstruction scheme was employed on the raw production files to generate a new data-set. In line with measurements reported by other studies [105], it was observed that the low-energy NaI(Tl) events could not be well reconstructed with this method due to integrating the PMT noise, which becomes dominant in this regime. Therefore, the charge estimation from [105] was implemented as an energy estimator instead, where only samples above a certain threshold are integrated. The threshold was fixed by determining the value above which the noise peak disappears (at 11 ADC units). This reconstruction method was used for the whole energy range.

Calibration and Resolution Estimation

Two different calibration functions were chosen to study the impact of different calibration schemes on the final QF estimation. A linear, single-point calibration using the 59.54 keV ^{241}Am γ-peak serves as a standard cross-check with previously reported measurements. A second single-point calibration using a ^{133}Ba source was used to evaluate the effect of using a low-energy peak to calibrate the energy scale. From the simulated spectrum in Fig. 2.11, the feature close to the noise peak was attributed to the escape of ^{127}I K_α X-rays following photoelectric absorption of the 35.1 keV K_β X-rays from ^{133}Ba in the NaI(Tl) crystal. A mean energy of 6.6 keV was obtained from the simulation, and used for calibration. The scintillation light response of NaI(Tl) generally exhibits an energy-dependent non-linearity [116, 117]. This effect is not considered here, since it is expected to be on the order of only a few percent in our region of interest ($E_{\mathrm{nr}} < 6$ keV). The energy scales are given in E_{ee}.

Fig. 2.11 shows the observed and the simulated Monte-Carlo spectrum for the ^{133}Ba calibration of Crystal 1.

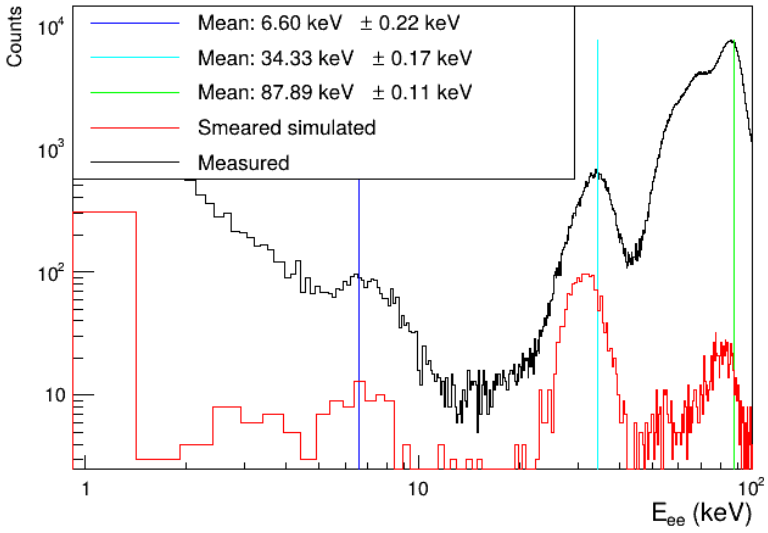

Figure 2.11: Observed and simulated spectrum in keV from the ^{133}Ba calibration of Crystal 1. The measured spectrum was calibrated using the 6.6 keV proportional response. The simulated spectrum is smeared by Gaussian convolution, where the width is given by the resolution function $\sigma(E) = \sqrt{aE} + bE$. The measured peaks are fitted with a Gaussian on top of a linear background. The 6.6 keV line is close to the noise peak, then, in order of increasing energy, the peaks are identified as the unresolved sum of 30.62 keV and 30.97 keV, and finally the 81.0 keV line. The vertical lines denote the fitted Gaussian mean converted to energy using the 6.6 keV proportional response.

The energy resolution of the peaks was fitted with a parametric function of the form $\sigma(E) = \sqrt{aE} + bE$ as shown in Fig. 2.12. In the literature, a resolution function of the form $\sigma(E) = \sqrt{aE} + bE + c$ is common [118]. We find that this is a poor fit to the data: the constant c was found to be $\mathcal{O}$(-1) keV for three out of the five crystals, resulting in a negative resolution at low energies. Imposing an artificial limit to ensure that the constant is positive-definite provided a fit comparable to $\sigma(E) = \sqrt{aE} + bE$.

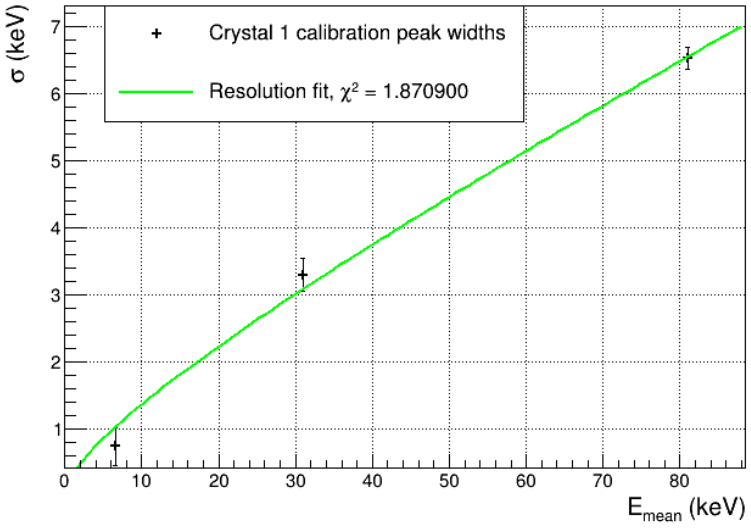

Figure 2.12: Resolution function fit for Crystal 1 ($\sigma(E) = \sqrt{0.0757E} + 0.0503E$).

Furthermore, unlike the other parameters used in the QF estimation, we explored both a fixed resolution function and a Gaussian prior for the parameters a and b in the MCMC-analysis used for QF estimation (see Sec. 2.4.4). We found that using a Gaussian prior for the resolution function produced results compatible with the fixed method. Therefore, in the interest of brevity, we only consider the fixed resolution function here.

Identification of Nuclear Recoils

A set of Pulse Shape Discrimination (PSD) cuts and timing cuts is applied to the events triggered by the BDs to select only scattered neutron events, while rejecting any accidental triggers due to ambient/scattered coincident gammas.

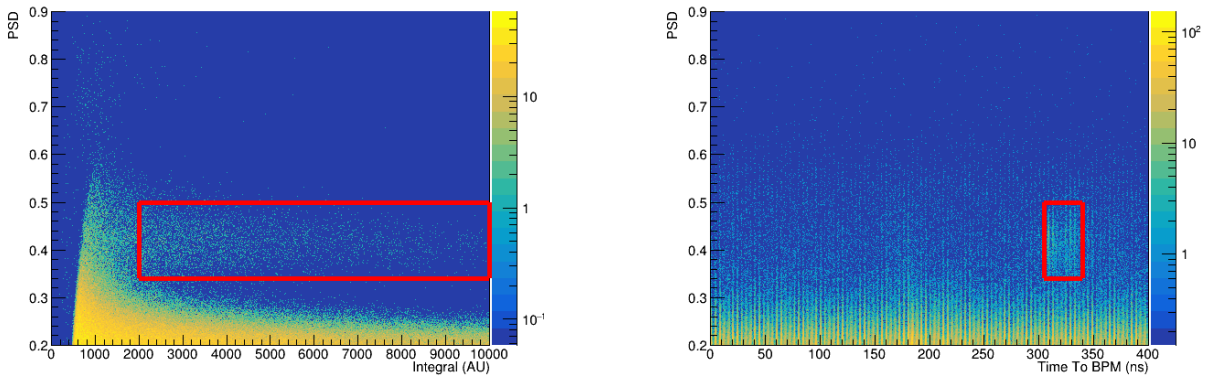

Figure 2.13: Left:PSD cut applied to triggered events of BD 0 for Crystal 1; **Right:**TOF cut applied to triggered events of BD 0 for Crystal 1.

The PSD cut is based on the charge comparison method, using the ratio of the deposited charge sum of the tail (Q_{tail}) to the total charge ($Q_{tot.}$). The integration time window for the tail was 340 ns, while the total integration time window was 400 ns.

An additional time-of-flight (TOF) cut removes any accidental triggers resulting from neutrons that may have scattered off different parts of the experimental setup and not off the crystal. This is particularly helpful as the TOF of the scattered neutrons from the Na or I nuclei to the BD is almost constant for an incident monoenergetic neutron beam (with a small spread due to a spread in the initial neutron beam energy). A final cut on the deposited charge in the BDs was applied to reduce noise triggers. The cuts applied to Crystal 1 and BD0 are shown in Fig. 2.13 while Fig. 2.14 shows the spectrum before and after applying the highlighted cuts.

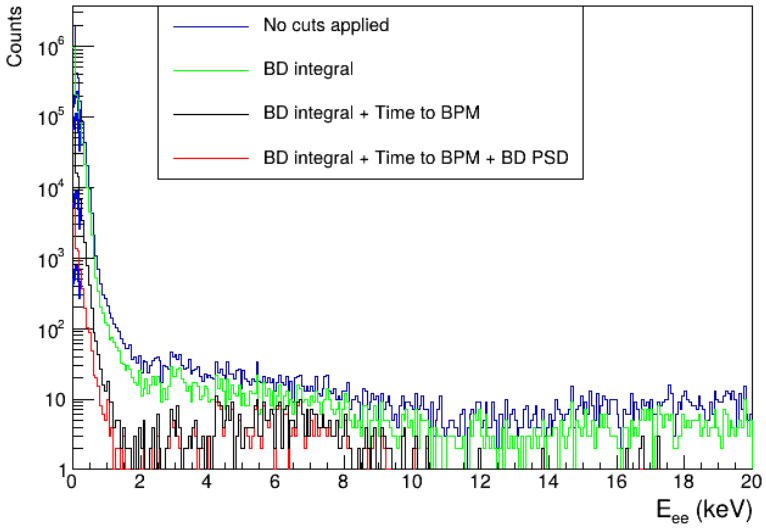

Figure 2.14: Spectra of BD0 for Crystal 1, showing the impact of each cut parameter on the spectra. The cut boxes are shown in Fig. 2.13.

2.4.3 Simulation

Simulated Geometry

An extensive Monte Carlo simulation was performed with the Geant4 [119–121] based software ImpCRESST [122], initially developed for the CRESST DM search experiment [65]. An ImpCRESST version equipped with Geant4 v10.6.3 and ROOT v6-22-08 [123] was used for this work. The primary goal of the simulation was to determine the distribution of nuclear recoil energies deposited in the NaI(Tl) crystal from scattered neutrons reaching each of the BDs. Additionally, the simulation was used to generate the energy spectrum resulting from interactions with the ^{133}Ba, ^{241}Am, and ^{137}Cs sources, which are employed for energy calibration as outlined in Sec. 2.4.2. Moreover, the simulation aimed to optimize the angular positioning parameters for the BDs to ensure each BD is exposed to a sufficient neutron flux within the energy range of interest. The results of the ImpCRESST simulation include detailed information on particle trajectories, energy deposition, particle types, interaction processes, and time of interaction.

The modeled geometry outlined in Fig. 2.15 comprises a neutron beam produced at the LiF target, directed at the NaI(Tl) crystal housed in an Al casing, positioned 1.016 m from the target. Scattered neutrons are detected by an array of 15 BDs, placed at varying angles (θ) and distances (1-1.5 m) from the crystal. Each BD consists of a liquid scintillator (EJ-309) enclosed in a cylindrical Al housing and shielded by a Pb cap. A separate BD, acting as a time-of-flight (TOF) detector, is placed 1.957 m away from the NaI(Tl) crystal, at 0° relative to the neutron beam. The detailed positions and angles of the BDs are listed in Table 2.3.

The amount of energy deposited in each experimental volume along with the respective time is recorded for each simulated neutron event. Two separate simulations were conducted, one under neutron irradiation and the other using three different gamma calibration

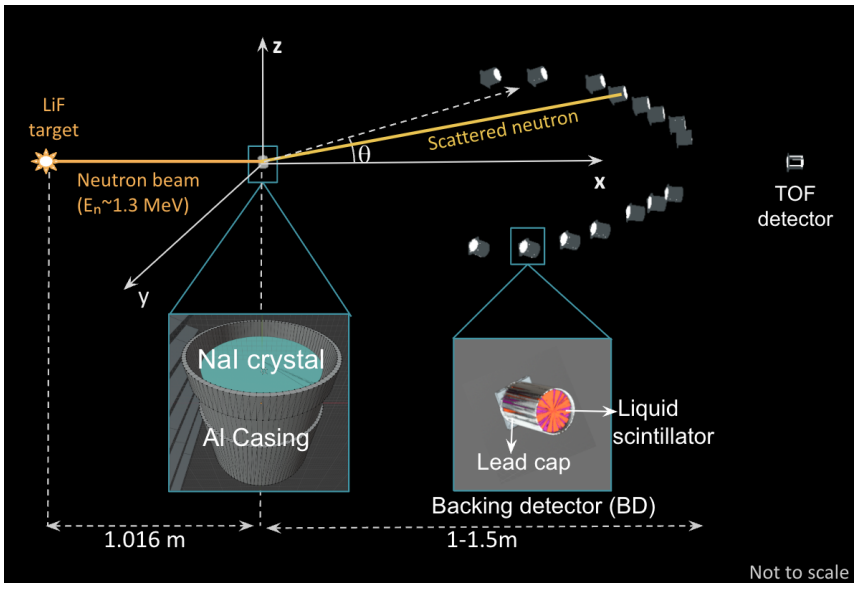

Figure 2.15: Schematic of the Geant4-simulated setup.

sources. Descriptions of both simulations, including their methodologies and outcomes, are provided below:

Simulation of the Gamma Calibration of the NaI(Tl) Crystal

For this study, simulations were conducted involving the encapsulated NaI(Tl) and each calibration source. Due to the absence of a precise description of the encapsulation for the ^{133}Ba and ^{241}Am sources, they were simulated as point sources and positioned at the top of the NaI(Tl) crystal in the simulation. Fig. 2.11 shows the measured calibration and the corresponding simulated spectrum for the ^{133}Ba source. For this analysis, calibration data from both ^{133}Ba and ^{241}Am were utilized. The simulation confirms the peak energies, which were then employed in the calibration process described in Sec. 2.4.2.

Simulation of nuclear recoil energy distribution in NaI(Tl)

To determine the true nuclear recoil energy for each BD, the geometry described in Sec. 2.4.3 and illustrated in Fig. 2.15 was modeled. This setup was irradiated by a quasi-monoenergetic neutron beam, treated as a point-like source, emitting neutrons confined to a narrow 2.356 ° angular range. 170 million neutrons were simulated using the input energy spectrum shown in Fig. 2.16, which is based on the neutron spectrum measured by the BPM during the interaction of protons with the LiF target. For each neutron simulation, the energy deposition, interaction time, interaction type, and the involved particle in each detector are recorded. If a scattered neutron is detected by one of the BDs after interacting with the NaI(Tl) detector, the event is tagged as a triggered event. The nuclear recoil energy depends on the scattering angle of the neutrons, as described by Eq. 2.13:

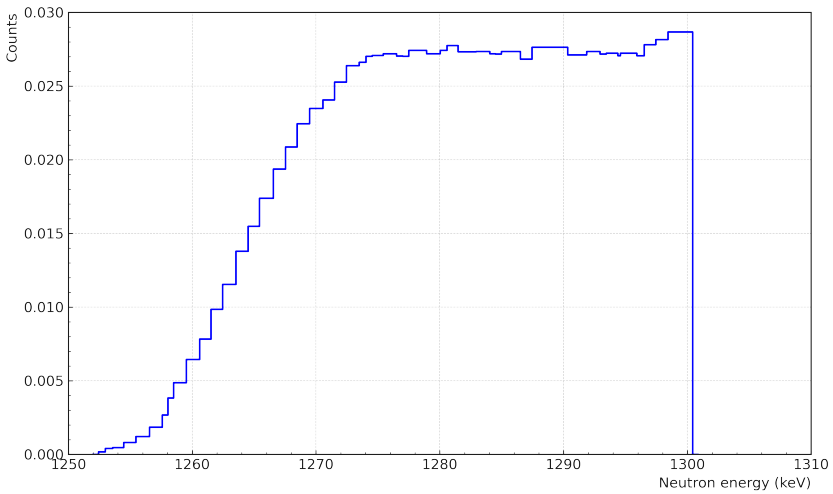

Figure 2.16: The neutron energy spectrum used in the simulation, obtained using measurements from the BPM.

$$E_{nr} = 2E_n \frac{m_n^2}{(m_n + m_N)^2} \times \left(\frac{m_N}{m_n} + \sin^2\theta - \cos\theta \sqrt{\frac{m_N^2}{m_n^2} - \sin^2\theta} \right) \tag{2.13}$$

where E_n is the incident neutron energy, θ is the neutron scattering angle, m_n is the neutron mass, and m_N is the target nuclide mass. For each neutron interaction in the NaI(Tl) crystal that triggers any BD, the interaction type (elastic or inelastic) and the specific nucleus involved (Na or I) are recorded. The simulation generates a distribution of the nuclear recoil energies in the NaI(Tl) crystal coinciding with any BD. The resulting nuclear recoil energy

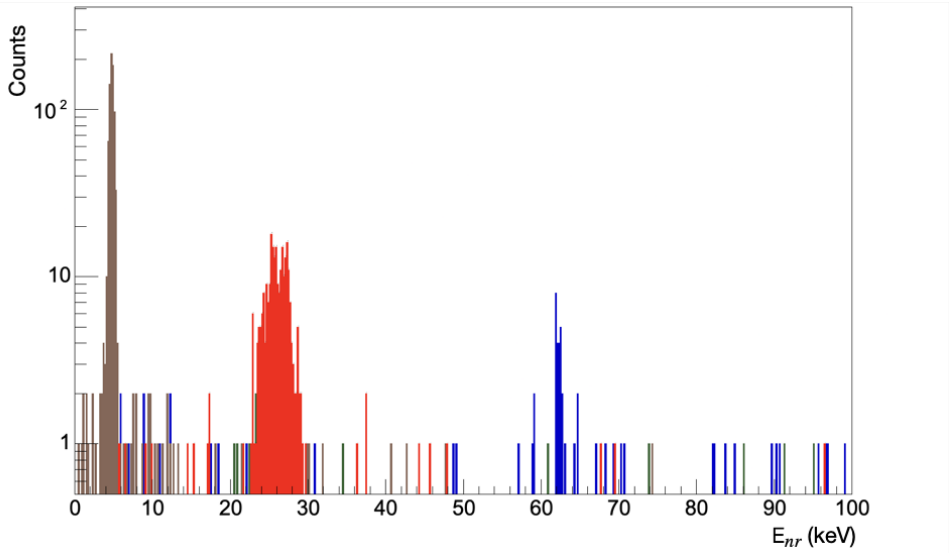

Figure 2.17: Simulated nuclear recoil energy deposition in the NaI(Tl) crystal, triggered by BD0. The elastic and inelastic scattering off ^{23}Na are shown in red and green, while the elastic and inelastic scattering of ^{127}I are shown in brown and blue, respectively.

deposited in the NaI(Tl) crystal for BD0 is shown in Fig. 2.17. The simulation accounts for uncertainties in detector positions, neutron beam angular spread, and detector dimensions, as well as potential backgrounds from multiple neutron scattering within the setup.

2.4.4 Quenching Factor Estimation

Signal and background modeling for QF extraction

The calibrated and cleaned energy spectra for nuclear recoils, expressed in the E_{ee} energy scale obtained in Sec. 2.4.2 and Sec. 2.4.2, are used together with the simulated nuclear recoil spectra obtained in Sec. 2.4.3, expressed in the E_{nr} scale, to extract the quenching factor for Na recoils (QF_{Na}) for different energies and for each crystal. It was not possible to estimate the quenching factor for iodine recoils (QF_I) in the current study. For the highest recoil energy, corresponding to events from BD0, the quenched energy for I recoils is expected to be only ~ 0.5 keV, which is below the noise pedestal in our measurements. To account for the differing background components in each crystal we define a background function that can vary freely between crystals and BDs. The background count is modeled as $BG(E) = ae^{bE} + cE^d$, with the free parameters a, b, c, d. The signal (Na recoils) is modeled by "quenching" the simulated recoil energy spectra with the QF, and smearing the resulting histograms with the resolution function obtained in Sec. 2.4.2. Each bin center from the simulated histograms is first multiplied with the QF, which is a free parameter per BD and crystal. This gives the quenched histogram bin centers $E_{q,j}$. For a given measured (i.e., quenched) energy value E, the value of the signal function $S(E)$ is then calculated by summing over the contributions from each simulated histogram bin:

$$S(E) = A \sum_{j}^{N_{\mathrm{bins,\,sim}}} S_j \left[\mathrm{Erf}\left(E + \frac{w}{2}, E_{q,j}, \sigma(E_{q,j})\right) - \mathrm{Erf}\left(E - \frac{w}{2}, E_{q,j}, \sigma(E_{q,j})\right) \right] \tag{2.14}$$

where S_j is the bin content of the simulated histogram bin j, w is the simulated histogram bin width, $\sigma(E_{q,j})$ the resolution evaluated at the quenched bin center, and Erf is the error function.

A parameter controlling the overall scale/count (A) of the signal is also included. The final smeared signal can be asymmetric around a central value, but the individual bin smearings are Gaussian distributed, which is a reasonable assumption as long as the binning of the original simulated histogram is fine enough. This signal is then added on top of the BG function to get the overall count per bin.

We fit the combined model using the Bayesian Analysis Toolkit (BAT) [124], ensuring that all related uncertainties in the QF analysis chain are properly accounted for and propagated. BAT is a Markov Chain Monte Carlo (MCMC) toolkit that explores the full

available parameter space. The Markov chain is then used to create posterior distributions, from which the global mode and uncertainties on the QF are obtained. All parameters have flat prior distributions, except for the resolution function, which is fixed. The resolution function parameters are obtained from Sec. 2.4.2. Convergence of the MCMC chains is evaluated by the $\hat{R}$-parameter [125], and the step size is optimized to ensure a chain efficiency between 15-35%. A pre-run of 500,000 steps was found to suffice for convergence and step size adjustment. The main MCMC is then run for 500,000 steps to construct the posterior. The upper and lower uncertainties are derived from the 16% and 86% distribution quantiles, with the global mode as the central value. Fig. 2.18 shows the resulting posterior distribution for the QF_{Na} parameter, which appears Gaussian and centered around the global mode.

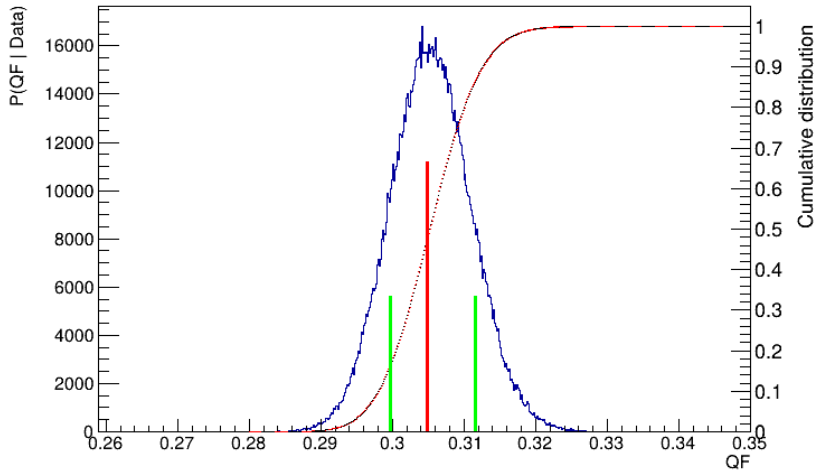

Figure 2.18: Posterior distribution for the QF for Crystal 1 BD 0, using the ^{133}Ba proportional response, and the $\sigma = \sqrt{aE} + bE$ resolution function. The green lines mark the 16% and 86% confidence limits, the red is the global mode.

Example fits to the nuclear recoil spectrum measured for Crystal 1 with BD0 and BD2 are shown in Fig. 2.19 and Fig. 2.20 respectively. As can be seen also in Fig. 2.19, the resolution is underestimated for BD0 in all crystals. This results in a higher QF_{Na} compared to the trend for the other BDs.

We exclude points where the signal scale (parameter A in Eq. 2.14) is much larger than the high-energy recoils global mode, as the signal contribution is clearly fitted to the background here. A transition on this scale was observed for low-recoil points, where the parameter increases from $\mathcal{O}(5)$ to $\mathcal{O}(50)$, and therefore deviates strongly from the norm. The simulated nuclear recoil spectrum already accounts for the different total number of signal events at different recoil angles, therefore no strong variation of the signal scale is expected. In particular, we reject fits where the scale is larger than 20, shown for Crystal 1 in Fig. 2.21. Using the log-likelihood (LL) ratio of fits with and without signal to reject results without a significant signal contribution was not sufficient, as the recoil peak can fit fluctuations in the background bins, resulting in a large LL value. This could be addressed with a more

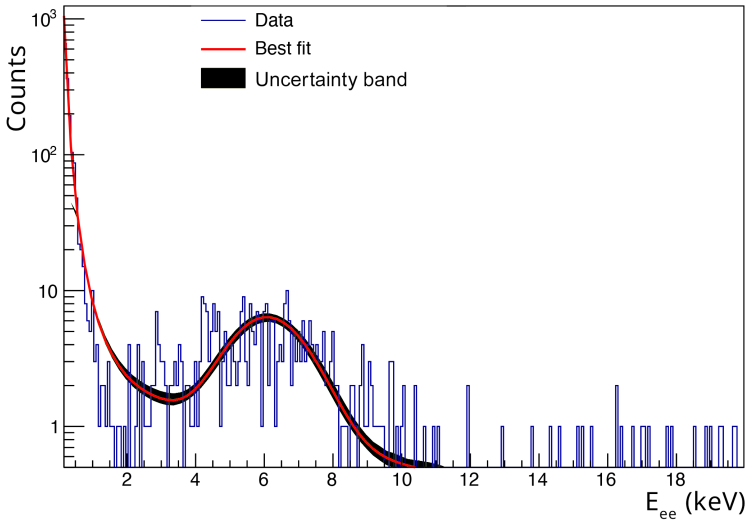

Figure 2.19: Fit of the recoil peak and background to the dataset of Crystal 1 and BD0.

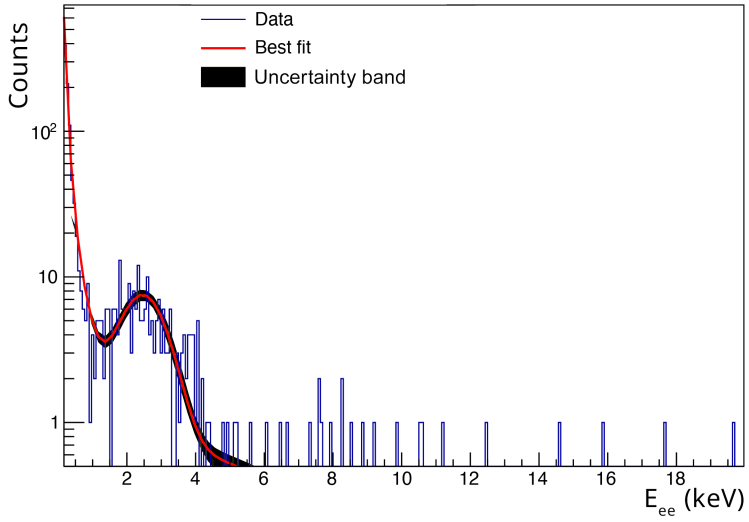

Figure 2.20: Fit of the recoil peak and background to the dataset of Crystal 1 and BD2.

sophisticated background model, or by including more detailed prior distributions for the signal parameters.

Geometrical uncertainites

As can be seen in Fig. 2.21, a sawtooth pattern is present in the results. The QF seems to oscillate above and below a "central" trend. This oscillation stems from the alternating geometry, where the BD corresponding to the highest recoil energy is on one side, and the next highest is on the opposite side, with respect to the beam line. We investigated whether an angular shift in the BD array, i.e., a rotation of the BD holder structure with respect to the beamline, would remove this feature.

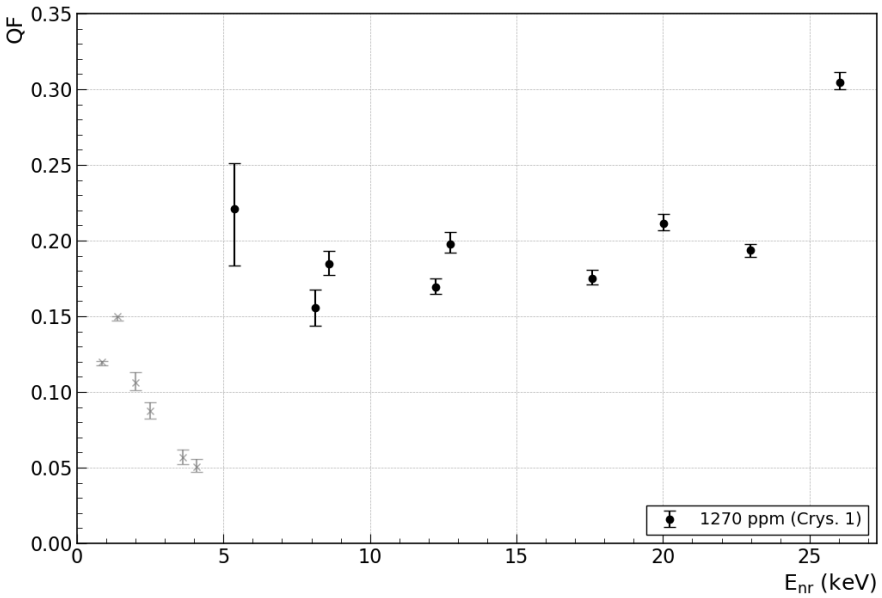

Figure 2.21: QF_{Na} for Crystal 1 (using the ^{133}Ba proportional response calibration) showing the rejection of fits to background, highlighted in gray.

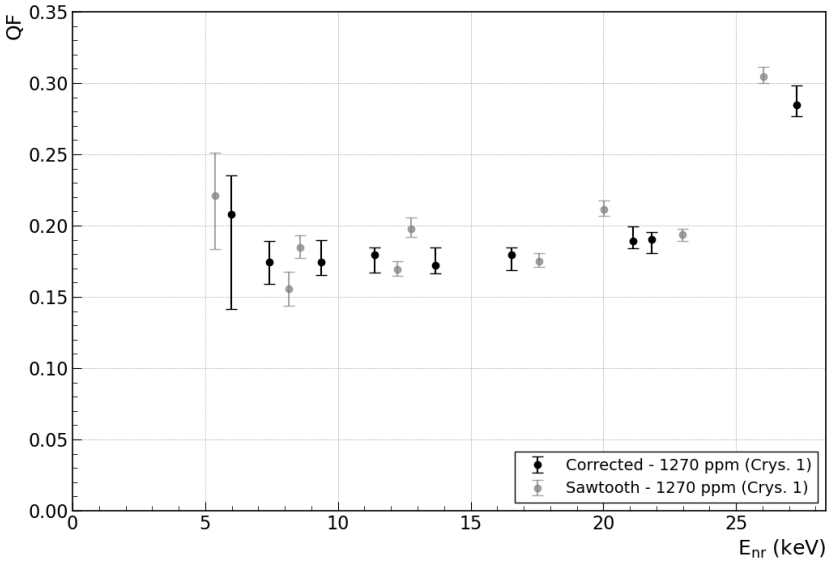

Figure 2.22: In gray: QF_{Na} for Crystal 1 with the sawtooth pattern; Black: "Flattened" QF_{Na} and nominal recoil energies corrected for an angular shift of 1°, outlined in Sec. 2.4.4.

BDs 2 and 12 on opposite sides of the array feature the highest nominal angles relative to the beamline with a difference of only 0.5°. By correcting the nominal recoil energies of these BDs such that the difference in their measured QFs becomes minimal, we obtain an angular shift of about 1°. This is calculated for each crystal, where only Crystal 4 deviates significantly, showing a smaller shift. The effect of a 1° rotation is therefore conservatively considered as the systematic uncertainty due to a possible rotation of the holder structure. Fig. 2.22 additionally shows the QFs and nuclear recoil energies that would result for Crystal 1 from correcting for this angular rotation. As the exact angle is not known, we add an asymmetric systematic uncertainty on the assumed nuclear recoil energy for all BDs instead of applying this correction directly. This uncertainty is propagated to the QFs. Additional variations in the individual BD positions are not accounted for.

2.4.5 Results

Energy dependence

QF_{Na} results for the measured crystals using the methodology described in Sec. 2.4.4 and calibration schemes described in Sec. 2.4.2 are shown in Fig. 2.23 and Fig. 2.24. The errors are the lower (16%) and upper (86%) quantiles of the posterior QF distribution, as shown in Fig. 2.18 for Crystal 1 and BD 0. We find a clear energy dependence of QF_{Na} for all five crystals, i.e., QF_{Na} decreases with nuclear recoil energy.

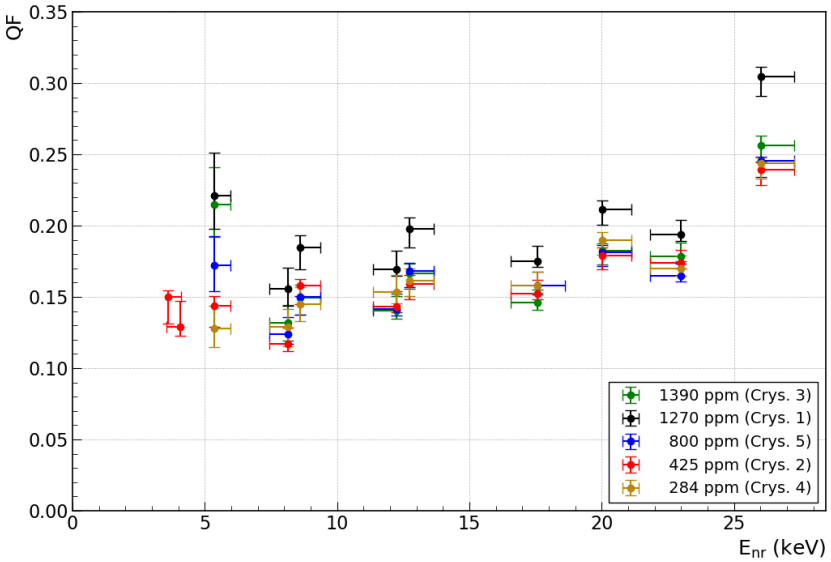

Figure 2.23: QF_{Na} as a function of energy for calibration with ^{133}Ba 6.6 keV.

Calibration with ^{241}Am 59.54 keV seems to yield slightly lower QF and cause more spread among the different crystals when compared to calibration with ^{133}Ba 6.6 keV. The lowest point we can resolve is BD5 for Crystal 2, corresponding to a recoil energy of 3.6 keV_{nr}.

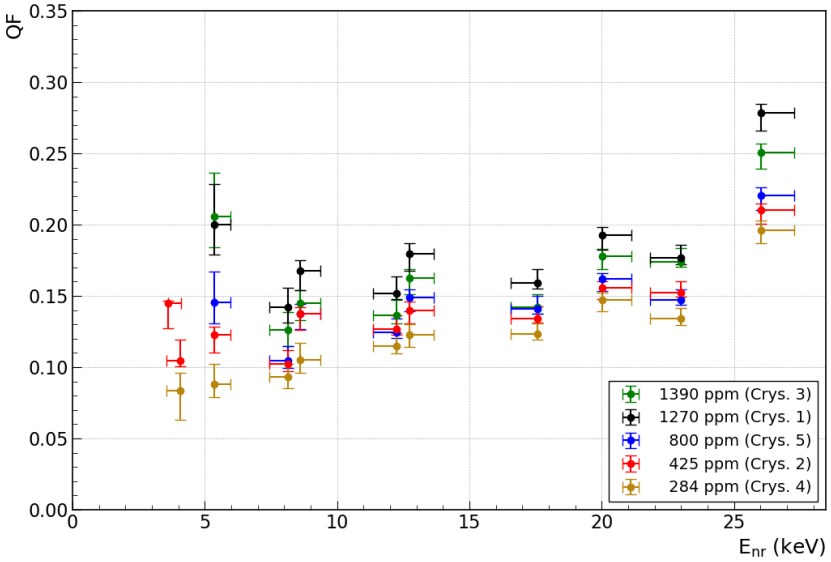

Figure 2.24: QF_{Na} as a function of energy for calibration with ^{241}Am 59.54 keV.

A comparison between the results of Crystal 1 and Crystal 4 with the ^{241}Am calibration scheme and previous measurements is shown in Fig. 2.25. All datasets yield lower QF_{Na} at lower nuclear recoil energies. Although our data agrees well with [106] and [107], there is a shift in comparison to [103], which reports higher QF values. Different calibration methods or the effect of Tl dopant level could explain this discrepancy, which is discussed in the following section.

Tl dependence

A possible Tl dependence of QF_{Na} was investigated by selecting a specific nuclear recoil energy across all crystals, and then plotting QF_{Na} for that energy as a function of Tl dopant level in the crystal. Three different fits were carried out for these plots: a constant fit, a linear fit, and a logarithmic fit of the form $a\log(x) + b$. By comparing the $\chi^2/n.d.f$ values of the constant fit to the linear one, we gauge whether there is a significant dependence. The logarithmic fit results were found to be comparable to the linear case. A comparison of the fits for a given BD energy is shown in Fig. 2.26 and Fig. 2.27.

We find that the Tl dopant dependence is strongly visible for calibration with the 59.54 keV peak from ^{241}Am (Fig. 2.27), i.e., constant QFs are a bad fit, while it is much less pronounced for ^{133}Ba 6.6 keV (Fig. 2.26). This indicates that the light yield of NaI(Tl) still has an influence on the results. However, a lower Tl dopant level seems to result in lower QF_{Na} overall. For a majority of recoil energies, the linear dependence describes the observed data better than the logarithmic dependence.

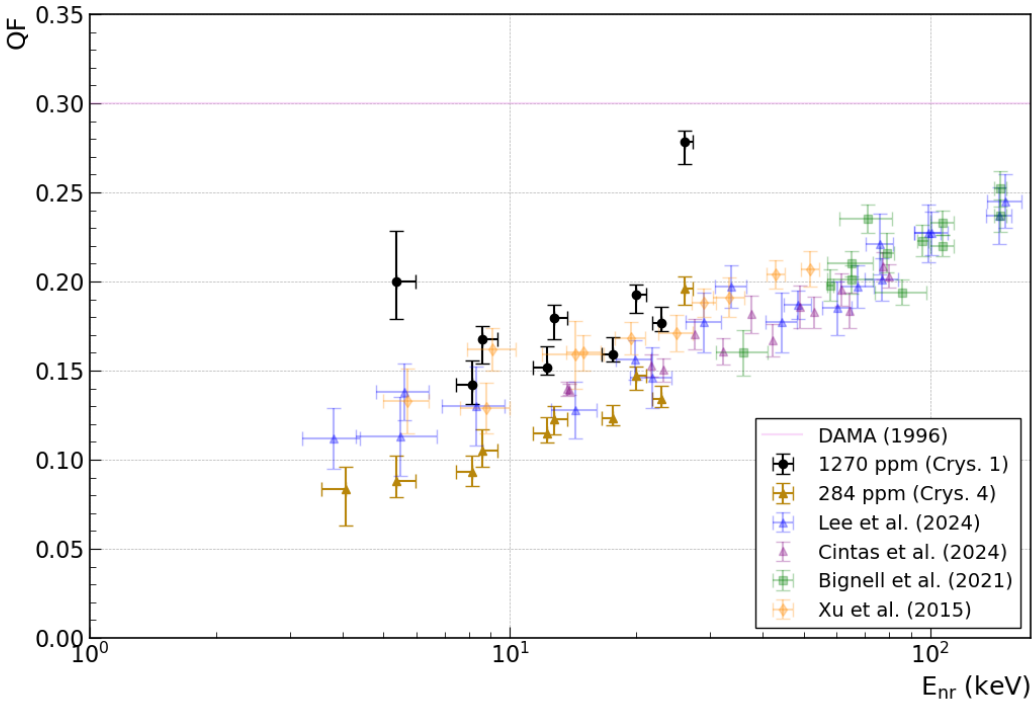

Figure 2.25: Comparison of QF_{Na} between Crystal 1 (black) and Crystal 4 (gold), alongside recent measurements [103–107]. Calibration of the data sets is based on either the 57.6 keV γ-line from ^{127}I(n,n'γ) process or the 59.54 keV γ-line from ^{241}Am.

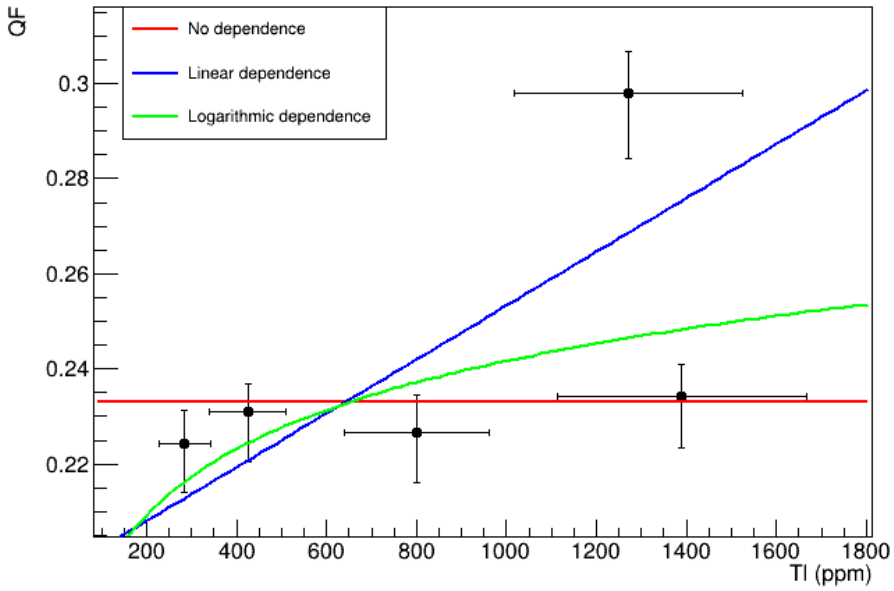

Figure 2.26: Tl dependence of QF_{Na} for a recoil energy of ~26 keV (BD0) with different functional assumptions, using ^{133}Ba 6.6 keV calibration.

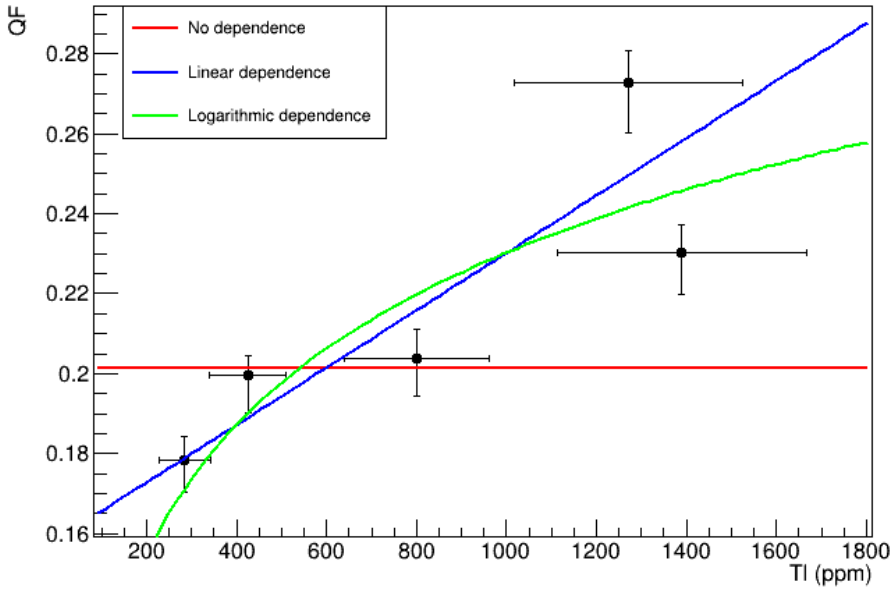

Figure 2.27: Tl dependence of QF_{Na} for a recoil energy of ~26 keV (BD0) with different functional assumptions, using ^{241}Am 59.54 keV calibration.

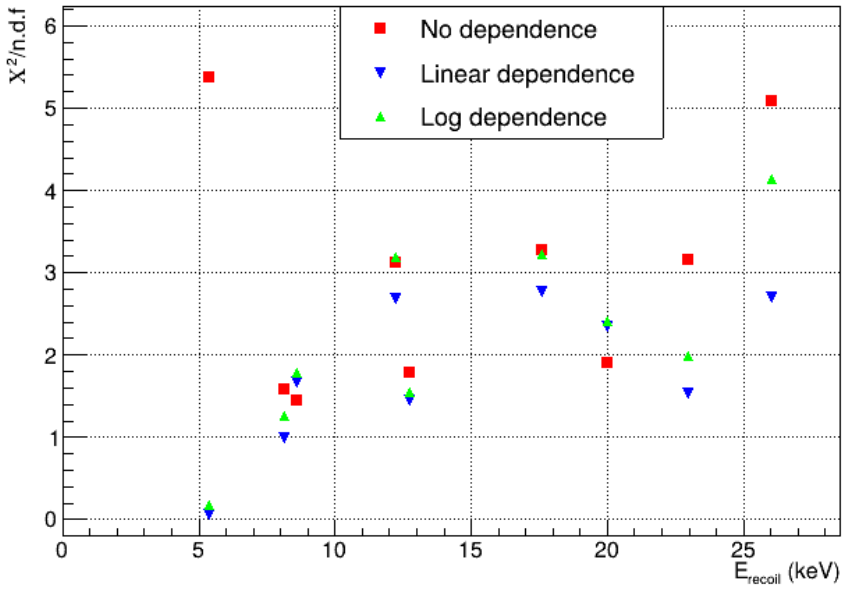

Figure 2.28: $\chi^2/n.d.f$ values for different functional assumptions on the Tl dependence of QF_{Na}, using ^{133}Ba 6.6 keV calibration.

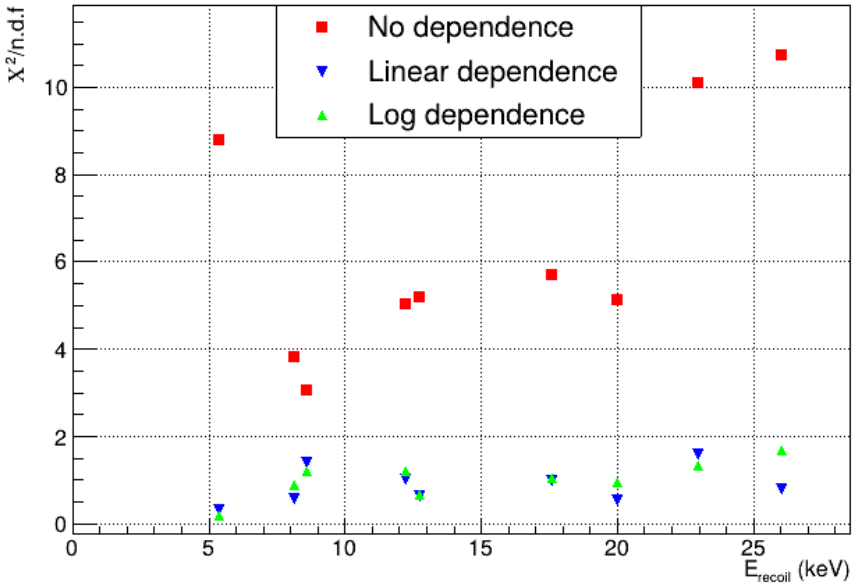

Figure 2.29: $\chi^2/n.d.f$ values for different functional assumptions on the Tl dependence of QF_{Na}, using ^{241}Am 59.54 keV calibration.

2.4.6 Conclusion

Recent years have seen important advancements in the study of QF in NaI(Tl) crystals, driven by a concerted effort from the scientific community to address the long-standing uncertainty that the QF poses in the interpretation of results from NaI(Tl)-based scintillation light-only direct DM search experiments. QF_{Na} was measured in five such crystals, each with a different Tl dopant concentration. The recoil energies are in the range (5-26) keV_{nr}. Each crystal was irradiated for 28-35 hours at TUNL by a quasi-monoenergetic neutron beam. To calibrate the crystals, ^{241}Am and ^{133}Ba sources were used in this work. The crystal response was calibrated by assuming proportional response to the 6.6 keV peak of ^{133}Ba and the 59.54 keV peak of ^{241}Am. The QF was determined through a bayesian fit using BAT, assuming a parametric background function and using quenched simulated nuclear recoil histograms for each BD, smeared with the measured PMT resolution function. The QFs have a visible energy dependence and are compatible with previous results from other measurements, and this study was able to extend the measurement data to lower recoil energies. The combination of limited detector resolution and low recoil energies prevented resolving I recoils in this work. A systematic geometrical effect (sawtooth pattern) is visible for all QFs, that is believed to originate from a rotation of the BD holder relative to the beam axis. This systematic uncertainty was estimated by calculating modified nuclear recoil energies with an angular shift of 1°. The pattern has also been observed in other measurements [106]. A potential Tl dependence of QF_{Na} was also studied, and it was found that a lower Tl concentration leads to a lower QF in general. However, the magnitude of this effect varies between the two calibration methods. This highlights the importance of the choice of calibration in such measurements. A future study of Tl dopant levels over a wider range of concentrations while exploring a broad range of recoil energies is needed

to extract a comprehensive model for the relationship between light yield and quenching characteristics. Understanding the non-linear light yield of NaI(Tl) crystals [116, 117] is another essential aspect.

2.5 The Case for COSINUS

To summarize, Sec. 2.3 and Sec. 2.4 outline the importance that the QF plays in the interpretation of the energy scale seen by scintillation-only direct DM experiments. The spread in reported QF measurements at lower energy scales depends on a multitude of factors including, but not limited to the calibration schemes, Tl dopant in the crystals, non-linearity in the light output and radiopurity of the crystals. Dedicated studies focusing on each of the factors need to be carried out. An approach to have an experiment that can in-situ measure the QF of the crystal while measuring the true nuclear recoil energy, while also being able to veto electron/gamma induced backgrounds serves as a viable approach to clear out any lingering open-standing questions once and for all.

The COSINUS experiment aims to do precisely this by running pure NaI crystals at cryogenic temperatures as scintillating calorimeters [126]. This method provides a direct measurement of the recoil energy via a phonon signal, which is nearly independent of the interacting particle type. As one may recall by looking back at the discussion following Eq. 2.12, most of the recoil energy is usually dissipated in the form of phonons. As the scintillation light is also measured using a second channel, the QF can be measured in-situ [66]. Thus, a direct measurement of these signals ensures that most of the original information regarding the initial recoil can be deduced. For a semi-intuitive picture of what COSINUS might see if one assumes the DAMA modulation to originate from DM elastic scattering, Fig. 2.30 shows the equivalent signal that a COSINUS detector would see with a 1 $\mathrm{keV_{nr}}$ energy threshold and 100 kg d gross exposure. The DM particle is assumed to have a mass of 10 GeV and $\sigma^0_{\mathrm{SI,\,nucleon}} = 2 \times 10^{-4}$ pb, while the radiogenic background is assumed to have a constant rate of 1 count per day/ (keV kg) and 20 ppb of ^{40}K intrinsic contamination of the NaI crystal.

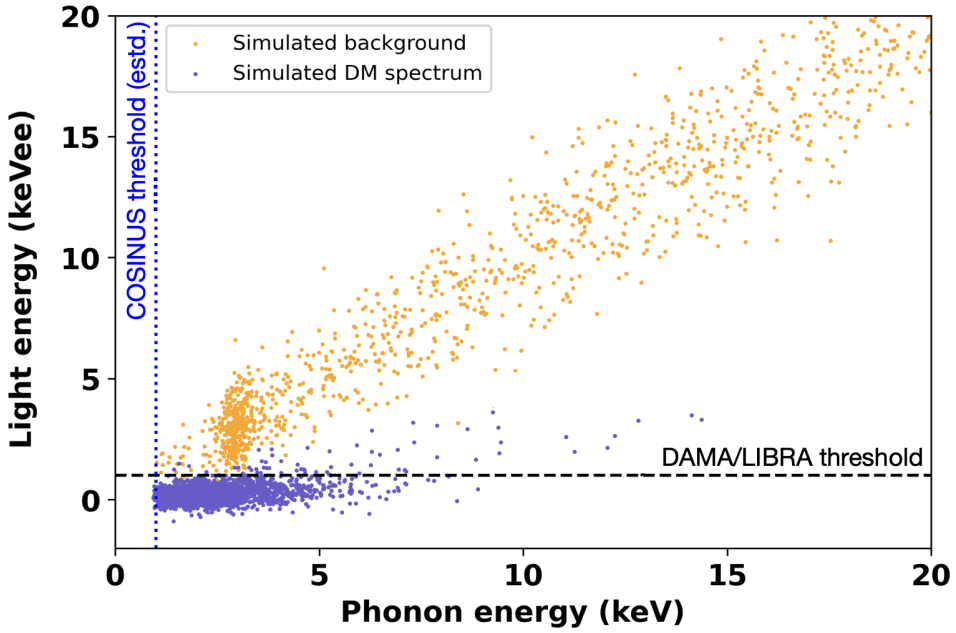

Figure 2.30: Energy-scale comparison of DAMA/LIBRA (black dotted line) versus a dual-channel readout used by COSINUS (blue dotted line). The black dashed line corresponds to the energy threshold of DAMA/LIBRA (measuring only scintillation light). Assuming the presence of a DM particle interaction in the crystal, only a very small percentage of this is "seen" in a single-channel scintillation-light readout experiment in accordance with Eq. 2.12. This is denoted by the violet events above the DAMA/LIBRA threshold. COSINUS sees more of the violet events as the threshold is lower as it directly measures the phonon channel. Due to its cryogenic dual channel readout approach, it can also perform particle identification on an event-by-event basis.

THE COSINUS EXPERIMENT

The COSINUS detector 3

If I have seen further it is by standing on the shoulders of Giants.
— Isaac Newton, *Letter to Robert Hooke*

3.1 Cryogenic Calorimeter Primer

The field of high-energy physics has extensively utilized calorimeters over the past four decades to measure the energy loss of particles in specified absorbers. A calorimeter is a device designed to absorb the energy of incoming particles and measure that energy through the resultant temperature increase or other secondary processes, via which one can extract information about the particles' properties. Its origins are even more ancient, with the first calorimetric measurement attributed to Samuel Pierpont Langley in 1878, who invented the bolometer to measure the energy flow of the sun in the far-infrared region [127].

One of the earliest publications on low-temperature calorimeters is attributed to F. Simon in 1935, who proposed using them to measure radioactive decays due to their higher sensitivity compared to conventional calorimeters [128]. A special mention goes to the publication by D.H. Andrews *et al.* in 1949, who used a bolometer made of a superconducting strip of niobium nitride to detect α-particles from a polonium source [129]. The noteworthy aspect here is the operating temperature of 15.5 K, corresponding to the center of the transition between the superconducting and normal conducting states of NbN. This work is likely the first test involving the property of Superconducting Phase-Transition thermometers, commonly known today as Transition Edge Sensors (TESs).* The 1970s and 1980s brought about the first practical implementations of low-temperature calorimeters and bolometers, mainly envisioned for neutrino and astrophysics experiments [130–132]. A workshop held at Castle Ringberg in Tegernsee, Munich, in 1987 led to the formalization of this field, with a range of applications explored since then, comprehensively covered in the proceedings of the Low Temperature Detectors (LTD) workshops [133].

In contrast to traditional calorimeters, which often rely on scintillation or ionization processes for signal readout at room temperature, cryogenic calorimeters offer superior energy resolution due to their reduced thermal noise as shown in Fig. 3.1. The low operating temperatures also enhance the signal-to-noise ratio, ensuring a low energy threshold for such detectors. This makes it an ideal candidate to carry out direct DM searches due to the ability to test out a wide range of materials to probe the DM parameter space as outlined in Chapter 2, combined with all the benefits listed above.

* At this stage, they only used it as a particle counter since the signal-to-background ratio was too high, and reliable cold amplifiers had not yet been developed.

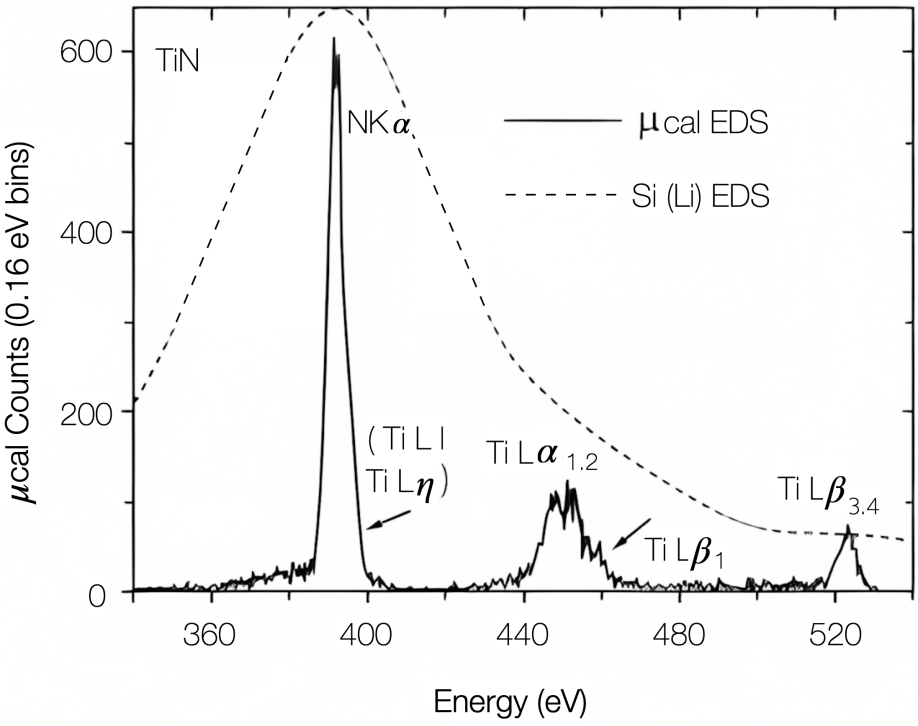

Figure 3.1: Comparison of X-ray spectra obtained with a state-of-the-art Si detector versus a cryogenic micro-calorimeter from the NIST group [134]. Image upscaled using [135].

3.1.1 Foundations

The design of a typical cryogenic calorimeter consists of three main elements: the absorber, the thermometer, and the heat sink (thermal bath). The absorber is the material where particle interactions occur, converting kinetic energy into thermal energy. The thermometer is a temperature sensor that measures the resultant temperature rise and is ideally thermally well-coupled to the absorber. The heat sink maintains the cryogenic operating temperature of the absorber by providing a weak thermal anchoring, allowing excess heat to dissipate.

For an absorber with a volume V and specific heat capacity c, the total heat capacity is $C_{\text{tot}} = c\text{V}$. If an energy E is deposited in the absorber and is fully thermalized, the temperature rise ΔT is given by:

$$\Delta\text{T} = \frac{\text{E}}{C_{\text{tot}}} \tag{3.1}$$

For cryogenic dielectric absorbers, the Debye model is used to calculate the specific heat, yielding:

$$c_{\text{dielectric}} \simeq c_{\text{ph}} = \beta \left(\frac{T}{\theta_D}\right)^3 \tag{3.2}$$

where $\beta = \frac{12}{5}\pi^4 R \approx 1944\,\text{J mol}^{-1}\,\text{K}^{-1}$, R is the gas constant, and θ_D is the Debye temperature of the crystal. c_{ph} denotes the contributions due to lattice vibrations. The contribution

due to electronic heat capacity, c_{el}, is negligible because of the absence of free electrons in dielectrics.

In the case of a metallic absorber that remains in the normal conducting state at the operating temperature, both lattice vibrations and thermally excited conduction electrons contribute to the heat capacity. The specific heat capacity, c_{metal}, is given by:

$$c_{\mathrm{metal}} = c_{\mathrm{ph}} + c_{\mathrm{el}} = \beta \left(\frac{\mathrm{T}}{\theta_D} \right)^3 + \gamma \mathrm{T} \tag{3.3}$$

where γ is the Sommerfeld constant, a material-dependent parameter representing the electronic contribution. For example, in gold (Au), at temperatures below 1 K, c_{el} dominates due to the high density of conduction electrons, causing the total specific heat capacity to decrease linearly with temperature.

In superconductors like aluminum (Al), which has a superconducting transition temperature, $\mathrm{T_c}$ of ~ 1.2 K, the specific heat capacity exhibits distinct behaviors in different temperature regimes. Above $\mathrm{T_c}$, the specific heat includes contributions from both phonons and normal-state electrons, similar to normal metals. Near $\mathrm{T_c}$, there is a sharp peak in the specific heat due to the superconducting transition, known as the superconducting anomaly. Below $\mathrm{T_c}$, the electronic contribution to the specific heat decreases exponentially with temperature because of the energy gap in the superconducting state. At temperatures much lower than $\mathrm{T_c}$, the specific heat is dominated by lattice vibrations, reverting to a dominant contribution from c_{ph}.

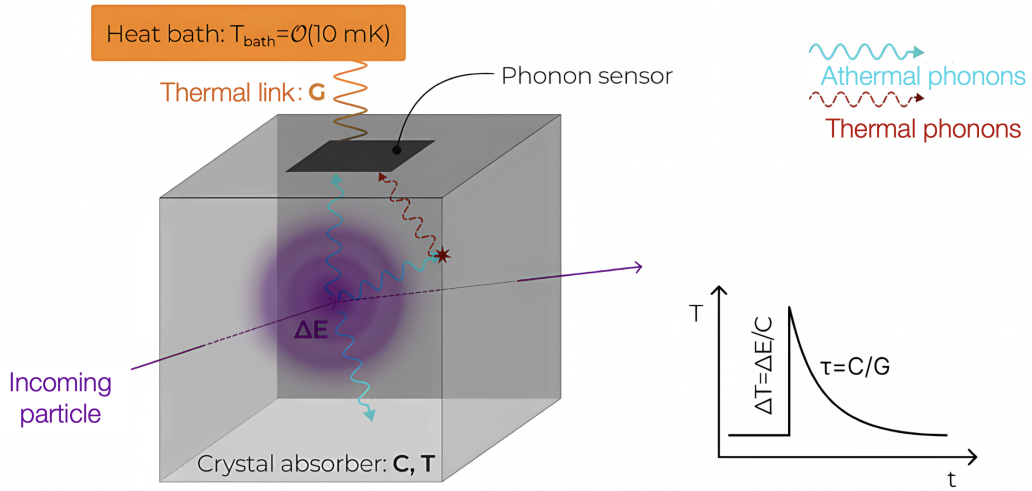

Figure 3.2: Schematic of a cryogenic calorimeter, depicting its general working principle. Adapted from [79].

Returning to the temperature rise, ΔT, assuming an initial bath temperature of $\mathrm{T_{bath}}$, the time required for the absorber to cool from $\mathrm{T_{bath}} + \Delta\mathrm{T}$ back to $\mathrm{T_{bath}}$ is given by the time constant, τ:

$$\tau = \frac{\mathrm{C_{tot}}}{\mathrm{G}} \tag{3.4}$$

where G denotes the thermal conductance of the weak thermal link to the heat bath.

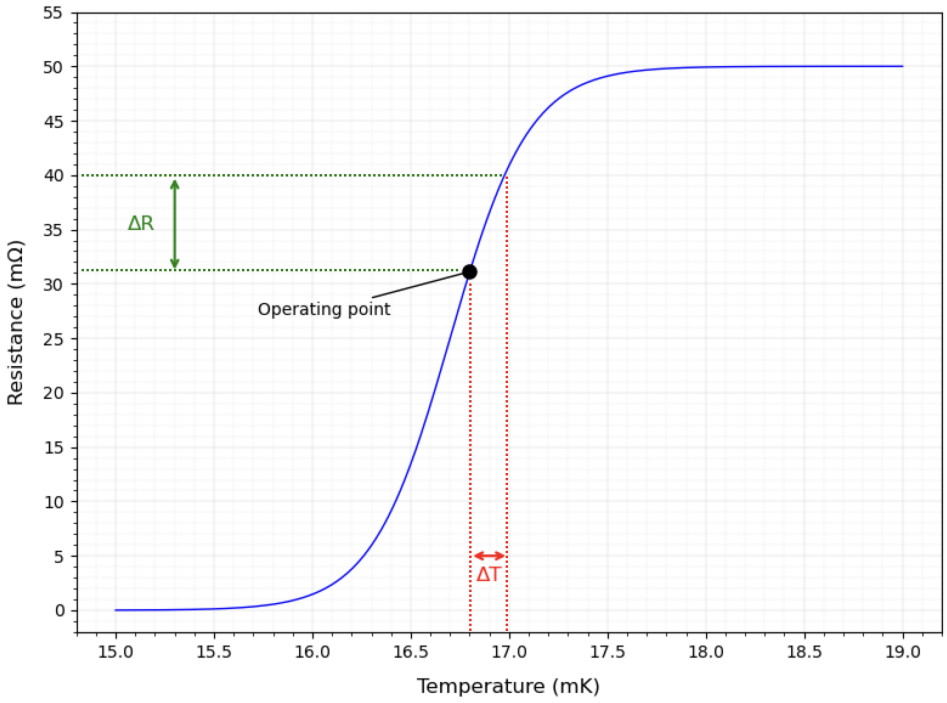

Figure 3.3: A typical transition curve representative of a TES film. A small temperature change ΔT ($\mathcal{O}(\mu K)$), caused by a particle interaction in the absorber, leads to a measurable change in the resistance ΔR of the TES. This change can then be recorded and amplified using integrated front-end electronics. An ohmic heater (ususally located in close proximity to the TES) is used to stabilize the Operating point (OP).

From Eq. 3.3, the cubic dependence of c_{ph} on temperature is significant, as this implies that at progressively lower temperatures, the ΔT can be appreciably higher for the same deposited energy, E. Thus, combining a low temperature, T, and a low total heat capacity, C_{tot} (achieved with smaller detector volumes and selecting a material with a high θ_D) provides an optimal starting point for designing a sensitive detector in accordance with Eq. 3.1 and Eq. 3.3. In COSINUS, we use dielectric crystals operated at mK temperatures with the help of dilution refrigerators, as covered in Chapter 4. However, this thermodynamical picture is an oversimplification, and a more formal treatment, considering other experimental parameters, yields a slightly different dependence which will be discussed in Sec. 3.2.1.

3.1.2 Detector Readout Schemes

Various sensors can be employed to read out these small temperature changes, each exploiting different physical principles to convert these changes into measurable electrical signals. Neutron Transmutation Doped (NTD) thermistors are semiconductor devices sensitive to temperature variations, commonly used for phonon detection due to their high sensitivity and low noise characteristics. Metallic Magnetic Calorimeters (MMCs) utilize paramagnetic materials whose magnetization changes with temperature, allowing for precise energy measurements through magnetic flux detection. Kinetic Inductance Detectors (KIDs) exploit changes in the kinetic inductance of superconducting materials caused by incident photons or particles, enabling high-speed and multiplexed readout

capabilities. Transition Edge Sensors (TESs) operate at the superconducting transition temperature, where a small temperature change results in a significant change in electrical resistance.

For the COSINUS experiment, the TES is utilized due to its high sensitivity, benefiting additionally from the extensive fabrication expertise developed in the CRESST experiment. Fig. 3.3 provides a pictorial representation of the operating principle of these sensors.

3.2 Detector Module

The COSINUS detector module comprises two independent channels: an undoped NaI absorber operated as a cryogenic scintillating calorimeter, coupled with a Si detector enclosing the absorber to collect the scintillation light, as shown in Fig. 3.5. The Si detector is also operated as a cryogenic calorimeter optimized for scintillation light detection. This configuration enables the simultaneous measurement of both phonon (heat) and scintillation (light) signals, with the ratio of the two, denoted by the light yield, allowing for a discrimination between different types of particle interactions. In addition, the QF of the crystal can also be determined in-situ as described in Chapter 6, thus overcoming the challenges faced by single-channel NaI-based experiments, as explained in Chapter 2.

The COSINUS NaI crystals are manufactured at the Shanghai Institute for Ceramics at the Chinese Academy of Sciences using a modified Bridgman process as described in [111], utlizing ultra-pure "Astro-grade" NaI powder procured from the Merck group [112]. Inductively Coupled Plasma Mass Spectrometry (ICP-MS) analysis performed at LNGS [113] revealed internal contamination levels of (6-22) ppb for ^{40}K, and < 1 ppb for both ^{208}Th and ^{238}U. For COSINUS Run 1, crystals of dimension (21x21x21) mm^3 will be used, as shown in Fig. 3.4.

Figure 3.4: Crystal production process at SICCAS: From left to right: **a)** A quartz (SiO_2) crucible lined with a Pt foil is used for crystal growth; **b)** NaI ingots obtained after the growth process; **c)** Dry clean room for mechanical processing and polishing of the crystals; **d)** A polished (21x21x21) mm^3 radio-pure crystal in a nitrogen-flushed, moisture controlled glove box prepared for R&D measurements.

The *remo*TES (remote Transition Edge Sensor), outlined in [136] and implemented in [137] is used for signal readout from particle interactions in NaI. The *remo*TES approach decouples the TES, and its associated fabrication, from direct contact with the hygroscopic NaI crystal.

This prevents potential degradation of the NaI crystal while maintaining high sensitivity. It consists of a Au-link which comprises the Au-film on the absorber, a Au-film overlapping the W-TES (referred to as the Au port) and a Au bond-wire connecting them together. A detailed study on the implementation and testing of the *remo*TES design is covered in Chapter 5, Chapter 6 and Chapter 7.

The Si detector features a hollow, beaker-shaped design with a height of 40 mm, an outer diameter of 40 mm and a wall thickness of 1 mm. The unique shape maximizes the collection efficiency of scintillation light produced by the absorber from a particle interaction. It is instrumented with a W-TES on the top face for signal read out from phonons generated by the absorption of the scintillation light, as well as from direct interactions within the Si itself. A detailed study to optimize the performance of the light detector is covered in Chapter 7.

The NaI phonon detector along with the Si "light" detector is paired together in a housing, which is defined as the *detector module*. The final design of the detector module, after undergoing optimizations outlined in Chapter 6 and Chapter 7 is shown in Fig. 3.5. The detector module features a design that ensures a complete 4π veto of the NaI crystal against surface decays (Read Chapter 7 for a detailed discussion), while maximizing the collection efficiency of scintillation light produced by the absorber upon a particle interaction.

The entire holding and support structure of the module is made from low-background NOSV Cu [138] that is subjected to multiple rounds of surface treatment in order to remove organic and inorganic contaminants, oxides, and residues followed by a passivation layer of citric acid and H_2O_2. The mechanical holding for the two detectors must be reasonably tight while also ensuring a weak thermal contact in order to ensure minimal phonon losses as described in Sec. 3.2.1. For this, brass screws with a tip made out of polyoxymethylene (POM) are used, as illustrated in Fig. 3.5. Electrical contacts for biasing and stabilizing the TES are carried out using 17 µm diameter Al wires, wedge-bonded to the TES and a copper-Kapton-copper (Cu-Ka-Cu) semi-flexible PCB (L.9 and P.12 in Fig. 3.5). For thermal contact, a 25 µm diameter Au-wire is bonded (can be either wedge or ball bond) to the weak thermal link of the TES and the Cu-Ka-Cu pads of L.9 and P.12.

3.2.1 Model of Pulse Formation

Picking up the discussion from Sec. 3.1.1, a more detailed treatment of the heat transport dynamics following a particle interaction within the NaI crystal is covered in the following subsection. A qualitative overview to visualize the relevant processes is first presented, followed by a quantitative treatment of a particle interaction resulting in a nuclear recoil, depositing 10 keV of energy within the NaI crystal. The crystal is initially assumed to be in thermal equilibrium with the heat bath[†] at a temperature $T_{bath} \approx 15$ mK. The crystal is thermally isolated, except for a weak thermal coupling established via the thermal link of the *remo*TES thermometer.

[†] This usually refers to the temperature of the cryostat stage the detector is mounted to.

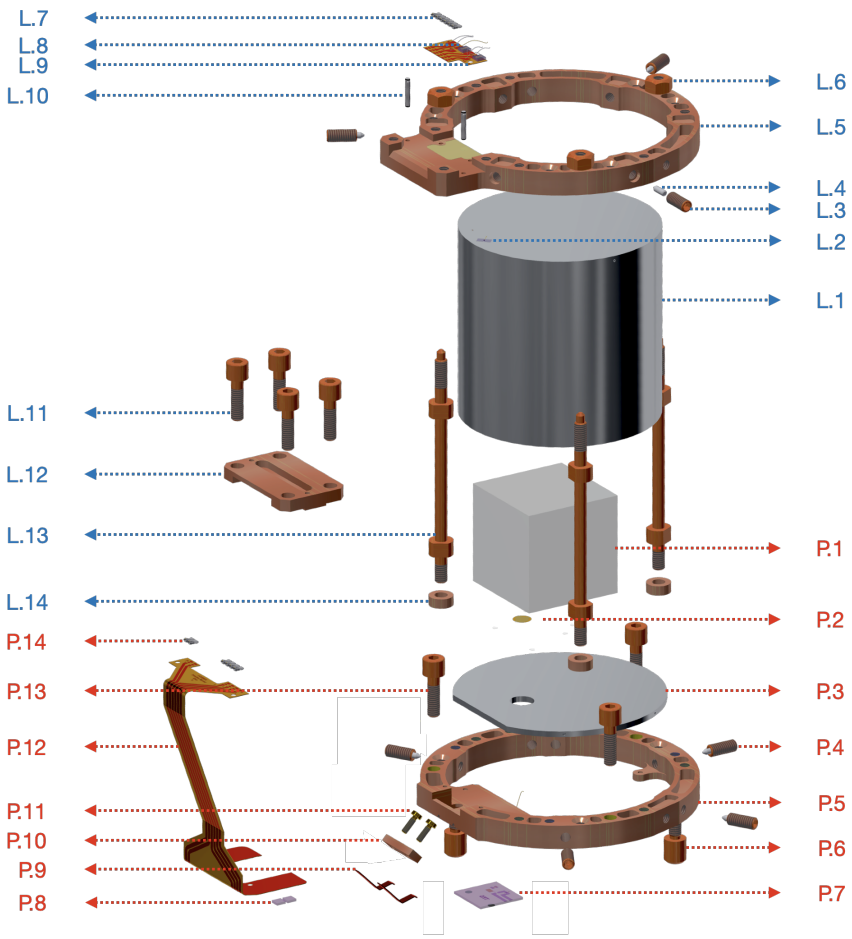

L.1: Si beaker
L.2: TES
L.3: POM holder
L.4: POM pin
L.5: Cu ring for detector mounting
L.6: Fixation nut connecting L.5 to L.13
L.7: Spring fingers for beaker readout
L.8: Shunts for beaker signal readout
L.9: Cu-Ka-Cu PCB for bonding
L.10: Support stems for securing P.12
L.11: M 2.5 hex screw for securing L.12
L.12: Cu-plate to press L.7 and P.14 against an external Cu-Ka-Cu PCB (not shown) to route signals outside the detector box.
L.13: Cu stems for mechanical fixation and support
L.14: Fixation nut securing L.13 and P.5

P.1: NaI crystal
P.2: Au-pad evaporated on P.1
P.3: Si lid on which P.1 is glued
P.4: POM pin
P.5: Cu ring for detector mounting
P.6: M 2.5 hex screw as a distance piece
P.7: remoTES wafer
P.8: Shunts for remoTES signal readout
P.9: Bronze clamps securing P.7
P.10: Tensioning Cu piece for P.9
P.11: Bronze M 1.2 screws for securing P.9 and P.10
P.12: Cu-Ka-Cu flexible PCB for bonding
P.13: M 2.5 hex screws to secure and thermalize module to the detector box
P.14: Spring fingers for NaI readout

Figure 3.5: A blown-up rendering of the module design for COSINUS. **In red:** The phonon channel comprising the NaI absorber (denoted via P.XX); **In Blue:** The Si detector enclosing the absorber to collect the emitted scintillation light when a particle interaction occurs within the crystal (denoted via L.XX).

At cryogenic temperatures, energy transfer occurs primarily through phonons due to the reduced thermal agitation of lattice vibrations. The energy deposited is initially localized around the recoil site, leading to the creation of high-frequency, high-energy phonons known as optical phonons. Optical phonons correspond to out-of-phase vibrations of atoms within the basis of the crystal lattice and typically have frequencies above 3 THz, as illustrated in Fig. 3.6. The corresponding energies of these phonons are $\mathcal{O}(20\,\text{meV})$, which are at a significantly higher energy than the thermal energy of the lattice ($E = k_B T_{bath} \approx 1\,\mu\text{eV}$ corresponding to a phonon frequency of $\approx 0.3\,\text{GHz}$). Over time scales of a few picoseconds to nanoseconds, this energy in the lattice is rapidly redistributed through continued phonon-phonon scattering. The optical phonons decay into multiple lower-energy acoustic phonons via processes such as Klemens decay, where an optical phonon decays into two acoustic phonons, while conserving energy and momentum.

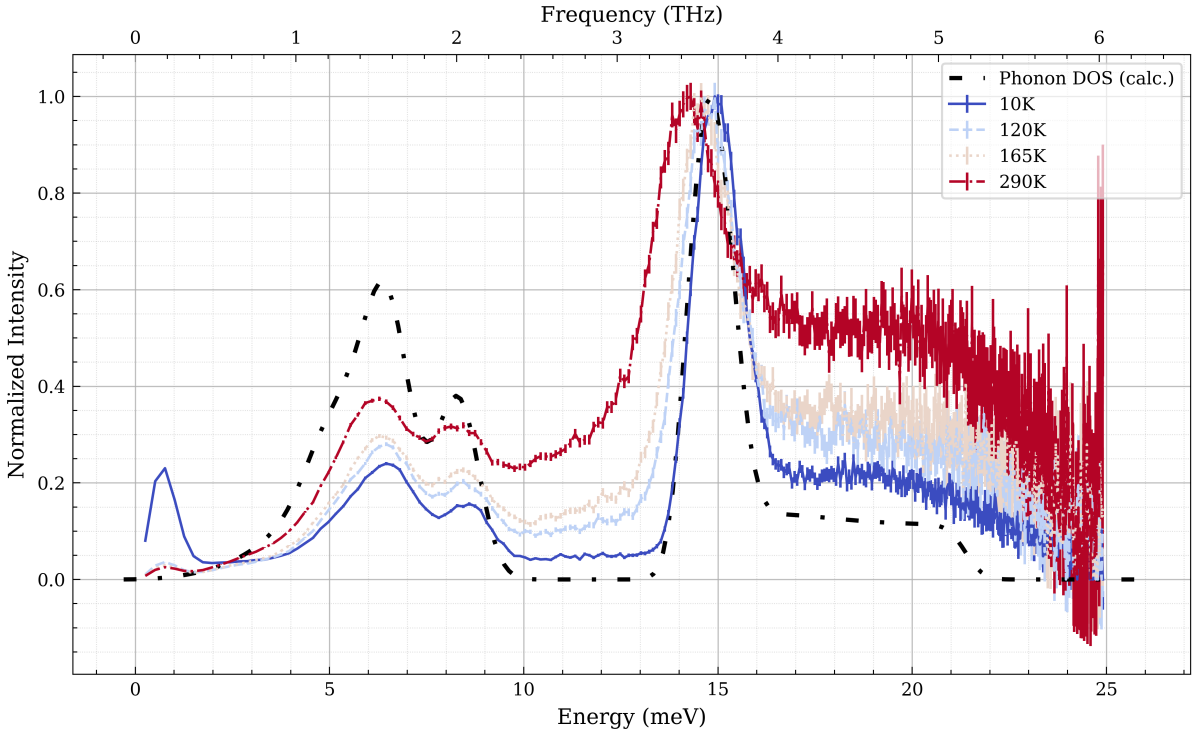

Figure 3.6: Comparison of experimental inelastic neutron scattering (INS) data at different temperatures (10 K, 120 K, 165 K, 290 K) [139] with the theoretically calculated phonon DOS (black curve) at 0 K for NaI [140]. All curves are normalized to their respective maxima and share a common zero-intensity axis. The mismatch in the low-energy region arises because the theoretical DOS, computed strictly at 0 K, does not include thermal population effects. In contrast, the experimental spectra capture the increasing occupation of low-energy phonon modes as temperature decreases. Consequently, at finite (and especially low) temperatures, one observes a noticeable rise in low-energy intensities in the experiment that is absent in the 0 K calculation.

Acoustic phonons correspond to in-phase vibrations of the lattice and have frequencies ranging from a few GHz up to ~ 2 THz in NaI [140]. Since these phonons have energies of $\mathcal{O}(10\,\text{meV})$ that are much larger than the thermal energy of the lattice, they are also called non-thermal phonons. As the acoustic phonons propagate, they gradually lose energy through various scattering processes, such as isotopic scattering, boundary scattering, and anharmonic interactions, leading to a decrease in their frequency and momentum. The

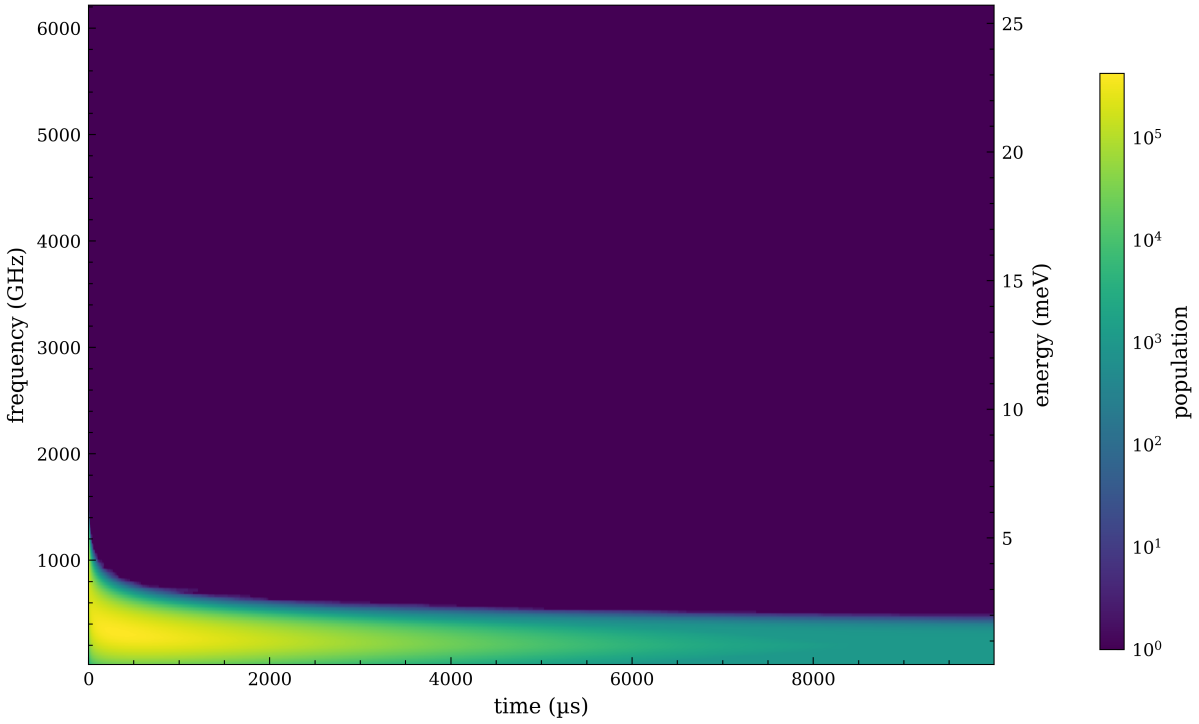

Figure 3.7: Phonon frequency distribution over time for a cryogenic NaI detector following a 10 keV energy deposit. The color scale represents the population of phonons in each frequency bin, demonstrating the rapid decay of high-frequency modes and the subsequent semi-equilibrium state reached when the frequencies are of $\mathcal{O}$(100 GHz).

dominant process among them being the anharmonic decay, has a very strong frequency dependence (ν^5). As a result, the initial frequency down conversion is very fast, but very quickly reaches a semi-equilibrium within the crystal. In NaI, this occurs once the phonons reach a frequency of $\mathcal{O}$(100 GHz). These phonons ballistically free stream throughout the crystal, spreading out uniformly before eventually resulting in the gradual thermalization of the phonon system via inelastic scatterings at the crystal surface or via impurity/defect sites within the crystal, bringing the lattice temperature back toward the bath temperature. This process can be intuitively visualized in Fig. 3.7.

For the *remo*TES architecture, phonons can also interact with the metallic Au layer interfacing one face of the crystal. For the following discussion, we assume that the Au layer is directly deposited onto the NaI crystal face following the process discussed in Chapter 7. Phonons reaching the NaI/Au interface undergo partial transmission, which are governed by the interfacial acoustic mismatch. The transmission regime: coherent (acoustic mismatch model, AMM) or incoherent (diffuse mismatch model, DMM), is determined by the ratio of phonon wavelength λ_{ph} to interfacial roughness σ_{rms}. Due to the softness of NaI, achieving polished surfaces with $\sigma_{\text{rms}} \approx 10$ Å, as seen in materials like Si and Ge, is extremely difficult. A conservative estimate for the following discussion assumes a $\sigma_{\text{rms}} \approx$ 100-200 Å, and considering the dominant phonon frequencies around 100 GHz (wavelength $\lambda_{\text{ph}} \approx 30$ Å in NaI), the interface condition falls within the DMM regime ($\lambda_{\text{ph}} \ll \sigma_{\text{rms}}$). An important caveat is the presence of an evaporated ~10 nm thick adhesion layer of titanium (Ti) between the NaI-Au interface, which makes the following discussion a bit more nuanced. While the

DMM regime would still describe the phonon transmission between the NaI-Ti layer, the AMM regime is a better fit for the Ti-Au layer. In cases where a two-component epoxy serves as the adhesion layer, as is the case in Chapter 6, accurate modelling is equally challenging. However, for simplicity and as a first-order approximation, we consider both models without accounting the influence of the Ti layer (or epoxy) in the following discussion.

Using AMM, the transmission coefficient between NaI ($Z_{\mathrm{NaI}} = \rho_{\mathrm{NaI}} v_{\mathrm{NaI}}$) and Au ($Z_{\mathrm{Au}} = \rho_{\mathrm{Au}} v_{\mathrm{Au}}$), averaged over all incident angles can be approximated as:

$$T_{\mathrm{AMM}} = \frac{2 Z_{\mathrm{NaI}} Z_{\mathrm{Au}}}{Z_{\mathrm{NaI}}^2 + Z_{\mathrm{Au}}^2} \tag{3.5}$$

Using the material properties and calculations summarized in Table 3.1, we find $T_{\mathrm{AMM}} \approx 0.43$ for the NaI-Au interface.

In contrast, the DMM transmission coefficient, which accounts for all polarization modes under the assumption of completely diffuse phonon scattering at the interface, can be written in a common isotropic approximation as:

$$T_{\mathrm{DMM}} = \frac{\rho_{\mathrm{Au}} \left(v_{L,\mathrm{Au}} + 2\, v_{T,\mathrm{Au}} \right)}{\rho_{\mathrm{NaI}} \left(v_{L,\mathrm{NaI}} + 2\, v_{T,\mathrm{NaI}} \right) + \rho_{\mathrm{Au}} \left(v_{L,\mathrm{Au}} + 2\, v_{T,\mathrm{Au}} \right)} \approx 0.19 \tag{3.6}$$

Here, ρ is the mass density, and v_{L} and v_{T} are the longitudinal and transverse sound velocities, respectively, for each material. The summation over all polarization modes effectively appears via the $v_{\mathrm{L}} + 2 v_{\mathrm{T}} v_{\mathrm{L}} + 2 \mathrm{v}_{\mathrm{T}}$ factor for a single-v_{T} isotropic approximation. More sophisticated DMM expressions likewise sum over each branch's density of states and velocity.

The choice of Au as the interface material is driven by its better acoustic impedance matching to NaI compared to other metals like tungsten (W). As shown in Table 3.1, the transmission coefficient for phonons from NaI to Au ($T_{\mathrm{NaI\text{-}Au}} \approx 0.43$ using AMM) is roughly 30% higher than that for phonons from NaI to W ($T_{\mathrm{NaI\text{-}W}} \approx 0.34$ using AMM). A similar calculation using the DMM also yields the same relative benefit for the NaI-Au interface.

The transmitted phonons in the Au-pad interact with conduction electrons via the electron-phonon coupling term:

$$\dot{Q}_{\mathrm{e\text{-}ph}} = \Sigma_{\mathrm{Au}} \mathcal{V} \left(T_{\mathrm{el}}^5 - T_{\mathrm{ph}}^5 \right) \tag{3.7}$$

where Σ_{Au} is the material-specific electron-phonon coupling constant for Au, and $\mathcal{V}$ is the absorber volume. This interaction facilitates the transfer of energy from the phonon system to the electronic system (which are the primary heat carriers in metals) in the Au-pad. The resulting electronic temperature rise $\Delta \mathrm{T_e}$ propagates to the W-TES through the Kapitza resistance $\mathrm{R_K}$ via a Au-bond wire, following the relationship:

$$\mathrm{R_K^{-1}} = \mathrm{G_K} = \alpha_{\mathrm{K}} \mathrm{A_{int}} \mathrm{T}^3 \tag{3.8}$$

where $\mathrm{G_K}$ and α_{K} are the Kapitza conductance and Kapitza conductance coefficient, respectively. A_{int} is the interface area between Au and W, and $\alpha_{\mathrm{K}} \approx 10$ kW $\mathrm{m^2 K^4}$ for Au/W

Table 3.1: Material properties, acoustic impedances, and transmission coefficients for NaI, Au, and W at 298 K. It must be noted here that these values correspond to the bulk materials and the sound velocities for thin films can deviate depending on the film quality, thickness and temperature.

Material/Interface	Density ρ (g/cm^3)	Longitudinal sound velocity v_L (km/s)	Acoustic impedance Z (MPa·s/m)	Transmission coefficient, T
NaI	3.67	3.46	12.7	–
Gold (Au)	19.3	3.24	62.5	–
Tungsten (W)	19.3	5.22	100.7	–
NaI-Au interface	–	–	–	0.43
NaI-W interface	–	–	–	0.34

interfaces at these temperatures.

A quantitive picture of such a pulse formation process, but for cryogenic absorbers with the W-TES deposited directly on it's surface for signal collection and readout is covered in [141]. For the *remo*TES readout, however, this is not as straightforward. A first approach would be to build upon the works outlined in [141, 142], using which one can build a thermal model of the entire setup as seen in Fig. 3.8 (**left**). However, ongoing investigations suggest that a traditional 2-component model successfully fits pulse shape characteristics just as well as a 3-component model [143] given optimization processes outlined in Chapter 5, Chapter 6, Chapter 7 and [144, 145]. In the context of the following discussion, one can thus approximate our model to the system as shown on Fig. 3.8 (**right**). This model treats the Au-link and TES as a single thermal component, assuming their electronic systems are strongly coupled with negligible interfacial thermal impedance ($G_{\text{link}} \rightarrow \infty$). This approximation eliminates heat capacity gradients between the two subsystems, effectively merging their thermal time constants ($\tau_{\text{link}} \ll \tau_{\text{TES}}$).

Thus, the energy split between the absorber and Au-TES system, as explained earlier, can be expressed as:

$$P_e(t) = \Theta(t) \cdot \varepsilon \cdot \frac{\Delta E}{\tau_n} e^{-t/\tau_n} \tag{3.9}$$

$$P_a(t) = \Theta(t) \cdot (1 - \varepsilon) \cdot \frac{\Delta E}{\tau_n} e^{-t/\tau_n} \tag{3.10}$$

where $P_e(t)$ denotes the time-dependent power input into the electron system of the Au-link and $P_a(t)$ denotes the time-dependent power input due to the thermalized phonon-population in the absorber. $\Theta(t)$ is the step function, since the model assumes an instantaneously homogeneous distribution of the non-thermal phonons initially produced in the absorber, and ΔE refers to the initial energy deposition due to the particle interaction. $\tau_n = (\tau_e^{-1} + \tau_a^{-1})^{-1}$ is the effective athermal phonon lifetime, and ε is the thermalization fraction in the Au-TES system. The thermalization time constants τ_e (Au-TES system) and

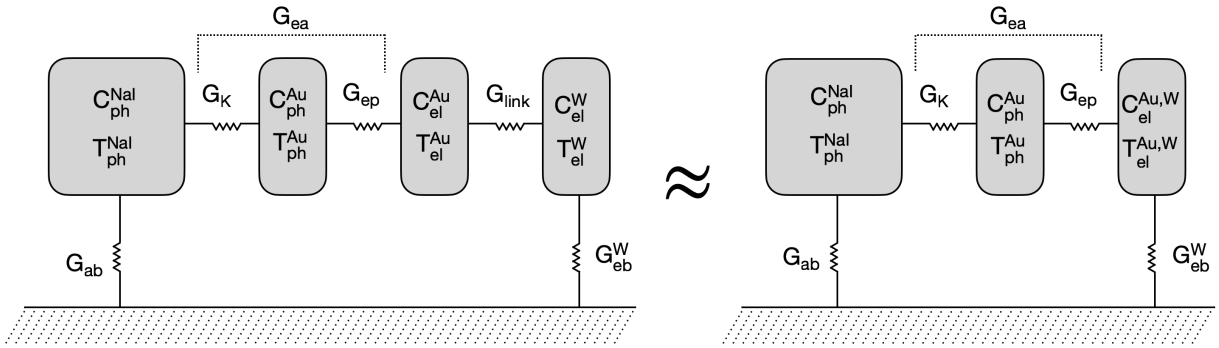

Figure 3.8: Left: Thermal model of the *remo*TES readout scheme; **Right:** Simplified thermal model of the detector system for $G_{link} \to \infty$. $T_{el}^{Au,W}$ and T_{ph}^{NaI} represent the electron temperature in the Au-TES system and phonon temperature in the absorber, respectively, with heat capacities $C_{el}^{Au,W} \simeq C_{el}^{Au}$ and T_{ph}^{NaI}. Thermal conductances G_{ea}, G_{link} (left only,) G_{eb}^{W}, and G_{ab} govern energy flow between components and the bath at T_{bath}.

τ_a (absorber) are primarily dependent on the interface properties and crystal geometry. Taking into account the energy losses from the absorber to the heat bath (via the holding structures), we can define a set of coupled differential heat equations following energy conservation:

$$C_{el}^{Au}\frac{dT_{el}^{Au}}{dt} = P_e(t) - G_{ea}(T_{el}^{Au} - T_{ph}^{NaI}) - G_{eb}^{W}(T_{el}^{Au} - T_{bath}) \tag{3.11}$$

$$C_{ph}^{NaI}\frac{dT_{ph}^{NaI}}{dt} = P_a(t) - G_{ea}(T_{ph}^{NaI} - T_{el}^{Au}) - G_{ab}(T_{ph}^{NaI} - T_{bath}) \tag{3.12}$$

where G_{ea}, G_{eb}^{W}, and G_{ab} represent the thermal conductances between the electron-phonon systems, electron-bath, and absorber-bath, respectively. For initial conditions $T_{el}^{Au}(0) = T_{ph}^{NaI}(0) = T_{bath}$, the solution yields the thermometer response:

$$\Delta T_{el}^{Au}(t) = \Theta(t)\left[A_n\left(e^{-t/\tau_n} - e^{-t/\tau_{intr}}\right) + A_t\left(e^{-t/\tau_t} - e^{-t/\tau_n}\right)\right] \tag{3.13}$$

with characteristic time constants:

$\tau_{intr} \approx C_{el}^{Au}/(G_{ea} + G_{eb}^{W})$: Intrinsic thermometer relaxation time

$\tau_t \approx C_{ph}^{NaI}/G_{ab}$: Absorber thermalization time

τ_n: Athermal phonon lifetime

Eq. 3.13 consists of a superposition of two exponential pulses, where the first component is referred to as the non-thermal component and the second component is referred to as the thermal component. The detector performance is characterized by two distinct operational modes, determined by the ratio τ_n/τ_{intr}.

Calorimetric Mode **($\tau_n \ll \tau_{intr}$)**

In the *Calorimetric Mode*, when the athermal phonon lifetime is significantly shorter than the intrinsic thermometer relaxation time ($\tau_n \ll \tau_{intr}$), the thermometer integrates the total energy input. This mode is characterized by:

- Amplitude: The amplitude A_n is approximately given by:

$$A_n \approx -\frac{\varepsilon \Delta E}{C_{el}^{Au}} \tag{3.14}$$

- Rise Time: The rise time of the signal is dictated by the athermal phonon lifetime, τ_n.
- Decay Time: The decay time is determined by the intrinsic thermometer relaxation time, τ_{intr}.

This operational mode is particularly well-suited for precise energy measurements, and it is implemented in detectors for space-based experiments designed for high-precision energy spectroscopy. Examples include light detectors in Cosmic Microwave Background (CMB) missions like Planck, or X-ray micro-calorimeters in future X-ray observatories.

Bolometric Mode **($\tau_n \gg \tau_{intr}$)**

Conversely, in the *Bolometric Mode*, where the athermal phonon lifetime is considerably longer than the intrinsic thermometer relaxation time ($\tau_n \gg \tau_{intr}$), the thermometer is capable of tracking the instantaneous phonon flux. The characteristics of this mode include:

- Amplitude: The amplitude A_n is proportional to:

$$A_n \propto \frac{\varepsilon \Delta E}{\tau_n G_{eb}^{W}} \tag{3.15}$$

- Rise Time: The rise time in this mode is governed by the intrinsic thermometer relaxation time, τ_{intr}.
- Decay Time: The decay time is determined by the athermal phonon lifetime, τ_n.

This mode enables time-resolved signal detection and is beneficial for space-based observations requiring fast response and the tracking of variable signals. Examples include detectors designed for time-domain astrophysics or for far-infrared missions studying transient events and variable sources.

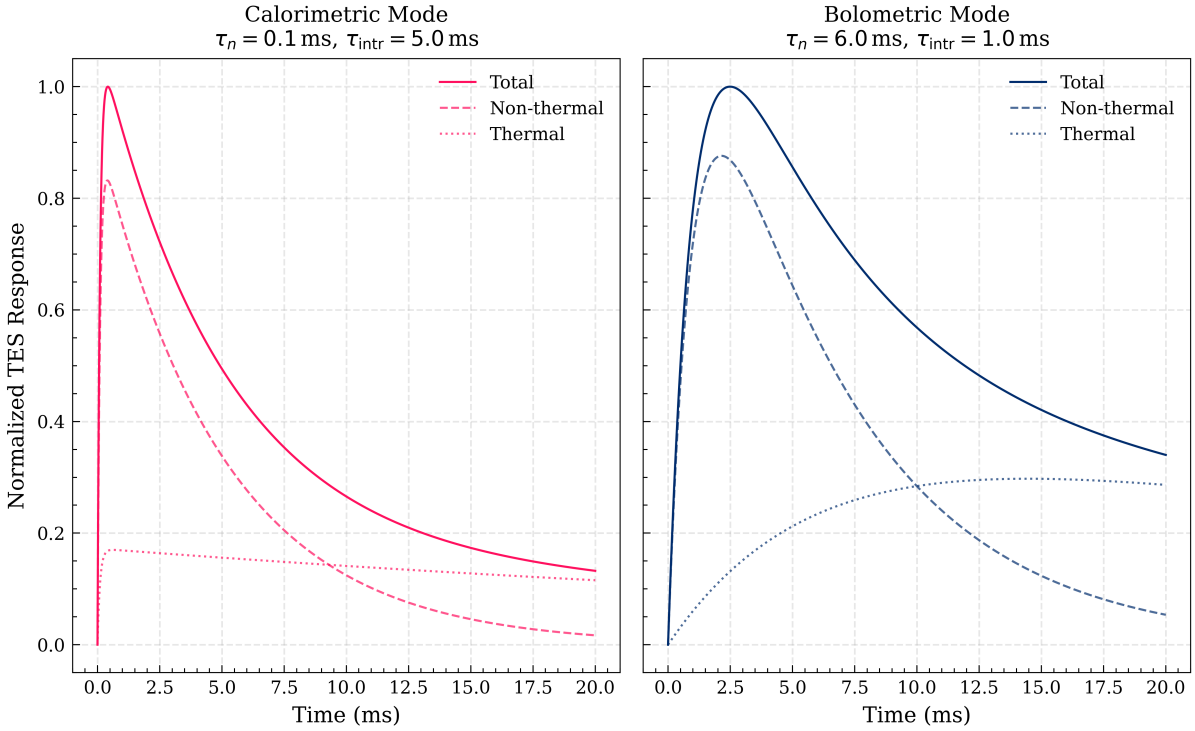

Figure 3.9: A sample pulse shape model following Eq. 3.13 for the calorimetric mode (Eq. 3.14) and the bolometric mode (Eq. 3.15) operating regimes.

3.3 Data-taking Schema

3.3.1 SQUID Readout

In order to measure the resistance changes caused by the temperature changes in the thermometer, the readout chain can be broken down into the following key stages, as illustrated in Fig. 3.10. Superconducting Quantum Interference Devices (SQUIDs) are integral to the chain due to their ultra-low noise amplification of the TES resistance, and consequently, current changes at cryogenic temperatures. A constant bias current, I_b is divided among the two parallel branches, with one branch consisting of the TES and the other with the input coil of the SQUID along with a pair of shunt resistors. These shunt resistors, denoted by L.4 and P.4 are highlighted in Fig. 3.5, corresponding to the light detector and the phonon detector channel, respectively.

At steady state, the current through the SQUID input coil, I_{sq}, is given by:

$$I_{sq} = I_b \frac{R_{TES}(T)}{R_{TES}(T) + R_s} \tag{3.16}$$

where I_b is the supplied bias current, $R_{TES}(T)$ is the resistance of the TES at its desired operation point and R_s is the shunt resistance. It must be noted that Eq. 3.16 and the discussion that follows neglects the effect of the inductance of the input circuit. The change

in current due to the resistance change of the TES is given by:

$$\Delta I_{sq} = \frac{\partial I_{sq}}{\partial R_{TES}(T)} \cdot \frac{\partial R_{TES}(T)}{\partial T} \cdot \Delta T = I_b \left(\frac{R_s}{(R_{TES}(T) + R_s)^2} \right) \cdot \frac{\partial R_{TES}(T)}{\partial T} \cdot \Delta T \tag{3.17}$$

Thus, for small changes in resistance, ΔI_{sq} is proportional to ΔT. For a given bias current, ΔI_{sq} is maximum when $R_s \approx R_{TES}(T)$. Eq. 3.17 can thus be re-written as:

$$\Delta I_{sq} = \frac{I_b}{4} \cdot \frac{1}{R_{TES}(T)} \cdot \frac{\partial R_{TES}(T)}{\partial T} \cdot \Delta T = \frac{I_b}{4} \alpha \Delta T \tag{3.18}$$

where α denotes the sensitivity of the TES (≈ 48 for the example shown in Fig. 3.3).

A typical SQUID amplifier used in COSINUS consists of a superconducting loop with two Josephson junctions (called a DC SQUID). To achieve optimal operation, it must be biased at a point where it exhibits maximum linearity and sensitivity. This is typically accomplished by applying a constant current and employing a feedback mechanism to maintain the SQUID at its optimal working point. Variations in current in the SQUID input coil alter the current flowing through the SQUID, which is then translated into a voltage signal for further processing. For COSINUS, SQUIDs manufactured by STAR cryoelectronics (model: SQ300) will be employed [146]. The subsequent data-acquisition setup is covered in Sec. 4.2.4.

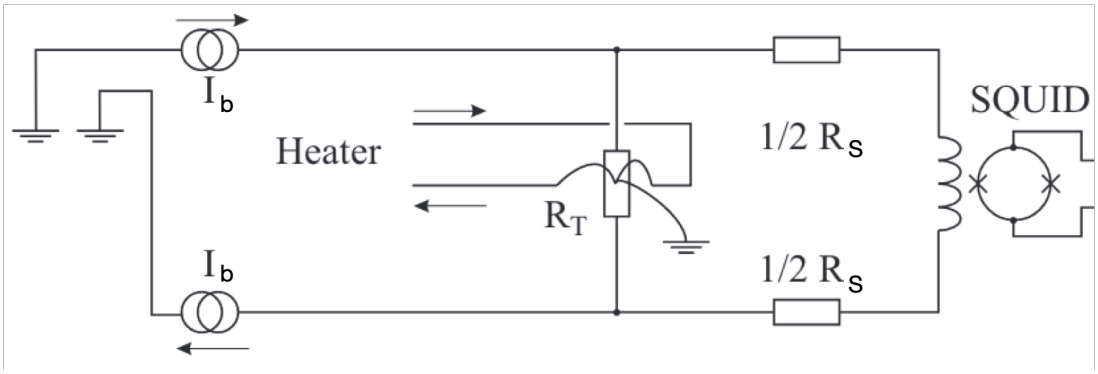

Figure 3.10: Simplified diagram of the COSINUS detector readout circuit. See text for details.

4 The COSINUS Facility

"In the depths of the earth, hidden truths await discovery."
— Jules Verne

The previous chapter delved into the conceptualization and operation of cryogenic detectors used in COSINUS, and its subsequent readout. This chapter covers the cryogenic infrastructure needed to actually cool down and operate these detectors reliably at such low temperatures, ideally in a low-background environment.

4.1 Infrastructure

Chapter 2 covered the importance of a low background environment, especially given how the expected WIMP interaction rate in a target material is $\mathcal{O}(10)$ events kg^{-1} year^{-1} in an energy range of around (1-10) keV. The COSINUS experiment is located in the Laboratori Nazionali del Gran Sasso (LNGS) in central Italy. The underground lab, located underneath the Gran Sasso mountains houses ~18 experiments at present, spread out over three main experimental halls, aptly named: hall A, hall B and hall C as shown in Fig. 4.1. The COSINUS experimental facility is located in hall B and has a rock overburden of ≈ 1400 m of dolomite rock, equivalent to about 3,600 m of water. This corresponds to a reduction in the flux of cosmic muons of roughly six orders of magnitude, down to about $\mathcal{O}(1\ \mathrm{m}^{-2}\ \mathrm{hr}^{-1})$ [147].

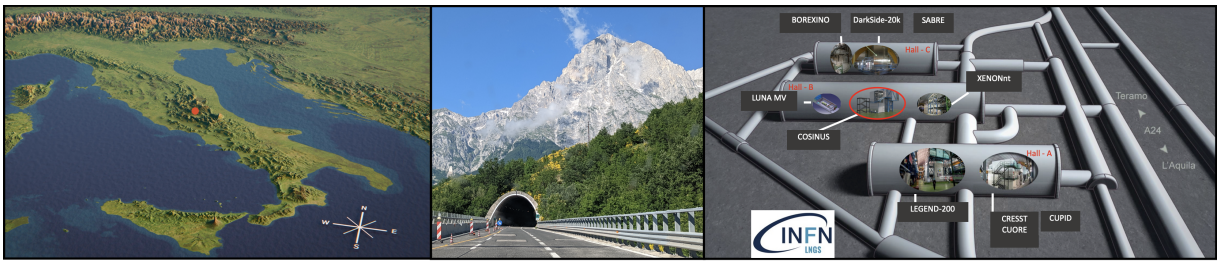

Figure 4.1: Left: Location of the LNGS underground lab; **Centre:** Entrance to the tunnel from the Teramo side; **Right:** Scheme of the LNGS experimental facility with some notable experiments indicated. The COSINUS experiment is highlighted in red.

The facility can be divided into the following sections, as outlined in Fig. 4.2. The support building seen on the left consists of three floors. The utility area, highlighted in green, hosts the Gas Handling System (GHS) and vacuum pumps of the dilution refrigerator (covered in Sec. 4.2.3). Gas handling lines connecting the dilution refrigerator to the GHS are routed via a sandbox in the clean room lock to reduce the transmission of vibrations. The control room serves as the office space for shifters on-site and contains the slow-control readout pc. The service room on the bottom floor houses the compressor for the dilution refrigerator, in addition to the clean room ventilations system and the water loop system

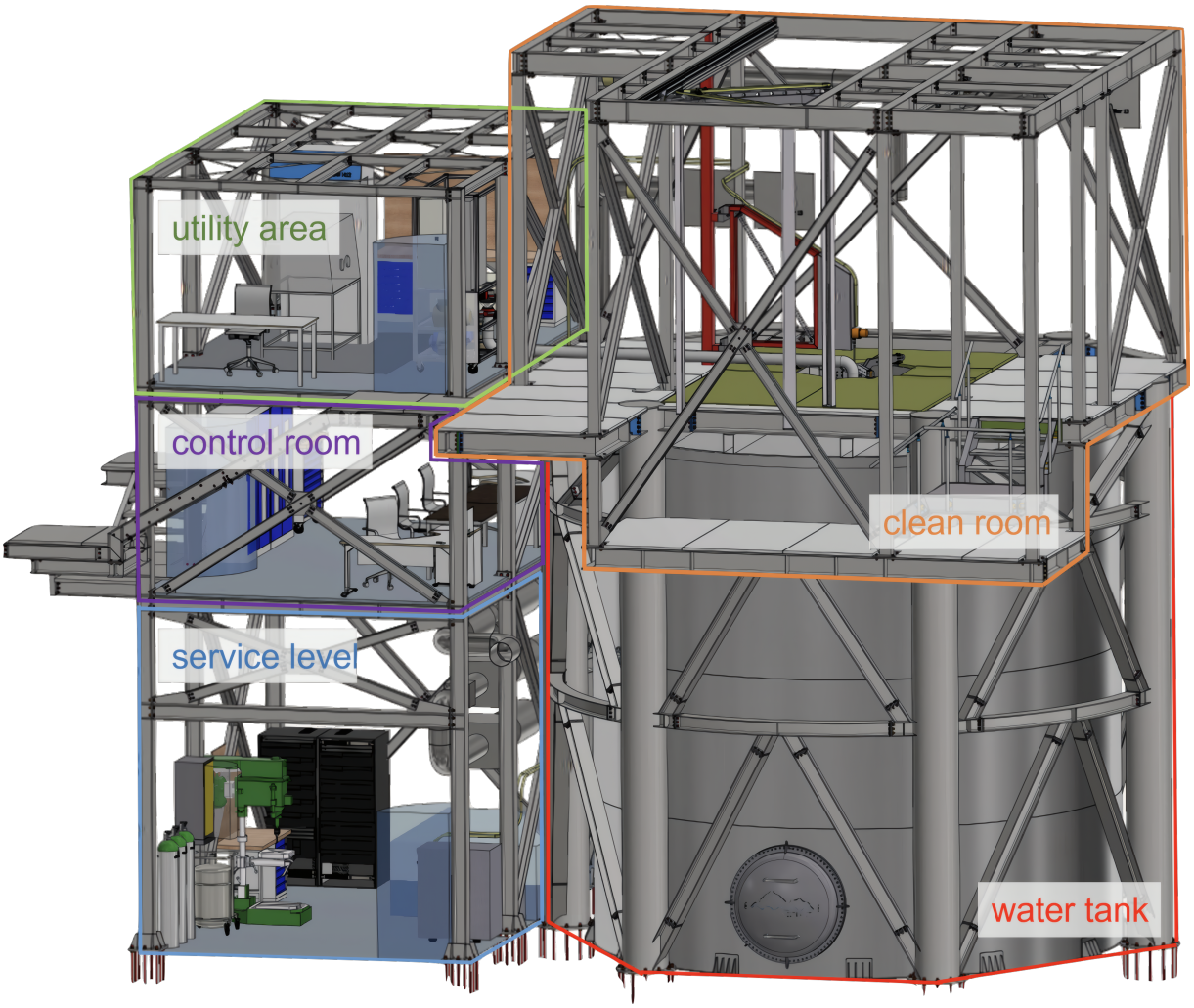

Figure 4.2: A rendering of the COSINUS setup at hall B, LNGS. *Image credits*: [148].

of the water tank. Further spares and basic machining tools are located here. The entire facility is protected with a 40 KWh UPS system to keep the dilution refrigerator running in case of emergencies. A detailed exploration into the water tank (Muon Veto system) and the clean room is provided in the following subsections.

4.1.1 Muon Veto System

The mountain rock, serves as a first passive shield to the experiment to block out most of the secondary particles generated due to cosmic-ray induced showers. The muon flux, which is the most dominant and also, the most penetrating component, still needs further vetoing. Muons can create a variety of secondary interactions with the ambient rock structure in hall B, materials surrounding the detector, or within the detector itself that could potentially mimic DM-like signals. To identify and tag these muon background events, the outermost region of the onion-layered vetoing system of COSINUS consists of a water-Cherenkov muon veto. Its design is based on the conceptual design study carried out in [149]. It is

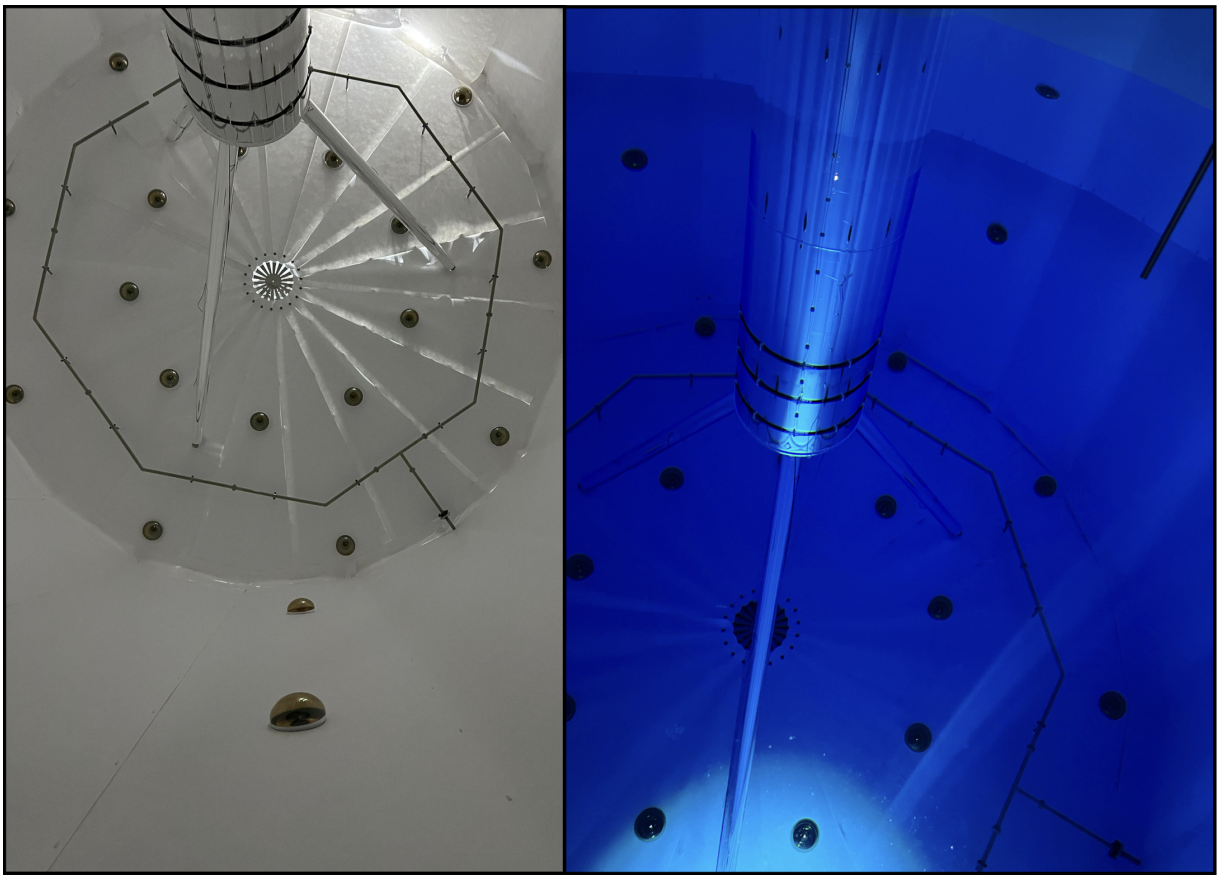

Figure 4.3: Left: A top-down view of the completed assembly of the muon-veto water tank before being filled with deionized water. The tri-layer Tyvek curtains with the PMTs poking out of their respective holders are visible; **Right**: A snapshot of the muon veto after water filling, when illuminated; The drywell with it's tripod holding structure, covered with a reflective foil (DF2000MA), produced by 3M [152] is visible in both. The magnetic field compensation coils wrapped around the lower half of the dry-well, corresponding to the three black coils, are also visible.

composed of a 7 m tall, 7 m wide and ≈ 7 mm thick* stainless steel cylindrical water tank consisting of 30 PMTs manufactured by Hamamatsu (model number: R-5912-100 [150]), spread out along the walls and the floor to have a high vetoing efficiency for both muon events and shower events in accordance with simulations performed in [151]. The volume of water also serves as an additional passive shield towards ambient γ and neutron radiation.

A layer of Tyvek-PE-Tyvek mounted 30 cm away from the walls and bottom of the tank† serves as an effective reflector for the generated Cherenkov photons as seen in Fig. 4.3. The effective dead layer to be introduced by the gap was also optimized and is outlined in [151]. The tri-layer design was chosen both for its structural rigidity and a reflectivity of over 95% for wavelengths ≥ 300 nm. A 4/5-fold coincidence PMT triggering scheme is foreseen to tag

* It consists of three different steel thicknesses throughout, with the bottom of the tank made with 8 mm thick walls while the middle is made with a 7 mm wall thickness and the top section is made with a 6 mm wall thickness.

† This distance is called the "dead layer" as it reduces the active volume of the muon veto. It allows us to mitigate triggers in the PMTs due to secondary interactions near the tank walls or from the ambient radioactivity of the tank walls itself.

any muon and muon-induced events while keeping the false trigger rate small, in addition to a coincidence cut with the detector to remove any secondary particles generated having short decay times. The simulated cosmogenic neutron rate in the detector is thus reduced from (3.5±0.7) counts/kg yr without an active veto to around (0.11±0.02) counts/kg yr for a detector threshold of 1 keV [151].

At the center of the water tank rests the drywell, which is a hollowed-out stainless steel cylinder of 4 mm wall thickness. It is supported by a tripod holding structure made of the same material. The walls of the drywell are covered with a specular reflector foil (DF2000MA) made by 3M [152], to reflect the Cherenkov photons. Fig. 4.3 shows the drywell centered in the water tank along with the PMTs poking out of the Tyvek curtain. The inside of the drywell hosts the dilution refrigerator, which is covered in Sec. 4.2.

The TESs used for reading out the module as outlined in Chapter 3 are susceptible to changes in the magnetic field (MF) strength perpendicular to the plane of the TES films. [153] touched upon the effects of varying MF on the TES stability and how crucial it is to have a non-varying MF within the vicinity of the detectors for stable, sensitive and long-term operation. Given the occasional use of heavy machinery in and around the COSINUS facility, an active magnetic compensation coil is installed around the outside of the drywell to mitigate any MF changes during these times. It consists of three equally interspaced coils, each consisting of ten windings of 20 AWG thick wires placed along the bottom half of the drywell (corresponding to where the detector modules would be inside the dilution refrigerator) to ensure a constant, non-varying MF, and is shown in Fig. 4.3.

4.1.2 Clean Room

The clean room, highlighted in Fig. 4.4, is situated atop the water tank. It is an ISO Class 7 clean room, and is designed to maintain particulate count $\leq$ ~350,000 counts m^{-3} at 0.5 µm during operation. A servo-controlled overhead lifting system specifically engineered for easy maneuverability along a set of guide rails and safe insertion of the dilution refrigerator within the drywell is also installed. A dedicated maintenance bay at the far end of the clean room serves as additional space to house the dilution refrigerator, where installation of the detector modules and any modifications/repairs can be carried out.

Mechanical vibration isolation is another crucial design aspect that needs to be considered, as sub-micron displacements can disrupt the thermal equilibrium of the cryogenic modules operating at $\mathcal{O}$(mK) temperatures, thus limiting their sensitivity. To address this, a dual stage vibration mitigation structure as outlined in [148, 154] is implemented. The system, as illustrated in Fig. 4.4, comprises an inner frame (highlighted in yellow) that is designed to host only the dilution refrigerator. It is decoupled from the outer frame (highlighted in blue) with a sail cloth partition composed of a PVC-coated polyster fabric in between to ensure air tightness in the clean room. All major vibration sources: the compressor, pumps and GHS are mounted to the outer frame in order to minimize the transmission of vibrations to the inner frame.

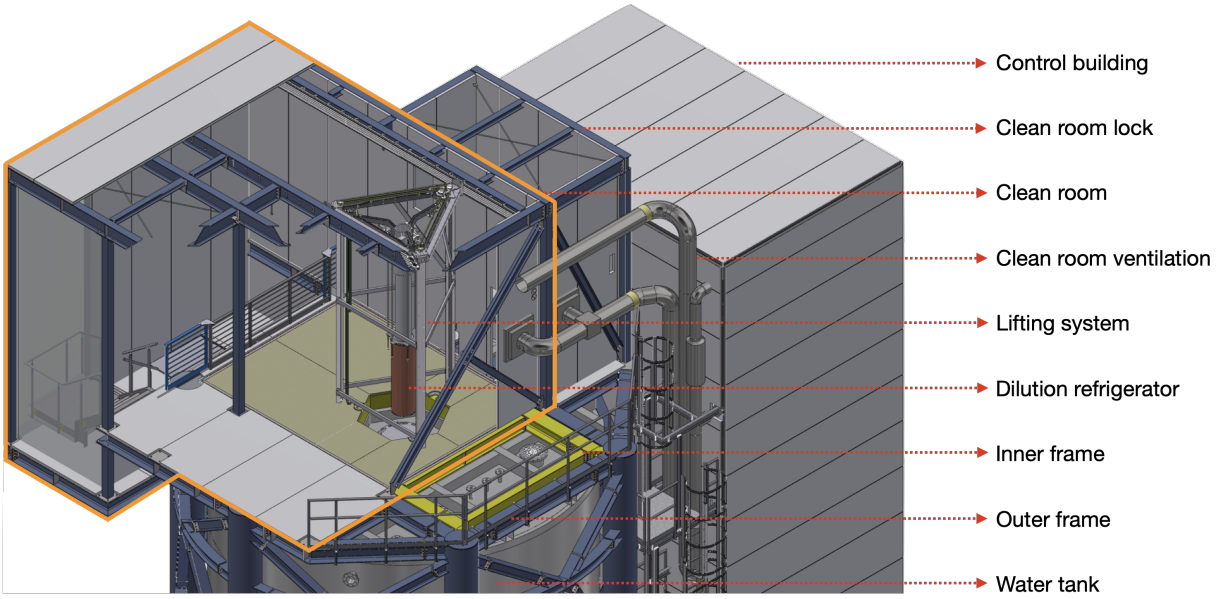

Figure 4.4: A schematic diagram of the clean room setup. The clean room lock serves as the transition area where personnel change before entering the controlled clean room environment. The clean room ventilation system can be adjusted to maintain the desired particulate level and, if necessary, regulate humidity levels within the clean room. The lifting system enables precise handling of the dilution refrigerator, allowing it to be moved into and out of the drywell and to be positioned in the detector mounting area (top left) via linear guide rails attached to the ceiling. The inner frame (highlighted in yellow) houses the dilution refrigerator and is mechanically decoupled from the outer frame (marked in blue) to minimize vibrational noise transfer from external sources.

4.1.3 Inner Passive Shielding

The outermost region of the onion-layered vetoing system described in Sec. 4.1.1, while efficient at tagging any prompt signals from muon events, muon-induced shower events and short-lived particles, cannot effectively veto out reactions that could produce long-lived isotopes [155]. To minimize the possibility of such particles reaching the detector, the bottom of the inner part of the drywell houses the second layer of our onion-layered vetoing system. This passive shielding structure consists of precision-machined oxygen-free high-conductivity (OFHC) Cu (C10100, 99.99 % purity) bricks with 8 cm cross-sectional thickness. The components were fabricated at the Max-Planck-Institut für Physik (MPP, Munich), followed by surface passivation through chemical etching according to the protocol detailed in Chapter 3. The assembly comprises four vertically stacked layers, each formed by twelve interlocking sector components, creating a continuous cylindrical barrier (~700 mm outer diameter). A Cu ground plate completes the shielding enclosure at the base. Fig. 4.5 documents key stages in the shield's fabrication and installation process.

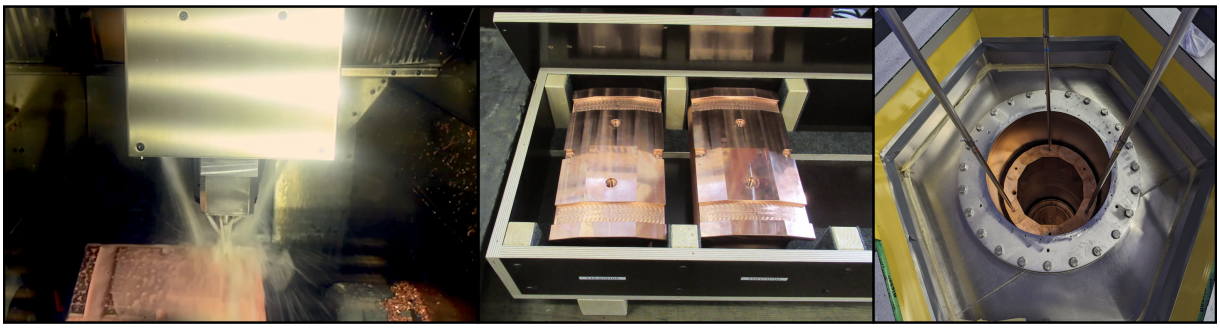

Figure 4.5: Left: CNC machining of the individual Cu bricks at MPP, Munich; **Centre:** Finished pieces ready for transport to LNGS; **Right:** Installation of a Cu shielding ring into the dry-well using the servo-controlled overhead lifting system within the clean room.

4.2 The Dilution Refrigerator

4.2.1 Pre-cooling with Closed Cycle Refrigeration

The innermost volume of the drywell's Cu shielding contains the dilution refrigerator, the main apparatus that allows COSINUS to reach temperatures < 10 mK. A cross-sectional schematic of the cryogenic system is shown in Fig. 4.10. Due to reduced cooling efficiency at very low temperatures, it is impractical to directly cool an entire cryostat from room temperature (298 K) down to mK levels (~0.0001 K). Therefore, the cooling process is divided into multiple stages. The initial stage, called pre-cooling, typically reduces the temperature to around 4 K. Based on the method used for this pre-cooling step, dilution refrigerators are categorized as either "wet" or "dry". If one utilizes liquid cryogens such as LN_2 and ^{4}He for the pre-cooling, they are referred to as wet dilution refrigerators. Traditionally, wet dilution refrigerators have been the most popular choice, given the relative ease of extracting and purifying liquid cryogens due to mature liquefaction technologies developed in the mid 20th century. ^{4}He, however, has experienced significant growth in demand over the past two decades, driven mainly by the rise of quantum computing and increased military applications. Consequently, its price has risen sharply, as illustrated in Fig. 4.6. Additionally, operational complexity, high maintenance requirements, and the necessity for skilled personnel trained in handling cryogenic liquids have further reduced its popularity.

This is where the so-called dry dilution refrigerators have started gaining widespread usage over the years. A direct mechanical cooler, termed as a Pulse Tube (PT) is used for the pre-cooling process. The underlying thermodynamic mechanism involves a regenerative cycle alternating between isochoric heat rejection and adiabatic expansion phases. This four-stage process (compression, heat transfer, expansion, and regeneration) enables continuous heat pumping through carefully timed pressure oscillations in the helium working gas. Since it is operated in a closed-loop cycle, it is also referred to as a closed cycle refrigerator (CCR). PT cryocoolers are categorized by their compressor-expander coupling methodology:

- Stirling-type systems maintain direct gas coupling between compressor and expander, enabling quasi-isothermal processes with theoretical Carnot efficiencies up to 40%

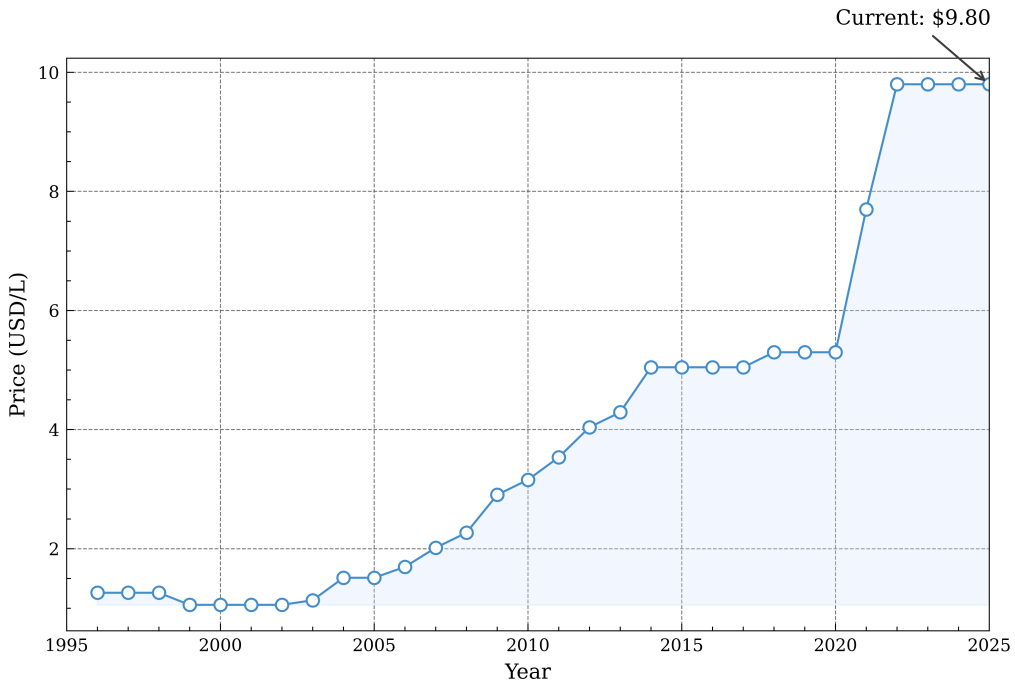

Figure 4.6: ^{4}He pricing over the years, with data extracted from annual reports by the U.S. Geological Survey (USGS) [156]. It must be noted that this illustration does not include the cost of liquefaction, storage, and handling of the liquid helium, which can be substantial depending on its initial origin and final destination.

[157]. However, their complex linear drive mechanisms and sensitivity to mechanical wear limit deployment to specialized applications such as space-based observatories, where mass efficiency and vibration suppression justify the increased development costs.

- Gifford-McMahon (GM) configurations decouple compression and expansion phases via rotary valve systems, sacrificing thermodynamic efficiency (typically 15–20% of Carnot) for enhanced reliability and maintenance accessibility. This makes GM cryocoolers preferable for laboratory-scale systems requiring continuous operation over multiple annual cycles.

Fig. 4.7 gives a schematic of the working principle of a GM type PT cryocooler.

4.2.2 Dilution Refrigeration Thermodynamics

To achieve base temperatures below 10 mK, both dry and wet dilution refrigerators employ a closed-cycle ^{3}He/^{4}He mixing circuit. The cooling mechanism exploits the temperature-independent phase separation of ^{3}He in liquid ^{4}He, where the enthalpy difference between concentrated (>6% ^{3}He) and dilute (<1% ^{3}He) phases provides continuous cooling power [158]. The dilution unit (DU), comprising a mixing chamber (MC), Still, and superconducting flow impedance (NbTi capillaries with 10^{-14} m^3/(Pa s) conductance), executes six operational phases as shown in Fig. 4.8:

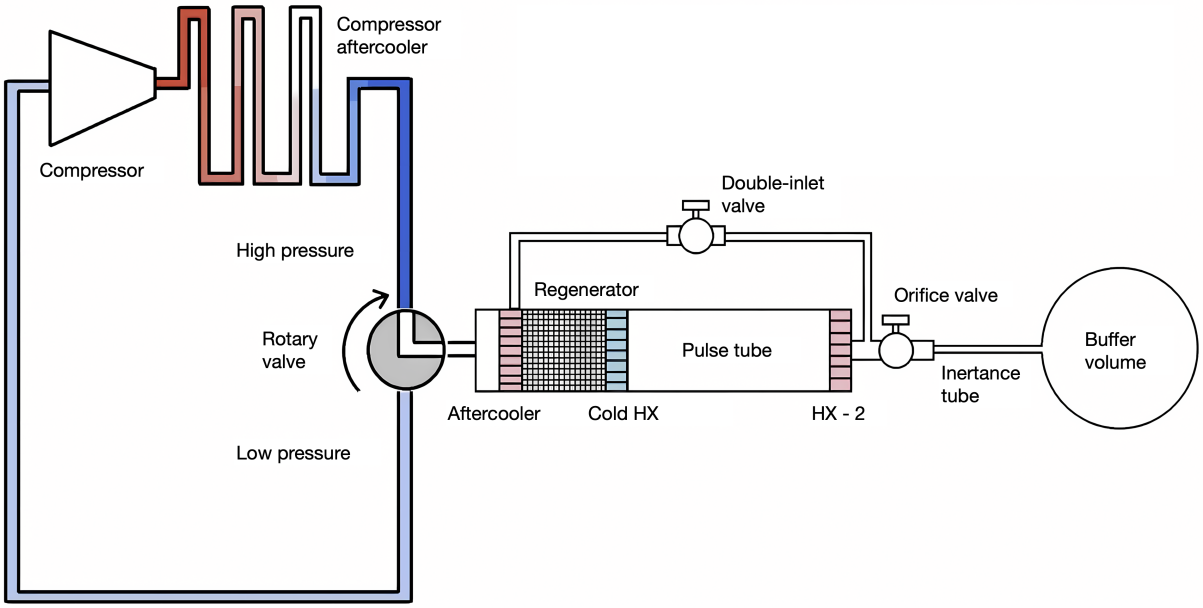

Figure 4.7: Schematic showing the working principle of the Gifford-McMahon type PT cryocooler. The compressor generates oscillating ^{4}He gas pressure waves, which are modulated by the rotary valve to alternate between high-pressure (compression) and low-pressure (expansion) phases. Compressed gas passes through the aftercooler, where waste heat is dissipated, before entering the regenerator. This is a porous matrix that cyclically stores and releases thermal energy to approximate isothermal processes. During expansion, ^{4}He flows into the PT, undergoing adiabatic cooling at the cold heat exchanger (Cold HX) via the thermoacoustic effect. Phase synchronization between pressure oscillations and gas flow is refined by the double-inlet valve and inertance tube, while the orifice valve and buffer volume stabilize residual pressure fluctuations; the latter acts as a gas reservoir to dampen acoustic oscillations, ensuring consistent phase relationships over successive cycles. The thermodynamic cycle comprises four stages: (1) compression-driven heat rejection at the aftercooler, (2) adiabatic expansion and cooling at the Cold HX, (3) regenerator-mediated thermal recovery during low-pressure gas return, and (4) inertance-driven phase correction to optimize energy recovery.

(i) **Pre-cooling**: Gaseous ^{3}He undergoes staged cooling through the PT's thermal interfaces: first to 60 K (1$^{\text{st}}$ - stage PT), then to 4 K (2$^{\text{nd}}$ - stage PT).

(ii) **Joule-Thomson (J-T) Condensation**: The ^{3}He stream passes through counter-flow heat exchangers (HX1/HX2, 95 % effectiveness) before isenthalpic expansion ($\Delta P \approx 1$ MPa) at the J-T stage, inducing liquefaction at 1.2 K [159].

(iii) **Sub-Kelvin Cooling**: Subsequent heat exchange with returning dilute-phase ^{3}He reduces the concentrated phase temperature to 100 mK (cold plate), facilitated by shifted silver sinter heat exchangers.

(iv) **Phase Separation**: In the MC (10 mK plate), ^{3}He atoms dissolve into the ^{4}He matrix. The cooling power as seen in [160] follows:

$$\dot{Q} = \dot{n}_{^3\text{He}} \times \Delta H \quad \text{where} \quad \Delta H = 84\text{kJ/mol}. \tag{4.1}$$

(v) **Phase Recovery**: Osmotic pressure drives the diluted mixture ($\sim 0.1\%$ ^{3}He) to the Still (0.8 K) plate, where resistive heating ($P_{\text{Still}} \approx 10$mW) exploits the vapor pressure disparity for selective ^{3}He separation.

(vi) **Re-circulation**: A turbo-molecular pump ($\dot{V} = 470$L/s) [161] extracts gaseous ^{3}He, which pre-cools incoming flow via HX2/HX1 before recompression.

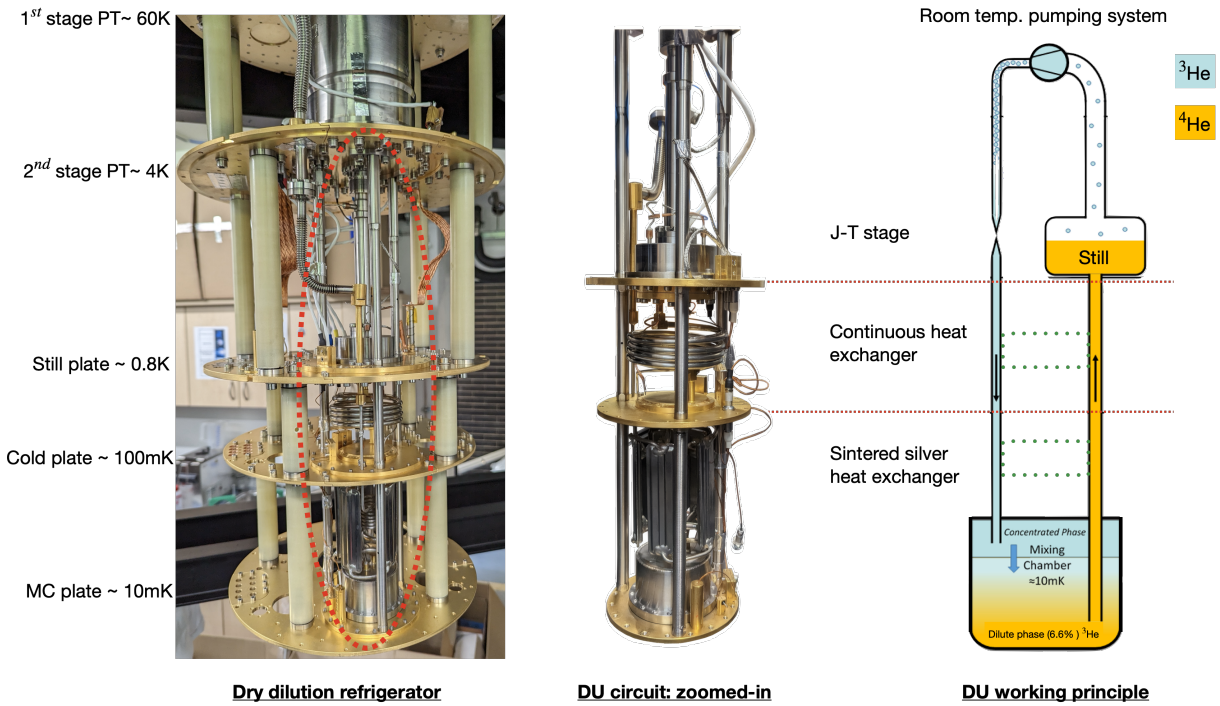

Figure 4.8: The figure illustrates three complementary views of a dilution refrigerator assembly: **Left:** A full-scale photograph of a dry dilution refrigerator, highlighting the DU circuit (outlined with a red dashed ellipse); **Centre:** A magnified photographic view of the DU, clearly depicting the arrangement of the thermal stages, heat exchangers, and the MC where mK temperature ranges are reached; **Right:** A schematic diagram illustrating the working principle of the DU cycle employing ^{3}He/^{4}He isotopic mixtures. The DU circuit (zoomed inset) illustrates the phase evolution: ^{3}He gas is precooled via the 1st and 2nd PT stages down to 4 K, condensed via J-T expansion, further cooled through HXs, then diluted in the MC to extract cooling power. Diluted ^{3}He is osmotically pumped to the Still for phase separation and recirculated;

The cooling power at 10 mK scales linearly with circulation rate ($\dot{n}_{^3\mathrm{He}}$ tpyically 300-500 µmol/s), provided that the turbo-molecular pump can handle the volume of gas up to the point wherein the rate of ^{3}He pumped away is higher than what is being dissolved. The base temperature depends critically on the pre-cooling efficiency, as insufficient thermalization at higher-temperature stages (60 K and 4 K) directly limits the minimum achievable temperature at the MC:

$$T_{\mathrm{base}} = T_{\mathrm{MC}} + \frac{\dot{Q}_{\mathrm{parasitic}}}{k_{\mathrm{He}} \dot{n}_{^3\mathrm{He}}} \tag{4.2}$$

where $k_{\mathrm{He}} = 9.4\,\mathrm{J/(mol \cdot K)}$ is the helium molar entropy. Parasitic heat loads (< 10 nW) from vibrational coupling and residual gas conduction dominate below 20 mK [162].

In practice, this entire process is mostly automated and is controlled via company-specific software that allows one to tune the parameters or take manual control in case of unintended emergencies that are not already accounted for in the software.

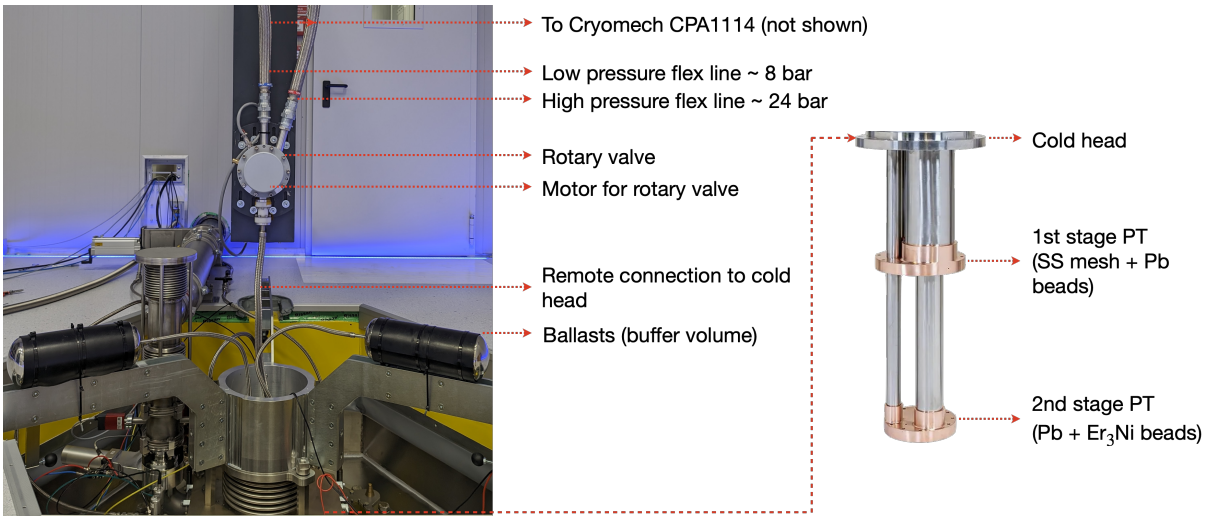

Figure 4.9: Simplified schematic of the GM-type PT-420RM used in the COSINUS experiment. Key components include high-pressure (24 bar) and low-pressure (8 bar) helium flex lines, rotary valves with motor drive, and ballast volumes for pressure stabilization. The remote cold head connection minimizes vibrational coupling to the dilution refrigerator. A Cryomech CPA1114 compressor is paired with the flex lines to achieve and maintain the 4 K precooling required.

4.2.3 The COSINUS Dry Dilution Refrigerator(s)

As illustrated in Fig. 4.9, the GM-type PT implementation adopted by COSINUS utilizes a two-stage system to reach the desired pre-cooling temperature of around 4 K. It is a cryomech PT420RM [163] unit which is coupled with a cryomech CPA1114 compressor unit with a rated power draw of ~ 23 KW (including the water-cooling unit). The rotary valve timing (optimized for 1.4 Hz operation) ensures phase coherence between pressure waves and displacer motion (for the current setup), maximizing the enthalpy flow. It must be noted however, that its not all sunshine and rainbows, as this setup introduces new moving parts which are operated at high pressures [164]. This introduces extra vibrational noise into the system, which, as described in Sec. 4.4, is not desirable to the detector operation and is quite difficult to decouple given its proximity to the dilution refrigerator. For the COSINUS installation at LNGS, a dry dilution refrigerator unit from Cryoconcept [165] is used. The vendor provides a patented solution to the vibrational noise discussed above, termed as Ultra Quiet Technology^{TM} (UQT) [166], which allows for a mechanical decoupling of the PT from the experimental volume. It consists of three main sub-systems, namely:

- **Pumping Duct Gas Exchanger**: Enables heat transfer between the pulse tube's 60 K/4 K stages and cryostat cold plates through gas-mediated thermal contact, eliminating solid mechanical connections that could transmit vibrations.
- **X-Y-Z Supple Bellows**: A multi-axis flexible coupling between the PT head and the top flange of the dilution refrigerator that absorbs mechanical vibrations through controlled deformation, while maintaining helium-tight sealing.
- **Double-Frame Architecture**: Physically separates the PT's reference frame from the dilution refrigerator's main structure, using independent tripod anchors to prevent vibration propagation through shared mechanical pathways.

A CAD rendering of the complete LNGS setup is shown in Fig. 4.10. The peculiar elongated geometry of the apparatus is to position the detector modules as far away as possible from the commercially used materials in the top stages which are not necessarily the most radio-pure. Furthermore, although the support structures for the individual stages are currently fabricated from glass fiber, these are also not radio-pure. Consequently, the support structures for the lower stages are planned to be substituted with Polyethylene Naphthalate (PEN)-based alternatives. Just like the inner Cu shields lining the inside of the drywell, the thermal shields are also made from NOSV Cu (see Sec. 4.1.2). To further block any direct line-of-sight from the detector modules to the top of the cryostat, an additional passive shield, composed of 190 kg of NOSV Cu, is installed below the MC plate. This shield is thermally anchored not to the MC plate but to the Still plate. It comprises ten individual Cu plates, each 300 mm in diameter and 30 mm in thickness.

In addition to the two levels of vibration decoupling discussed in Sec. 4.1.2, there is also a spring-based decoupling stage at the detector level. The detector plate, on which the detector box is mounted, is suspended by three strings placed 120° apart. Each string provides spring-like vertical decoupling and, simultaneously, a pendulum mechanism for horizontal decoupling. These strings are affixed to the internal particle shield, which owing to its 190 kg mass, acts as a more inertial (i.e., quieter) reference than the MC plate. Each string contains a spring and a Kevlar wire that allows adjustment of length while also providing thermal isolation between the detector plate and the radiation shield. A soft Cu strip between the MC and detector box serves as a thermal anchor, ensuring that the detectors can cool down to mK temperatures. Details on the experimental validation and optimization of this setup can be found in Refs. [97, 154].

In the initial phase of the experiment (scheduled for 2025), a detector box comprising eight modules, following the design outlined in Chapter 3, will be installed for the initial data-taking. This is expected to yield sufficient exposure to provide a model-independent test of the DAMA-LIBRA claim. Under the assumption of zero background events in the region of interest and an energy threshold of 1 keV for nuclear recoils, COSINUS will reach a 90% confidence level exclusion with an exposure of approximately 125 kg d, a 95% confidence level exclusion with 171 kg d, and a 99% confidence level exclusion with around 292 kg d [167]. A second phase with two additional detector boxes comprising 16 additional modules will also be deployed.

A smaller, nearly identical twin system is installed at the MPP building in Garching. This compact version does not include the 1.5 m extension of the 4 K plate found in the LNGS refrigerator. This setup allows for all necessary cabling and sub-component designs (as depicted in Fig. 4.10) to be tested and refined without requiring travel to the LNGS site. The two systems installed at LNGS and MPP, respectively, are shown in Fig. 4.11.

Each refrigerator stage is equipped with a dedicated thermometer to monitor its temperature and thereby evaluate cooling performance or detect any issues during cooldown. Depending on the temperature range, the first and second stages of the PT incorporate Cernox thermometers (calibrated from Lakeshore using a standard noise thermometer). At lower stages, a combination of full-range thermometers (on the Still and MC) and a RuO_2

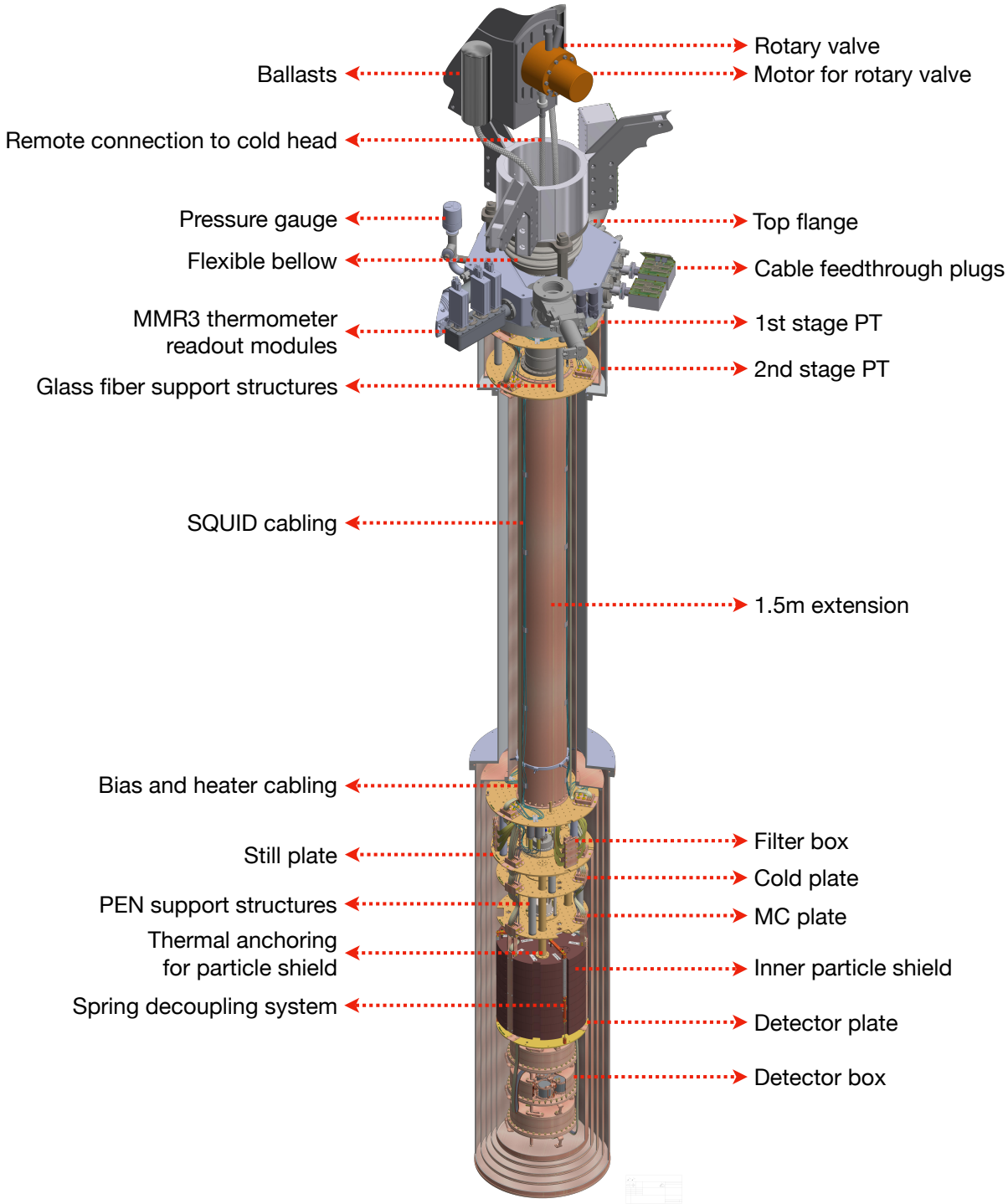

Figure 4.10: A cross-sectional view of the dry dilution refrigerator installed at LNGS. The principle components are highlighted, with a discussion of the same in text.

Figure 4.11: The COSINUS dry dilution refrigerators (images are not to scale).**Left:** The dry dilution refrigerator (nicknamed Calippo) installed at LNGS, prior to being lowered into the drywell for it's first cooldown; **Right:** The dry dilution refirgerator (nicknamed Giovanni Giorgio) installed at MPP, ready for it's first cooldown at the Garching campus.

thermometer (on the detector plate) is employed (factory-calibrated by cryoconcept using a standard noise thermometer). For R&D runs, additional Cernox thermometers were installed on the thermal anchor rods of the particle shield, as well as on the top and bottom of the shield, to verify robust thermal coupling among its ten plates. These thermometers are read out using MMR3 modules, which interface with cryoconcept software for data monitoring, storage, and visualization. The cooldown process is largely automated through cryoconcept's dedicated software, which also integrates with the GHS to carry out predefined procedures in a largely hands-off manner. Via InfluxDB, all relevant dilution refrigerator parameters can be accessed remotely to track and analyze performance between optimization cycles.

4.2.4 Data Acquisition

The data acquisition system is designed to capture and digitize the signals from the TES-SQUID setup with high fidelity. The main data acquisition components (similar for

both dilution refrigerators) are highlighted in Fig. 4.13. The three main areas highlighted are: the bias supply line denoted in black, the heater supply line denoted in red and the signal readout line denoted in blue. A Field Programmable Gate Array (FPGA) based data-acquisition system (DAQ) located at room temperature (RT), is used to supply bias and heater currents while also measuring and recording the amplified output signal from the SQUIDs. Each detector needs two pairs of cables running from the top of the cryostat, with one pair carrying the bias current and the other to supply the heater current for stabilization of the TES in its operating point. For a detector box containing eight modules, 16 pairs of cables for the bias and 16 pairs for the heater channels are needed. These are routed through the top flange of the dilution refrigerator using SCSI plugs at the top of the dilution refrigerator. The bias and heater lines are made from niobium-titanium (Nb-Ti) wires, with each pair twisted and woven with an insulating thread made of formvar/teflon. To reduce the impact of cross-talk, ground carrying single wires are woven between the pairs. The Nb-Ti wires are clad with a thin-layer of Cu-Ni, since NbTi becomes superconducting below 9 K which is a bad thermal conductor. Thus, this matrix‡ allows the cables to cool down at lower temperature stages. The resulting 16-pair cables are woven together such that they form a flat band cable. The cables themselves are thermalized at each temperature stage by pressing them between Cu-plates consolidated into a Cu-block, which is mounted to the refrigerator plates (denoted in dark green in Fig. 4.13). This ensures the cables are thermally well anchored, minimizing any heat leaks via the cables. Filter boxes, mounted on the Still plate, provide a low-pass filtering for both the bias and heater cables. They consist of Cu-Ka-Cu PCBs designed with masks for surface mounted components, which define the cutoff frequency. A schematic of the mounting setup of the filter box is shown on Fig. 4.12.

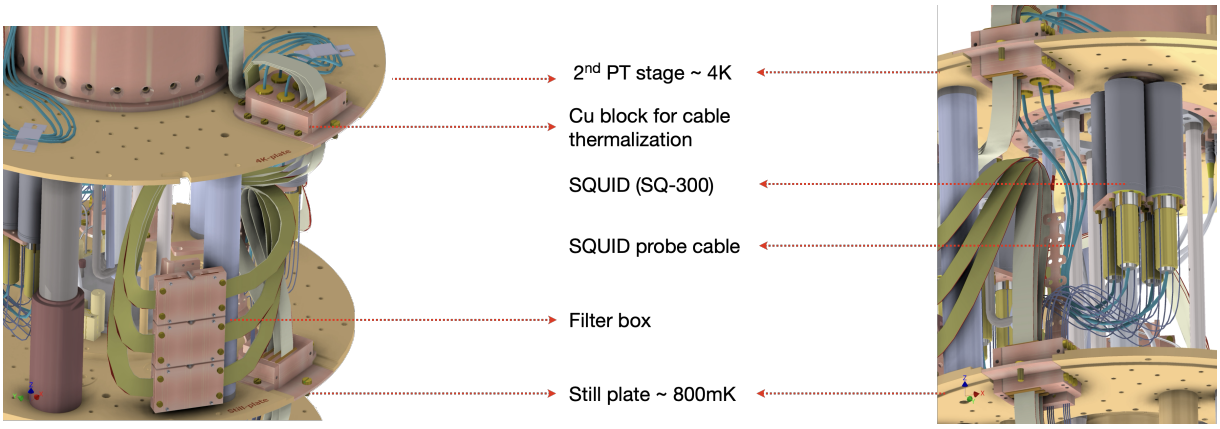

Figure 4.12: Left: A close-up of the thermalization of the filter box on the Still plate; **Right:** A close-up of the thermalization of the SQUIDs on the 2nd stage of the PT. The SQUID probe cable (in blue) carrying the signal to the upper stages and the NbTi superconducting cables (in gray) carrying the signal from the detector box are clearly visible.

A connector employing Spring Finger Contacts (SFCs) was developed for establishing connections between the twisted Nb-Ti cables to the filter box. SFCs consist of spring-mounted contact pins soldered onto the Cu-Ka-Cu PCBs, providing reliable electrical

‡ This matrix also serves an essential role in enabling effective soldering, particularly with lead-free solder formulations, as these exhibit poor adhesion directly to the NbTi filaments

connections through mechanical pressure against corresponding counterpart surfaces (denoted in pink in Fig. 4.13). A similar connection is also used between the filter box and cables that travel down to the detector box.

In order to supply the bias and heater lines to the module and to read out the signals from the modules in the detector box, another set of spring finger connectors are used. The signal lines connecting to the SQUID inputs are carried out through single twisted pairs of NbTi wires just like the bias and heater wires. In order to read out the 16 signal channels from all 8 modules, 4 quad SQUIDs from STAR Cryoelectronics (SQ-300) [146] are mounted on the 4 K stage. A schematic of the mounting setup of the SQUIDs is shown on Fig. 4.12. The SQUID output is then carried out to RT via dedicated SQUID probe cables which are a part of the system procured from StarCryo. The thermalization implemented for these cables is similar to that of the bias and heater cable lines, with the primary differentiator being that the cables would be glued into Au-coated Cu blocks at each temperature stage. Given the outlook for COSINUS Run 1 and Run 2, a total of 48 SQ-300 SQUIDS will be installed at the LNGS dilution refrigerator (allowing a theoretical readout of 48 detectors) while the R&D dilution refrigerator at MPP will have 16 SQ-300 SQUIDs installed.

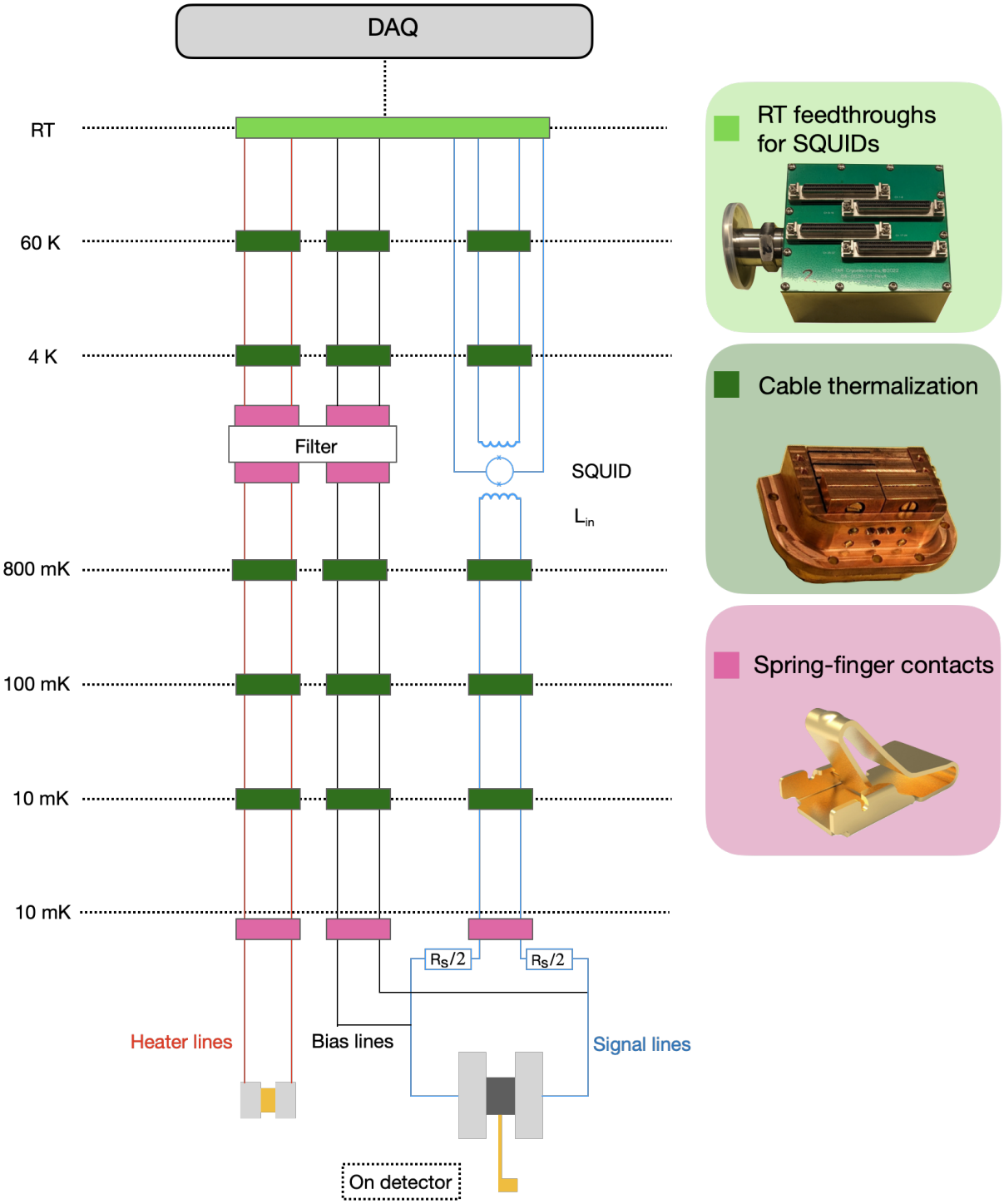

Figure 4.13: Flow-chart of the data acquisition and triggering process in the COSINUS experiment. The SQUIDs are thermalized at the 4 K plate while the filter box is thermalized on the Still plate at 800 mK.

Detector Development & Optimization

The *remo*TES Design 5

The real voyage of discovery consists not in seeking new landscapes, but in having new eyes.
— Marcel Proust, (*Attributed*)

This chapter introduces the rationale behind the *remo*TES-based detector design and details its initial experimental realization. To validate the design concept, preliminary tests were conducted first using a Si absorber, followed by additional tests with a α-TeO_2 absorber. Subsequent studies focused on improving the baseline resolution and identifying and resolving signal bottlenecks introduced by this new design. Contributions from the author to these works included sample fabrication, detector mounting, setup and optimization of TES parameters and subsequent data acquisition, operation and maintenance of the dilution refrigerator during these measurements.

The content in the following sections draws upon and integrates findings from these peer-reviewed publications:

First measurements of *remo*TES cryogenic calorimeters: Easy-to-fabricate particle detectors for a wide choice of target materials, G. Angloher et al. (COSINUS Collaboration) Nucl. Instrum. Methods Phys. Res. A, **1045**, 167532, (2023)

***remo*TES: A novel cryogenic detector for rare-event searches** , M.R. Bharadwaj et al. (COSINUS Collaboration) Proc. Sci., **441**, 060, (2024)

Description and Performance of the COSINUS *remo*TES Design , V. Zema et al. (COSINUS Collaboration) J. Low Temp. Phys., **217**, 393–400, (2024)

5.1 An Introduction to The *remo*TES Design

The direct deposition of the TES thermometer onto an absorber of choice ensures a good transmission of the non-thermal phonons to the TES thin-film, provided it is supported via sufficiently good acoustic matching between the materials used. This integrated setup is favored as long as the absorber material can withstand the processes necessary for the fabrication of the TES, i.e., multiple electron-beam evaporation cycles (requiring temperatures above 700 °C), sputtering, chemical etching and photolithography*. However, absorber materials that have a low melting point and/or are hygroscopic cannot undergo these processes. Furthermore, sensor fabrication may negatively impact the radiopurity of the absorber crystal. A work-around solution for delicate materials, such as for the NaI crystals used in the COSINUS experiment [169], was the so-called composite design [170]: the TES is fabricated onto a separate substrate which in turn is connected to the

* Nonetheless, the fabrication process might induce stresses in the crystal lattice, which is one of the main potential origins of the excess signal at low energies observed in several experiments [168].

absorber via an amorphous interface (glue, oil, or grease). In the following, we call the TES substrate used in the composite design "carrier" or "carrier crystal". This approach requires the phonons produced by a particle interacting in the absorber to propagate through the interface, the carrier, and finally couple to the TES. A fraction of the signal reaching the interface is lost in this process due to poor phonon transmission in case of an acoustic mismatch between the different materials of the carrier and the absorber [171]. In COSINUS, Al_2O_3, Si, $CaWO_4$, and $CdWO_4$ were tested as carrier materials, which all have a high acoustic mismatch to soft absorber materials like NaI. Furthermore, in the case of a good scintillator like NaI, a carrier crystal which is not fully transparent to the scintillation light will reabsorb part of the light, causing an additional power input to the TES. In this case, the resulting pulse shape in the TES will be a superposition of the NaI scintillation signal and the primary thermal signal [142]. This effect was observed in earlier COSINUS prototypes and will be the subject of a future publication.

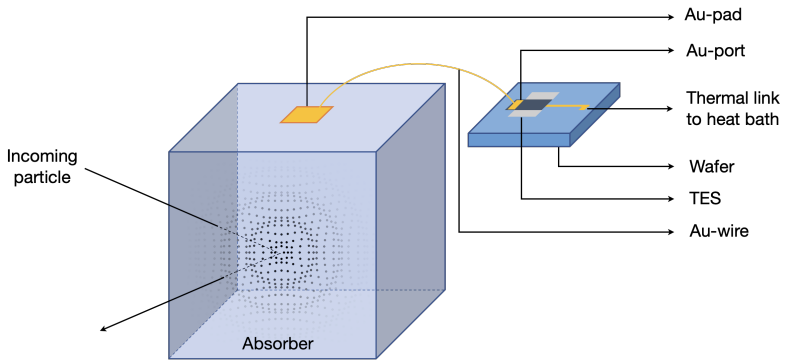

Figure 5.1: Schematic illustration of the *remo*TES design. The Au-link comprises a Au-pad on the absorber and Au-port on the TES, connected via a Au bond-wire.

In [136], the authors propose a TES-based detector concept, denoted *remo*TES in the following, which does not suffer from these disadvantages and features a simpler production process. The design of a *remo*TES detector is schematically depicted in Figure 5.1. It avoids the carrier crystal by coupling the TES directly to the target crystal via a Au-link that transmits the phonon signal from an interaction in the absorber to the TES. The Au-link comprises a Au-pad on the absorber and a Au-pad on the TES (denoted as Au-port), connected via a Au bond-wire. The TES is fabricated onto a separate substrate, which is placed on the Cu holder, according to the scheme in Figure 5.2. In the following we refer to the TES substrate used in the *remo*TES design as "wafer". A significant advantage of this design is that it improves the collection of athermal phonons into the Au-pad, which could otherwise be reflected due to the acoustic mismatch between absorber crystal and carrier crystal. Even more importantly, phonons directly couple to the electronic system of the Au-pad via electron-phonon coupling [172]. In the literature, this coupling in Au is found to be comparable to or larger than in W [136, 141, 173–175].

The decoupling of the TES fabrication from the absorber crystal as outlined above can streamline the production process, by enhancing the production of reliable and reproducibile TES wafers, and expanding the choice of absorbers to accommodate even delicate materials. The following sections present the first experimental implementation and results

of the *remo*TES detector design concept. It also outlines follow-up optimization tests carried out to improve the baseline resolution, identify, and remove the bottlenecks introduced by such a design change [144].

5.2 Detector Design of The *remo*TES-prototypes

A first set of studies were undertaken with Si and tellurium dioxide (α-TeO_2) to test the viability of this design as a sensitive cryogenic detector. A 2.33 g Si crystal served as a first study, given the wide prevalence of Si as a cryogenic detector. A follow-up with a 2.27 g α-TeO_2 crystal was carried out, mainly due to similar solid-state properties it shared with NaI, in particular regarding the heat capacity and the gap between the acoustic and optical phonon modes [176, 177]. Fig. 5.2 shows a scheme of α-TeO_2 module. The Si module is similarly assembled, but the brass screw is not present, as shown in Fig. 5.3.

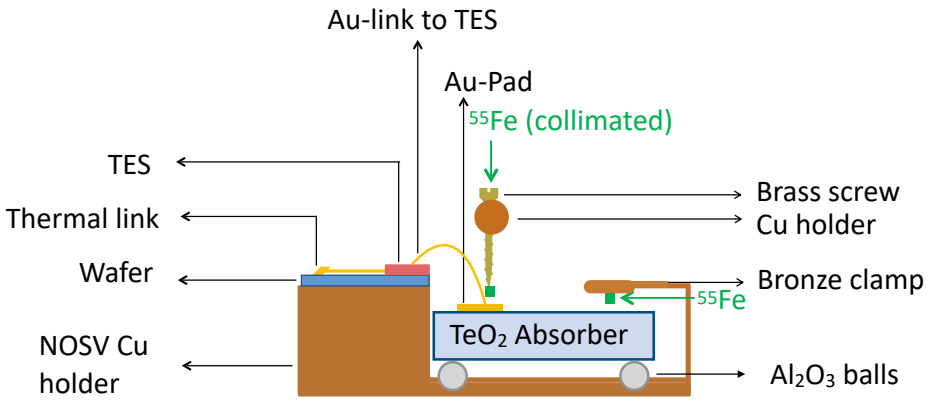

Figure 5.2: Scheme of the complete α-TeO_2-module.

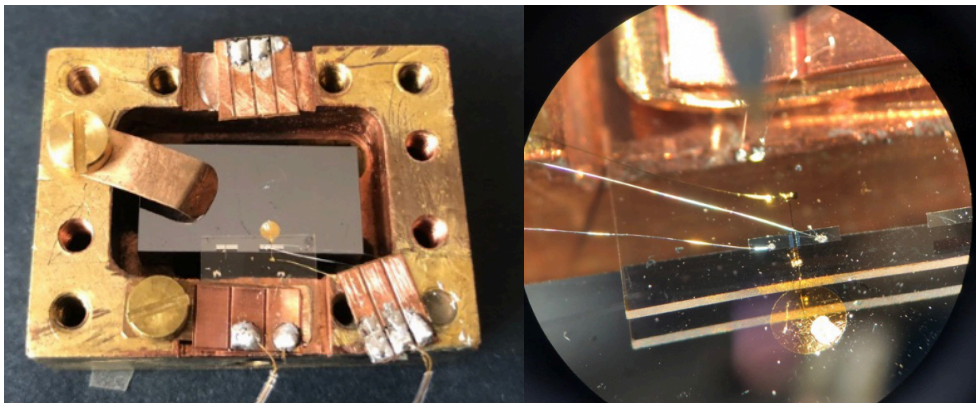

Figure 5.3: Left: Image of the Si *remo*TES, surrounded by the Cu housing; **Right:** Zoomed-in view on the TES and Au-pad.

On the Si absorber ((20x10x5) mm^3), a Au-film of circular shape (3 mm diameter) of 200 nm thickness was deposited by Magnetron-sputtering. The connection between the Au-pad on the Si absorber and the TES on the wafer was provided via a 17 µm thick and 2-3 mm

long Au-bonding wire. While the Au-wire was wedge-bonded onto the Au-pad of the TES, it was connected to the Au-pad on the Si absorber by using a silver-loaded epoxy (≈25 µg). Avoiding wedge-bonding on the Au-pad of the absorber opens up the possibility to also introduce very soft and fragile absorber crystals to this field of research, which would be damaged by solid phase welding processes (e.g., wedge and ball bonding). The Au-pad on the TeO_2 absorber ((20x10x2) mm^3) consists of a 400 nm thick Au-foil glued onto its surface by using a two-component epoxy resin. The electrical and thermal contact between the Au-pad on the TeO_2 and the TES was realized with a wedge-bond on both sides, respectively.

The use of Au foils has two important consequences: a better thermal conductance due to the fact that the Residual Resistance Ratio (RRR) is larger with respect to the sputtered film, and the possibility to avoid any microfabrication process on the crystal surface. Table 5.2 summarizes the condensed information on both prototype detectors. It is worth mentioning that the two configurations here were not meant to be used for performance comparison, but rather to illustrate the flexibility of the *remo*TES concept, and the possibility to adapt it to various absorber materials.

The TES on the thin Al_2O_3 wafer ((10x10x0.4) mm^3) was identical for both measurements. It consists of a 100 nm-thick tungsten (W) film of an area of (220x300) μm^2 and two aluminum (Al) pads for biasing of the sensor. The area of the W-film not overlapping with the pads is (70x300) μm^2. The weak thermal link to the heat bath consists of a 1 mm long Au-stripe (20 µm in width, 80 nm in thickness).An additional Au-stripe ((200x130) μm^2, 0.1 µm thick) was evaporated on the wafer at about 2.5 mm of distance from the sensor. It is used to inject heat pulses to monitor the operating point of the TES.

5.3 First Experimental Results

The measurements reported here were carried out in a dilution refrigerator of the CRESST group at the Max-Planck-Institut für Physik in Munich, Germany. This is an above-ground, liquid ^{4}He-precooled dilution refrigerator for R&D measurements and TES testing. It is equipped with four SQUID channels from APS [178] and a VME-based data acquisition using a hardware-triggered readout. The total exposure was 1.06 g d for the Si detector and 2.28 g d for TeO_2. For the purpose of energy calibration both prototype detectors were irradiated by an uncollimated ^{55}Fe-source shining onto the side of the absorber opposite to the face with the Au-pad. Furthermore, the TeO_2 detector was equipped with an additional collimated ^{55}Fe-source irradiating solely the Au-pad glued onto the absorber.

5.3.1 Data Analysis

Different event classes were observed in both detectors. Standard events (SEVs = averaged pulses scaled to an amplitude of 1 V) for these classes are shown in Figure 5.4; they were created from a small, selected sample of pulses with the same shape for each class. For both

detectors, there is a dominant class of events, depicted in green, which is characterized by a (10%-90%) rise time of ≈1 ms, with a (90%-10%) decay time of ≈44 ms for the Si prototype, and ≈122 ms for the TeO_2 prototype. The high rate of these events (cf. Table 5.1) is consistent with hits in the absorber, considering that the ^{55}Fe source shining on the "bottom" of the absorber cannot be seen by the wafer carrying the TES. Hits in the latter (orange in Figure 5.4) feature much faster signals: the rise times are only ≈0.16 ms (Si measurement) and ≈0.07 ms (TeO_2 measurement), while the decay times are ≈11.2 ms and ≈1.2 ms, respectively.

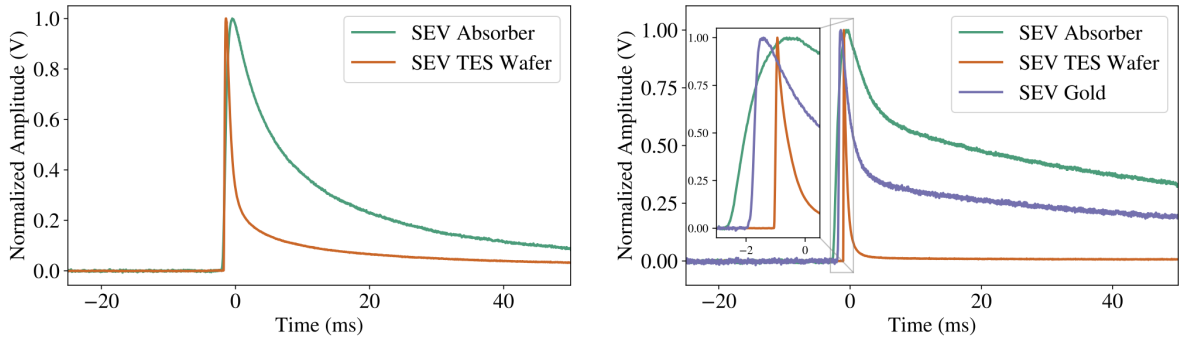

Figure 5.4: Standard events (SEVs) for the two prototype detectors. **Left:** Events in the Si absorber (green) and the TES wafer (orange); **Right:** Events in the TeO_2 absorber (green), the TES wafer (orange) and the gold pad on the TeO_2 (violet). The pulse onsets for each event class are slightly shifted for visualization purposes.

The TeO_2 prototype exhibits an additional event class. We identify these comparatively rare events (cf. Table 5.1) as hits from the collimated ^{55}Fe-source irradiating the Au-pad on the absorber. The rise time of the pulse is driven by the time needed to transport energy to the TES which depends on the energy carriers. The transport is fast for electrons and non-thermal phonons, which are the dominant energy carriers for the events created by interactions in the Au-pad or the wafer. In the TeO_2 absorber, a larger part of the initial phonon population undergoes thermalization, consequently leading to slower pulses. The Au-pad events are visible in Fig. 5.5 as a cluster of events in the violet box. Their decay time is faster than the one of absorber events, but slower than the one of wafer events. The explanation for the difference between gold and wafer events can be two-fold: firstly, energy deposited in the Au-pad is partially transmitted back and forth, to and from the absorber, leading to a larger decay time; secondly, the heat capacity of Au affects the decay time, leading to even slower pulses. The Au-pad is small in comparison to the absorber, and connected directly to the TES. Therefore, pad events in Fig. 5.5 are distributed around a larger pulse height (~ 0.07 V) with respect to the pulse height of the ^{55}Fe-events in the absorber (~ 0.04 V).

Few basic quality cuts are applied to the complete dataset: events coinciding with a decaying baseline from a previous pulse are removed by placing a cut on the pre-trigger baseline slope. Additionally, events with a reconstructed pulse onset more than 1 ms away from the trigger position are discarded. To separate different event classes reliably, the root mean square (RMS) from a truncated standard event fit is used. This method is described in e.g. [179]: a SEV is fitted to a subset of samples for each pulse, where only samples below a

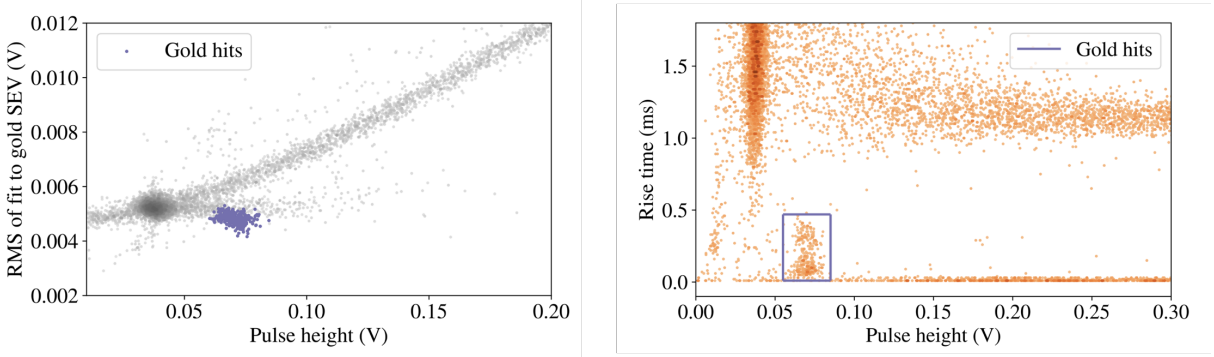

Figure 5.5: TeO_2-*remo*TES data set: **Left:** Rise time versus moving average pulse height distribution. The violet box encloses the events in the gold foil produced by the collimated ^{55}Fe-source; **Right:** Fit RMS for the gold SEV as a function of the pulse height distribution. The events from the violet box on the left panel are tagged and depicted in violet.

given truncation limit (relative to the baseline) are considered. We fit each pulse with all three SEVs, and the dataset for each event contains only those events where the respective fit yields the lowest RMS. As an example, the discrimination between absorber and wafer events is shown in Fig. 5.6. Fig. 5.5 illustrates the discrimination between absorber events and ^{55}Fe Au-pad events: The latter are marked in violet, and have been identified as a cluster in Fig. 5.5 using their fast rise time. Table 5.1 shows the number of surviving events for each prototype and event class; as stated before, absorber events are the dominant event class in both measurements, and Au-hits are less frequent than wafer hits for the TeO_2 detector.

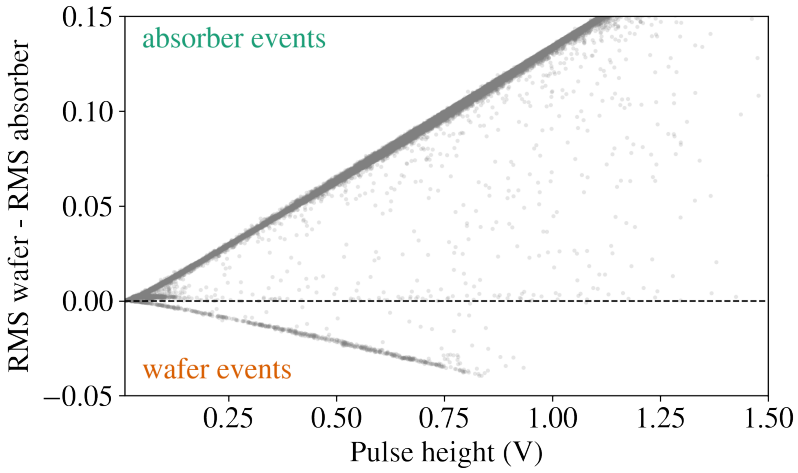

Figure 5.6: Difference between RMS values from the wafer SEV fit and the absorber SEV fit as a function of moving-average pulse height for the TeO_2 prototype; different event bands corresponding to the different classes are visible. The event population between the absorber and the wafer band corresponds to the Au hits; its pulse shape is a mixture of the former two classes, and their shapes match it equally well.

In addition to the events produced by particles interacting in the active detector parts, we periodically inject electrical pulses with known amplitudes into the heater of each detector. These heater pulses allow monitoring the detector response over time, and accounting for nonlinearity and the effect of saturation in the TES, which influence the pulse shape at

Table 5.1: Number of surviving events after quality cuts for each measurement and event class (see text for details).

Absorber material	"Absorber" events	"Wafer" events	"Gold" events
Si	6072	398	-
TeO_2	28555	711	314

high energies (see e.g. [179]). A truncated fit with a dedicated heater SEV is performed for all heater pulses, and the resulting amplitude is used in combination with the input pulser setting to compensate non-linearities and time-variations of the reconstructed (fitted) amplitude for particle-induced events [180].

5.3.2 Energy Calibration and Resolution

The K_α peak from the ^{55}Fe source (5.89 keV) prominent in the spectrum of the Si and TeO_2 detector is used to calibrate the detector response, which is given by the truncated fit result for absorber events corrected by the heater response information. We chose the truncated fit over the usual method of optimal filtering [181] here, since the noise conditions in both measurements changed over time, and the filter relies on a stable noise power spectrum. The resulting spectra for absorber events are given in Figure 5.7. For the TeO_2 detector, K_α and K_β lines are not resolved, and the left flank of the single peak structure was used for calibration.

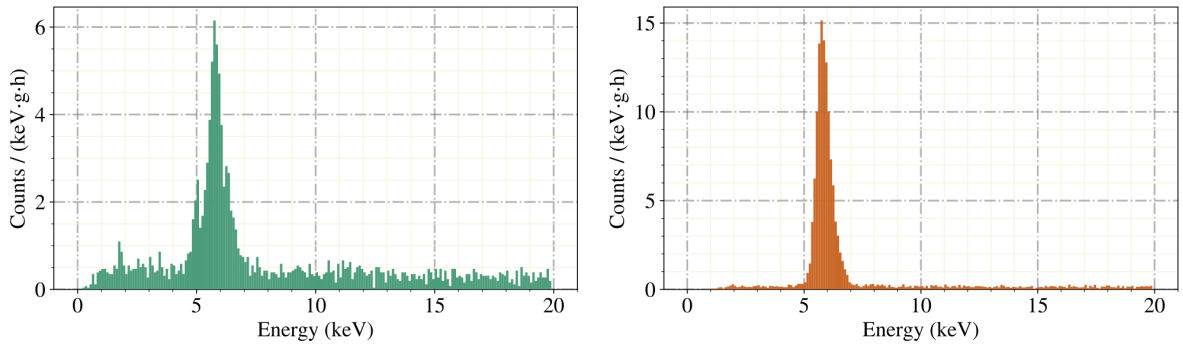

Figure 5.7: The energy spectra of the two prototype detectors: **Left:** Si absorber and **Right:** TeO_2 absorber. The intensity of the ^{55}Fe-source producing X-rays of 5.89 keV (K_α) and 6.49 keV (K_β) was significantly stronger for the TeO_2 absorber. The energies of the additional peaks in the Si detector (≈1.8 keV and ≈5 keV) are consistent with X-ray emission from the K-shell of Si (1.84 keV), and an escape line due to the Cu holder (Cu L1 at 1.10 keV).

The baseline resolution is determined for each detector in the following way: in each measurement, records without a trigger event are taken in regular intervals. These "empty baselines" are then cleaned, removing random coincidences with pulses and artifacts. Subsequently, we superimpose the SEV for a given detector with all remaining empty baselines. These artificial events (122 for the Si detector and 1932 for TeO_2) are passed

through the analysis chain and reconstruction algorithm, and the detector resolution is extracted from the reconstructed amplitudes. The resolutions (all in σ) are (18.4 ± 1.2) mV for the Si, and (1.22 ± 0.02) mV for the TeO_2 absorber, corresponding to (87.8 ± 5.6) eV and (193.5 ± 3.1) eV, respectively (cf. Table 5.2). Typically, the achievable threshold of a TES is about five times the baseline resolution [58, 182].

Table 5.2: Summary of the two measurements using the *remo*TES design.

Absorber	Si	α-TeO_2
Volume	(20x10x5) mm^3	(20x10x2) mm^3
Au-link	**Au-pad on Si**	**Au-pad on α-TeO_2**
	Thickness: 200 nm	Thickness: 400 nm
	Magnetron sputtering	Glue: Epo-Tek 301-2 [183]
	Au-wire	**Au-wire**
	Diameter: 17 µm	Diameter: 17 µm
	Wedge bonded	Silver-loaded epoxy
Al_2O_3 wafer	Volume: (10x10x0.4) mm^3	Volume: (10x10x0.4) mm^3
W-TES on wafer	Area: (220x300) μm^2	Area: (220x300) μm^2
	Thickness: 100 nm	Thickness: 100 nm
	T_C: 28 mK	
Heater on wafer	Area: (200x130) μm^2	Area: (200x130) μm^2
	Thickness: 100 nm Au	Thickness: 100 nm Au
Effective exposure	1.06 g d	2.28 g d
Baseline resolution	(87.8±5.6) eV	(193.5±3.1) eV

5.4 Optimization Studies

The Au-link of the *remo*TES readout scheme introduces a new set of additional parameters that need to be optimized to ensure a good collection of the athermal phonons and their effective coupling to the electronic system of the Au-link. The follow-up studies outlined below were carried out to improve the baseline resolution, identify, and remove the bottlenecks introduced by this design change [144]. A Si absorber was used to characterize and study the effects of each individual component of the Au-link on the detector performance. Si was selected due to its well-established fabrication methods and straightforward handling. Its non-hygroscopic nature, in contrast to NaI, was particularly beneficial for accelerating the prototyping phase.

5.4.1 Fabrication and Assembly

For the following studies, a holder made from NOSV copper (Cu) was used to house a 2.33 g Si absorber with dimensions (20x10x5) mm^3. The crystal rests on a trio of sapphire

(Al_2O_3) balls to thermally insulate it from the Cu holder. Two additional metallic support tips were used to fix the crystal's position. A low count-rate ^{55}Fe X-ray source is taped onto the Cu holder such that it irradiated one of the faces of the crystal while an additional collimated ^{55}Fe source is shining onto the Au-pad. The K_α (5.89 keV) and K_β (6.49 keV) lines are used to calibrate the detector in the offline analysis. Fig. 5.8 shows a schematic of the assembled Si-*remo*TES detector.

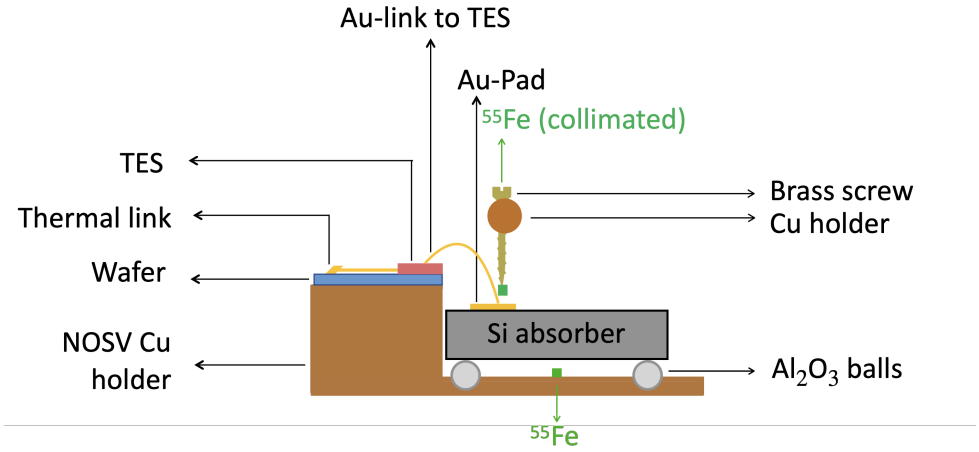

Figure 5.8: Schematic representation of the Si *remo*TES detector design.

For the reference measurement (labelled Reference-1), the Si absorber was equipped with a 1 µm thick Au-pad having an area of 7.5 mm^2 glued to the absorber using Epo-Tek 301-2 [183], a low-outgassing two component epoxy. A 17 µm thick Au-wire was used to connect the Au-pad on the absorber side to the Au-pad on the TES side, employing a wedge bonding method on both ends. The TES is a tungsten (W)-based thin-flim which was deposited onto a Al_2O_3 wafer. With the following setup, a baseline resolution of σ = (280±9) eV was obtained.

5.4.2 Optimization Results

A subsequent measurement (labelled Reference-2) was carried out with a Si absorber having the same mass of 2.33 g, but with dimensions of (10x10x10) mm^3. In this configuration, a baseline resolution, σ = (440±13) eV was obtained. The reason for this mismatch in performance with respect to Reference-1 was revealed by an examination of the Au-wire connection under a high magnification microscope. This revealed tears in the Au-pad on Si around the wedge-bond foot in the case of Reference-2, likely attributed to the shear forces concentrated around the small bond site as seen in Fig. 5.9.

A ball bonding technique typically exerts lower shear forces compared to wedge bonding. This is due to the way the Au-wire is shaped into a ball towards the end, before being pressed onto the Au-pad. The shape of the ball and the bonding process distributes the stress over a larger area, reducing the risk of tears in the thin Au-pads. Consequently, a follow-up set of studies were carried out with ball-bonding being employed on the Au-pad.

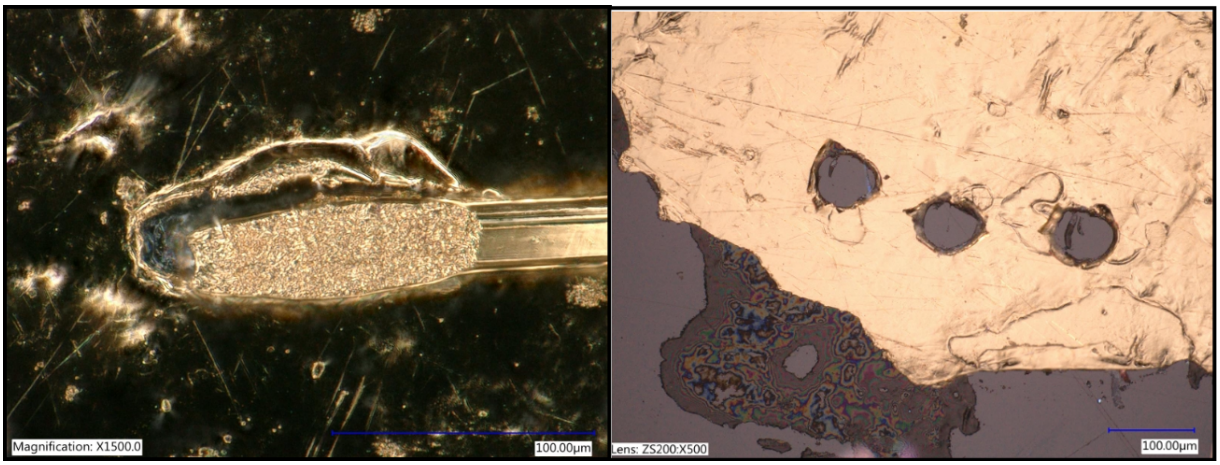

Figure 5.9: Left: A zoom-in of the bond feet for Reference-2, where the wedge-bond caused a rupture in the Au-film; **Right:** A zoom-in of the bond feet for ball-bonding tests carried out on a 1 µm thick Au-pad glued on a Si absorber with Epo-Tek 301-2. Elevated bonding temperatures caused adhesive failure, resulting in film delamination and hole formation during bonding attempts.

Initial trials using 1 µm thick Au-pads adhered with Epo-Tek 301-2 revealed thermal degradation of the adhesive layer during the ball formation phase (≥ 200 °C), leading to pad delamination (Fig. 5.9)[†]. A second iteration utilized 200 nm sputtered Au-pads to eliminate adhesive interfaces. Although occasional bonding difficulties persisted, a functional sample (Ball bond test -1 in Table 5.3) was successfully fabricated. Bond integrity was verified through microscopic inspection and mechanical stress testing, ensuring adequate adhesion without excessive structural strain. A third configuration employed 8 µm thick Au-pads bonded with Epo-Tek 301-2 (Ball bond test -2). This increased thickness meant the pads had sufficient thermal mass to absorb and dissipate the heat generated during ball formation, effectively preventing the adhesive from degrading. Fig. 5.10 illustrates both detector configurations, and shows the assembled detector for the two ball-bond tests.

A performance comparison of the different detectors with Reference-1 is shown in Table 5.3. It can be seen that by employing the ball-bonding technique, the performance of the detectors in comparison to the reference measurement was improved. The improvement in baseline resolution observed when using the 8 µm Au-pad shows that heat capacity is not yet the dominant factor limiting detector performance.

A closer look at the pulse shapes of particle interactions directly in the Au-pad for the ball-bond tests in Fig. 5.12 (left) shows a larger thermal component present in the 8 µm Au-pad events as evident from the longer tail of the pulse.

In order to check if the effect was purely a consequence of the additional heat capacity and not due to signal bottlenecks on the TES Au-port, a follow-up test was performed wherein the current design with a partial overlap of the Au-pad on the W-TES side (dubbed the TES Au-bridge design) was replaced with a new sensor layout wherein the Au-pad completely overlapped the W-TES (dubbed the TES Au-island design). A close-up of the two designs is shown in Fig. 5.11.

[†] While sporadic successful bonds could be achieved through iterative attempts, the compromised film integrity would likely fail long-term stability requirements.

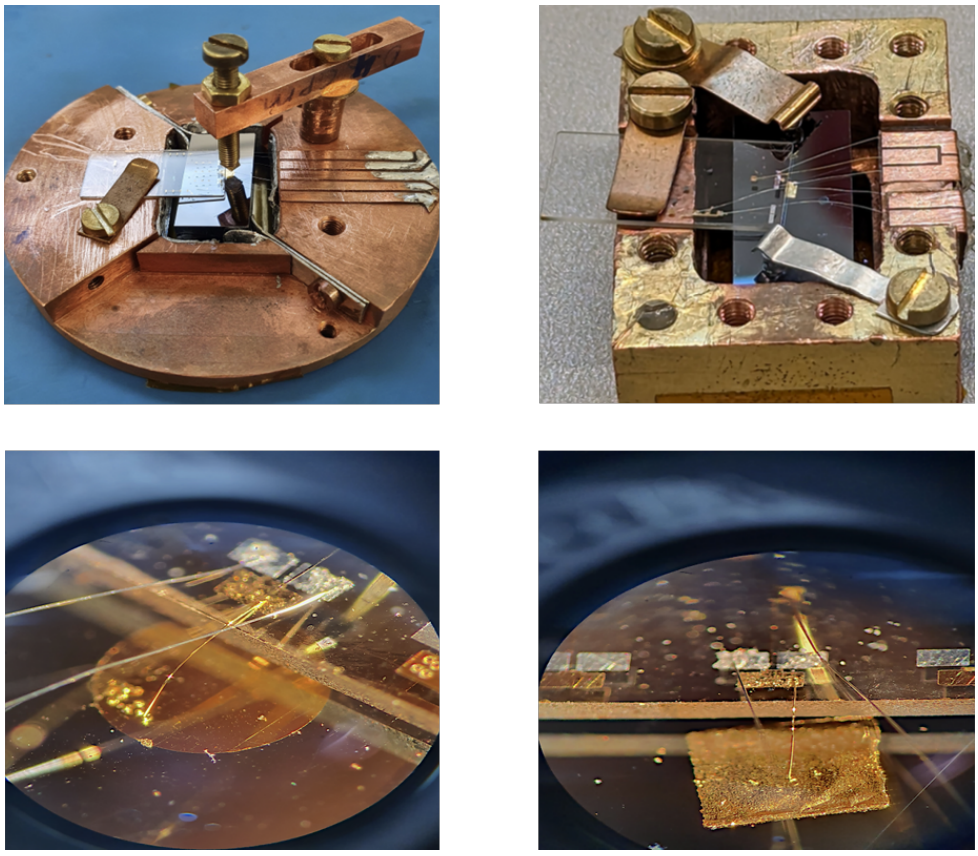

Figure 5.10: Left: Fully assembled detector for the Ball-bond test - 1. The image on the bottom shows a close-up view of the ball-bond on the 200 nm sputtered Au-film; **Right:** Fully assembled detector module for the Ball-bond test - 2. The image on the bottom shows a close-up view of the ball-bond on the glued Au-film having a thickness of 8 µm.

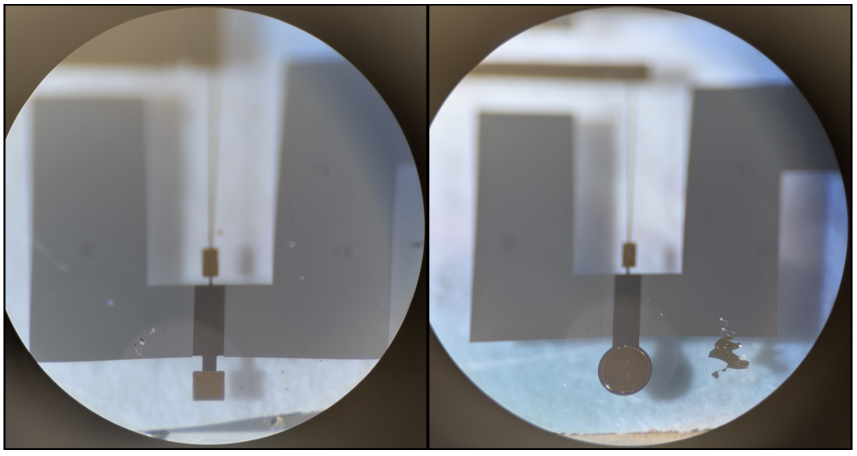

Figure 5.11: Left: A zoomed-in image of the TES with the Au-bridge design. It is observed here that there is only a partial overlap of the Au-film with the W-film; **Right:** A zoomed-in image of the TES with the Au-Island design. Here, the Au-island is completely deposited on the W-film with no overlap region on the bare wafer.

The Au-pad thickness on the absorber side was kept unchanged at 8 µm. A comparison of the pulse shapes of Au-pad events of the two designs is depicted in Fig. 5.12 (right). It shows that the modified Au-island design shows a much shorter tail, indicating a quicker decay time. A plausible explanation of the improvement due to the design change can be

Table 5.3: Performance comparison among different Si-*remo*TES designs.

Test	Reference-1	Ball bond test - 1	Ball bond test - 2
Au-link	**Au-pad**	**Au-pad**	**Au-pad**
	Thickness: 1 µm	Thickness: 200 nm	Thickness: 8 µm
	Glue: Epo-Tek 301-2	Sputtering	Glue: Epo-Tek 301-2
	Au-wire	**Au-wire**	**Au-wire**
	Diameter: 17 µm	Diameter: 25 µm	Diameter: 25 µm
	Wedge-bonding	Ball-bonding	Ball-bonding
Resolution	(280±9) eV	(133±3) eV	(89±2) eV
TES design	Bridge design	Bridge design	Bridge design

attributed to poor signal conductance between the Au/W interface in the design with the Au-bridge, which could impede signal transmission and cause a backflow of the signal to the Au-pad on the absorber.

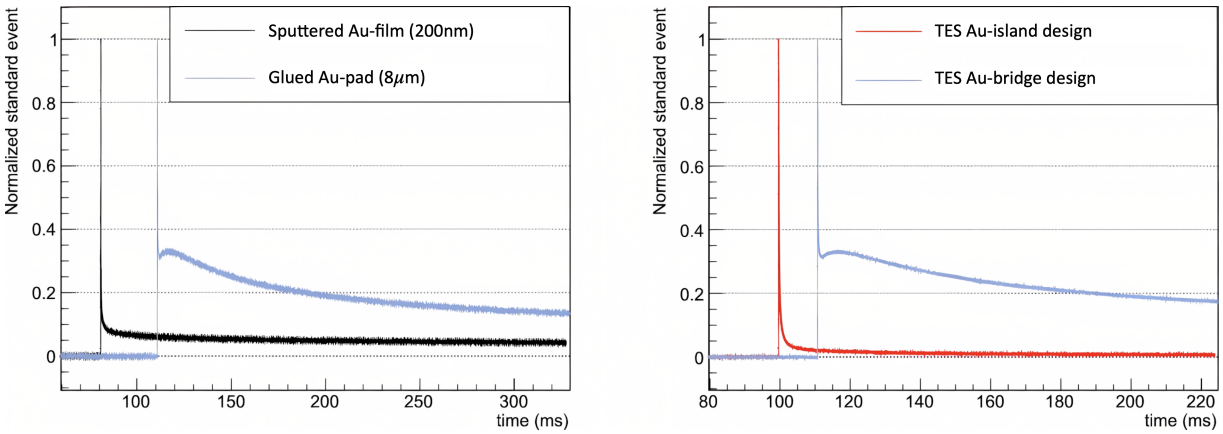

Figure 5.12: A comparison of pulse shapes of particle interactions directly in the Au-pad. **Left:** A comparison between pulse shapes of detectors having different Au-pad thickness read out with the TES bridge design; **Right:** Pulse shapes of detectors having the same Au-pad thickness (8 µm pad glued to the absorber) but different TES designs.

NaI *remo*TES Prototyping 6

This chapter covers the experimental implementation of the *remo*TES-based detector design for reading out signals from cryogenic NaI scintillating crystals. The first part discusses the initial above-ground test, demonstrating particle discrimination capabilities using a NaI absorber. The second part addresses subsequent underground measurements conducted for enhanced sensitivity. Contributions from the author to these works included sample fabrication, detector mounting, setup and optimization of TES parameters and subsequent data acquisition, operation and maintenance of the dilution refrigerator during these measurements. The author served as one of the corresponding authors for the second publication.

This chapter integrates results presented in the following peer-reviewed publications:

Particle discrimination in a NaI crystal using the COSINUS remote TES design ,G. Angloher et al. (COSINUS Collaboration) Phys. Rev. D, **109**, 082003, (2024)

Deep-underground dark matter search with a COSINUS detector prototype ,G. Angloher et al. (COSINUS Collaboration) Phys. Rev. D, **110**, 043010, (2024)

6.1 Detector Module

The detector module consists of a *remo*TES phonon detector [137] and a separate silicon-on-sapphire (SOS) wafer as light detector, as shown in Figs. 6.1, 6.2 and 6.3.

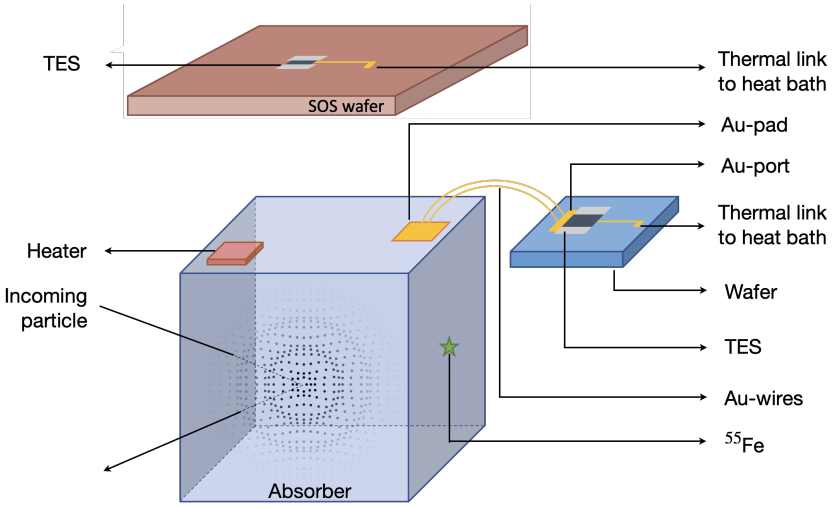

Figure 6.1: Schematic of *remo*TES and light detector. In the *remo*TES, the TES is deposited on a wafer, which is separated from the absorber crystal. The coupling between the absorber and the TES consists of a Au-pad glued on the absorber surface and connected to the TES by two Au-wire bonds [137]. The TES of the light detector is deposited directly onto the SOS light absorber.

The absorber is a NaI-crystal grown by the Shanghai Institute of Ceramics (SICCAS). A Au-pad, cut from an ingot, is glued on the absorber with Epo-Tek 301-2, a two component low out-gassing epoxy resin [183]. The Au-pad is coupled to the TES wafer with two Au-wire bonds, as indicated in Fig. 6.2. A zoomed picture of the *remo*TES coupling to the absorber is shown in Fig. 6.2 (**Right**). An ohmic heater, fabricated on a Si pad, is glued with Epo-Tek 301-2 on the surface of the NaI-absorber to inject heater pulses into the crystal. A ^{55}Fe X-ray source with an activity of 3 mBq is taped to the copper holder facing the NaI-absorber and irradiating it from the side as indicated in Fig. 6.2 (**Left**). The TES wafer is made from Al_2O_3. The TES is a thin W-film and features two aluminum bonding pads for the connection to the bias circuit. The Au-wires from the Au-pad are bonded onto a second pad, with the Au-bridge design as highlighted in Sec. 5.4.2. A Au-thermal-link is used to connect the TES to the thermal bath. A Au-heater deposited on the wafer surface, is used to inject heater pulses to monitor the temperature of the TES, map its linear range and allows for the monitoring of its stability over the complete data-taking.

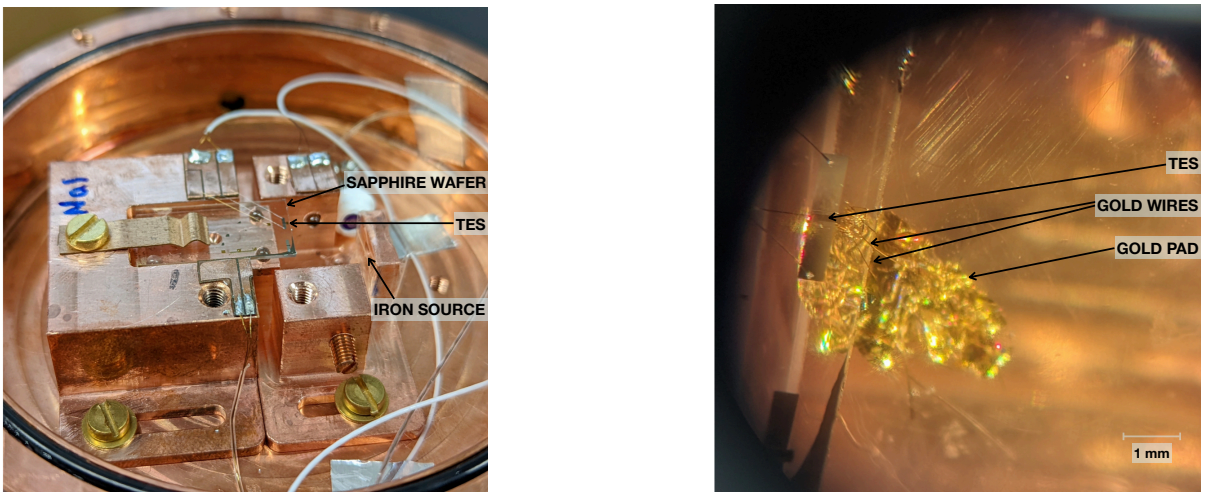

Figure 6.2: Left: The *remo*TES wafer mounted in the copper holder. The sapphire wafer is placed on sapphire balls and held by a bronze clamp. A ^{55}Fe source is taped on a copper piece facing the absorber for the purpose of energy calibration; **Right:** Microscopic view of the Au-pad glued on the NaI-crystal and the wire bonding to the *remo*TES.

The light detector is a SOS wafer, equipped with a W-TES which has two phonon collectors (Al/W bilayers) [184]. It is mounted on the lid of the copper holder, which is used to protect the NaI from humid air. The light detector is irradiated with a second ^{55}Fe calibration source of similar activity as the one shining on the absorber. A picture of the light detector and an enlarged view of the wire bonding of its TES are shown in Fig. 6.3. In the following, we refer to the NaI-*remo*TES as the phonon detector (PD) and the light detector (LD) as the light channel, interchangeably. The description of the detector components is summarized in Table 6.1.

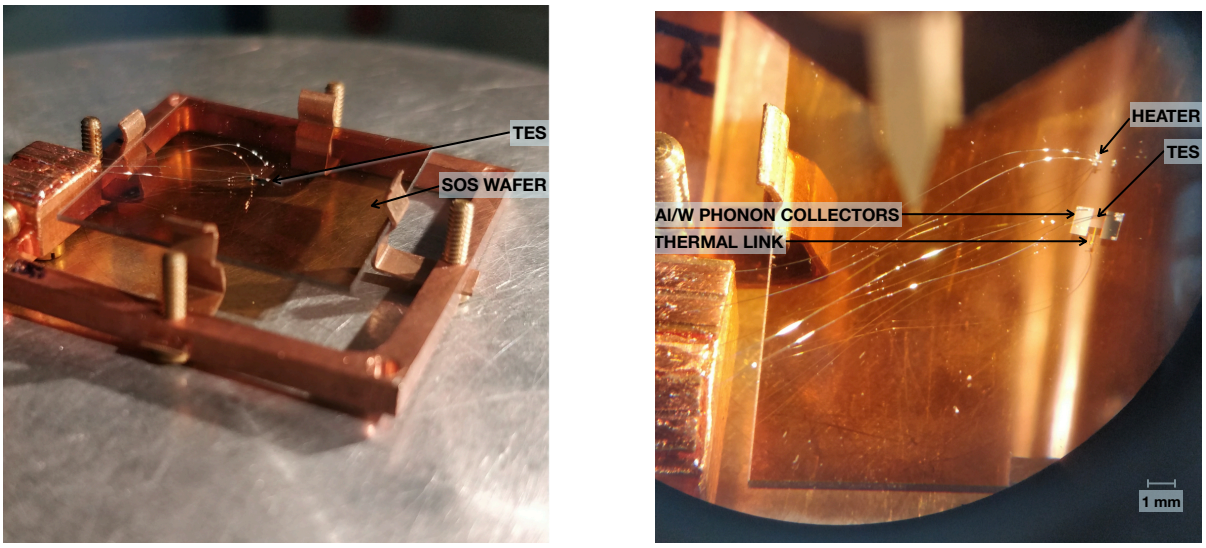

Figure 6.3: Left: SOS light detector mounted in a copper holder; **Right:** Microscopic view of the electrical connections of the light detector TES and of its separate ohmic heater.

Table 6.1: Summary of phonon detector (PD) and light detector (LD) component properties. RRR: residual resistivity ratio.

	Component	Properties
PD	NaI-absorber	(10×10×10) mm^3
		Mass: 3.7 g
	Au-pad on NaI	Area: 4 mm^2
		Thickness: 1 µm
		RRR: ~ 22
	Two Au-wires	Lengths: (6.7, 10.3) mm
		Diameter: 17 µm
	W-TES on wafer	Area: (100×407) $µm^2$
		Thickness: 156 nm
	Al_2O_3 wafer	(10×20×1) mm^3
	Thermal link	Resistance (300 K): 82.3 Ω
LD	SOS wafer	(20×20×0.4) mm^3
	W-TES on SOS wafer	Area: (284×423) $µm^2$
		Thickness: 200 nm
	Phonon collectors	Al/W bilayers
		Area: (526×1027) $µm^2$
		Thickness: 1 µm

6.2 Experimental Results and Discussion

6.2.1 Data Taking

The measurement was carried out in an above-ground wet dilution refrigerator at the Max-Planck-Institut für Physik in Munich. The cryostat is equipped with four superconducting quantum interference devices (SQUIDs) from the APS company [178] and continuously read out with a 16-bit analog-digital converter at a sampling frequency of 50 kS/s. To reduce the background event rate induced by cosmic and ambient radiation, a lead wall with a thickness of 10 cm was built around the refrigerator. Three subsequent datasets were recorded and are discussed in this work: a background dataset with only the (module-internal) ^{55}Fe sources present, a ^{57}Co calibration dataset, and an additional neutron calibration dataset using an AmBe source. The duration and effective exposure of each dataset are given in Table 6.2.

Table 6.2: Measuring times, raw exposure, event rates (counts above threshold) and calibration sources for the three datasets. The dataset where only the ^{55}Fe source was present is used as a background dataset. The ^{55}Fe source is not visible in the data as it is below the energy threshold.

Measuring time (h)	Calibration sources	Event rate (cps)	Exposure (g d)
17.73	^{55}Fe, ^{57}Co	0.57	2.73
16.40	^{55}Fe, AmBe	0.62	2.53
24.61	^{55}Fe	0.37	3.79

6.2.2 Data Analysis

For the three datasets discussed above, the continuous stream from the phonon channel is triggered in software using an optimal filter trigger (cf. Ref. [181] and Ref. [179]). The light channel is passively read out in parallel. The filter is created from a parametric description of the NaI channel pulse shape based on Ref. [141] and a noise power spectrum obtained from randomly drawn empty noise traces. The typical pulse shape of absorber recoils for the NaI channel is shown in Fig. 6.4 and features a very long decay time.

Both channels are calibrated using the 122 keV peak visible in the ^{57}Co dataset. The result is illustrated in Fig. 6.7, where also additional γ lines due to ^{57}Co are highlighted for comparison. Peaks from the ^{55}Fe source could not be observed, as their energies of 5.9 keV and 6.4 keV are below the energy threshold in both phonon and light channel. The optimum filter amplitude is used as energy estimator. In the energy range from threshold up to ~500 keV, we see no change in the pulse shape of the phonon channel, and no saturation effects, indicating an overall linear detector performance.

A baseline energy resolution of the phonon channel of (2.07±0.01) keV is determined by superimposing the pulse shape onto a set of randomly drawn empty baselines and reconstructing these artificial events. The deviation from the nominal injected energy is illustrated in Fig. 6.5. The baseline resolution of the SOS light detector for events which

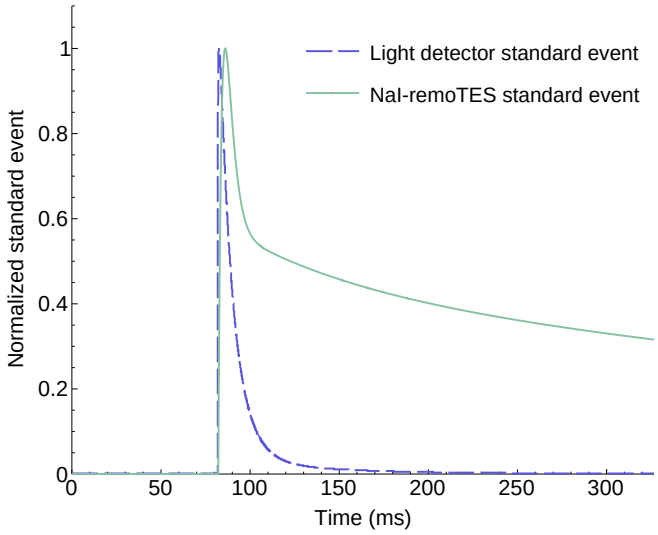

Figure 6.4: Normalized averaged pulses in the light detector (dashed, dark-blue curve) and in the NaI-*remo*TES detector (solid, water-green curve). A cleaned sample of non-saturated events from the Co57 dataset was used for averaging.

generate scintillation light in the absorber was determined to be (2.02±0.05) keV_{ee} using the same technique. All datasets were triggered in software with a threshold of 10 keV in the phonon channel.

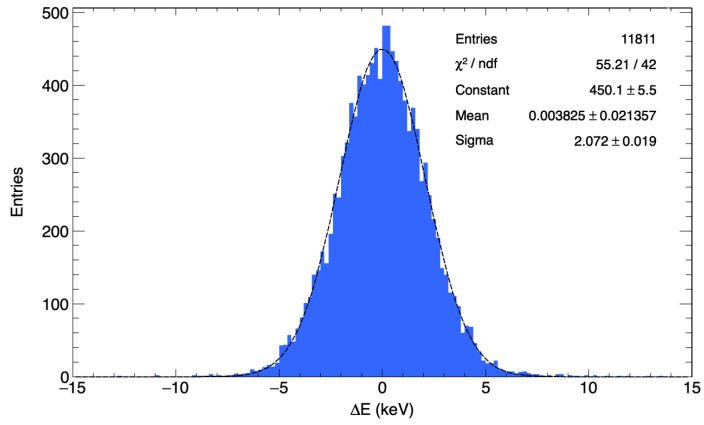

Figure 6.5: Deviation of reconstructed energy from nominal energy for simulated events, obtained by superimposing scaled averaged signal pulses onto empty traces for the phonon channel.

Each dataset was cleaned by applying a set of quality cuts: Severely unstable detector operation intervals are removed by monitoring the reconstructed amplitude of injected heater pulses over time. Single voltage spike events are removed by cutting on the ratio of the numerical derivative of the pulse to the baseline RMS. The RMS from the optimal filter reconstruction and the RMS from an additional truncated averaged pulse fit reconstruction (cf. e.g. Ref. [185]) are used to remove pile-up events and events from particle interactions in the sapphire wafer. The effect of each quality cut is assessed by simulating pulses with an

exponentially decreasing energy spectrum on the set of randomly drawn detector baselines and studying the fraction of surviving events as a function of the simulated energy. Fig. 6.6 shows the overall survival probability for signal events in the analysis obtained from the background dataset. We find that the detector threshold of 10 keV is only nominal, i.e. only few simulated signal events survive down to this energy. This is due to varying noise conditions in the above-ground setup, very long pulse decay time resulting in pile-up, and the presence of particle recoils in the wafer, which require strong quality cuts to be discarded. An analysis threshold of 20 keV is used in the following, where the signal survival probability is still about 20%. Above this threshold, no wafer-induced events or noise events are observed in the background dataset.

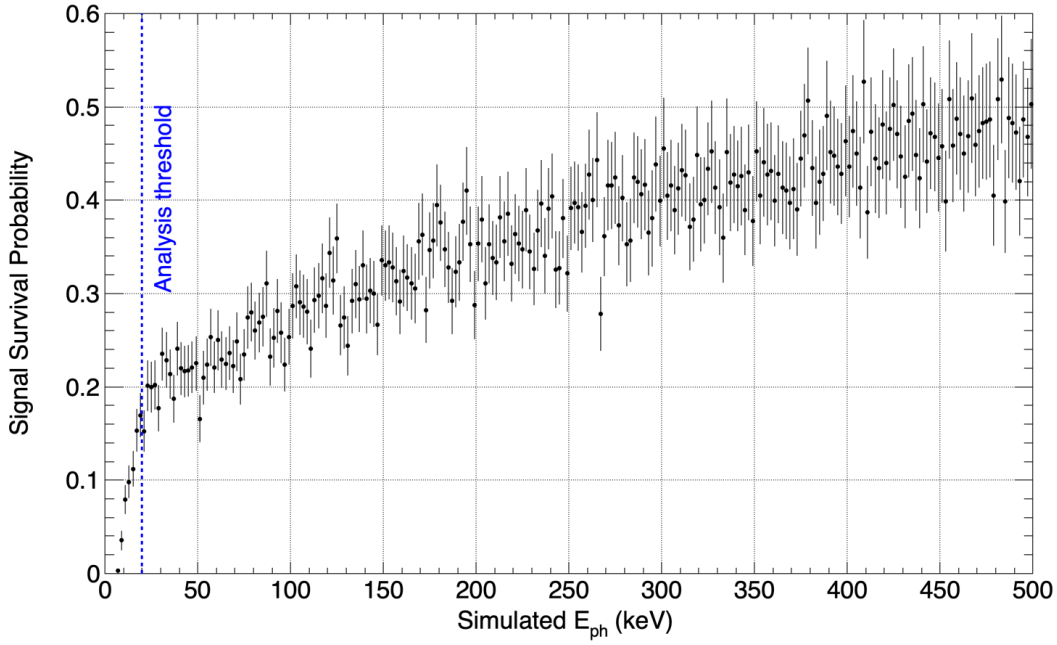

Figure 6.6: Survival probability for simulated events in the analysis chain, estimated using the background dataset. An exponentially decaying energy spectrum was simulated to allow for better statistics at low energies. Statistical uncertainties are indicated for each energy bin. The analysis threshold at an efficiency of 20% is marked by a dashed blue line.

6.2.3 Discrimination of Nuclear Recoil Bands

The light yield (LY) is defined as the ratio between the electron-equivalent energy measured in the light channel and the energy measured in the phonon channel for each event. It enables the discrimination of different recoil event classes. In Figs. 6.8 and 6.9 the LY is shown as a function of the phonon channel energy for the background and the neutron calibration datasets, respectively. The phonon channel energy E_{ph} is used here as an approximation of the total recoil energy per event $E_t = \eta \cdot E_L + (1 - \eta) \cdot E_{ph}$, to which the light channel energy E_L only contributes a small fraction, as the scintillation efficiency η is typically on the order of a few percent. We fit an empirical description based on [186] to the datasets in an unbinned likelihood approach, containing parameters for the combined e^-/γ

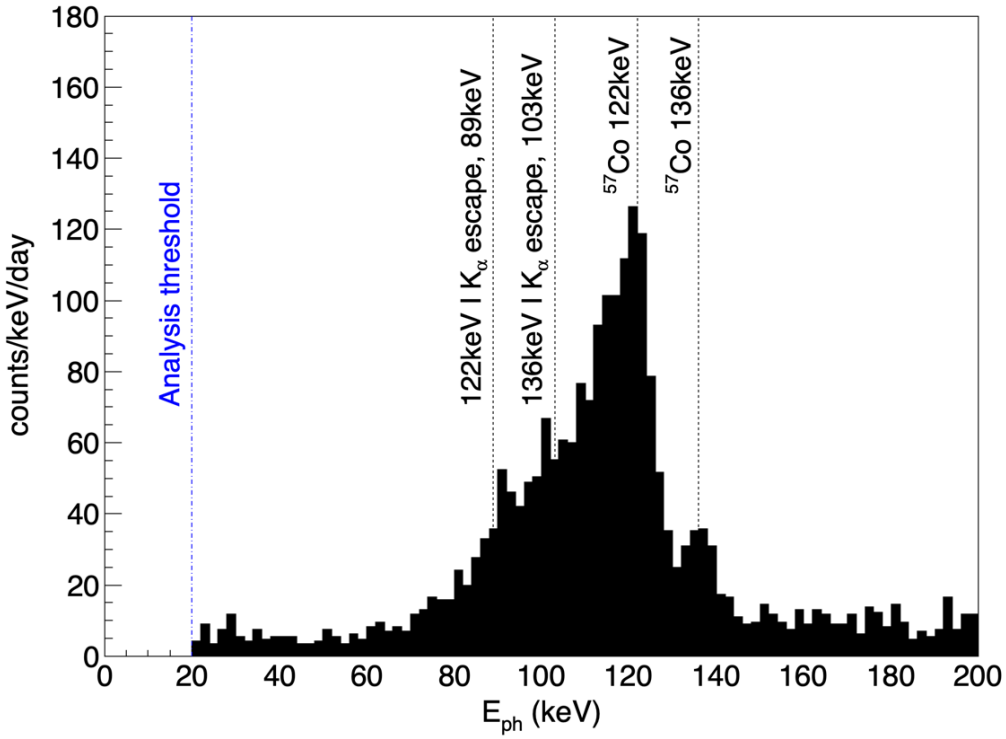

Figure 6.7: Energy spectrum from the ^{57}Co γ calibration measurement. A constant conversion factor from pulse amplitude to energy was extracted by fitting a gaussian function to the right shoulder of the 122 keV, and used to calibrate the spectrum. The additional ^{57}Co 136 keV peak and two γ escape peaks due to I K-α, expected at around 88.8 keV and 102.8 keV, are used to cross-check the result. The latter deviate by about 2% from their nominal value.

band, the Na and I nuclear recoil bands, and the energy spectra in each band. The gaussian width of the LY bands as a function of energy is given by the energy dependent resolutions of the two channels. These are described by second degree polynomials, where the constant is given by the phonon and light channel resolutions at threshold, and the remaining coefficients are fitted. The mean line of the e^-/γ band is allowed to vary linearly with phonon energy. Relative to the e^-/γ mean line $\overline{L}$, the mean lines of the Na and I bands are defined by $\overline{N}_i = Q_i \cdot \overline{L} \cdot (1 - (q_{0,i} \cdot exp(-\frac{E}{q_{1,i}})))$ with the constant quenching factors Q_{Na} and Q_I at high energies, and an exponential non-proportionality at low energies. For events in the electron band, the LY is normalized to 1 by definition, as both channels were calibrated using the 122 keV γ peak from the ^{57}Co source. The spectral description of events in the e^-/γ band consists of a constant and a linear term plus a compton scattering contribution. The compton part is empirically described as $p_0 \cdot exp(-E \cdot p_1) \cdot (p_2 \cdot E - \frac{p_3}{E})$, where p_i are fit parameters, and originates from cosmogenic ionized particles inducing secondary electrons which in turn produce bremsstrahlung seen by the detector. Consequently, this part is assumed to be the same for neutron and background dataset, while the other contributions are determined separately for both, as the AmBe neutron source introduces additional e^-/γ background. Nuclear recoil spectra in the neutron calibration dataset are described with an exponential spectrum $p_{0,i} \cdot exp(-\frac{E}{p_{1,i}})$ each, where $p_{0,i}$ and $p_{1,i}$ are fit parameters. A detailed motivation and description of the parametrization will be addressed in a future

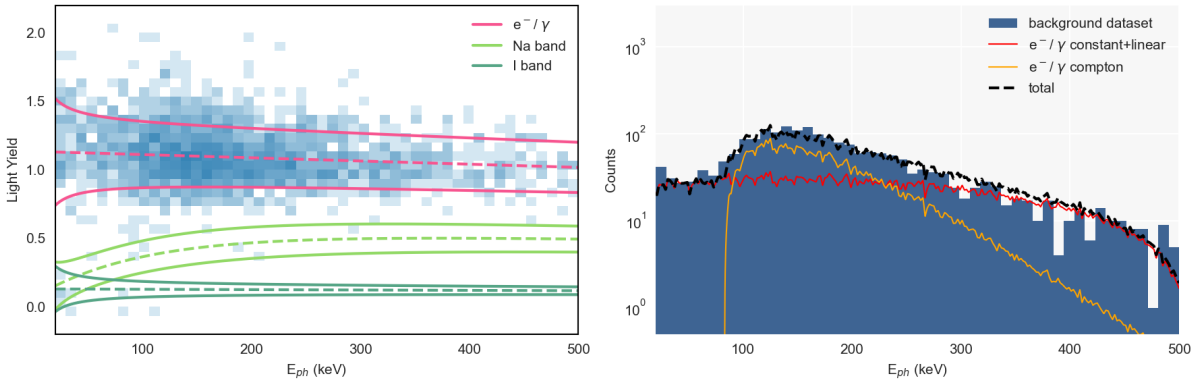

Figure 6.8: Left: 2D histogram of LY versus phonon channel energy for the background dataset with color-coded number of entries; **Right:** Energy spectrum of the background dataset. Different contributions are highlighted.

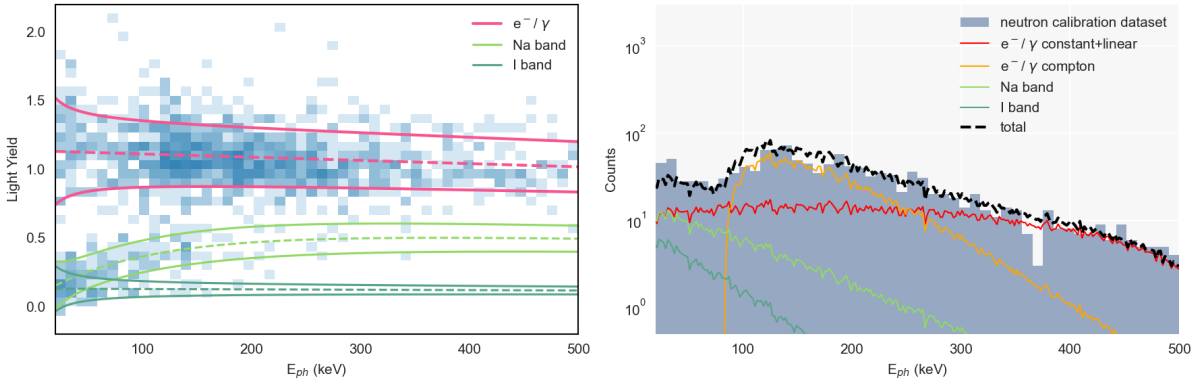

Figure 6.9: Left: 2D histogram of LY versus phonon channel energy for the neutron calibration dataset with color-coded number of entries; **Right:** Combined energy spectrum of the neutron calibration dataset. Different contributions from the recoil bands are indicated with their respective color. Additionally, the compton contribution to the e^-/γ spectrum, determined from the background dataset, is highlighted in orange.

publication [187].

Figs. 6.8 and 6.9 also show the result of the likelihood fit for the two datasets. 90% boundaries are drawn for the e^-/γ and Na/I nuclear recoil bands. It can be clearly seen that two new populations of events appear below the e^-/γ band in the neutron calibration dataset, far outside the 2σ boundary, which are well described by the nuclear recoil band description introduced above. In the spectrum (Fig. 6.9 right panel), the number of nuclear recoil events is similar to the amount of e^-/γ background events below ≈100 keV. The additional bands are quenched in LY, where the constant quenching factors are $Q_{\mathrm{Na}} = 0.489 \pm 0.072$ and $Q_{\mathrm{I}} = 0.115 \pm 0.013$, and the LY appears to be decreasing below ~150 keV as the recoil energy approaches the threshold. In Ref. [188], a similar decline of the quenching factor in NaI at lower energies was reported for measurements at room temperature and with Tl-doped crystals. However, non-proportionality to the e^-/γ mean line at low energies may also be explained simply by a low number of scintillation photons, which results in poisson-distributed rather than gaussian-distributed LY. At increasing phonon channel energy, a slight downward tilt of the e^-/γ band is visible, which is due to increasing

non-linearity of the light detector response. A small number of nuclear recoils is also observed in the background dataset, and visible in Fig. 6.9. These are due to neutrons from the lead wall surrounding the cryostat. In all bands, the event density decreases at low energies due to decreasing survival probability in the analysis (cf. Fig. 6.6), which is accounted for in the fit. As this survival probability was obtained from the background dataset, the higher overall event rate (i.e., more dead time) in the neutron calibration data results in a small overestimation of the e^-/γ and nuclear recoil spectra in Fig. 6.9. The total number of events in the neutron calibration dataset is 1296, where the fit expects 1378. The background dataset contains 2118 events, 2076 of which are accounted for.
The scintillation efficiency η of the crystal could not be determined in this measurement. This parameter could be estimated from γ peaks, which should appear slightly tilted in the LY vs E_{ph} plane due to the difference between E_{ph} and E_t [189]. Unfortunately, the ^{55}Fe peaks are below threshold here, and the ^{57}Co spectrum is too complex to reliably extract this information.
In future measurements and in the final COSINUS design, particle discrimination will be further improved by using low-mass Si beakers as light detectors. These will fully surround the NaI crystal, and thus feature much better light collection efficiency [190] and resolution than the SOS wafer.

6.3 Conclusions

This measurement marks the first proof of event-by-event particle discrimination in a cryogenic NaI detector. We operated a COSINUS prototype with a *remo*TES sensor, which displayed a baseline resolution of 2.07 keV despite suboptimal, above-ground conditions. It was calibrated with a ^{57}Co γ source and analyzed with a nuclear recoil threshold of 20 keV. Particle discrimination was verified with neutrons from an AmBe source. In Ref. [137], the *remo*TES design was suggested as an improved readout for delicate absorber materials, which are for example hygroscopic or feature a low melting point. This work shows that the design is indeed suitable for NaI absorbers. The next step in the COSINUS detector optimization strategy in the direction of achieving an energy threshold of 1 keV is an underground measurement with a similar detector, in order to assess its performance in a low-background environment. This measurement is the focus of the subsequent sections.

6.4 First Underground Test

The study reported here describes an improved detector design operated in an underground cryostat at LNGS, yielding the best energy resolution achieved by a NaI-based detector for nuclear recoils at the time of publication. Sec. 6.4.1 describes the detector module design, which includes a NaI phonon channel with *remo*TES readout and a silicon (Si) light channel with TES readout. Sec. 6.4.2 details the experimental setup and DAQ used for data taking and Sec. 6.4.3 describes a simulation done with GEANT4 to estimate the expected neutron rate during calibration periods. In Sec. 6.5 and 6.6, the collected data are analyzed, and the resulting DM-nucleon scattering cross-section limit for this measurement is presented.

6.4.1 Detector Module

The detector module consists of two independent channels: a NaI absorber operated as a cryogenic calorimeter (phonon channel) and a light absorber to detect the corresponding scintillation photons generated by a particle interaction in NaI (light channel). A schematic breakdown of the module is depicted in Fig. 6.10 and 6.11.

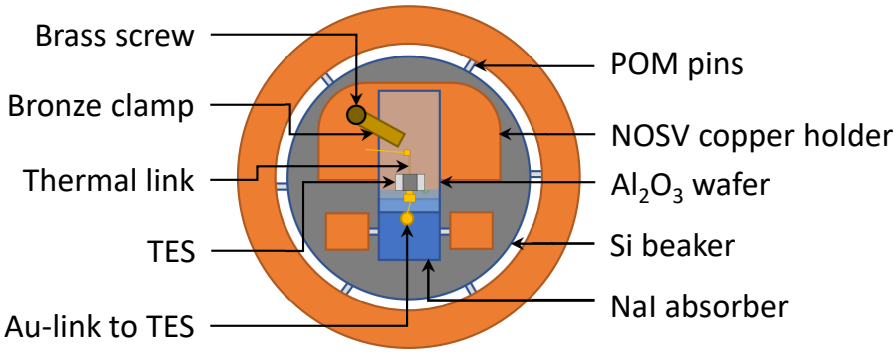

Figure 6.10: Top view of the detector module.

The phonon channel consists of a 3.67 g NaI crystal mounted in a holder fabricated from electrolytic tough pitch (NOSV) Cu [138]. The NaI crystal was grown by SICCAS with a modified Bridgman technique as described in [111] using "Astro-Grade" powder procured from Merck group [112]. ICP-MS measurements performed at LNGS [113] revealed an internal contamination at a level of 6-22 ppb for ^{40}K and <1 ppb for ^{208}Th and ^{238}U. The crystal used for this particular measurement had a Tl-dopant level of 730 ± 73 ppm.

The crystal rests on a trio of Al_2O_3 balls to thermally insulate it from the Cu holder. Two additional support tips made out of polyoxymethylene (POM) fix the crystal's position. An ^{55}Fe X-ray source with an activity of 0.11 Bq is taped onto the Cu holder such that it irradiated one of the faces of the crystal. The resultant K_α and K_β lines are used to calibrate the detector response in the offline analysis. The *remo*TES scheme, outlined in [136] and implemented in [137], utilizes a Au-link for signal read out via the TES from

particle interactions within the absorber. For the present study, this link consists of a Au-pad adhered to NaI, with a thin Au-wire connecting the pad to the Au-port on the TES (based on the Au-bridge design). All components of the phonon channel and their properties are shown in Table 6.3. The TES consists of a W-based superconducting thin-film evaporated onto a Al_2O_3 wafer using infrastructure and technology of the CRESST group at MPP in Munich, Germany. A Au stripe (thermal link) connecting the TES to the thermal bath is used for weak thermal coupling (65 Ω at room temperature) to slowly dissipate heat. An ohmic heater film was deposited onto the wafer to adjust the TES-temperature to the optimal operation point. Externally injected "test pulses" at regular intervals via the heater serve to precisely measure the detector response over its entire dynamic range and to monitor potential changes with time.

Table 6.3: Properties of the phonon channel.

Component	**Properties**
NaI absorber	Volume: (10x10x10) mm^3
Au-link	Au-pad on NaI
	Area: 1.77 mm^2
	Thickness: 1 μm
	Glue: Epo-Tek 301-2 [183]
	Au-wire
	Length: ~ 10 mm
	Diameter: 17 μm
Al_2O_3 wafer	Volume: (10x20x1) mm^3
W-TES on wafer	Area: (100x400) μm^2
	Thickness: 156 nm
	T_C: 28 mK
Heater on wafer	Area: (200x150) μm^2
	Thickness: 100 nm gold

Assembly of the module took place in a moisture-regulated nitrogen glovebox (< 50 ppm) to avoid degradation of the NaI(Tl) crystal.

With the help of a Cu pillar, the Si beaker is positioned to enclose the NaI crystal as depicted in Fig. 6.11. A photograph of the complete, dual channel system is shown in Fig. 6.12.

To collect the scintillation light, a beaker-shaped Si crystal with a mass of 15.38 g was used. It was mounted on a separate Cu frame with the help of six POM tips (applying even pressure from all sides). An ^{55}Fe X-ray source with an activity of 3.3 mBq was taped onto the Cu holder to irradiate the beaker. A W-TES was deposited directly on the Si beaker. To efficiently collect athermal phonons and deliver their energy, it is flanked by two superconducting aluminium phonon collectors [191]. A thermal link (15.8 Ω at room temperature) and a separate heater were also deposited on the Si beaker, similar to the scheme described for the phonon channel TES. All components of the light channel and their features are shown in Table 6.4.

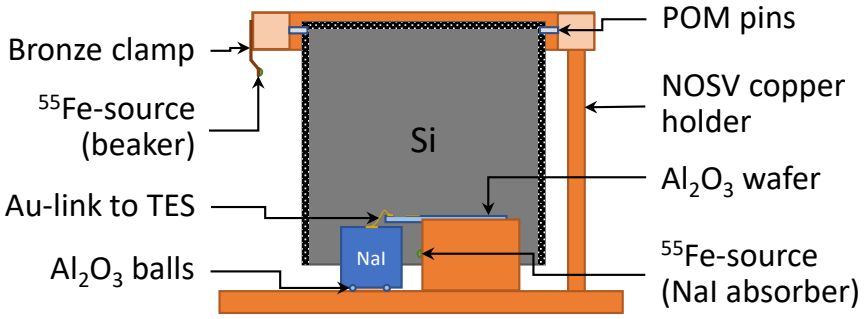

Figure 6.11: Cross-sectional view of the detector module.

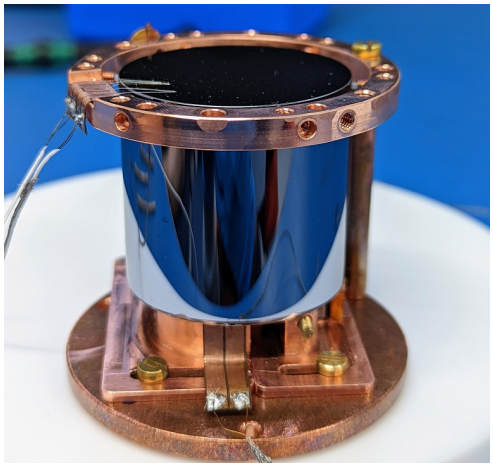

Figure 6.12: Photograph of the assembled detector module, consisting of the phonon and light channel.

Table 6.4: Properties of the light channel.

Component	Properties
Si-absorber	Hollow cylinder
	Height: 40 mm
	Outer diameter: 40 mm
	Thickness: 1 mm
W-TES on Si	Area: (100x400) µm^2
	Thickness: 80 nm
	T_C: ~18 mK
Heater on Si	Area: (200x150) µm^2
	Thickness: 100 nm gold

6.4.2 Measurement Setup and DAQ

The measurement was carried out at LNGS in a ^{3}He/^{4}He-dilution refrigerator of type MINIKELVIN 400-TOF from Leiden Cryogenics B.V. [192] provided by the CRESST group of MPP. It is located underground in a side tunnel between hall A and hall B at LNGS

with an overburden of 3600 m w.e. [193]. Two SQUIDs manufactured by Applied Physics Systems (APS) [178] are used for signal amplification [194].

The refrigerator is equipped with an external Pb-shield with a thickness of 100 mm. A cylindrical internal radiation shield made from low-background lead (Pb) with a diameter of 90 mm and a thickness of 100 mm is mounted above the detector module. To decouple the sensors from vibrations, the detector module was appended on a bronze (CuSn6)-spring with a resonance frequency of a few Hertz. The thermalization of all parts was ensured by screwed Cu-wire connections to the mixing chamber. A photograph of the mounting scheme is shown in Fig. 6.13.

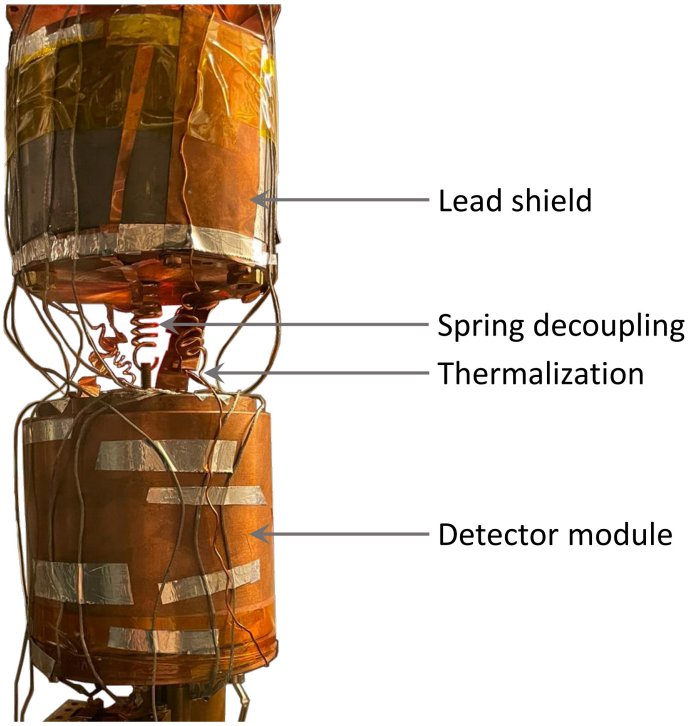

Figure 6.13: Photograph of the detector module mounted onto the mixing chamber of the dilution refrigerator.

The detector signals were read out in parallel with two separate systems at a sampling rate of 50 kS/s, a commercial, hardware-triggered DAQ and a continuous DAQ. To set up and stabilize the detectors, the hardware-triggered DAQ was used. In total about ten days of stream data were taken over the first two weeks of June, 2022. Sixteen hours were measured with an external ^{57}Co γ-source (122 keV) with an activity of 430 Bq located inside the external lead-shield. About twenty six hours were measured with an AmBe neutron-source with an activity of 2000 Bq located outside the external lead-shield. With a background data-taking period lasting for 76 h, an overall exposure of 11.6 g d was collected.

6.4.3 Simulation Study

To estimate the expected neutron interaction rate in the phonon channel for the measurement with the AmBe source, a GEANT4 (v11.0) based simulation [119–121] of the setup was

carried out. The simulated geometry includes the detector module, the vacuum chambers and helium bath of the refrigerator and the external lead shield. A top view of the setup as implemented in the software is shown in Fig. 6.14.

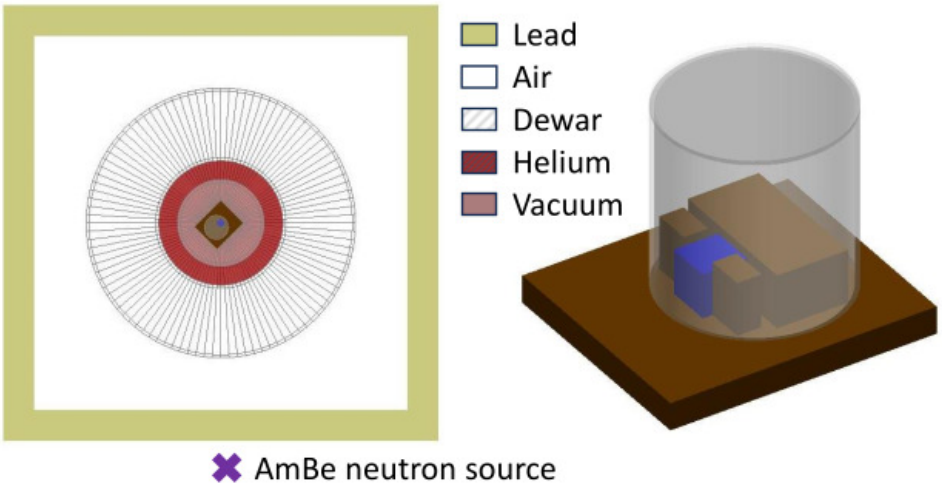

Figure 6.14: Geometry as simulated in GEANT4. **Left:** top view on the refrigerator; **Right:** 3D view of the simulated detector module.

In the simulation an isotropically emitting, point-like neutron source with an activity of 2000 neutrons/s was placed outside the external lead shielding, including an additional 1 cm of polyethylene between the external Pb-shield and the source. The height of the source was varied in 5 cm increments to the detector plane, as the source's precise position with respect to the detector module could not be determined during the run. For each position of the neutron source, five simulations with different seeds were computed. The expected position-dependent neutron rate above a given threshold can then be calculated from mean and standard deviation of these five simulations. To validate the data analysis, the simulated neutron rate can be compared to the measured rate in an energy range which is clearly above threshold (8 keV). The measured neutron rate is calculated by subtracting the rate in the background files, after analysis cuts (described in the next section), from the rate of the neutron calibration data after analysis cuts. The rates from simulation and measurement agree and are displayed in Fig. 6.15.

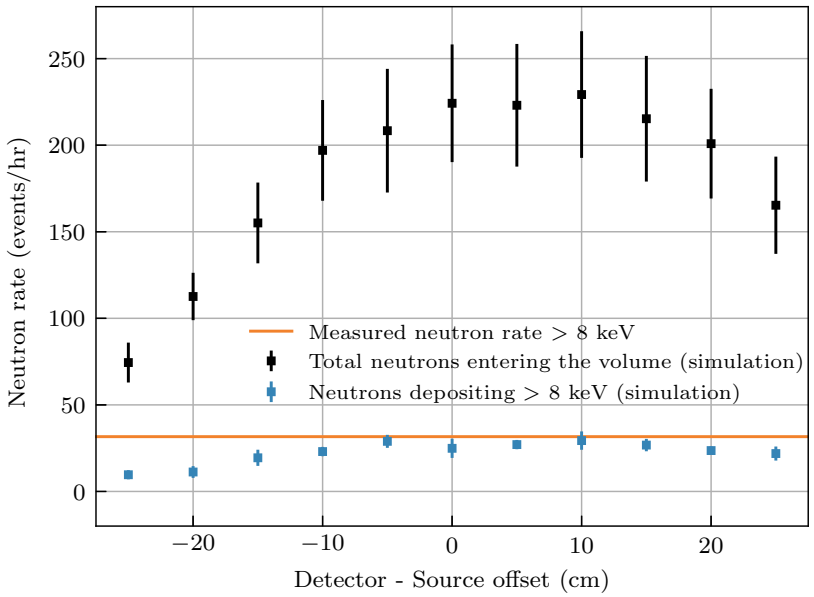

Figure 6.15: Simulated and measured neutron rate in the phonon channel.

6.5 Data Analysis

6.5.1 Raw Data Analysis

The data used in the subsequent analysis was acquired with the continuous DAQ system, using offline triggering with an optimum filter (OF) trigger on the continuous stream [181]. Two components are needed to calculate the OF for each channel: a representative noise power spectrum (NPS) of the detector, and the pulse shape of the events of interest in the respective channel. For the detector NPS, several hundred empty and cleaned noise traces were collected from the hardware-triggered (HWT) background data, and their respective NPS were averaged. From the same HWT background data, a common set of pulses for both channels is selected from a narrow energy region, summed up, and re-scaled to get a first estimate of the so-called standard event (SE). The SEs are then fitted with the pulse model described in [142] to eliminate any remaining noise. In a *remo*TES-detector, we expect different pulse shapes attributed to different detector parts [137]. As we are interested in recoil events taking place in the NaI crystal, we use only *absorber events* for generating the SEs and in the subsequent analysis steps. The trigger threshold was determined employing the method described in [195], using empty and cleaned noise traces from the HWT data. With the criterion of one noise trigger per kg d exposure, we fix the trigger threshold at 2 mV in the phonon and 6 mV in the light channel.

A set of quality cuts was applied, aiming to discard pulse shapes different from the SE, artifacts caused by interference, as well as noise triggers. The majority of these cuts only affect the phonon channel. The OF amplitude is used to reconstruct the amplitude of the pulses. Moreover, the amplitudes are corrected for small drifts in the detector response over time using the test pulses.

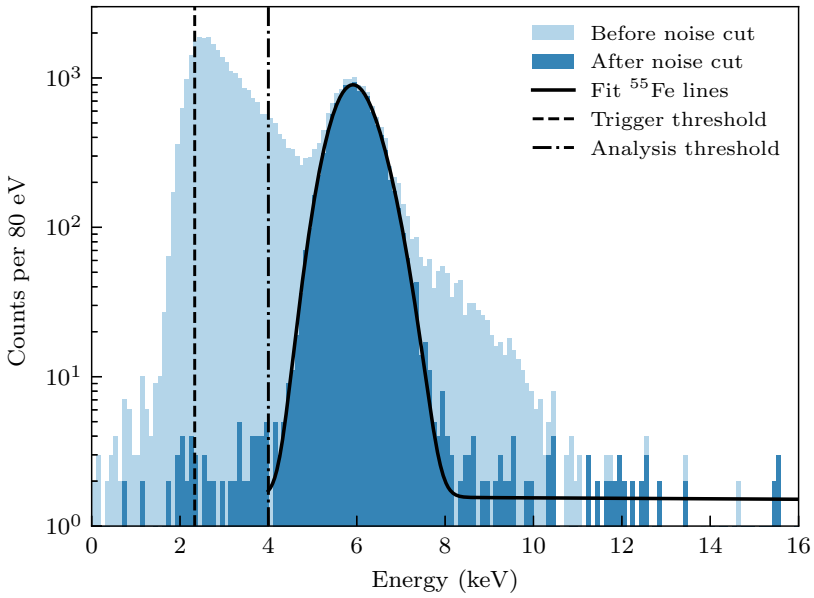

Figure 6.16: The energy spectrum of the background data set below 16 keV before (light blue) and after the noise-leakage removal cut (blue). The black dashed line marks the threshold used for the optimum filter trigger, and the black dashed-dotted line the threshold that was used in the subsequent analysis steps. A fit to the the ^{55}Mn K_α (5.89 keV) and K_β (6.49 keV) lines gives the solid black line, yielding a resolution of the detector at these energies of 0.450 ± 0.007 keV.

We want to describe one cut performed on the phonon channel in more detail. Although the software trigger thresholds determined above should ensure only minimal leakage of noise events over the threshold, there is a significant accumulation of events visible in the phonon channel close to the triggering threshold, shown in Fig. 6.16. Due to the non-gaussian shape of this noise distribution, we assume that the method in [195] is not entirely applicable to our prototype measurement, and the point of one noise trigger per kg d would be at a higher voltage. At low energies, one expects that the reconstruction of a true particle pulse amplitude with an optimum filter should yield the same result as fitting a SE to the pulse. To remove the noise leakage and maintain a low analysis threshold, we compare these two amplitudes for the pulses in the phonon channel and disregard any events where the values differ more than 20%. As can be seen in Fig. 6.16, this cut removes the majority of noise events, while leaving events from the iron line untouched.

The energy calibration in both channels is performed by fitting a double Gaussian peak to the ^{55}Mn K_α (5.9 keV) and K_β (6.5 keV) lines of the built-in ^{55}Fe X-ray sources (see also Fig. 6.16). As the iron lines are close to threshold in both light and phonon channel, an additional calibration was performed with a ^{57}Co γ-source (122 keV). A slight non-linearity between the two points of calibration was observed, which can be attributed to a non-linear detector response at high deposited energies. For energy depositions above a certain magnitude, the connected TES can be heated up close to its normal conducting phase. Since the transition curve of the TES flattens at this point, the resulting pulse shape is distorted and amplitude reconstruction with the optimum filter becomes infeasible. In order to avoid energies outside the linear range of the detector, we limit the region of interest (ROI) to a maximum energy of 200 keV in both channels.

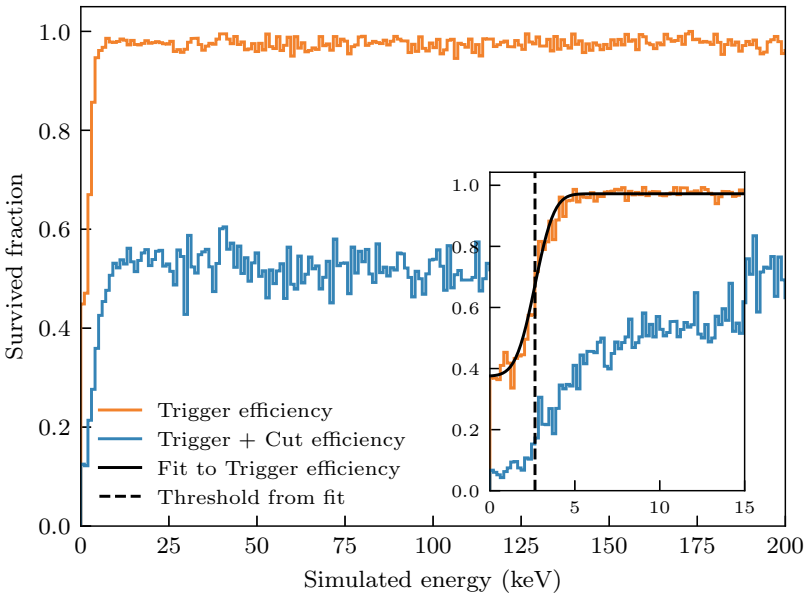

Figure 6.17: The orange line shows the trigger efficiency, the blue line the trigger and cut efficiency as determined from simulated pulses. In the inset we show a zoom-in to lower energies, showing also an error function fit to the trigger efficiency (solid black line), which can be used to estimate the detector threshold to 2.656 ± 0.041 keV (dashed black line).

The cuts described aim at eliminating only artifacts, noise, and pulses of shape different from the events of interest. However, there is still an energy-dependent probability of whether a valid event passes the triggering procedure and the subsequent analysis steps. We evaluate the trigger and cut survival probabilities by applying the whole analysis chain to 𝔒 (10000) artificial events. In Fig. 6.17 we illustrate the results of this procedure. We show the binned fraction of triggered artificial events in the phonon channel, after removing artificial pile-ups, in black, and the fraction of events additionally surviving the subsequent analysis chain in blue. An extended error function is fitted to the trigger efficiency (orange line)

$$\mathrm{eff}_{\mathrm{trigger}}(E) = c\left((1-\epsilon)\times 0.5\,\mathrm{erf}\left(\frac{(E-t_p)}{\sqrt{2}\sigma}\right)+\epsilon\right), \tag{6.1}$$

where c, ϵ, σ and t_p are free parameters. The fit resulted in a detector threshold of t_p = 2.656 ± 0.041 keV.

To determine the baseline resolution we superimpose the SE particle template upon cleaned, empty noise traces picked at random times from the full stream. Fitting a Gaussian to the distribution of the filtered amplitudes of these simulated events estimates the resolution as σ_p = 0.3779 ± 0.0086 mV/ 0.441 ± 0.011 keV in the phonon and σ_l = 0.930 ± 0.021 mV/ 0.988 ± 0.052 keV electron equivalent ($\mathrm{keV_{ee}}$) in the light channel [195]. At approximately five times the baseline resolution, the above estimate of the threshold agrees well. For practical purposes of this prototype measurement, in all the following steps, we set the analysis threshold to E_{thr} = 4 keV, a value at which the cut efficiency has reached about

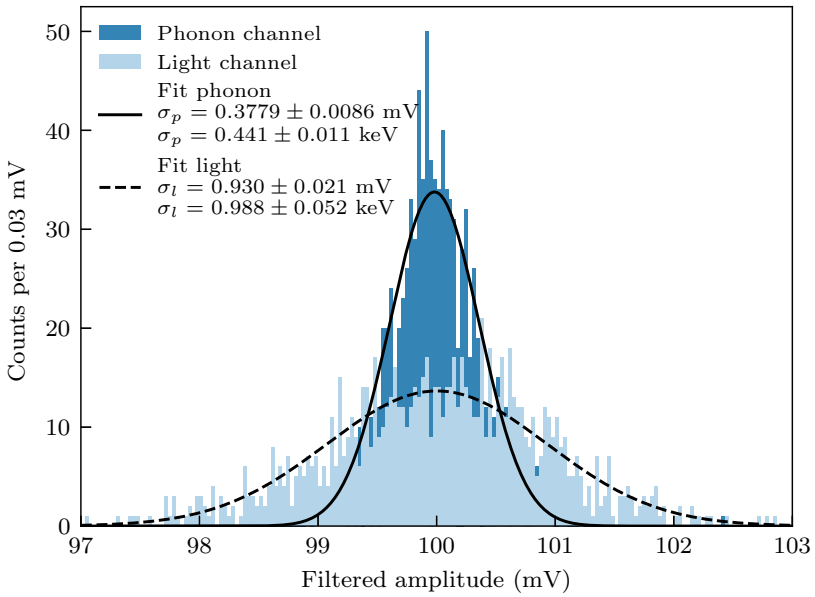

Figure 6.18: Histogram of the filtered amplitudes of simulated pulses in both phonon (blue) and light channel (light blue), used to determine the detector baseline resolutions. The solid/dashed line is a fit of a Gaussian to the phonon/light channel data, the width of which gives a measure of the baseline resolution.

50% of its plateauing value.

6.5.2 High-Level Analysis

For an event with light yield $LY = E_l/E_p \neq 1$, the energy in the phonon channel E_p is not a direct measure of the total energy deposited in the target crystal, as a fraction of the energy is dissipated into scintillation light E_l. As both phonon and light energy are measured, we calculate the total deposited energy as $E = \eta E_l + (1 - \eta)E_p$ [196]. The correct value of η is determined by gradually increasing η, applying the shift to the data, and fitting a double peak function to the iron lines in Fig. 6.16. The correct value for η is then the one, for which the fitted resolution of the iron lines is minimal. Minimizing the width of the calibration peaks is equivalent to correcting the tilt in the energy-light yield plane described in [196]. With this method, we estimate a scintillation efficiency η of 9.1% and a resolution of the detector at the position of the iron lines of 0.450 ± 0.007 keV which agrees with the baseline resolution. Following the results of the low-level analysis, the region of interest ROI is set to [4, 200] keV in total deposited energy E. Moreover, we restrict the light yield LY to [-10, 10].

The novel feature of COSINUS, compared to other DM searches with NaI target materials, is the combination of phonon and light signal which is used to discriminate between e^-/γ and nuclear recoil events via their different light yield. Fig. 6.19 displays the light yield vs. energy scatter plot for both background and neutron calibration data. The quenched nuclear recoil events in the neutron calibration are clearly separable from the bulk of the e^- and γ recoil events. In Fig. 6.20 this separation is illustrated down to low energies. Under

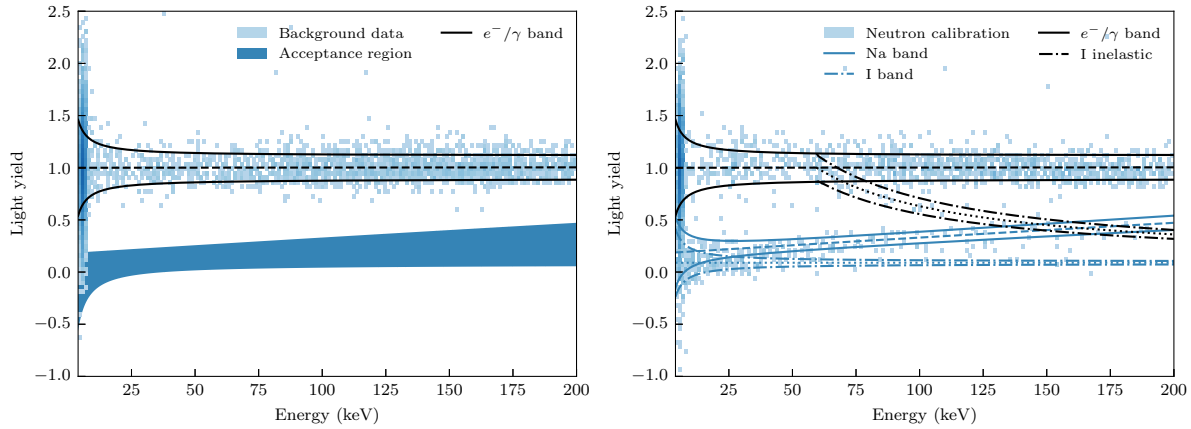

Figure 6.19: 2D Histogram of light yield vs. the total deposited energy for both background (left) and neutron calibration data (right). Both figures show the fit to the e^-/γ band (black) as found by the combined likelihood fit. Together with the neutron calibration data we also show the fit results for the nuclear and inelastic recoil bands. The blue-shaded region in the left panel marks the acceptance region for DM inference with the Yellin method.

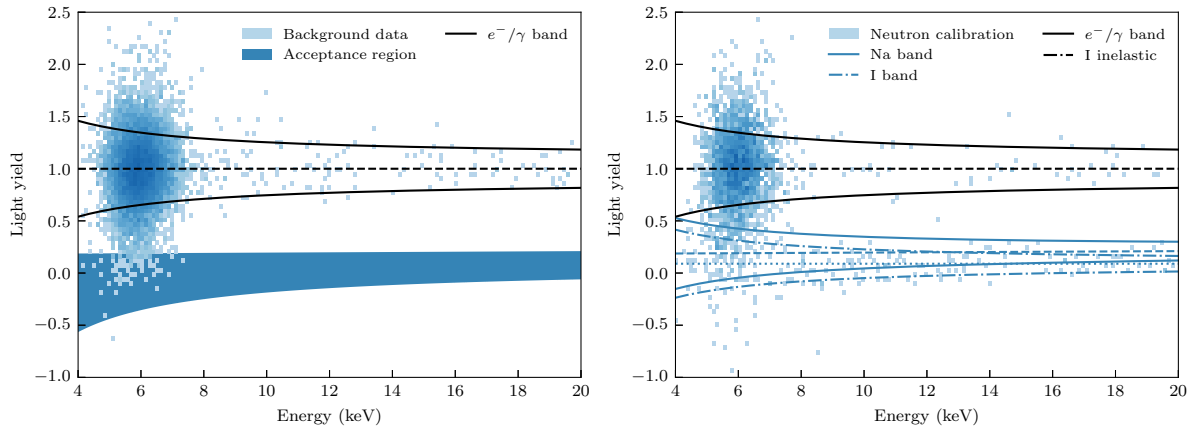

Figure 6.20: Zoom-in to low energies of Fig. 6.19.

the assumption that DM particles will mainly recoil off nuclei, the acceptance region for the DM analysis (employing Yellin's optimum interval method [197, 198]) is dependent on the position of the nuclear recoil bands in Fig. 6.19. The positions of the e^-, γ, and nuclear recoil bands are determined by an unbinned likelihood-fit to the whole data set (background and neutron calibration), in both phonon and light energy simultaneously. The parameterization of the energy spectra and quenching factors is based on [186]. The minimization of the total likelihood function was performed using *iminuit* [199], the Python implementation of the Minuit framework [200]. In addition to the light yield vs. energy plot in Fig. 6.19, Fig. 5.7 illustrates the performance of the fit in the context of the energy spectra. The selected background model consists of a decreasing flat background, the ^{55}Fe calibration lines (at 5.89 keV and 6.49 keV), elastic and inelastic nuclear scattering events, as well as a bump-like description of events caused by δ-electrons created by charged high-energy particles interacting with the surrounding of the detector (labeled "Compton" in Fig. 6.21). The model provides a reasonably good representation of the measured data. We want to note that a full model necessitates further studies and simulations to better

understand the possible backgrounds associated with the detector.

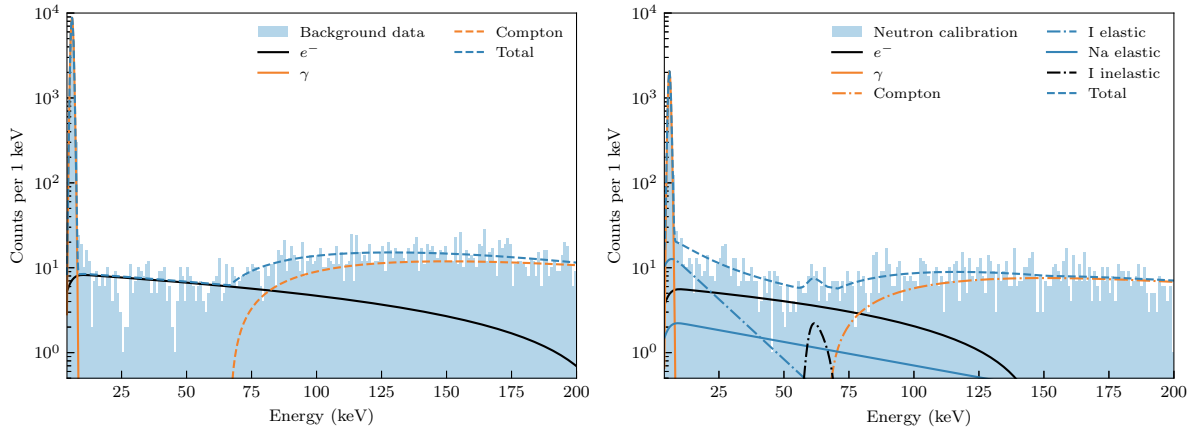

Figure 6.21: Energy spectra (total energy, shift corrected) of the ROI for both background (left) and neutron calibration data (right). The plots also show the parametric descriptions of the energy spectra as yielded by the combined likelihood fit.

For the nuclear band n we describe the quenching factor as $\mathrm{QF}_n(E) = E_{l,n}(E)/E_{l,e^-}(E)$, where $E_{l,n}(E)$ is the energy dependent mean light of the nuclear recoil band and $E_{l,e^-}(E)$ the mean light for electron recoils. Per definition, the mean light yield of the electron band is one at the calibration energy and we introduce a linear, energy dependent description to account for detector effects. We note here, that we did not observe any non-proportionality in the scintillation light output. We define the fit functions for the light output as follows:

$$E_{l,e^-}(E) = l_0 E + l_1 E^2 \tag{6.2}$$

$$E_{l,n}(E) = \left(l_0 E + l_1 E^2\right) \times k_{QF,n} \left(1 - a_n e^{-E/d_n}\right) \tag{6.3}$$

The variables $l_0, l_1, k_{QF,n}, a_n, d_n$ are free parameters determined from the fit. Using eq. (6.2) and (6.3) we can directly extract the energy dependent quenching factors from the result of the likelihood fit. We determined the quenching factors at 10 keV nuclear recoil energy as $\mathrm{QF_{Na}}(10\,\mathrm{keV}) = 0.197 \pm 0.019$ and $\mathrm{QF_I}(10\,\mathrm{keV}) = 0.0892 \pm 0.0037$. We want to highlight that the quenching factors are measured intrinsically and specifically for this crystal, such that uncertainties stem purely from the fit. One interesting observation we made in the analysis of this measurement, is that the light yield of the nuclear recoil events increases towards higher deposited energies. This behavior is contrary to observations made in other materials, such as $CaWO_4$ [201]. Together with the quenching factors at 10 keV, other results from the fit are noted in Table 6.5.

Using the results from the fit, we then define the acceptance region as the area in the energy - light yield plane between the mean of the sodium and the 99.5% lower limit of the iodine band. The acceptance region is marked in blue in Fig. 6.19. From the likelihood fit we estimate the leakage from the e^-/γ-band into the acceptance region to 0.48 ± 0.11 % between 4 and 6 keV, and $(6.7 \pm 2.3) \times 10^{-4}$ % between 6 and 200 keV. Considering the background level in the described data set, this corresponds to a leakage of 1 counts/(keV g d) and 1.5×10^{-5} counts/(keV g d), respectively. We note here, that the exponential description of

the energy dependent light yield for the nuclear recoil band is purely phenomenological. To ensure that the parametrization of the nuclear recoil bands does not affect the DM analysis, we performed the whole high-level analysis chain with various descriptions of the energy dependent light quenching, all leading to comparable limits.

Table 6.5: Fit values of the parameters necessary to describe the energy-dependent light quenching of the nuclear recoil bands in Eq. 6.2 as acquired by the Maximum Likelihood fit. The last two rows state the values of the quenching factors for sodium and iodine at 10 keV total deposited energy.

Parameter	**Fit value**
l_0	0.8131 ± 0.0026
l_1	$8.98 \times 10^{-4} \pm 0.28 \times 10^{-5}$ keV^{-1}
$k_{QF,\mathrm{Na}}$	2.864 ± 0.079
a_{Na}	0.9197 ± 0.0032
d_{Na}	$1.91 \times 10^3 \pm 0.12 \times 10^3$ keV
$k_{QF,\mathrm{I}}$	0.1005 ± 0.0041
a_{I}	680 ± 450
d_{I}	0.071 ± 0.031 keV
$\mathrm{QF_{Na}}(10\,\mathrm{keV})$	0.197 ± 0.019
$\mathrm{QF_{I}}(10\,\mathrm{keV})$	0.0892 ± 0.0037

6.6 Dark Matter Result

To give a comparable measure of the detector performance and the impact of the event-by-event discrimination on a DM analysis, we use the background data set to obtain limits on the nucleon-DM spin-independent elastic scattering cross section. The expected DM interaction rate $\frac{dR_{\mathrm{det}}}{dE}$ as observed by the detector is characterized by the standard spin-independent scattering model. It includes detector-specific quantities such as the threshold E_{thr}, the trigger and cut efficiency $\varepsilon(E)$, as well as the probability $p_{\mathrm{ACR}}(E)$ that a DM recoil event lies within the acceptance region. The resolution of the phonon channel is dominated by the Gaussian baseline noise and, therefore, taken into account by convolution with a Gaussian Ga of width σ_p:

$$\begin{aligned}\frac{dR_{\mathrm{det}}}{dE}(E) = \theta(E - E_{\mathrm{thr}})\,\varepsilon(E)\; p_{\mathrm{ACR}}(E) \\ \int_0^\infty \frac{dR_{\mathrm{theo}}}{dE'}(E') Ga(E - E', \sigma_p^2) dE'\end{aligned} \tag{6.4}$$

The theoretical model $\frac{dR_{\mathrm{theo}}}{dE'}$ is based on the standard assumptions for an isothermal DM

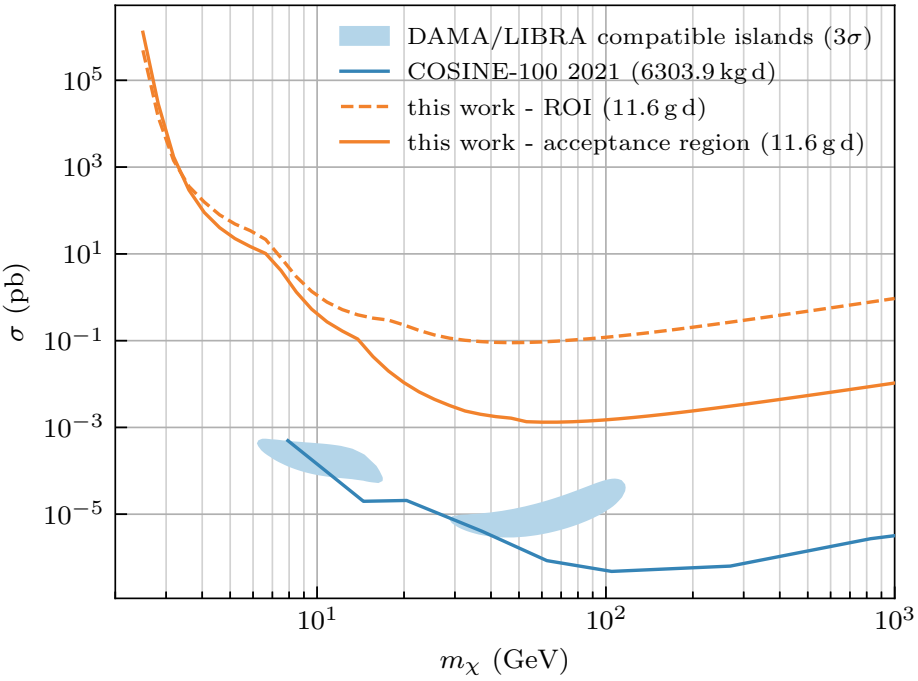

Figure 6.22: 90% confidence level upper limit on the spin-independent, elastic nucleon-DM scattering cross-section in the standard scenario, σ(pb) as a function of the DM mass, m_χ. The orange lines show the results of this work from a background data set with 11.6 g d of exposure. The dashed line is the limit achieved considering all events in the ROI; for the solid line only the events in the acceptance region were considered. As a comparison, we show contours compatible with the DAMA/LIBRA result [203] and the COSINE-100 result from 6303.9 kg d exposure [204], a factor ~10^5 higher than the current study.

halo [202]. Effects of the nuclear shape for the sodium and iodine nuclei are modeled by the Helm (extended by Lewin and Smith) form factor [94, 95], while the low contribution of Tl is conservatively considered negligible in the calculation

Using Yellin's optimum interval method [197, 198], we obtain the 90% confidence level upper limits displayed in Fig. 6.22. Besides the limit calculated from the acceptance region (solid line), we also show the limits calculated from all data points in the ROI (dashed line). A comparison of the two lines shows, that COSINUS' unique event-by-event discrimination enables to set an up to two orders stricter limit in the standard scenario. We emphasize that the limits from the acceptance region with 11.6 g d of exposure are only three orders of magnitude less strict than the limits from COSINE-100 with 6303.9 kg d exposure (blue line) shown for comparison. In addition, we note that the sensitivity of the prototype was limited due to leakage from the e^-/γ band to the nuclear recoil bands. The majority of these leakage events stem from the ^{55}Fe calibration source (compare with Fig. 6.20), as well as the overall e^-/γ background present in the dilution refrigerator. We count 11111 events in the energy interval [4,8] keV, and the likelihood fit assigns 11070 ± 140 events to the iron lines in this energy range. We will have a significant improvement for such measurements in the final low-background facility of COSINUS [205]. This is also directly related to the convergence of the limits from the acceptance region (solid orange) and the ROI (dashed orange) at lower DM masses, which correspond to lower energies where the discrimination power is reduced. Thus, we expect a profile-likelihood ratio approach for the DM analysis,

instead of the Yellin method, to further improve the sensitivity [187].

6.7 Conclusion

In this work, the results of the first underground operation of a NaI based cryogenic scintillating calorimeter were reported. A baseline resolution of 0.441 keV for nuclear recoils was achieved for the phonon channel. Together with the Si-based light channel, the dual channel readout was operated successfully, enabling particle discrimination between e^-/γ and nuclear recoils on an event-by-event basis. Based on these results, we determine the energy dependent quenching factors for sodium and iodine as observed in the operated crystal to $QF_{Na}(10\,keV) = 0.197 \pm 0.019$ and $QF_I(10\,keV) = 0.0892 \pm 0.0037$. Furthermore, we give limits on the standard spin-independent, elastic scattering cross section, based on 11.6 g d exposure of this R&D run's background data set, demonstrating how our unique background discrimination increases the sensitivity of a COSINUS detector with respect to NaI experiments with single-channel readout.

The 4π Module Design 7

"Progress lies not in enhancing what is, but in advancing
toward what will be."
— Khalil Gibran

Scaling up the detector production process requires a standardization of the various steps involved in detector fabrication. This chapter outlines the steps taken to tackle this and is divided into two parts. The first half delves into processes undertaken to have a uniform and reproducible connection of the Au-link between the absorber and the TES. The second half delves into the production and performance of the Si light detector.

7.1 Evaporation of Au films on NaI Crystals

7.1.1 Motivation

As outlined in Sec. 5.4.2, the process of gluing Au-pads to a crystal is prone to irreproducibility. This mainly stems from not just the amount of glue (which can be reasonably standardized with the help of a glue dispensing machine), but rather the procedure adopted. This can be mainly visualized as follows: As NaI is hygroscopic, gluing of the Au-pad must take place within e.g., nitrogen-controlled glovebox with moisture levels under 100 ppm. Tests showed that Epo-Tek 301-2 [183] needs a curing period of $\sim$ 6 hours to achieve optimal viscosity and handling of the glue for reproducible droplet formation. The initial procedure involved dropping an epoxy droplet onto the NaI crystal within the glovebox. This was then followed up with dropping the crystal with glue side down on a sheet of Au-foil procured from a commercial manufacturer of desired thickness. A controlled force was then applied on the crystal to develop a good contact between the crystal and glue. After a curing time of about 48 hours at RT, the Au-foil was manually peeled away from the sides, leaving behind the adhered Au-film, as seen in Fig. 7.1. There were three main limitations due to this method:

- Inconsistent epoxy spread due to variable pressure application.
- Delamination artifacts during foil removal.
- Handling challenges for sub-micron Au foils, which exhibit mechanical instability under glovebox overpressure.

A natural solution would be to cut the Au-foil to the desired dimension. However, handling of 1 µm thin Au-foils was found to be very delicate due to how thin and flexible they were. To improve dimensional control without compromising on the film quality, 1 µm Au-films were sectioned using a microtome from a Au-nugget. While this enabled precise thickness adjustment, residual bending from the cutting process impeded flat contact with NaI

surfaces when attempting such a gluing process inside the glovebox. Figure 7.1 illustrates resultant non-uniformities.

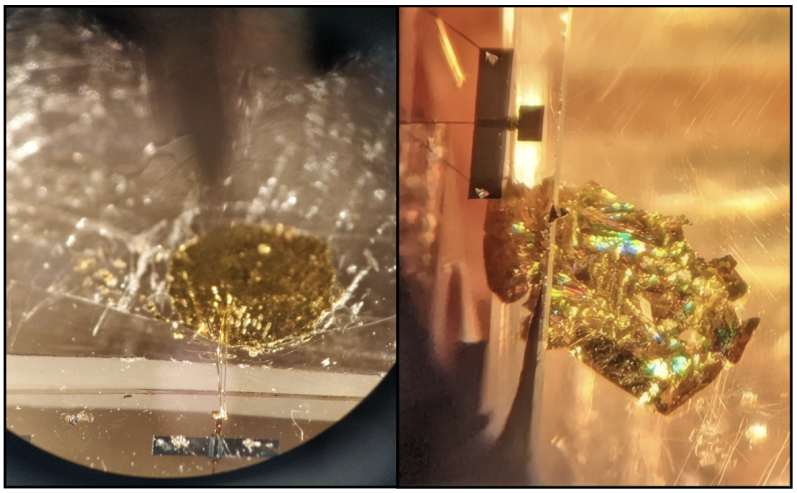

Figure 7.1: Left: A close-up of the Au-pad on a NaI absorber used in an initial test. The 1 µm thick Au-film was glued to the crystal using the method outlined initially in Sec. 7.1.1 **Right:** A close-up of the Au-pad glued on the NaI absorber used in the above-ground measurement outlined in Chapter 6. The 1 µm thick Au-film was cut with microtome and glued to the crystal with Epo-Tek 301-2.

Follow-up tests were carried out during the *remo*TES optimization runs carried out in Sec. 5.4.2 and for the cryogenic NaI test highlighted in [206]. They utilized 8 µm Au-foils procured from Goodfellow. The increased thickness permitted a relatively straightforward manual cutting with a scalpel outside the glovebox. The increased rigidity improved handling and adhesion reproducibility, as shown in Fig. 7.2. Laser-cut foils were also explored, to enable precise cutting of Au-foils with a 1 µm thickness. Challenges in reproducibility arose, due to which this process was discontinued. Further details on the laser-assisted technique can be found in [145].

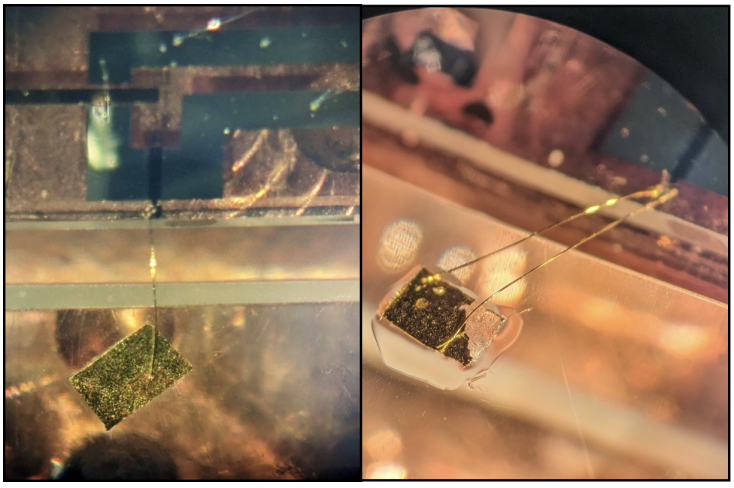

Figure 7.2: Close-up views of the Au-film (8 µm thick) glued onto an NaI crystal. The increased thickness improves handling and reproducibility.

7.1.2 The Evaporation Process

The challenges in standardizing the adhesion of Au pads to NaI crystals (Sec. 7.1.1) motivated the development of a direct evaporation process. Due to the hygroscopic nature of NaI, it is essential to maintain a dry environment during the entire process. This meant a specialized setup that could accommodate an evaporation machine within a glovebox.

With this in mind, the evaporation process was conducted within an argon-filled glovebox, utilizing a Tectra Mini Coater system [207] at the TUM Group for Physics of Energy Conversion and Storage [208]. The system, originally designed for solid-state battery electrode fabrication, was adapted for Au deposition on NaI. The Mini Coater, a compact physical vapor deposition (PVD) system designed for research applications, features resistive heating via replaceable, boat-shaped W-crucibles. It consists of a dual-boat evaporation setup. Boat 1 accommodates high melting-point materials (Au: 1337.3 K, Ti: 1941.0 K), while Boat 2 is reserved for reactive materials like Li (454.6 K). Both boats feature bilateral clamping for an optimal electrical contact during the resistive heating phase. In addition, dual mechanical shutters are present to isolate the sample and evaporation sources during initial thermal stabilization. A 6 MHz INFICON quartz crystal microbalance (QCM) [209], provides real-time deposition rate control, once calibrated to account for the vertical offset between the QCM and sample plane. Due to a different setup used by the ECS group for testing their samples, the position of the QCM is calibrated against a deposition height that is higher than the position of the crystal. Thus, the material dependent conversion factor (also called as the tooling factor) one gets from the QCM is only useful as a reference for subsequent depositions, given the height of the NaI sample is the same between runs. The evaporation machine with its components is shown in Fig. 7.3.

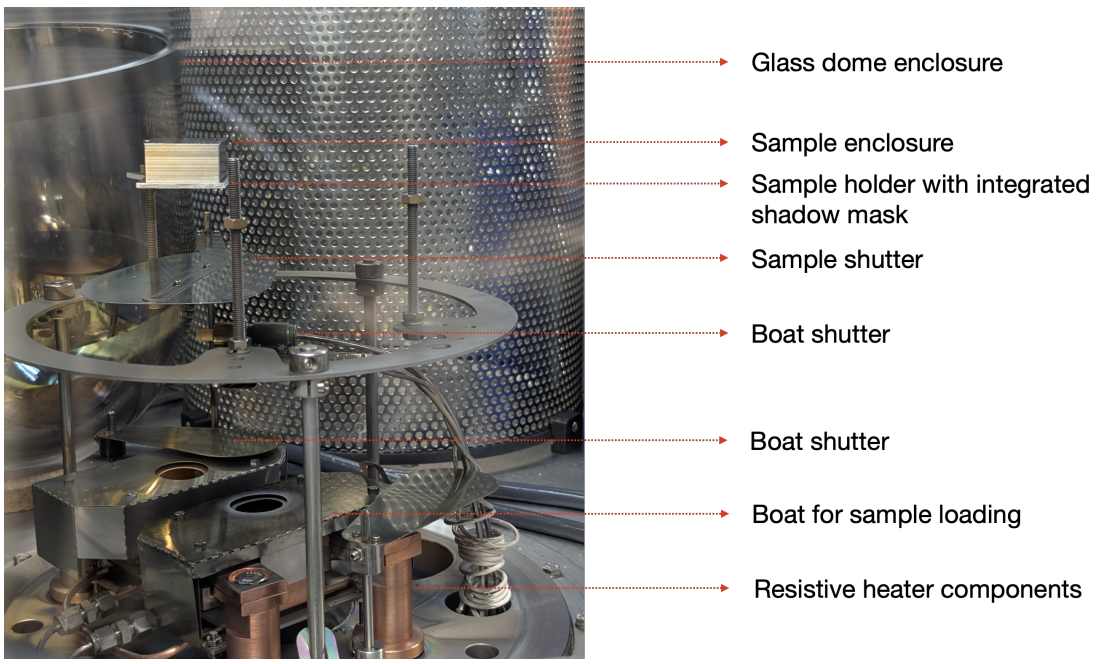

Figure 7.3: Schematic of the Tectra Mini Coater system within the argon filled glovebox. The sample holder along with the dual shutter system, the resistive heating boats and the glass dome enclosure is highlighted.

7.1.3 Feasibility Studies

Analogous to the SiO_2 adhesion layer required for Au deposition on Si substrates (Sec. 5.4.2), a thin Ti interlayer was determined to be crucial for robust Au-film adhesion to NaI crystals [210]. The high chemical affinity of Ti for both Au and the ionic crystal surface promotes strong interfacial bonding. This is critical for preventing delamination, a failure mode often exacerbated by the thermal stresses induced during cryogenic cooling cycles. Initial validation tests were performed using NaI crystals with dimensions of (20 x 10 x 5) mm^3. Through thickness optimization studies, it was found that a Ti layer with a nominal thickness of approximately 10 nm represents the minimum required to ensure sufficient adhesion against peel-off forces for the subsequent Au-film deposition.

Beyond basic adhesion, the deposited film structure must also withstand the mechanical stresses introduced during subsequent detector assembly steps, most notably ball bonding. To specifically assess the impact of the Ti interlayer on the integrity of the Au-film during this process, dedicated ball-bonding tests were conducted. For these mechanical tests, Al_2O_3 wafers were used as the substrate. Here, a ~ 7 nm Ti adhesion layer was deposited, followed by a 2.8 µm thick Au layer. Fig. 7.4 contrasts the behavior of regions with and without the Ti adhesion layer subjected to identical ball-bonding procedures. In regions lacking the Ti interlayer, the bonding process induced localized delamination of the Au film beneath the bond point. This damage often propagated, causing stress concentrations and visible warping in adjacent film areas. Conversely, in regions where the ~ 7 nm Ti layer was present, the Au film maintained its structural integrity.

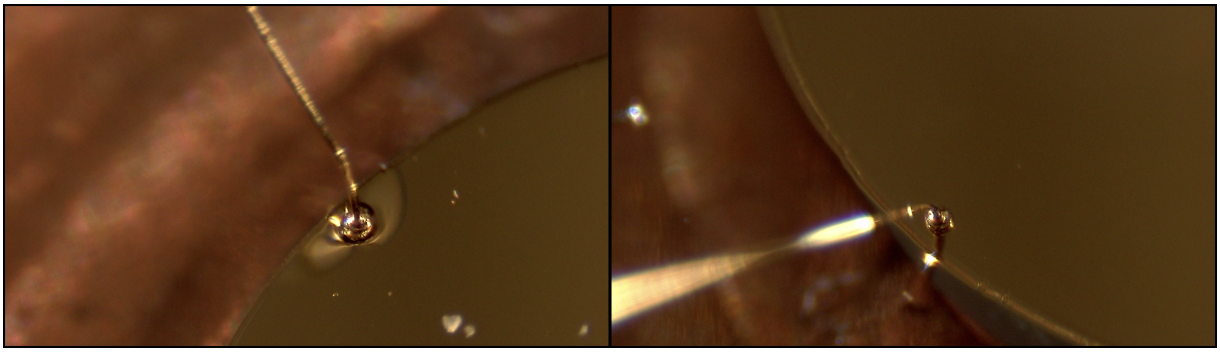

Figure 7.4: Comparative analysis of interfacial adhesion in a Au-Al_2O_3 system for ball-bonding; **Left:** Microscopic image reveals localized delamination and film deformation at the bonding site in the absence of a Ti interlayer; **Right:** Intact Au film morphology observed with a ~7 nm Ti adhesion layer under identical bonding parameters.

7.1.4 First Tests

A series of deposition tests were performed on NaI crystals measuring $(10 \times 10 \times 10)\,mm^3$, $(10 \times 10 \times 20)\,mm^3$, and $(21 \times 21 \times 21)\,mm^3$. The complete evaporation process was as follows: first, the W evaporation boat was loaded with the desired material, as illustrated in Fig. 7.5. For the adhesion and primary layer, Ti pellets (diameter (3.175×3.175) mm, 99.995 % purity, Kurt J. Lesker [211]) and Au granules (diameters (2-5) mm, 99.999 % purity,

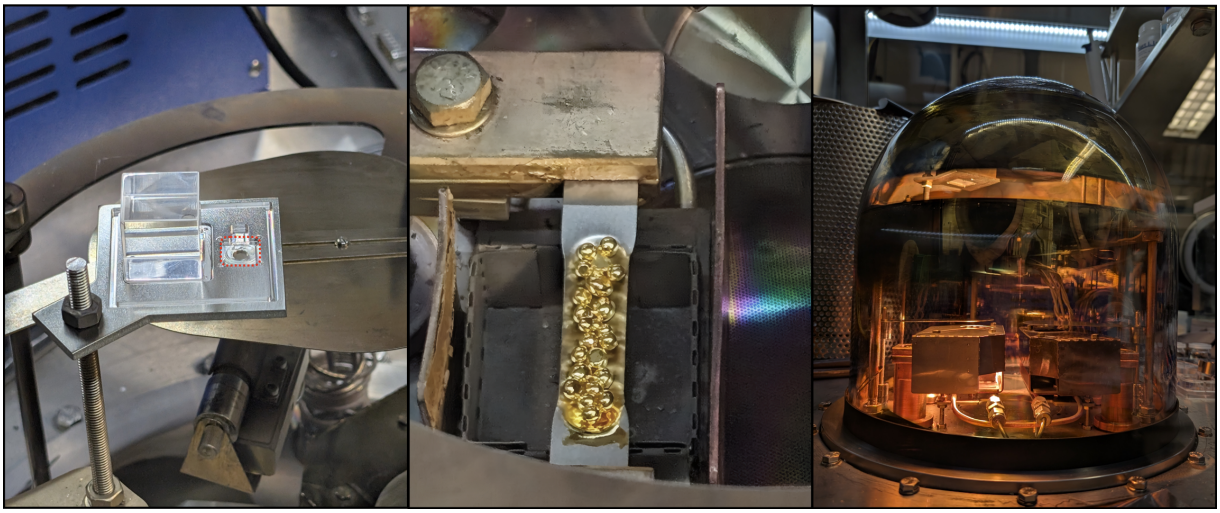

Figure 7.5: Operational view of the Tectra Mini Coater during Au evaporation. **Left:** The NaI crystal, along with the reference sample (highlighted in red), mounted on a custom stainless steel holder; **Centre:** The W-boat loaded with ~ 7 g of Au-granules prior to starting the evaporation; **Right:** The glow emanting due to the resistive heating of the W-boat once the glass dome has been evacuated down to a pressure of ~ 9×10^{-7} mbar.

g-materials [212]) were used respectively. The NaI crystal was secured on a custom stainless steel holder to ensure optimal positioning above the boat. An additional Al_2O_3 wafer with dimensions $(10 \times 10 \times 0.5)\,mm^3$ was positioned alongside the crystal, serving as a reference sample for subsequent thickness measurements. A stainless steel cap was then positioned above the holder to protect the remaining crystal surfaces from undesired deposition or contamination. Once the holder and crystal were installed, the deposition chamber was sealed with a borosilicate glass dome to form a vacuum-tight enclosure. The system was evacuated to a pressure of $\sim 9 \times 10^{-7}$ mbar using a turbo-molecular pump in series with a backing pump. The resistive heating current could then be gradually increased until the material began to vaporize, at which point the boat shutter was opened to allow vaporized atoms to reach the QCM chip. Once the QCM indicated a stable evaporation rate, the sample shutter was retracted, permitting the material to deposit onto both the crystal and the reference wafer. Fig. 7.5 shows the evaporation apparatus in operation. When the target thickness is achieved, both shutters were closed and the heating current was lowered in a controlled manner. Film thickness measurements employed a Tencor P-7 Stylus Profiler from KLA Corporation [213] on the Al_2O_3 reference samples co-deposited with the NaI crystals. The profiler was placed in a class 100 clean room belonging to the CRESST group at MPP. This contact profilometry system combined a diamond-tipped stylus with a capacitive displacement sensor to achieve vertical resolution of 1 nm under a controlled contact force (3 mg). The stylus traverses the sample surface along a pre-defined scan path, generating topographic maps through differential height measurements across deposited and masked regions. Comparative studies documented in [145] also evaluated alternative techniques, including crystal weighing and the Van-der-Pauw method. Initial trials across 10 crystals provided mixed results when compared against the reported values from the QCM chip, with the main uncertainty arising due to the geometric tooling factors used. Future iterations will determine a set of tooling factors for a modified crystal holder to

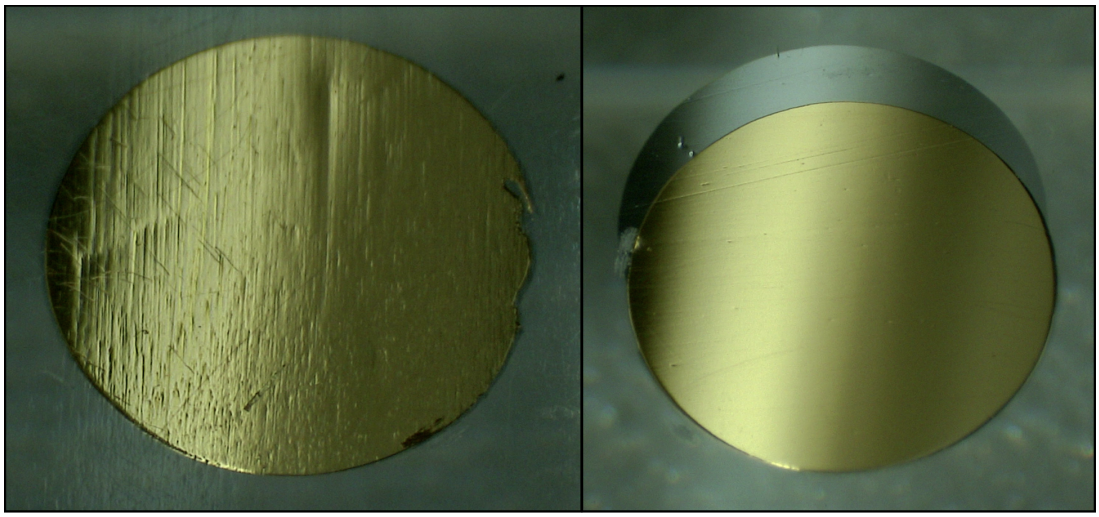

Figure 7.6: Comparative analysis of Au-films deposited under identical evaporation conditions, highlighting the importance of surface polishing: **Left:** Discontinuous morphology with groove-like features observed on a relatively high-surface-roughness NaI sample; **Right:** Continuous film formation achieved on a polished NaI sample; A Au-film thickness of 2.7 µm was achieved on both under identical deposition parameters: $9{\times}10^{-7}$ mbar base pressure and (18-31) nm s^{-1} growth rate of the Au-film.

remove any such position and angular uncertainties, thus enabling reliable in-situ thickness prediction within $\mathcal{O}$(nm), negating the need for a separate reference sample.
A further improvement in film quality is contingent on the quality of the crystal polishing itself. As illustrated in Fig. 7.6, one can clearly see the impact of a crystal with a surface roughness in the $\mathcal{O}$(100 nm) compared to a crystal with a surface roughness in the $\mathcal{O}$(10 nm).

7.2 Towards a Standardized Gluing Procedure for NaI

A reproducible gluing protocol for NaI crystals is critical for ensuring mechanical stability and minimizing stress-induced microcracks during cryogenic operation. The procedure must address two key challenges:

- **Controlled placement**: Precise alignment of the crystal on the Si lid to avoid asymmetrical stress buildup.
- **Glue spot optimization**: Optimization of glue spot geometry to balance the differential thermal contraction effects while maintaining adhesion strength.

The first placement prototype (Fig. 7.7), developed at MPP, revealed three operational constraints during testing. The elastic retention system produced variable preload forces complicating consistent crystal positioning. Micrometer-driven vertical alignment stages, while effective during open-air prototyping, became impractical within the glovebox environment due to restricted tactile feedback through butyl gloves and limited access to adjustment mechanisms. Furthermore, disengagement of the rubber band retention mechanism once lowered down risked crystal displacement during the critical glue curing phase.

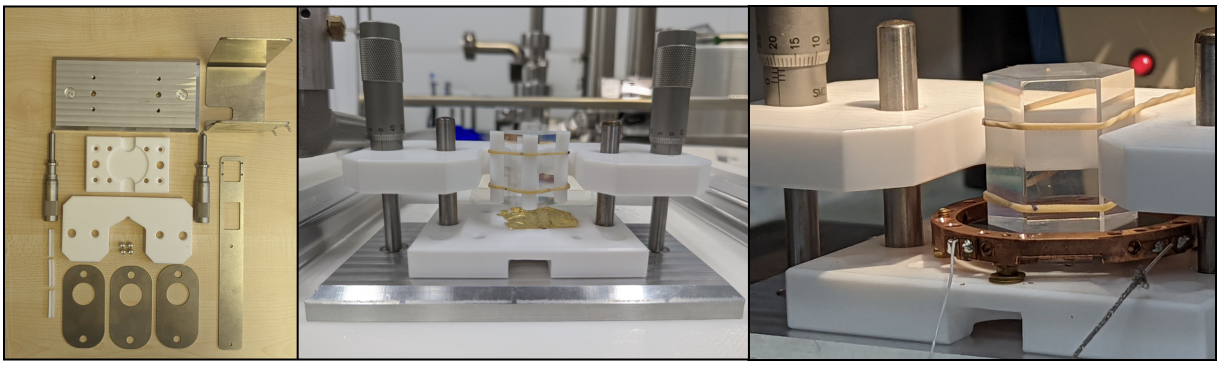

Figure 7.7: First-generation crystal placement prototype: **Left:** An exploded view of the different components; **Centre:** The assembled prototype with a hexagonal NaI crystal held in place with the elastomeric retention system, ready for gluing of the Au-film following the process initially outlined in Sec. 7.1.1; **Right:** The placement prototype being used to lower the crystal onto the Si lid.

A subsequent design iteration, intended to be used for the final module design outlined in Chapter 3, is currently under development.

The NaI crystals used for COSINUS Run 1 are glued to the Si lid with five glue spots arranged in an X - shaped configuration. While initially carried out with the help of a micropipette needle, the manual deposition exhibited run-to-run variability in terms of the glue volume and positional accuracy. To address this, a Musashi 350PC Smart automated dispensing system [214] (Fig. 7.8) was provided through an agreement with the Belle-II detector group at MPP. This pneumatic deposition system enables a precise control of Epo-Tek 301-2 epoxy parameters through three key variables: The machine can output pre-defined dosages of the glue, with the glue spot diameter and thickness being able to be contolled via fine tuning the input air pressure and time, and the nozzle diameter used for the Epo-Tek glue. The locations of the glue spots can also be programmed via the in-built Mu-CAD software, for when different sized crystals are to be tested in the future.

Figure 7.8: The Musashi 350PC Smart automated dispensing system used for precise pneumatic deposition of Epo-Tek 301-2. It offers fine control over glue spot diameter and thickness by adjusting air pressure, dispensing time, and nozzle size. Different glue-spot patterns can be programmed via the built-in Mu-CAD software for various crystal sizes.

7.3 The Si Light Detector

So far, the discussion has mostly evolved around the various optimization steps carried out for the phonon channel. The following subsections outline the process carried out for the light channel and are part of an ongoing manuscript which is currently under internal draft.

7.3.1 Introduction

As outlined in Chapter 3, the simultaneous measurement of scintillation light is essential for distinguishing between different recoiling particles in the NaI crystal. Optimizing the NaI crystal production to achieve high light yields at cryogenic temperatures is thus strongly motivated and necessary. To evaluate individual scintillator crystals, it is necessary to determine the amount of scintillation light they produce for a given deposited energy. Dedicated measurements studying the scintillation light efficiency for an undoped NaI crystal show it is highly temperature-dependent [215]. The light yield peaks at temperatures around 50 K before decreasing again as temperatures approach mK scales. The scintillation mechanism is thus mainly determined by the intrinsic photoluminescence due to localized exciton states [216]. Since particle discrimination in our setup depends on the amount of detected light, improvements can be made also by enhancing the light detection capability of the entire module. This can be achieved in two ways: Firstly, by ensuring all the surfaces are made/coated with a highly reflective material to ensure most of the scintillation light is collected by the light detector, or secondly, having a big enough light detector that can completely enclose the crystal to ensure an almost 4π light collection, thus ensuring any potential losses due to re-absorption in either the detector housing or the crystal is minimized.

Due to the cryogenic temperatures needed to operate these detectors, a reasonable method can be to opt for the first design. This ensures that the heat capacity of the light detector is kept to a minimum, which can lead to an increased sensitivity with sufficient optimization of the relevant TES parameters. However, a drawback of this is the reduced vetoing power of the light detector, since it does not enclose the absorber completely. To tackle this, COSINUS set out to use an enclosed beaker design, which should help in terms of light collection and also in the sense that the target crystal has no line of sight to any non-instrumented material.

7.3.2 Experimental Setup

The Beaker Design

To effectively collect scintillation light emitted by a particle interaction in the NaI crystal, the Si light detector has been designed in a beaker-shaped design, dubbed Obelix for illustrative purposes henceforth. The shape ensures most of the scintillation light (~400 nm),

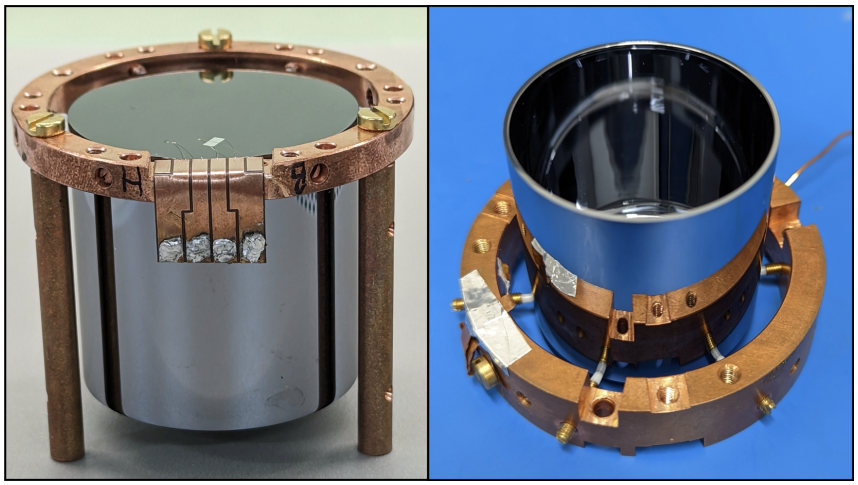

Figure 7.9: Left: A photograph of the Si-beaker shaped light detector, with the W-TES deposited on top. The bias and readout channels are wire-bonded to the Cu-Ka-Cu pad; **Right:** An inside view, showcasing the hollowed-out design.

emitted by NaI when a particle interaction occurs, is effectively absorbed by the inner surfaces of Obelix. Consequently, this generates athermal phonons, creating a secondary phonon population. The detector is fabricated by OPTEC [217] using a semi-proprietary technology to mill a mono-crystalline Si crystal (undoped, 8-16 kΩ/cm) to the desired shape. It then undergoes optical polishing to ensure the surface has a smooth finish with a surface roughness of ~ 1 nm. It is crucial to ensure that the surfaces are flat as imperfect edges are basically hot spots for the athermal phonons to thermalize. It was mounted on a circular Cu frame with the help of six POM tips, applying even pressure from all sides. An ^{55}Fe X-ray source with an activity of 3.3 mBq was taped onto the Cu holder to irradiate Obelix. A TES thin-film was deposited directly on the top side as seen in Fig. 7.9. The TES consists of a W-based superconducting thin-film evaporated using infrastructure and technology of the CRESST group at MPP in Munich, Germany. A Au stripe (thermal link) connecting the TES to the thermal bath is used for weak thermal coupling (15.8 Ω at room temperature) to slowly dissipate heat. An ohmic heater film was also deposited to adjust the TES-temperature to the optimal operation point. Externally injected "test pulses" at regular intervals via the heater serve to measure the detector response precisely over its entire dynamic range and to monitor potential changes with time. The general properties of the light detector are described in Table 7.1.

To efficiently collect athermal phonons and deliver their energy, it is flanked by two superconducting Al phonon collectors [191]. With the aim of achieving the lowest energy resolution, a series of measurements were performed, spread out across 2021, 2022, 2023 and 2024, to determine the optimal coverage area of the phonon collectors.

A first set of measurements were carried out with a reduced thickness of the wall diameter to profit from the reduced overall mass, expecting an increase in baseline resolution in line with results from [218]. It was instead observed that the reduced wall thickness led to the emergence of a position dependence of the recorded signals as well as worse energy resolution. The cause was attributed to the increased rate of phonon scatterings within the walls, leading to a thermalization of the phonons well before reaching the TES. A similar

Table 7.1: Properties of the light detector Obelix.

Component	Properties
Si-absorber	Mass: 15.38 g
	Hollow cylinder
	Height: 40 mm
	Outer diameter: 40 mm
	Thickness: 1 mm
W-TES on Si	Area: (100x400) μm^2
	Thickness: 80 nm
	T_C: ~18 mK
Heater on Si	Area: (200x150) μm^2
	Thickness: 100 nm gold

effect was observed in a pair of detector prototype measurements involving a similar Si beaker design, which was carried out by the CRESST collaboration [219].

7.3.3 Measurement Setup and DAQ

The measurements from 2021, 2022 and 2023 were carried out in a ^{3}He/^{4}He-dilution refrigerator of type MINIKELVIN 400-TOF from Leiden Cryogenics B.V. [192], dubbed "cryo2", provided by the CRESST group at MPP. It was located above ground in the cryo-lab at MPP, Munich, Germany. Four SQUIDs manufactured by APS [178] were used for sensor readout and signal amplification [194]. The refrigerator was optionally equipped with an external Pb-shield with a thickness of 100 mm for some runs. The thermalization of all parts was ensured by screwed Cu-wire connections to the MC. The measurement setup for the underground(UG) measurement is described in Sec. 6.4.2. The set of measurements from 2024 were carried out in the COSINUS dry dilution refrigerator from Cryoconcept installed at MPP, Garching, Germany. Three SQUIDs manufactured by Magnicon [220] were used for sensor readout and signal amplification.

7.3.4 Measurement Campaigns

The detector signals were initially read out in parallel with two separate systems: a hardware-triggered DAQ with a sampling rate of 50 kS/s and a continuous DAQ system designed by the Vienna COSINUS group. To set up and stabilize the detectors, the hardware-triggered DAQ was used. The runs in 2024 were read out and stabilized, using the continuous DAQ, as outlined in Sec. 4.2.4. In total, eleven measurement campaigns have been carried out so far, which are outlined in Table 7.2. The underground campaigns were measured with an external ^{57}Co γ-source (122 keV) with an activity of 430 Bq while the above ground campaigns had an external ^{57}Co γ-source (122 keV) having an activity of ~5000 Bq. All the

Table 7.2: Experimental runs in chronological order with corresponding baseline resolutions and phonon collector sizes.

Setup	Baseline resolution (eV)	Phonon collector size (mm^2)
No Pb castle	19.3	2 × (1×1)
No Pb castle	10.2	2 × (1×1)
No Pb castle	20.2	2 × (1×0.5)
Pb castle	28 (+ Si lid)	2 × (1.5×2.3)
UG (LNGS)	20.8	2 × (1.5×2.3)
UG (LNGS)	11 (prel.)	2 × (1.5×1.9)
Pb castle	—	2 × (1.5×1.9)
Pb castle	23	2 × (1.5×1.9)
Pb castle	15	(1.5×1.4) & (1.5×1.3)
No Pb castle	18.7 (prel.)	not measured

measurements also had an additional NaI crystal (of varying sizes depending on the run) enclosed within, leading to a trigger rate of ~4 Hz for the above ground measurements.

7.3.5 Optimization of Phonon Collectors

A substantial body of work, including that by the CRESST [194, 221] and SuperCDMS [222, 223] collaborations, has demonstrated that tailoring the design of phonon collectors can substantially enhance the phonon collection efficiency. The principal objectives in optimizing these collectors are to (i) maximize the fraction of athermal phonons absorbed by the sensor rather than lost to thermalization, (ii) maintain a low sensor heat capacity to optimize the signal-to-noise ratio, and (iii) minimize position-dependent variations in pulse shapes. Experimental investigations indicate that the geometry, area, and material properties of phonon collectors have a direct impact on energy resolution. Enlarging the collector coverage or strategically segmenting it enables a larger fraction of phonons to be converted into quasiparticles, which subsequently diffuse into the TES following the propagation scheme outlined in Fig. 7.10. Conversely, additional material in direct contact with the TES can increase the overall heat capacity and introduce extra noise channels.

Superconducting materials such as Al are commonly employed for phonon collectors because of their relatively large superconducting gap and long quasiparticle lifetimes [221]. In a typical design, high-frequency phonons entering the Al film break Cooper pairs, creating quasiparticles that diffuse toward the lower-gap TES material (e.g., W). This difference in gap energies promotes the diffusion of quasiparticles from the higher-gap Al into the lower-gap material, enhancing the efficiency of energy collection by the TES and thus improving the signal. Optimizing the thickness, length, and spacing of the Al fins has been studied in experiments like SuperCDMS and CRESST, where sub-100 eV thresholds, and more recently, even eV-scale baseline resolutions have been achieved [72, 224].

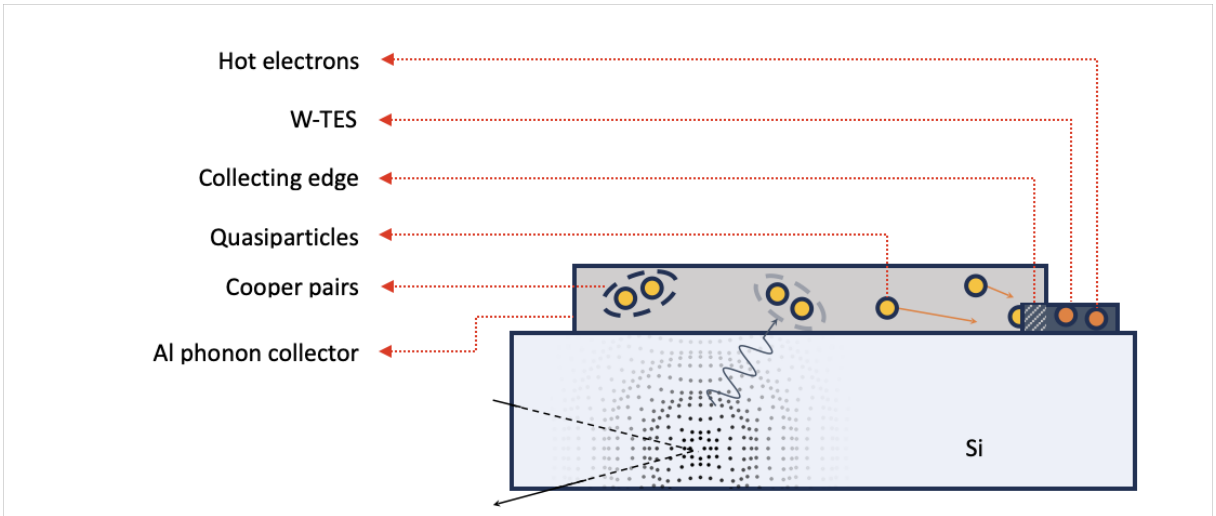

Figure 7.10: Schematic representation of a cryogenic phonon-collector design. High-frequency phonons generated in the Si beaker (bottom) enter the Al phonon collector, where they break Cooper pairs and form quasiparticles. These quasiparticles diffuse toward the W- TES, where they are converted into a measurable signal. Optimizing the geometry, material properties, and collecting edges of this interface can help in achieving high phonon collection efficiency and improved energy resolution.

In summary, the measurement results outlined in Table 7.2 demonstrate that carefully reducing the collector area in the current beaker-shaped crystal design leads to an improvement in energy resolution, a result that is consistent with the trade-off between enhanced phonon collection and the quasiparticle diffusion losses. Although the data presented here suggest that reducing the phonon collector area can yield a better energy resolutions for beaker-shaped designs, further investigations are necessary to conclusively determine the optimal geometry. Key factors such as quasiparticle diffusion lengths, phonon mean free paths, gap engineering at the Al–W interface, and potential effects of partial coverage or segmentation on event topology remain under active study. Theoretical studies, including quasiparticle downconversion models [225], along with additional experimental prototypes, will help to better investigate this interplay between collector size, sensor heat capacity, and energy resolution.

7.4 The 4π Module

While the previous section focused on achieving high scintillation light-collection efficiency, the 4π module design offers an additional advantage: in mitigating radioactive backgrounds. Radon, which is commonly present in ambient air, can deposit its progeny (notably ^{222}Rn and ^{210}Po) onto the detector surfaces or the surrounding holder materials unless specialized radon-exclusion measures are applied at every stage of detector handling. The ^{210}Po isotope is particularly problematic due to its half-life of 134 days. It decays via an α of 5.304 MeV into ^{206}Pb, leaving the recoiling Pb nucleus with approximately 103 keV of kinetic energy. In cases where the α is emitted outward into the surrounding material (due to say, radon adsorption on the NaI crystal surface), the Pb recoil may deposit its full energy in the crystal, creating a low-energy event that could mimic a nuclear recoil if not properly identified. By

enclosing the crystal within a nearly 4π solid angle of instrumented Si, referred to here as the "4π" design, the module can detect this escaping α via the instrumented beaker in coincidence with the Pb recoil deposit in NaI. Consequently, this arrangement not only enhances light-collection efficiency but also serves as a crucial element for suppressing surface-related α contamination from radon progeny, thus supressing a dangerous nuclear recoil background. Since the Si lid itself is not instrumented, a 100% veto efficiency is not guaranteed. However, tests with the lid pressed against the beaker (see Table 7.2) achieved a ~2% transmission efficiency for lid-origin events recorded by the beaker's TES. This efficiency is sufficient to tag α particles in coincidence with the Pb recoil deposit in NaI. The drawback is a slight performance degradation of the beaker itself, which is undesirable. Future investigations may explore further optimization or direct instrumentation of the Si lid as well.

7.4.1 COSINUS Module Assembly Procedure (Run 1)

In the following, a detailed procedure is presented for the fabrication of the final COSINUS modules. This recipe summarizes the optimizations carried out over the course of this thesis and outlines the steps necessary to ensure high-quality assembly and optimal performance of the detectors, while carefully managing the risks of crystal damage and ensuring reproducibility.

1. **NaI Crystal Examination:**
   - Verify that the crystal is completely transparent, well-polished, and free of visible cracks. A smooth surface ensures better acoustic matching for phonon propagation while also allowing for a well-defined Au-film evaporation (see Fig. 7.6) .
   - Handle the crystal exclusively with non-abrasive, clean room approved tools in a dry atmosphere (humidity < 100 ppm). Due to a Mohs hardness rating of only 2 (for reference, glass scratches at a level 6) [226], extreme care must be taken during the entire handling process.
2. **Au-Film Evaporation:**
   - Carefully re-seal the inspected NaI crystal into an ESD-safe bag or transfer it into a pressure-seal borosilicate glass.
   - Verify the stainless steel holder and enclosure are residue-free. If needed, clean with acetone, iso-propanol, de-ionized water and letting it dry in a nitrogen cabinet.
   - Transfer the crystal (plus the holder and enclosure) to an evaporation machine housed in a glovebox (currently located at the ECS lab, TUM).
   - Carefully mount the stainless steel holder on the evaporation machine at a pre-determined height, and place the crystal in its enclosure (See Fig. 7.5).
   - Ensure that the crystal face being exposed to the evaporation process has not come in contact with any handling tools from the previous steps.

- Ensure a firm W-boat placement, initially loaded with Ti pellets, to guarantee good contact while avoiding overfilling to prevent the melt from being wicked away from the corners when heated.
- Double-check that the dual shutters are operating as expected.
- Once the dome is pumped down to a vacuum of approximately 10^{-7} mbar, gradually increase the resistive heating.
- When any residual contaminants vaporize (indicated by a momentary spike in pressure that stabilizes after a while), further increase the heating until the Ti has molten.
- Open the boat shutter and adjust the heating to ensure a stable QCM rate reading.
- Open the sample shutter until a ~10 nm Ti layer is deposited.
- Repeat a similar process for the Au layer, aiming for a ~1 μm thick film.
- Take care during the change of the W-boat to avoid moving the apparatus too harshly, which could lead to misalignment between the two layers.
- If tooling factors are not re-calibrated, simultaneously deposit a film on a reference sample for non-destructive thickness measurement.

3. **Si Light Detector Assembly:**

- Prior to assembly, ensuring clean surfaces for all components is a necessity.
- For the Cu parts, ensure that there is no surface oxidation. Depending on the severity, use an abrasive brush to gently remove surface oxidation, or an ultrasonic cleaner if needed. Post cleaning, rinse using iso-propanol, followed by de-ionized water.
- Similarly, the Si-beaker needs to be inspected for any dust/organic remnants on it's surfaces. Using a non-abrasive clean room wipe with acetone (to remove organic substances), followed by iso-propanol and de-ionized water (necessary since acetone itself can leave a thin film on the surface) is recommended in this case.
- Further drying using a pressurized nitrogen line is a good option to dry these components to avoid the formation of any water stains, but care must be taken that this is performed under a flow-box.
- The Si-beaker is secured by six POM - tipped grub screws within their Cu rings. The grub screw tips should engage with the designated notches on the Si-beaker.
- Use a microscope to ensure the tips are well-aligned with the notches before tightening. Ensure they are adequately tightened, but take care not to overtighten.
- After mounting the Si beaker into the Cu ring, proceed with bonding the TES. Verify bond integrity using a gentle push-pull test and by inspecting the bond feet.
- The bonding parameters for the wedge-bonds are an ultrasonic power of ~170, time of 200 ms and force of 30 cN for the first bond and an ultrasonic power of ~200 , time of 200 ms and force of 30 cN. These values are intended to serve as a starting point and must be adjusted depending on bonding conditions and bond-wire material.

4. **Si lid and *remo*TES-Wafer Assembly:**
   - Inspect and clean all the surfaces similar to the steps outlined for the Si light detector.
   - The Si lid is secured by six POM - tipped grub screws within their Cu rings. The grub screw tips should engage with the designated notches on the Si-lid. Use a microscope to ensure the tips are well-aligned with the notches before tightening. Ensure they are adequately tightened, but take care not to overtighten.
   - Insert the TES-wafer into the free slot for the *remo*TES wafer on the Cu ring with the Si-disk.
   - Secure the wafer by pressing it with two bronze clamps, after which the TES is ready to be bonded.
   - Proceed with bonding for the TES and verify the bond integrity as before.
5. **Crystal Gluing to the Si-lid:**
   - Mix the Epo-Tek 301-2 epoxy and wait for approximately 6 hours before application. Insufficient waiting time risks damaging the crystal due to the catalyst, while an excessively long waiting time may render the glue too non-viscous for proper adhesion.
   - Ensure the mixed volume is homogeneous, clean, and free of any micro-bubbles.
   - Apply the epoxy to the Si-lid with the help of the Musashi 350PC automated dispensing system. For a $(21 \times 21 \times 21)$ mm^3 crystal, five glue spots are foreseen.
   - To minimize shear forces during cooldown, opt for glue spots with smaller diameters.
   - Check that the glovebox working surfaces are properly grounded to avoid any static discharge in the next step.
   - Carefully transfer the Si lid with the glue spots into the glovebox. Ensure a flat alignment to avoid breaking any TES bonds on the underside.
   - Lower the NaI absorber onto the glue spots with the help of a crystal placement tool, ensuring alignment of the Au-film with the corresponding hole in the Si-lid. Verify that the distance piece (~ 5-25 μm thickness) used is properly aligned and lies completely flat on the lid, allowing for easy removal later.
   - Allow the glue to dry for approximately 48 hours.
6. **Connecting the Absorber via the *remo*TES design:**
   - After the glue has cured, gently remove the distance piece and mount pillars to the Cu ring to facilitate handling without contacting the absorber crystal.
   - Carefully flip the crystal upside down to verify the stability of the gluing (nicknamed the "Blizzard test").
   - Perform the ball bond between the Au-film and the TES using the Au-island design with the assistance of a dedicated ball bonding machine in the glovebox.
   - The Au ball-bond parameters are: an ultrasonic power of ~55, time of 200 ms and force of 80 cN for the first bond and an ultrasonic power of ~210, time of 200 ms and force of 200 cN for the second bond . As stated earlier, these values are intended to serve only as a starting point and must be adjusted depending on the Au-film condition.

7. **Final Assembly:**
   - Once all bonded connections are complete, secure both Cu rings together as outlined in Sec. 3.2.
   - Care must be taken to ensure all screws are sufficiently tightend to have a good thermal contact. However, due to lack of tactile feedback inside the glovebox, it is easy to overtighten and destroy the threads.
   - Ensure that the Si-beaker does not contact the Si-lid.
   - Secure the detectors with additional thermalization links to ensure good thermal contact between components.

Upon completion of these steps, the module is ready for mounting in a detector box.

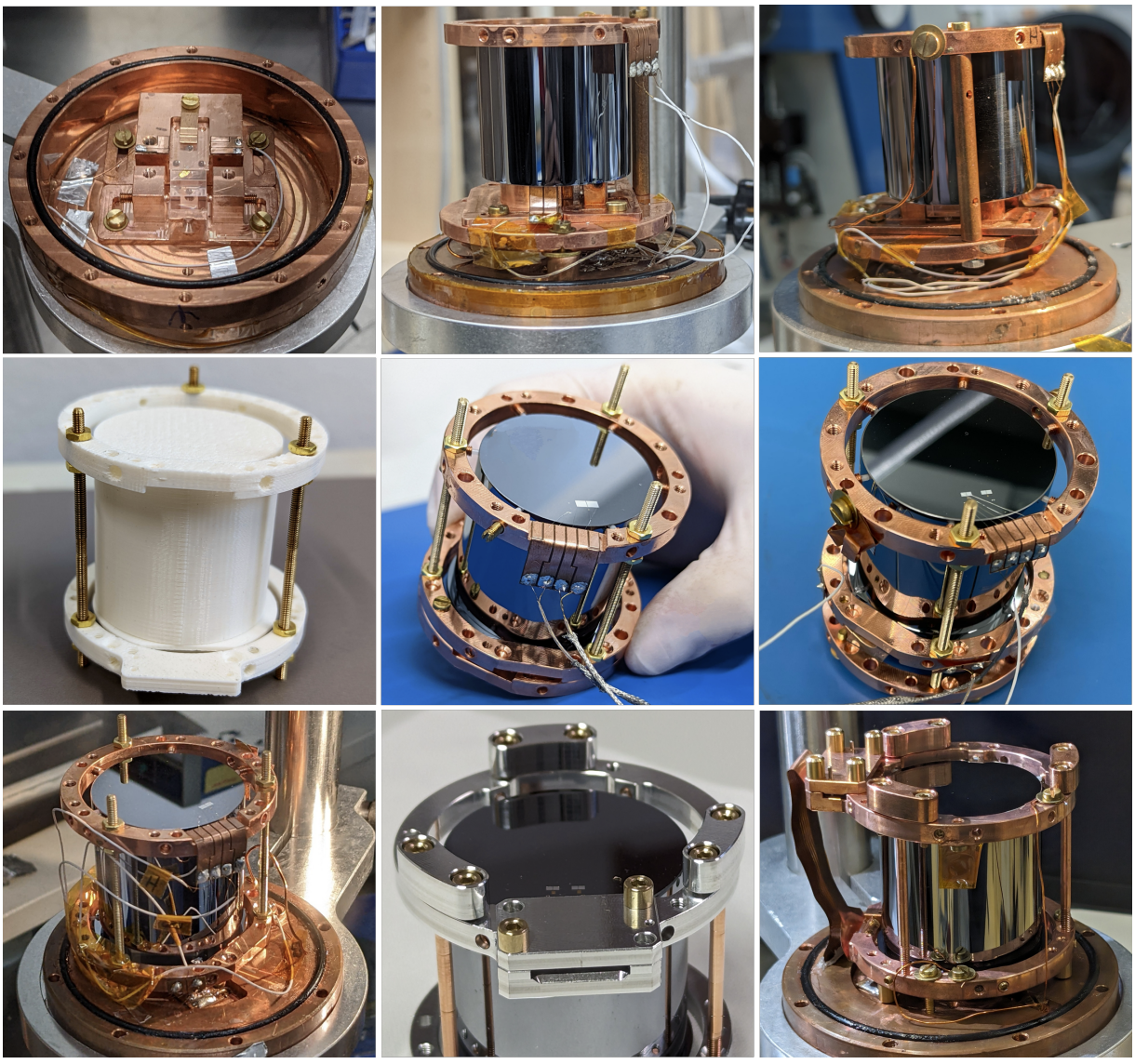

Figure 7.11: A snapshot of all the module design iterations in the context of this thesis. Earliest design on top left to newest on bottom right.

Epilogue

8 Conclusion

We shall not cease from exploration
and the end of all our exploring
will be to arrive where we started
and know the place for the first time.
— T.S. Eliot (from Little Gidding)

8.1 Looking Back

COSINUS, a novel direct DM search experiment, aims to provide a model-independent cross-check of the DAMA/LIBRA claim of an observed annual modulation signal above the expected background rate (see Chapter 2). The experiment is based on cryogenic NaI detectors that simultaneously measure the phonon signal and the corresponding scintillation light, thereby enabling event-by-event particle discrimination, as detailed in Chapter 3. For this purpose, a dedicated experimental facility has been constructed and commissioned at the Laboratori Nazionali del Gran Sasso (LNGS) in Italy (see Chapter 4).

The *remo*TES readout, developed in the context of this thesis, is a novel scheme particularly suited for mass fabrication of TES samples on a separate wafer. This approach facilitates the readout of a variety of absorbers, both standard and non-standard, at cryogenic temperatures. The initial development and implementation of the *remo*TES readout scheme is presented in Chapter 5. An above-ground test using a NaI crystal yielded promising results, demonstrating the first instance of event-by-event particle discrimination for such a cryogenic sample using this technique. A subsequent underground measurement produced the first DM limits, reaching within one to two orders of magnitude of the DAMA/LIBRA benchmark region with only 11.6 g d of exposure (see Chapter 6). Furthermore, several optimizations were investigated and implemented to address potential signal bottlenecks and improve performance (see Chapter 5). The work presented in Chapter 7 details the tests carried out to standardize the detector development process for mass fabrication intended for COSINUS Run 1.

8.2 Looking Ahead

Humanity has a history of figuring out how stuff works, with scientific explorations of the 20th century being instrumental in understanding how the macroscopic and microscopic works around us, both physical and biological. The 21st century will bring about a new understanding in the quest to explain the as yet unanswered puzzles, such as the nature of

DM and a more nuanced understanding of the interplay that goes on in the human mind and, by extension, the body.

Circling back to the introduction (Chapter 1), just as Cajal's microscope opened new vistas in neuroscience, today's DM experiments, including COSINUS, should be viewed not just as endpoints in a search, but as apertures: advanced tools that redefine the questions we can ask about the universe and, ultimately, expand the boundaries of what we can know.

Although significant progress has been made in the development and optimization of the *remo*TES design presented in this work, further improvements are required for its performance to fully match state-of-the-art detectors employing direct TES deposition onto standard absorbers. Future research avenues are numerous and promising. Exploring absorber-specific thin films and investigating multilayer thin-film structures for enhanced phonon transmission efficiency, developing multi-absorber readout schemes for improved scalability, and integrating novel absorber materials such as aluminum (Al), gallium arsenide (GaAs), or silicon carbide (SiC) represent just some of the potential paths forward.

With the dedicated R&D facility at MPP and the underground experimental facility at LNGS fully operational, and the foundations laid by the development of the *remo*TES readout, as detailed in this thesis, the stage is set to pursue these interconnected research directions. Exciting times await for COSINUS Run 1 and beyond!

Bibliography

[1] F. Zwicky. 'Die Rotverschiebung von extragalaktischen Nebeln'. In: *Helvetica Physica Acta* 6 (1933), pp. 110–127 (cited on page 3).

[2] C.H. Gingrich. 'The eighty-second meeting of the American Astronomical Society'. In: *Popular Astronomy* 58 (1950), p. 1 (cited on page 4).

[3] E. Hubble. 'A Relation Between Distance and Radial Velocity Among Extra-Galactic Nebulae'. In: *Proceedings of the National Academy of Sciences of the United States of America* 15 (1929), pp. 168–173. DOI: 10.1073/pnas.15.3.168 (cited on page 4).

[4] E. Hoge. 'The 200-Inch Telescope Takes its First Pictures'. In: *Engineering and Science* 12.8 (1949), pp. 3–7 (cited on page 4).

[5] 'Saint Gobain'. In: *https://www.saint-gobain-glass.com/* (2025) (cited on page 4).

[6] M. Simmons. *Building the 100-Inch telescope*. 1984. URL: https://www.mtwilson.edu/old/Simmons4.html (cited on page 4).

[7] T. Tag. 'Lens rotation'. In: *https://uslhs.org/node/1614* (2025) (cited on page 4).

[8] Carnegie Library. *Carnegie Library*. 2025. URL: https://www.carnegielibrary.org (cited on page 4).

[9] Huntington Library. *Huntington Library*. 2025. URL: https://www.huntington.org (cited on page 4).

[10] F. Zwicky. 'On the Masses of Nebulae and of Clusters of Nebulae'. In: *The Astrophysical Journal* 86 (1937), pp. 217–246. DOI: 10.1086/143864 (cited on page 5).

[11] M. F. Kessler et al. 'The Infrared Space Observatory (ISO) mission'. In: *Astronomy and Astrophysics* 315 (1996), pp. 27–31 (cited on page 5).

[12] A. Dressler et al. 'Hubble Space Telescope Observations of the Coma Cluster'. In: *The Astrophysical Journal* 490 (1997), pp. 577–593. DOI: 10.1086/304881 (cited on page 5).

[13] F. Jansen et al. 'XMM-Newton observatory. I. The spacecraft and operations'. In: *Astronomy and Astrophysics* 365 (2001), pp. L1–L6. DOI: 10.1051/0004-6361:20000036 (cited on page 5).

[14] M. Schwarzschild. 'Mass distribution and mass-luminosity ratio in galaxies'. In: *Annual review of Astronomy and Astrophysics* 59 (1954), p. 273. DOI: 10.1086/107013 (cited on page 6).

[15] P. Glafkides. *Photographic Chemistry*. Trans. by K. M. Hornsby. Vol. 2. Translated from the French by Keith M. Hornsby, F.R.P.S. Fountain Press, London, 1960 (cited on page 6).

[16] Smithsonian Institution. *Smithsonian Institution*. 2025. URL: https://www.si.edu (cited on page 7).

[17] V. C. Rubin and W. K. Ford Jr. 'Rotation of the Andromeda Nebula from a Spectroscopic Survey of Emission Regions'. In: *The Astrophysical Journal* 159 (1970), pp. 379–403. DOI: 10.1086/150317 (cited on pages 6–8).

[18] V. C. Rubin, W. K. Ford Jr., and N. Thonnard. 'Extended rotation curves of high-luminosity spiral galaxies. IV. Systematic dynamical properties, Sa -> Sc.' In: *The Astrophysical Journal letters* 225 (1978), pp. L107–L111. DOI: 10.1086/182804 (cited on page 6).

[19] V.C. Rubin. 'Seeing dark matter in the Andromeda galaxy'. In: *Physics Today* 59.12 (2006), pp. 8–9. DOI: 10.1063/1.2435662 (cited on page 8).

[20] M. S. Roberts and R. N. Whitehurst. 'The rotation curve and geometry of M31 at large galactocentric distances.' In: *The Astrophysical Journal* 201 (1975), pp. 327–346. DOI: 10.1086/153889 (cited on page 8).

[21] G. Squires et al. 'The Dark Matter, Gas, and Galaxy Distributions in Abell 2218: A Weak Gravitational Lensing and X-Ray Analysis'. In: *The Astrophysical Journal* 461 (1996), p. 572. DOI: 10.1086/177085 (cited on page 8).

[22] P. Natarajan and J.P. Kneib. 'Probing the dynamics of cluster-lenses'. In: *Monthly Notices of the Royal Astronomical Society* 283.3 (1996), pp. 1031–1046. DOI: 10.1093/mnras/283.3.1031 (cited on page 9).

[23] D. Clowe et al. 'A Direct Empirical Proof of the Existence of Dark Matter'. In: *The Astrophysical Journal Letters* 648 (2006), pp. L109–L113. DOI: 10.1086/508162 (cited on page 8).

[24] S. Alam et al. 'Completed SDSS-IV extended Baryon Oscillation Spectroscopic Survey: Cosmological implications from two decades of spectroscopic surveys at the Apache Point Observatory'. In: *Phys. Rev. D* 103 (8 2021), p. 083533. DOI: 10.1103/PhysRevD.103.083533 (cited on page 9).

[25] G. F. Smoot et al. 'Structure in the COBE Differential Microwave Radiometer First-Year Maps'. In: *Astrophys. J.* 396 (1992), pp. L1–L5. DOI: 10.1086/186504 (cited on page 9).

[26] NASA Goddard Space Flight Center. *COBE Differential Microwave Radiometers (DMR)*. 2025. URL: https://lambda.gsfc.nasa.gov/product/cobe/about_dmr.html (cited on page 10).

[27] NASA WMAP Science Team. *Wilkinson Microwave Anisotropy Probe (WMAP) Mission*. 2025. URL: https://map.gsfc.nasa.gov/ (cited on page 10).

[28] ESA and The Planck Collaboration. *Planck Mission*. 2025. URL: https://www.cosmos.esa.int/web/planck/planck-collaboration (cited on page 10).

[29] C. L. Bennett et al. 'Nine-Year Wilkinson Microwave Anisotropy Probe (WMAP) Observations: Final Maps and Results'. In: *Astrophys. J. Suppl.* 208 (2013), p. 20. DOI: 10.1088/0067-0049/208/2/20 (cited on pages 9, 10).

[30] S. Navas et al. 'Review of particle physics'. In: *Phys. Rev. D* 110.3 (2024), p. 030001. DOI: 10.1103/PhysRevD.110.030001 (cited on page 11).

[31] N. Aghanim et al. 'Planck 2018 results. VI. Cosmological parameters'. In: *Astronomy and Astrophysics* 641, A6 (2020), A6. DOI: 10.1051/0004-6361/201833910 (cited on page 10).

[32] R. G. Bower et al. 'Breaking the hierarchy of galaxy formation'. In: *Monthly Notices of the Royal Astronomical Society* 370.2 (2006), pp. 645–655. DOI: 10.1111/j.1365-2966.2006.10519.x (cited on pages 10, 12).

[33] M. Vogelsberger et al. 'Introducing the Illustris Project: simulating the coevolution of dark and visible matter in the Universe'. In: *Monthly Notices of the Royal Astronomical Society* 444.2 (2014), pp. 1518–1547. DOI: 10.1093/mnras/stu1536 (cited on page 10).

[34] M. Giannotti. 'Aspects of Axions and ALPs Phenomenology'. In: *Journal of Physics: Conference Series* 2502.1 (2023), p. 012003. DOI: 10.1088/1742-6596/2502/1/012003 (cited on page 13).

[35] A. Boyarsky et al. 'Sterile neutrino Dark Matter'. In: *Progress in Particle and Nuclear Physics* 104 (2019), pp. 1–45. DOI: https://doi.org/10.1016/j.ppnp.2018.07.004 (cited on page 13).

[36] R. Foot and S. Vagnozzi. 'Dissipative hidden sector dark matter'. In: *Phys. Rev. D* 91.2, 023512 (2015), p. 023512. DOI: 10.1103/PhysRevD.91.023512 (cited on page 13).

[37] D. Agius et al. 'Feedback in the dark: a critical examination of CMB bounds on primordial black holes'. In: (2024) (cited on page 13).

[38] M. Cirelli, A. Strumia, and J. Zupan. 'Dark Matter'. In: *arXiv e-prints*, arXiv:2406.01705 (2024), arXiv:2406.01705. DOI: 10.48550/arXiv.2406.01705 (cited on page 14).

[39] Chandra X-ray Center (CXC). *Chandra X-ray Observatory Official Website*. 2025. URL: https://chandra.harvard.edu/ (cited on page 13).

[40] Japan Aerospace Exploration Agency (JAXA). *XRISM (X-Ray Imaging and Spectroscopy Mission) Official Website*. 2025. URL: https://www.xrism.jaxa.jp/en/ (cited on page 13).

[41] P. Predehl et al. 'The eROSITA X-ray telescope on SRG'. In: *Astronomy and Astrophysics* 647, A1 (2021), A1. DOI: 10.1051/0004-6361/202039313 (cited on page 13).

[42] J. Cortina et al. 'Status and First Results of the Magic Telescope'. In: *Astrophysics and Space Science* 297 (2005), pp. 245–255. DOI: 10.1007/s10509-005-7627-5 (cited on page 13).

[43] M. Actis et al. 'Design concepts for the Cherenkov Telescope Array CTA: an advanced facility for ground-based high-energy gamma-ray astronomy'. In: *Experimental Astronomy* 32.3 (2011), pp. 193–316. DOI: 10.1007/s10686-011-9247-0 (cited on page 13).

[44] W. B. Atwood et al. 'The Large Area Telescope on the Fermi Gamma-ray Space Telescope Mission'. In: *Astrophys. J.* 697 (2009), pp. 1071–1102. DOI: 10.1088/0004-637X/697/2/1071 (cited on page 13).

[45] M. Aguilar et al. 'Antiproton Flux, Antiproton-to-Proton Flux Ratio, and Properties of Elementary Particle Fluxes in Primary Cosmic Rays Measured with the Alpha Magnetic Spectrometer on the International Space Station'. In: *Phys. Rev. Lett.* 117.9 (2016), p. 091103. DOI: 10.1103/PhysRevLett.117.091103 (cited on page 13).

[46] L. Evans and P. Bryant. 'The LHC Machine'. In: *JINST* 3 (2008), S08001. DOI: 10.1088/1748-0221/3/08/S08001 (cited on page 14).

[47] R. Barate et al. 'Search for the standard model Higgs boson at LEP'. In: *Phys. Lett. B* 565 (2003), pp. 61–75. DOI: 10.1016/S0370-2693(03)00614-2 (cited on page 14).

[48] R. Wilson. 'A Future Program of Muon Scattering at the Tevatron'. In: *FERMILAB-PROPOSAL-0786* (1988). DOI: 10.2172/992260 (cited on page 14).

[49] G. Aad et al. 'The ATLAS Experiment at the CERN Large Hadron Collider'. In: *JINST* 3 (2008), S08003. DOI: 10.1088/1748-0221/3/08/S08003 (cited on page 14).

[50] S. Chatrchyan et al. 'The CMS Experiment at the CERN LHC'. In: *JINST* 3 (2008), S08004. DOI: 10.1088/1748-0221/3/08/S08004 (cited on page 14).

[51] M. Aaboud et al. 'Search for dark matter in association with a Higgs boson decaying to b-quarks in pp collisions at 13 TeV with the ATLAS detector'. In: *Phys. Lett. B* 96 (2017), p. 112994. DOI: 10.1103/PhysRevD.96.112004 (cited on page 14).

[52] O. Brüning et al. 'High-Luminosity Large Hadron Collider (HL-LHC): Technical design report'. In: *CERN-2020-010* 10/2020 (Dec. 2020). DOI: 10.23731/CYRM-2020-0010 (cited on page 14).

[53] A. Abada et al. 'FCC-ee: The Lepton Collider: Future Circular Collider Conceptual Design Report Volume 2'. In: *Eur. Phys. J. ST* 228.2 (2019), pp. 261–623. DOI: 10.1140/epjst/e2019-900045-4 (cited on page 14).

[54] R. Bernabei et al. 'First results from DAMA/LIBRA and the combined results with DAMA/NaI'. In: *Eur. Phys. J. C* 56 (2008), pp. 333–355. DOI: 10.1140/epjc/s10052-008-0662-y (cited on page 15).

[55] E. Aprile et al. 'First Dark Matter Results from the XENON100 Experiment'. In: *Phys. Rev. Lett.* 105 (2010), p. 131302. DOI: 10.1103/PhysRevLett.105.131302 (cited on page 15).

[56] D. S. Akerib et al. 'First results from the LUX dark matter experiment at the Sanford Underground Research Facility'. In: *Phys. Rev. Lett.* 112 (2014), p. 091303. DOI: 10.1103/PhysRevLett.112.091303 (cited on page 15).

[57] D. S. Akerib et al. 'First Results from the Cryogenic Dark Matter Search in the Soudan Underground Lab'. In: *Phys. Rev. Lett.* 93 (2004), p. 211301. DOI: 10.1103/PhysRevLett.93.211301 (cited on page 15).

[58] G. Angloher et al. 'Results on Light Dark Matter Particles with a Low-Threshold CRESST-II Detector'. In: *The European Physical Journal C* 76 (2016), p. 25. DOI: 10.1140/epjc/s10052-016-3877-3 (cited on pages 15, 96).

[59] Z. Bo et al. 'Dark Matter Search Results from 1.54 Tonne · Year Exposure of PandaX-4T'. In: *Phys. Rev. Lett.* 134 (1 2025), p. 011805. DOI: 10.1103/PhysRevLett.134.011805 (cited on page 15).

[60] D. S. Akerib et al. 'The LUX-ZEPLIN (LZ) Experiment'. In: *Nucl. Instrum. Meth. A* 953 (2020), p. 163047. DOI: 10.1016/j.nima.2019.163047 (cited on pages 15, 21).

[61] E. Aprile et al. 'First Dark Matter Search with Nuclear Recoils from the XENONnT Experiment'. In: *Phys. Rev. Lett.* 131.4 (2023), p. 041003. DOI: 10.1103/PhysRevLett.131.041003 (cited on pages 15, 21).

[62] W. Ma et al. 'Search for Solar ^{8}B Neutrinos in the PandaX-4T Experiment Using Neutrino-Nucleus Coherent Scattering'. In: *Phys. Rev. Lett.* 130 (2 2023), p. 021802. DOI: 10.1103/PhysRevLett.130.021802 (cited on pages 15, 23).

[63] E. Aprile et al. 'First Indication of Solar ^{8}B Neutrinos via Coherent Elastic Neutrino-Nucleus Scattering with XENONnT'. In: *Phys. Rev. Lett.* 133 (19 2024), p. 191002. DOI: 10.1103/PhysRevLett.133.191002 (cited on pages 15, 23).

[64] R. Agnese et al. 'Search for low-mass dark matter with CDMSlite using a profile likelihood fit'. In: *Phys. Rev. D* 99.6 (2019), p. 062001. DOI: 10.1103/PhysRevD.99.062001 (cited on page 15).

[65] A.H. Abdelhameed et al. 'First results from the CRESST-III low-mass dark matter program'. In: *Phys. Rev. D* 100.10 (2019), p. 102002. DOI: 10.1103/PhysRevD.100.102002 (cited on pages 15, 22, 38).

[66] G. Angloher et al. 'Deep-underground dark matter search with a COSINUS detector prototype'. In: *Phys. Rev. D* 110 (4 2024), p. 043010. DOI: 10.1103/PhysRevD.110.043010 (cited on pages 15, 22, 50).

[67] R.A. Petersen et al. 'Demonstration of the HeRALD superfluid helium detector concept'. In: *Phys. Rev. D* 110.7 (2024), p. 072006. DOI: 10.1103/PhysRevD.110.072006 (cited on pages 15, 22).

[68] L. Baudis. 'DARWIN/XLZD: A future xenon observatory for dark matter and other rare interactions'. In: *Nucl. Phys. B* 1003 (2024), p. 116473. DOI: 10.1016/j.nuclphysb.2024.116473 (cited on page 15).

[69] R. Caldwell and M. Kamionkowski. 'Dark Matter and Dark Energy'. In: *Nature* 458 (2009), pp. 587–589. DOI: 10.1038/458587a (cited on page 18).

[70] R. J. Gaitskell. *Dark Matter WIMPs: Current Status and Future Prospects*. Presentation at the 15th International Conference on Identification of Dark Matter (IDM 2022), Vienna, Austria. 2022. URL: https://indico.cern.ch/event/922783/contributions/4897441/attachments/2481313/4261857/220718_Dark_Matter_WIMPs_Gaitskell_(IDM,Vienna,July_2022)_v18.pdf (cited on page 21).

[71] J. Aalbers et al. 'DARWIN: towards the ultimate dark matter detector'. In: *JCAP* 11 (2016), p. 017. DOI: 10.1088/1475-7516/2016/11/017 (cited on page 21).

[72] I. Alkhatib et al. 'Light Dark Matter Search with a High-Resolution Athermal Phonon Detector Operated above Ground'. In: *Phys. Rev. Lett.* 127.6 (2021), p. 061801. DOI: 10.1103/PhysRevLett.127.061801 (cited on pages 22, 135).

[73] E. Armengaud et al. 'Searching for low-mass dark matter particles with a massive Ge bolometer operated above ground'. In: *Phys. Rev. D* 99 (8 2019), p. 082003. DOI: 10.1103/PhysRevD.99.082003 (cited on page 22).

[74] S. Knapen, J. Kozaczuk, and T. Lin. 'Migdal Effect in Semiconductors'. In: *Phys. Rev. Lett.* 127 (8 2021), p. 081805. DOI: 10.1103/PhysRevLett.127.081805 (cited on page 22).

[75] N. Di Marco et al. 'NEWSdm: an emulsion-based directional Dark Matter experiment'. In: *Journal of Physics: Conference Series* 1056.1 (2018), p. 012018. DOI: 10.1088/1742-6596/1056/1/012018 (cited on page 22).

[76] C. Amole et al. 'Dark matter search results from the complete exposure of the PICO-60 C_3F_8 bubble chamber'. In: *Phys. Rev. D* 100 (2 2019), p. 022001. DOI: 10.1103/PhysRevD.100.022001 (cited on page 23).

[77] S. Baum et al. 'New Projections for Dark Matter Searches with Paleo-Detectors'. In: *Instruments* 5.2 (2021). DOI: 10.3390/instruments5020021 (cited on page 23).

[78] J. Billard et al. 'Direct detection of dark matter—APPEC committee report'. In: *Reports on Progress in Physics* 85.5 (2022), p. 056201. DOI: 10.1088/1361-6633/ac5754 (cited on page 23).

[79] M. Kaznacheeva and K. Schaeffner. 'Scintillating low-temperature calorimeters for direct dark matter search'. In: *Journal of Advanced Instrumentation in Science* 2024.1 (2024). DOI: https://doi.org/10.31526/jais.2024.514 (cited on pages 24, 57).

[80] R. Bernabei et al. 'New limits on WIMP search with large-mass low-radioactivity NaI(Tl) set-up at Gran Sasso'. In: *Phys. Lett. B* 389 (1996), p. 757. DOI: 10.1016/S0370-2693(96)80020-7 (cited on pages 23, 31).

[81] K. Fushimi et al. 'Application of a large-volume NaI scintillator to search for dark matter'. In: *Phys. Rev. C* 47 (2 1993), R425–R428. DOI: 10.1103/PhysRevC.47.R425 (cited on page 23).

[82] R. Bernabei et al. 'The DAMA/LIBRA apparatus'. In: *Nuclear Instruments and Methods in Physics Research Section A: Accelerators, Spectrometers, Detectors and Associated Equipment* 592.3 (2008), pp. 297–315. DOI: https://doi.org/10.1016/j.nima.2008.04.082 (cited on page 25).

[83] R. Bernabei et al. 'Dark Matter: DAMA/LIBRA and its perspectives'. In: *SciPost Phys. Proc.* (2023), p. 025. DOI: 10.21468/SciPostPhysProc.12.025 (cited on pages 24, 25).

[84] J. Amaré et al. *Towards a robust model-independent test of the DAMA/LIBRA dark matter signal: ANAIS-112 results with six years of data*. 2025. URL: https://arxiv.org/abs/2502.01542 (cited on page 25).

[85] G. Adhikari et al. 'Three-year annual modulation search with COSINE-100'. In: *Phys. Rev. D* 106 (5 2022), p. 052005. DOI: 10.1103/PhysRevD.106.052005 (cited on page 25).

[86] G.H. Yu et al. 'Lowering threshold of NaI(Tl) scintillator to 0.7 keV in the COSINE-100 experiment'. In: *Journal of Instrumentation* 19.12 (2024), P12013. DOI: 10.1088/1748-0221/19/12/P12013 (cited on page 26).

[87] G.H. Yu et al. *Limits on WIMP dark matter with NaI(Tl) crystals in three years of COSINE-100 data*. 2025. URL: https://arxiv.org/abs/2501.13665 (cited on page 26).

[88] K. Fushimi et al. 'Picolon Dark Matter Search Project'. In: *Journal of Physics: Conference Series* 2156.1 (2021), p. 012045. DOI: 10.1088/1742-6596/2156/1/012045 (cited on page 26).

[89] F. Calaprice et al. 'Performance of the SABRE Detector Module in a Purely Passive Shielding'. In: *The European Physical Journal C* 82.12 (2022). DOI: 10.1140/epjc/s10052-022-11108-z (cited on page 26).

[90] E. Barberio et al. 'Simulation and Background Characterisation of the SABRE South Experiment: SABRE South Collaboration'. In: *The European Physical Journal C* 83.9 (2023). DOI: 10.1140/epjc/s10052-023-11817-z (cited on page 26).

[91] D. D'Angelo et al. 'The ASTAROTH Project'. In: AIP Conference Proceedings 2908.1 (2023), p. 100007. DOI: 10.1063/5.0161723 (cited on page 27).

[92] M. Vogelsberger et al. 'Phase-space structure in the local dark matter distribution and its signature in direct detection experiments'. In: *Monthly Notices of the Royal Astronomical Society* 395.2 (2009), pp. 797–811. DOI: 10.1111/j.1365-2966.2009.14630.x (cited on page 27).

[93] N.W. Evans, C.A. O'Hare, and C. McCabe. *SHM^{++}: A Refinement of the Standard Halo Model for Dark Matter Searches in Light of the Gaia Sausage*. 2018. URL: https://arxiv.org/abs/1810.11468 (cited on page 27).

[94] R. H. Helm. 'Inelastic and Elastic Scattering of 187-Mev Electrons from Selected Even-Even Nuclei'. In: *Phys. Rev.* 104 (1956), pp. 1466–1475. DOI: 10.1103/PhysRev.104.1466 (cited on pages 28, 122).

[95] J.D. Lewin and P.F. Smith. 'Review of mathematics, numerical factors, and corrections for dark matter experiments based on elastic nuclear recoil'. In: *Astropart. Phys.* 6.1 (1996), pp. 87–112. DOI: https://doi.org/10.1016/S0927-6505(96)00047-3 (cited on pages 28, 122).

[96] C. J. Horowitz et al. 'Weak charge form factor and radius of ^{208}Pb through parity violation in electron scattering'. In: *Phys. Rev. C* 85 (3 2012), p. 032501. DOI: 10.1103/PhysRevC.85.032501 (cited on page 28).

[97] M Kellermann. 'Development and Operation of Next-Generation Low-Temperature Detectors for the COSINUS Dark Matter Search'. PhD thesis. Technische Universität München, 2025 (cited on pages 29, 81).

[98] N. Spooner et al. 'The scintillation efficiency of sodium and iodine recoils in a NaI(Tl) detector for dark matter searches'. In: *Phys. Lett. B* 321 (1994), p. 156. DOI: 10.1016/0370-2693(94)90343-3 (cited on page 31).

[99] G. Gerbier et al. 'Pulse shape discrimination and dark matter search with NaI(Tl) scintillator'. In: *Astropart. Phys.* 11 (1999), p. 287. DOI: 10.1016/S0927-6505(99)00004-3 (cited on page 31).

[100] E. Simon et al. 'SICANE: A detector array for the measurement of nuclear recoil quenching factors using a monoenergetic neutron beam'. In: *Nucl. Instrum. Methods A* 507 (2003), p. 643. DOI: 10.1016/S0168-9002(03)01438-4 (cited on page 31).

[101] H. Chagani et al. 'Measurement of the quenching factor of Na recoils in NaI(Tl)'. In: *J. Inst.* 3 (2008), P06003. DOI: 10.1088/1748-0221/3/06/P06003 (cited on page 31).

[102] J. I. Collar. 'Quenching and channeling of nuclear recoils in NaI(Tl): Implications for dark-matter searches'. In: *Phys. Rev. C* 88 (2013), p. 035806. DOI: 10.1103/PhysRevC.88.035806 (cited on page 31).

[103] J. Xu et al. 'Scintillation efficiency measurement of Na recoils in NaI(Tl) below the DAMA/LIBRA energy threshold'. In: *Phys. Rev. C* 92 (2015), p. 015807. DOI: 10.1103/PhysRevC.92.015807 (cited on pages 31, 46, 47).

[104] H. Joo et al. 'Quenching factor measurement for NaI(Tl) scintillation crystal'. In: *Astropart. Phys.* 108 (2019), p. 50. DOI: 10.1016/j.astropartphys.2019.01.001 (cited on pages 31, 47).

[105] L. J. Bignell et al. 'Quenching factor measurements of sodium nuclear recoils in NaI:Tl determined by spectrum fitting'. In: *Journal of Instrumentation* 16 (07 2021), P07034. DOI: 10.1088/1748-0221/16/07/P07034 (cited on pages 31, 33, 35, 47).

[106] D. Cintas et al. 'Measurement of the sodium and iodine scintillation quenching factors across multiple NaI(Tl) detectors to identify systematics'. In: *Phys. Rev. C* 110 (1 2024), p. 014613. DOI: 10.1103/PhysRevC.110.014613 (cited on pages 31, 33, 46, 47, 49).

[107] S. H. Lee et al. 'Measurements of low-energy nuclear recoil quenching factors for Na and I recoils in the NaI(Tl) scintillator'. In: *Phys. Rev. C* 110 (1 2024), p. 014614. DOI: 10.1103/PhysRevC.110.014614 (cited on pages 31, 46, 47).

[108] G. Lawrence, R. Beauchamp, and J. McKibben. 'Direct extraction of negative ion beams of good intensity from a duoplasmatron '. In: *Nucl. Instrum. and Meth.* 32 (2 1965), pp. 357–359. DOI: 10.1016/0029-554X(65)90539-2 (cited on page 31).

[109] H. Liskien and A. Paulsen. 'Neutron production cross-sections and energies for the reactions ^{7}Li$(p,n)^{7}$Be and ^{7}Li$(p,n)^{7}$Be$_{*}$ '. In: *Atomic Data and Nuclear Data Tables* 15.1 (1975), pp. 57–84. DOI: https://doi.org/10.1016/0092-640X(75)90004-2 (cited on page 31).

[110] M. Friedman et al. 'Simulation of the neutron spectrum from the ^{7}Li(p,n) reaction with a liquid-lithium target at Soreq Applied Research Accelerator Facility'. In: *Nucl. Instrum. and Meth. Phys. A* 698 (2013), pp. 117–126. DOI: https://doi.org/10.1016/j.nima.2012.09.027 (cited on page 31).

[111] Y. Zhu et al. 'Production of ultra-low radioactivity NaI (Tl) crystals for Dark Matter detectors'. In: *2018 IEEE Nucl. Sci. Conference Proceedings (NSS/MIC)*. IEEE. 2018, pp. 1–3. DOI: 10.1109/NSSMIC.2018.8824322 (cited on pages 32, 59, 110).

[112] Merck Group. *Astrograde powder*. 2023. URL: https://www.merckgroup.com/en (cited on pages 32, 59, 110).

[113] S. Nisi et al. 'ICP-MS measurement of natural radioactivity at LNGS.' In: *Int. J. of Modern Phys. A* 32 (30 2017), p. 1743003. DOI: 10.1142/S0217751X17430035 (cited on pages 32, 59, 110).

[114] A. Tomanin et al. 'Characterization of a cubic EJ-309 liquid scintillator detector'. In: *Nucl. Instrum. and Meth. Phys. A* 756 (2014), pp. 45–54. DOI: https://doi.org/10.1016/j.nima.2014.03.028. (cited on page 33).

[115] *A toolkit for data acquisition control and analysis for waveform digitizers including GAGE, XIA, and Struck*. https://code.ornl.gov/CASA/ngmdaq (cited on page 34).

[116] D. W. Aitken et al. 'The Fluorescent Response of NaI(Tl), CsI(Tl), CsI(Na) and CaF2(Eu) to X-Rays and Low Energy Gamma Rays'. In: *IEEE Transactions on Nuclear Science* 14.1 (1967), pp. 468–477. DOI: 10.1109/TNS.1967.4324457 (cited on pages 35, 50).

[117] B.D. Rooney and J.D. Valentine. 'Scintillator light yield nonproportionality: calculating photon response using measured electron response'. In: *IEEE Transactions on Nuclear Science* 44.3 (1997), pp. 509–516. DOI: 10.1109/23.603702 (cited on pages 35, 50).

[118] G.R. Gilmore. 'Scintillation Spectrometry'. In: *Practical Gamma-Ray Spectrometry*. John Wiley and Sons, Ltd, 2008. Chap. 10, pp. 205–219. DOI: 10.1002/9780470861981.ch10 (cited on page 36).

[119] S. Agostinelli et al. 'Geant4 — a simulation toolkit'. In: *Nucl. Instrum. Methods:A* 506.3 (2003), pp. 250–303. DOI: 10.1016/S0168-9002(03)01368-8 (cited on pages 38, 113).

[120] J. Allison et al. 'Geant4 developments and applications'. In: *IEEE Transactions on Nuclear Science* 53.1 (2006), pp. 270–278. DOI: 10.1109/TNS.2006.869826 (cited on pages 38, 113).

[121] J. Allison et al. 'Recent developments in Geant4'. In: *Nucl. Instrum. Methods:A* 835.1 (2016), pp. 186–225. DOI: 10.1016/j.nima.2016.06.125 (cited on pages 38, 113).

[122] A. H. Abdelhameed et al. 'GEANT4-based electromagnetic background model for the CRESST dark matter experiment'. In: *Eur. Phys. J. C* 79.10 (2019), p. 881. DOI: 10.1140/epjc/s10052-019-7504-y (cited on page 38).

[123] R. Brun and F. Rademakers. 'ROOT—An object oriented data analysis framework'. In: *Nucl. Instrum. and Meth. A* 389.1-2 (1997), pp. 81–86. DOI: 10.1016/S0168-9002(97)00048-X (cited on page 38).

[124] A. Caldwell and K. Kollár D.and Kröninger. 'BAT – The Bayesian analysis toolkit'. In: *Computer Physics Communications* 180.11 (2009), pp. 2197–2209. DOI: 10.1016/j.cpc.2009.06.026 (cited on page 41).

[125] S. Brooks and A. Gelman. 'General Methods for Monitoring Convergence of Iterative Simulations'. In: *J. Comput. Graphi. Stat.* 7 (1998), pp. 434–455. DOI: 10.1080/10618600.1998.10474787 (cited on page 42).

[126] G. Angloher et al. 'Particle discrimination in a NaI crystal using the COSINUS remote TES design'. In: *Phys. Rev. D* 109 (8 2024), p. 082003. DOI: 10.1103/PhysRevD.109.082003 (cited on page 50).

[127] S. P. Langley. 'The Bolometer and Radiant Energy'. In: *Proceedings of the American Academy of Arts and Sciences* 16 (1880), pp. 342–358 (cited on page 55).

[128] F. Simon. 'Application of Low Temperature Calorimetry to Radioactive Measurements'. In: *Nature* 135 (1935), p. 763 (cited on page 55).

[129] D. H. Andrews, R. D. Fowler, and M. C. Williams. 'The Effect of Alpha-particles on a Superconductor'. In: *Phys. Rev.* 76 (1949), pp. 154–155. DOI: 10.1103/PhysRev.76.154.2 (cited on page 55).

[130] E. Fiorini and T. Niinikoski. 'Low-temperature calorimetry for rare decays'. In: *Nuclear Instruments and Methods in Physics Research* 224.1 (1984), pp. 83–88. DOI: 10.1016/0167-5087(84)90449-6 (cited on page 55).

[131] A. Drukier and L. Stodolsky. 'Principles and applications of a neutral-current detector for neutrino physics and astronomy'. In: *Phys. Rev. D* 30 (1984), pp. 2295–2309. DOI: 10.1103/PhysRevD.30.2295 (cited on page 55).

[132] B. Cabrera, L. M. Krauss, and F. Wilczek. 'Bolometric detection of neutrinos'. In: *Phys. Rev. Lett.* 55 (1985), pp. 25–28. DOI: 10.1103/PhysRevLett.55.25 (cited on page 55).

[133] K. Pretzl, N. Schmitz, and L. Stodolsky. *Low Temperature Detectors for Neutrinos and Dark Matter: Proceedings of a Workshop, Held at Ringberg Castle, Tegernsee, May 12–13, 1987*. Springer Berlin, Heidelberg, 1987 (cited on page 55).

[134] K. Pretzl. 'Cryogenic Detectors'. In: *Particle Physics Reference Library*. Ed. by C. Fabjan and H. Schopper. Cham: Springer, 2020. DOI: 10.1007/978-3-030-35318-6_19 (cited on page 56).

[135] Upscayl. *An Open Source Image Upscaler*. https://github.com/upscayl/upscayl. 2025 (cited on page 56).

[136] M. Pyle et al. 'Optimized designs for very low temperature massive calorimeters'. In: *arXiv:1503.01200* (2015). DOI: 10.48550/arXiv.1503.01200 (cited on pages 59, 90, 110).

[137] G Angloher et al. 'First measurements of remoTES cryogenic calorimeters: Easy-to-fabricate particle detectors for a wide choice of target materials'. In: *Nucl. Instrum. Methods: A* 1045 (2023), p. 167532. DOI: 10.1016/j.nima.2022.167532 (cited on pages 59, 101, 109, 110, 115).

[138] Aurubis AG. *NOSV copper*. 2025. URL: https://www.aurubis.com/en/ (cited on pages 60, 110).

[139] M Kempa et al. 'The temperature dependence of the phononic band gap of NaI'. In: *Journal of Physics: Condensed Matter* 25.5 (2013), p. 055403. DOI: 10.1088/0953-8984/25/5/055403 (cited on page 62).

[140] G. Petretto et al. 'High-Throughput Density-Functional Perturbation Theory Phonons for Inorganic Materials'. In: *Scientific Data* 5 (2018), p. 180065. DOI: 10.1038/sdata.2018.65 (cited on page 62).

[141] F. Pröbst et al. 'Model for cryogenic particle detectors with superconducting phase transition thermometers'. In: *Journal of low temperature physics* 100 (1995), pp. 69–104. DOI: 10.1007/BF00753837 (cited on pages 65, 90, 104).

[142] V. Zema. 'Unveiling the Nature of Dark Matter with Direct Detection Experiments'. PhD thesis. Chalmers U. Tech., 2020 (cited on pages 65, 90, 115).

[143] S. Braun. 'Pulse Shape studies (In preparation)'. MA thesis. Technische Universität München, 2025 (cited on page 65).

[144] K. Shera. 'Studies on remoTES-based Cryogenic Calorimeters for the COSINUS Experiment'. MA thesis. Technische Universität München, 2024 (cited on pages 65, 91, 96).

[145] K. Heim. 'Au evaporation studies on the performance of cryogenic NaI calorimeters'. MA thesis. Technische Universität München, 2025 (cited on pages 65, 126, 129).

[146] STAR Cryoelectronics. *STAR Cryoelectronics Official Website*. 2025. URL: https://starcryo.com/ (cited on pages 69, 85).

[147] W. Woodley, A. Fedynitch, and M.C. Piro. 'Cosmic Ray Muons in Laboratories Deep Underground'. In: *Phys. Rev. D* 110 (2024), p. 063006. DOI: 10.1103/PhysRevD.110.063006 (cited on page 71).

[148] M. Hughes et al. 'The COSINUS underground cryogenic facility'. In: *arXiv:1503.01200* (2024). DOI: 10.22323/1.441.0096 (cited on pages 72, 74).

[149] G. Angloher et al. 'Simulation-Based Design Study for the Passive Shielding of the COSINUS Dark Matter Experiment'. In: *The European Physical Journal C* 82.3 (2022). DOI: 10.1140/epjc/s10052-022-10184-5 (cited on page 72).

[150] Hamamatsu Photonics K.K. *Large Area Photomultiplier Tube (PMT) Technical Data Sheet*. 2025. URL: https://hep.hamamatsu.com/content/dam/hamamatsu-photonics/sites/documents/99_SALES_LIBRARY/etd/LARGE_AREA_PMT_TPMH1376E.pdf (cited on page 73).

[151] G. Angloher et al. 'Water Cherenkov Muon Veto for the COSINUS Experiment: Design and Simulation Optimization'. In: *The European Physical Journal C* 84 (2024), p. 551. DOI: 10.1140/epjc/s10052-024-12923-2 (cited on pages 73, 74).

[152] 3M Company. *3M™ Specular Film DF2000MA Technical Data Sheet*. 2025. URL: https://multimedia.3m.com/mws/media/9824490/3mtm-specular-film-df2000ma-technical-data-sheet.pdf (cited on pages 73, 74).

[153] J. F. M. Rothe. 'Low-Threshold Cryogenic Detectors for Low-Mass Dark Matter Search and Coherent Neutrino Scattering'. PhD thesis. Technische Universität München, 2021 (cited on page 74).

[154] M. Kellermann et al. 'A Vibration Decoupling System for TES Operation in the COSINUS Dry Dilution Refrigerator'. In: *Journal of Low Temperature Physics* 217 (2024), pp. 418–425. DOI: 10.1007/s10909-024-03206-x (cited on pages 74, 81).

[155] C. Arpesella. 'Background Measurements at Gran Sasso Laboratory'. In: *Nucl. Phys. B (Proceedings Supplements* 28 A (1992), pp. 420–424 (cited on page 75).

[156] U.S. Geological Survey (USGS). *Helium Statistics and Information*. 2025. URL: https://www.usgs.gov/centers/national-minerals-information-center/helium-statistics-and-information (cited on page 77).

[157] Z. Zhao and C. Wang, eds. *Cryogenic engineering and technologies: principles and applications of cryogen-free systems*. Boca Raton: CRC Press, 2022 (cited on page 77).

[158] D. D. Osheroff, R. C. Richardson, and D. M. Lee. 'Evidence for a New Phase of Solid He^3'. In: *Phys. Rev. Lett.* 28 (14 1972), pp. 885–888. DOI: 10.1103/PhysRevLett.28.885 (cited on page 77).

[159] S.W. Van Sciver. *Helium Cryogenics*. International Cryogenics Monograph Series. Springer New York, 2012 (cited on page 78).

[160] J.C. Wheatley. 'Experimental properties of superfluid ^{3}He'. In: *Rev. Mod. Phys.* 47 (2 1975), pp. 415–470. DOI: 10.1103/RevModPhys.47.415 (cited on page 78).

[161] Kurt J. Lesker Company. *HiPace 400 Turbomolecular Pump Manual*. Kurt J. Lesker Company, 2025 (cited on page 78).

[162] K. Uhlig. 'Concepts for a low-vibration and cryogen-free tabletop dilution refrigerator'. In: *Cryogenics* 87 (2017), pp. 29–34. DOI: https://doi.org/10.1016/j.cryogenics.2017.08.003 (cited on page 79).

[163] Bluefors Oy. *PT420 Cryocooler with Remote Motor Option*. 2021. URL: https://bluefors.com/products/pulse-tube-cryocoolers/pt420-pulse-tube-cryocooler/ (cited on page 80).

[164] E. Olivieri et al. 'Vibrations on Pulse Tube Based Dry Dilution Refrigerators for Low Noise Measurements'. In: *Nuclear Instruments and Methods in Physics Research Section A: Accelerators, Spectrometers, Detectors and Associated Equipment* 858 (2017), pp. 73–79. DOI: 10.1016/j.nima.2017.03.045 (cited on page 80).

[165] CryoConcept. *CryoConcept*. 2025. URL: https://cryoconcept.com/ (cited on page 80).

[166] CryoConcept. *The Ultra-Quiet Technology Product Page*. 2025. URL: https://cryoconcept.com/product/the-ultra-quiet-technology/ (cited on page 80).

[167] G. Angloher et al. 'COSINUS model-independent sensitivity to the DAMA/LIBRA dark matter signal'. In: *Collaboration Review (in preparation)* (2025) (cited on page 81).

[168] P. Adari et al. 'EXCESS workshop: Descriptions of rising low-energy spectra'. In: *arXiv:2202.05097* (2022). DOI: 10.48550/arXiv.2202.05097 (cited on page 89).

[169] G. Angloher et al. 'The COSINUS project: perspectives of a NaI scintillating calorimeter for dark matter search'. In: *Eur. Phys. J. C* 76 (8 2016), p. 441. DOI: 10.1140/epjc/s10052-016-4278-3 (cited on page 89).

[170] G. Angloher et al. 'Composite $CaWO_4$ Detectors for the CRESST-II Experiment'. In: *AIP Conference Proceedings*. Vol. 1185. AIP Publishing, 2009, pp. 651–654. DOI: 10.1063/1.3292426 (cited on page 89).

[171] K.E. Gray. *Nonequilibrium superconductivity, phonons, and Kapitza boundaries*. Vol. 65. Springer Science & Business Media, 2012 (cited on page 90).

[172] W.A. Little. 'The transport of heat between dissimilar solids at low temperatures'. In: *Canadian Journal of Physics* 37.3 (1959), pp. 334–349 (cited on page 90).

[173] M. Sisti et al. 'Massive cryogenic particle detectors with low energy threshold'. In: *Nuclear Instruments and Methods in Physics Research Section A: Accelerators, Spectrometers, Detectors and Associated Equipment* 466.3 (2001), pp. 499–508. DOI: 10.1016/S0168-9002(01)00801-4 (cited on page 90).

[174] J.T. Karvonen et al. 'Electron–phonon interaction in thin copper and gold films'. In: *physica status solidi (c)* 1.11 (2004), pp. 2799–2802. DOI: 10.1002/pssc.200405326 (cited on page 90).

[175] S.J. Hart et al. 'Phase separation in tungsten transition edge sensors'. In: *AIP Conference Proceedings*. Vol. 1185. American Institute of Physics. 2009, pp. 215–218. DOI: 10.1063/1.3292318 (cited on page 90).

[176] A. Jain et al. 'The Materials Project: A materials genome approach to accelerating materials innovation'. In: *APL Materials* 1.011002 (2013). DOI: 10.1063/1.4812323 (cited on page 91).

[177] Y. Hinuma et al. 'Band structure diagram paths based on crystallography'. In: *Computational Materials Science* 128 (2017), pp. 140–184 (cited on page 91).

[178] Applied Physics Systems. *SQUID sensors*. 2025. URL: https://appliedphysics.com/ (cited on pages 92, 104, 113, 134).

[179] G. Angloher et al. 'Results on MeV-scale dark matter from a gram-scale cryogenic calorimeter operated above ground'. In: *Eur. Phys. J. C* 77.9 (2017), p. 637. DOI: 10.1140/epjc/s10052-017-5223-9 (cited on pages 93, 95, 104).

[180] G Angloher et al. 'Limits on WIMP dark matter using sapphire cryogenic detectors'. In: *Astropart. Phys.* 18.1 (2002), pp. 43–55. DOI: 10.1016/S0927-6505(02)00111-1 (cited on page 95).

[181] E. Gatti and P. F. Manfredi. 'Processing the Signals From Solid State Detectors in Elementary Particle Physics'. In: *Riv. Nuovo Cim.* 9.1 (1986), pp. 1–146. DOI: 10.1007/BF02822156 (cited on pages 95, 104, 115).

[182] G. Angloher, A. Bento, C. Bucci, et al. 'Results on Low Mass WIMPs Using an Upgraded CRESST-II Detector'. In: *The European Physical Journal C* 74 (2014), p. 3184. DOI: 10.1140/epjc/s10052-014-3184-9 (cited on page 96).

[183] Epoxy Technologies. *EPO-TEK®*. 2025. URL: https://www.epotek.com/ (cited on pages 96, 97, 102, 111, 125).

[184] G. Angloher et al. 'Limits on WIMP dark matter using scintillating $CaWO_4$ cryogenic detectors with active background suppression'. In: *Astropart. Phys.* 23 (2005), pp. 325–339. DOI: 10.1016/j.astropartphys.2005.01.006 (cited on page 102).

[185] G. Angloher et al. 'Commissioning run of the CRESST-II dark matter search'. In: *Astropart. Phys.* 31.4 (2009), pp. 270–276. DOI: 10.1016/j.astropartphys.2009.02.007 (cited on page 105).

[186] D. Schmiedmayer. 'Calculation of dark-matter exclusions-limits using a maximum Likelihood approach'. MA thesis. Technische Universität Wien, 2019 (cited on pages 106, 119).

[187] G. Angloher et al. 'A likelihood framework for cryogenic scintillating calorimeters used in the CRESST dark matter search'. In: *Eur. Phys. J. C* 84.922 (2024). DOI: 10.1140/epjc/s10052-024-13141-6 (cited on pages 108, 123).

[188] D Cintas et al. 'Quenching Factor consistency across several NaI(Tl) crystals'. In: *Journal of Physics: Conference Series*. Vol. 2156. 1. IOP Publishing. 2021, p. 012065. DOI: 10.1088/1742-6596/2156/1/012065 (cited on page 108).

[189] G Angloher et al. 'Results on low mass WIMPs using an upgraded CRESST-II detector'. In: *The European Physical Journal C* 74.12 (2014), pp. 1–6. DOI: 10.1140/epjc/s10052-014-3184-9 (cited on page 109).

[190] F. Reindl et al. 'Results of the first NaI scintillating calorimeter prototypes by COSINUS'. In: *J. Phys. Conf. Ser.* 1342.1 (2020). Ed. by Ken Clark et al., p. 012099. DOI: 10.1088/1742-6596/1342/1/012099 (cited on page 109).

[191] G. Angloher et al. 'Quasiparticle Diffusion in CRESST Light Detectors'. In: *J. Low. Temp. Phys.* 184 (2016), pp. 323–329. DOI: 10.1007/s10909-016-1512-1 (cited on pages 111, 133).

[192] Leiden Cryogenics BV. *Dilution refrigerator*. 2025. URL: https://leidencryogenics.nl/ (cited on pages 112, 134).

[193] D. Protopopescu et al. 'Theia: An advanced optical neutrino detector'. In: *Journal of Instrumentation* 15 (2020), P05003. DOI: 10.1088/1748-0221/15/05/P05003 (cited on page 113).

[194] K. J. Schäffner. 'Study of Backgrounds in the CRESST Dark Matter Search'. PhD thesis. Technische Universität München, 2013 (cited on pages 113, 134, 135).

[195] M. Mancuso et al. 'A method to define the energy threshold depending on noise level for rare event searches'. In: *Nucl. Instrum. Methods:A* 940 (2019), pp. 492–496. DOI: https://doi.org/10.1016/j.nima.2019.06.030 (cited on pages 115–117).

[196] G. Angloher et al. 'Results on low mass WIMPs using an upgraded CRESST-II detector'. In: *Eur. Phys. J. C* 74.12 (2014), p. 3184. DOI: 10.1140/epjc/s10052-014-3184-9 (cited on page 118).

[197] S. Yellin. 'Finding an upper limit in the presence of an unknown background'. In: *Phys. Rev. D* 66 (3 2002), p. 032005. DOI: 10.1103/PhysRevD.66.032005 (cited on pages 119, 122).

[198] S. Yellin. *Extending the optimum interval method*. 2007 (cited on pages 119, 122).

[199] H. Dembinski et al. *scikit-hep/iminuit*. 2020. DOI: 10.5281/zenodo.3949207. URL: https://doi.org/10.5281/zenodo.3949207 (cited on page 119).

[200] F. James and M. Roos. 'Minuit: A System for Function Minimization and Analysis of the Parameter Errors and Correlations'. In: *Comput. Phys. Commun.* 10 (1975), pp. 343–367. DOI: 10.1016/0010-4655(75)90039-9 (cited on page 119).

[201] R. Strauss et al. 'Energy-dependent light quenching in $CaWO_4$ crystals at mK temperatures'. In: *Eur. Phys. J. C* 74.7 (2014). DOI: 10.1140/epjc/s10052-014-2957-5 (cited on page 120).

[202] D. Baxter et al. 'Recommended conventions for reporting results from direct dark matter searches'. In: *Eur. Phys. J. C* 81.10 (2021), p. 907. DOI: 10.1140/epjc/s10052-021-09655-y (cited on page 122).

[203] C. Savage et al. 'Compatibility of DAMA/LIBRA dark matter detection with other searches'. In: *J. Cosmol. Astropart. Phys.* 010.04 (2009). DOI: 10.1088/1475-7516/2009/04/010 (cited on page 122).

[204] Govinda Adhikari et al. 'An experiment to search for dark-matter interactions using sodium iodide detectors'. In: *Nature* 564.7734 (2018), pp. 83–86. DOI: 10.1038/s41586-018-0739-1 (cited on page 122).

[205] G. Angloher et al. 'Simulation-based design study for the passive shielding of the COSINUS dark matter experiment'. In: *Eur. Phys. J. C* 82.3 (2022), p. 248. DOI: 10.1140/epjc/s10052-022-10184-5 (cited on page 122).

[206] F Wagner. 'Towards next-generation cryogenic dark matter searches with superconducting thermometers'. PhD thesis. Technische Universität Wien, 2023 (cited on page 126).

[207] Tectra Systems. *Tectra Deposition Progress Systems Product Page*. 2025. URL: https://tectra.de/deposition-progress/systems/ (cited on page 127).

[208] ECS Group. *Physics of Energy Conversion and Storage*. 2025. URL: https://www.ph.nat.tum.de/energy/ecs/ (cited on page 127).

[209] INFICON. *Quarzmonitorkristalle*. 2025. URL: https://www.inficon.com/de/produkte/d%C3%BCnnschichtabscheidung/quarz-monitor-kristall (cited on page 127).

[210] M. Todeschini et al. 'Influence of Ti and Cr Adhesion Layers on Ultrathin Au Films'. In: *ACS Applied Materials & Interfaces* 9.42 (2017), pp. 37374–37385. DOI: 10.1021/acsami.7b10136 (cited on page 128).

[211] Kurt J. Lesker Company. *Titan (Ti) Pellets Aufdampfmaterialien*. 2025. URL: https://de.lesker.com/newweb/deposition_materials/depositionmaterials_evaporationmaterials_1.cfm?pgid=ti1 (cited on page 128).

[212] G-Materials. *G-Materials: High Quality Scientific Resources*. 2025. URL: https://www.g-materials.de (cited on page 129).

[213] KLA Corporation. *Tencor P-7 Stylus Profiler | Benchtop Profilometer*. 2025. URL: https://www.kla.com/products/instruments/stylus-profilers/p-7 (cited on page 129).

[214] Musashi Engineering, Inc. *350PC Smart Desktop Robot*. 2025. URL: https://www.musashi-engineering.co.jp/products/desktop-robot/image-desktop-robot/350PC-smart-SM%CE%A9X (cited on page 131).

[215] C. Sailer et al. 'Low Temperature Light Yield Measurements in NaI and NaI(Tl)'. In: *The European Physical Journal C* 72 (2012), p. 2061. DOI: 10.1140/epjc/s10052-012-2061-7 (cited on page 132).

[216] M. P. Fontana, H. Blume, and W. J. van Sciver. 'Properties of Exciton States in NaI - The Intrinsic Photoluminescence'. In: *physica status solidi (b)* 29.1 (1968), pp. 159–166. DOI: https://doi.org/10.1002/pssb.19680290117 (cited on page 132).

[217] OPTEC München. *Si cutting and polishing*. 2025. URL: https://www.optec-muenchen.de/ (cited on page 133).

[218] R. Strauss et al. 'Gram-scale cryogenic calorimeters for rare-event searches'. In: *Phys. Rev. D* 96 (2 2017), p. 022009. DOI: 10.1103/PhysRevD.96.022009 (cited on page 133).

[219] M. Wüstrich. 'Improving Particle Discrimination and Achieving a 4π-Veto Detector Concept for the CRESST Experiment'. PhD thesis. Technische Universität München, 2020, p. 194 (cited on page 134).

[220] Magnicon GmbH. *SQUID Sensors*. 2025. URL: http://www.magnicon.com/squid-sensors (cited on page 134).

[221] M. Loidl et al. 'Quasiparticle diffusion over several mm in cryogenic detectors'. In: *Nuclear Instruments and Methods in Physics Research Section A* 465 (2001), pp. 440–446. DOI: 10.1016/S0168-9002(01)00621-0 (cited on page 135).

[222] R. Agnese et al. 'First Dark Matter Constraints from a SuperCDMS Single-Charge Sensitive Detector'. In: *Physical Review Letters* 121 (2018), p. 051301. DOI: 10.1103/PhysRevLett.121.051301 (cited on page 135).

[223] R. Agnese et al. 'Projected Sensitivity of the SuperCDMS SNOLAB Experiment'. In: *Physical Review D* 95 (2017), p. 082002. DOI: 10.1103/PhysRevD.95.082002 (cited on page 135).

[224] M. Mancuso et al. 'Searches for Light Dark Matter with the CRESST-III Experiment'. In: *Journal of Low Temperature Physics* 199 (2020), pp. 547–555. DOI: 10.1007/s10909-020-02343-3 (cited on page 135).

[225] A. G. Kozorezov et al. 'Phonon noise in cryogenic detectors: Downconversion and nonequilibrium dynamics'. In: *Physical Review B* 61 (2000), pp. 11807–11819. DOI: 10.1103/PhysRevB.61.11807 (cited on page 136).

[226] F. Mohs. *Grund-Riß der Mineralogie. Erster Theil. Terminologie, Systematik, Nomenklatur, Charakteristik*. Dresden: Arnoldischen Buchhandlung, 1822 (cited on page 137).